

# FRAMATOME COGEMA FUELS

December 15, 2000  
GR0192.doc

U. S. Nuclear Regulatory Commission  
ATTN: Document Control Desk  
Washington, DC 20555

Subject: Submittal of Accepted Version of Topical Report BAW-10228P,  
"SCIENCE."

Gentlemen:

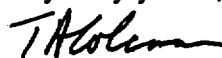
Enclosed are fifteen (15) copies of Topical Report BAW-10228P-A and twelve (12) copies of BAW-10228-A. These reports will serve as the accepted versions, proprietary and non-proprietary, of BAW-10228P which was recently reviewed and found to be acceptable by the NRC staff.

A copy of the NRC acceptance letter and accompanying SER is included between the title page and abstract of the report.

During the course of the review of BAW-10228P, Framatome Cogema Fuels (FCF) has provided additional information to the NRC for the purpose of clarifying certain portions of the report. That additional information is enclosed as appendix A of BAW-10228P.

In accordance with the provisions of 10 CFR 2.790 Framatome Cogema Fuels (FCF) requests that BAW-10228P-A be withheld from public disclosure. An affidavit supporting this request is attached.

Very truly yours,



T. A. Coleman, Vice President  
Government Relations

cc: A. C. Attard, NRC  
S. N. Bailey, NRC



Framatome Cogema Fuels  
3315 Old Forest Road, P.O. Box 10935, Lynchburg, VA 24506-0935  
Telephone: 804-832-3000 Fax: 804-832-3663

*TOOB 1/12*

cc: J. B. Andrews  
A. B. Copsey  
R. C. Deveney  
J. D. Gale  
C. F. McPhatter  
B. J. Delano  
P. M. Suhocki

AFFIDAVIT OF THOMAS A. COLEMAN

- A. My name is Thomas A. Coleman. I am Vice President of Government Relations for Framatome Cogema Fuels (FCF). Therefore, I am authorized to execute this Affidavit.
- B. I am familiar with the criteria applied by FCF to determine whether certain information of FCF is proprietary and I am familiar with the procedures established within FCF to ensure the proper application of these criteria.
- C. In determining whether an FCF document is to be classified as proprietary information, an initial determination is made by the Unit Manager, who is responsible for originating the document, as to whether it falls within the criteria set forth in Paragraph D hereof. If the information falls within any one of these criteria, it is classified as proprietary by the originating Unit Manager. This initial determination is reviewed by the cognizant Section Manager. If the document is designated as proprietary, it is reviewed again by personnel and other management within FCF as designated by the Vice President of Government Relations to assure that the regulatory requirements of 10 CFR Section 2.790 are met.
- D. The following information is provided to demonstrate that the provisions of 10 CFR Section 2.790 of the Commission's regulations have been considered:
- (i) The information has been held in confidence by FCF. Copies of the document are clearly identified as proprietary. In addition, whenever FCF transmits the information to a customer, customer's agent, potential customer or regulatory agency, the transmittal requests the recipient to hold the information as proprietary. Also, in order to strictly limit any potential or actual customer's use of proprietary information, the substance of the following provision is included in all agreements entered into by FCF, and an equivalent version of the proprietary provision is included in all of FCF's proposals:

AFFIDAVIT OF THOMAS A. COLEMAN (Cont'd.)

"Any proprietary information concerning Company's or its Supplier's products or manufacturing processes which is so designated by Company or its Suppliers and disclosed to Purchaser incident to the performance of such contract shall remain the property of Company or its Suppliers and is disclosed in confidence, and Purchaser shall not publish or otherwise disclose it to others without the written approval of Company, and no rights, implied or otherwise, are granted to produce or have produced any products or to practice or cause to be practiced any manufacturing processes covered thereby.

Notwithstanding the above, Purchaser may provide the NRC or any other regulatory agency with any such proprietary information as the NRC or such other agency may require; provided, however, that Purchaser shall first give Company written notice of such proposed disclosure and Company shall have the right to amend such proprietary information so as to make it non-proprietary. In the event that Company cannot amend such proprietary information, Purchaser shall, prior to disclosing such information, use its best efforts to obtain a commitment from NRC or such other agency to have such information withheld from public inspection.

Company shall be given the right to participate in pursuit of such confidential treatment."

AFFIDAVIT OF THOMAS A. COLEMAN (Cont'd.)

- (ii) The following criteria are customarily applied by FCF in a rational decision process to determine whether the information should be classified as proprietary. Information may be classified as proprietary if one or more of the following criteria are met:
- a. Information reveals cost or price information, commercial strategies, production capabilities, or budget levels of FCF, its customers or suppliers.
  - b. The information reveals data or material concerning FCF research or development plans or programs of present or potential competitive advantage to FCF.
  - c. The use of the information by a competitor would decrease his expenditures, in time or resources, in designing, producing or marketing a similar product.
  - d. The information consists of test data or other similar data concerning a process, method or component, the application of which results in a competitive advantage to FCF.
  - e. The information reveals special aspects of a process, method, component or the like, the exclusive use of which results in a competitive advantage to FCF.
  - f. The information contains ideas for which patent protection may be sought.

AFFIDAVIT OF THOMAS A. COLEMAN (Cont'd.)

The document(s) listed on Exhibit "A", which is attached hereto and made a part hereof, has been evaluated in accordance with normal FCF procedures with respect to classification and has been found to contain information which falls within one or more of the criteria enumerated above. Exhibit "B", which is attached hereto and made a part hereof, specifically identifies the criteria applicable to the document(s) listed in Exhibit "A".

- (iii) The document(s) listed in Exhibit "A", which has been made available to the United States Nuclear Regulatory Commission was made available in confidence with a request that the document(s) and the information contained therein be withheld from public disclosure.
- (iv) The information is not available in the open literature and to the best of our knowledge is not known by Combustion Engineering, Siemens, General Electric, Westinghouse or other current or potential domestic or foreign competitors of Framatome Cogema Fuels.
- (v) Specific information with regard to whether public disclosure of the information is likely to cause harm to the competitive position of FCF, taking into account the value of the information to FCF; the amount of effort or money expended by FCF developing the information; and the ease or difficulty with which the information could be properly duplicated by others is given in Exhibit "B".

E. I have personally reviewed the document(s) listed on Exhibit "A" and have found that it is considered proprietary by FCF because it contains information which falls within one or more of the criteria enumerated in Paragraph D, and it is information which is customarily held in confidence and protected as proprietary information by FCF. This report comprises information utilized by FCF in its business which afford FCF an opportunity to obtain a

AFFIDAVIT OF THOMAS A. COLEMAN (Cont'd.)

competitive advantage over those who may wish to know or use the information contained in the document(s).

T.A. Coleman

THOMAS A. COLEMAN

State of Virginia)

) SS. Lynchburg

City of Lynchburg)

Thomas A. Coleman, being duly sworn, on his oath deposes and says that he is the person who subscribed his name to the foregoing statement, and that the matters and facts set forth in the statement are true.

T.A. Coleman

THOMAS A. COLEMAN

Subscribed and sworn before me  
this 20<sup>th</sup> day of December, 2000.

Wanda L. Wade  
Notary Public in and for the City  
of Lynchburg, State of Virginia.

My Commission Expires 8/31/01

**EXHIBITS A & B**

**EXHIBIT A**

FCF Topical Report BAW-10228P-A, "SCIENCE"

**EXHIBIT B**

The above listed document contains information which is considered Proprietary in accordance with Criteria b, c, d, and e of the attached affidavit.

BAW-10228-A  
December 2000

# SCIENCE

FRAMATOME COGEMA FUELS

# FRAMATOME COGEMA FUELS

December 15, 2000

GR0192.doc

U. S. Nuclear Regulatory Commission  
ATTN: Document Control Desk  
Washington, DC 20555

Subject: Submittal of Accepted Version of Topical Report BAW-10228P,  
"SCIENCE."

Gentlemen:

Enclosed are fifteen (15) copies of Topical Report BAW-10228P-A and twelve (12) copies of BAW-10228-A. These reports will serve as the accepted versions, proprietary and non-proprietary, of BAW-10228P which was recently reviewed and found to be acceptable by the NRC staff.

A copy of the NRC acceptance letter and accompanying SER is included between the title page and abstract of the report.

During the course of the review of BAW-10228P, Framatome Cogema Fuels (FCF) has provided additional information to the NRC for the purpose of clarifying certain portions of the report. That additional information is enclosed as appendix A of BAW-10228P.

In accordance with the provisions of 10 CFR 2.790 Framatome Cogema Fuels (FCF) requests that BAW-10228P-A be withheld from public disclosure. An affidavit supporting this request is attached.

Very truly yours,



T. A. Coleman, Vice President  
Government Relations

cc: A. C. Attard, NRC  
S. N. Bailey, NRC



Framatome Cogema Fuels  
3315 Old Forest Road, P.O. Box 10935, Lynchburg, VA 24506-0935  
Telephone: 804-832-3000 Fax: 804-832-3663

# SCIENCE

by

R. C. Deveney  
G. H. Hobson  
P. L. Holman  
B. M. Palmer  
R. Aigle  
L. Daudin  
C. Garat  
P. Marotte  
A. Sargeni

FRAMATOME COGEMA FUELS  
P. O. Box 10935  
Lynchburg, Virginia 24506-0935



UNITED STATES  
NUCLEAR REGULATORY COMMISSION  
WASHINGTON, D.C. 20555-0001

May 24, 2000

Mr. T. A. Coleman, Vice President  
Government Relations  
Framatome Cogema Fuels, Inc.  
3315 Old Forest Road  
P.O. Box 10935  
Lynchburg, Virginia 24506-0935

SUBJECT: CORRECTION TO SAFETY EVALUATION OF TOPICAL REPORT BAW-10228P,  
"SCIENCE" (TAC NO. MA4599)

Dear Mr. Coleman:

By letter dated October 26, 1999, the NRC staff issued the safety evaluation (SE) for topical report BAW-10228P, "SCIENCE." The SE defines the basis for acceptance of the report and also provides the conditions and limitations on its use. The third condition (page 5 of the SE), third bullet, erroneously stated that the total rod worth uncertainty should be 100%. The total rod worth uncertainty should be 10%. We apologize for any inconvenience this may have caused.

In accordance with the procedures established in NUREG-0390, please publish accepted versions of this report, proprietary and non-proprietary, within 3 months of receipt of this letter. The accepted version should incorporate this letter along with the staff's October 26, 1999, letter and SE between the title page and the abstract. The accepted versions shall include an "-A" (designating accepted) following the report identification number.

If our criteria or regulations change so that our conclusions about the acceptability of the report are invalidated, FCF and the licensees referencing the topical report will be expected to revise and resubmit their respective documentation or to submit justification for the continued effective applicability of the topical report without revision of the respective documentation.

This concludes NRC review activity for this report (TAC No. MA4599). If you have any questions regarding this matter please contact Stewart Bailey, Project Manager, at (301) 415-1321, or by email at [snb@nrc.gov](mailto:snb@nrc.gov).

Sincerely,

Stuart A. Richards, Director  
Project Directorate IV & Decommissioning  
Division of Licensing Project Management  
Office of Nuclear Reactor Regulation

Project No. 693

cc: See next page



UNITED STATES  
NUCLEAR REGULATORY COMMISSION  
WASHINGTON, D.C. 20555-0001

October 26, 1999

Mr. T. A. Coleman, Vice President  
Government Relations  
Framatome Cogema Fuels, Inc.  
3315 Old Forest Road  
P.O. Box 10935  
Lynchburg, Virginia 24506-0935

SUBJECT: SAFETY EVALUATION OF TOPICAL REPORT BAW-10228P, "SCIENCE"  
(TAC NO. MA4599)

Dear Mr. Coleman:

We have completed our review of the subject topical report that Framatome Cogema Fuels, Inc., (FCF) submitted by letter dated February 5, 1998. The report is acceptable for referencing in licensing applications to the extent specified, and under the limitations delineated in the reports and in the associated U.S. Nuclear Regulatory Commission (NRC) safety evaluation, which is enclosed. The safety evaluation defines the basis for acceptance of the reports.

When the report appears as a reference in license applications, we do not intend to repeat our review of the matters described in the report that we found acceptable, except to ensure that the material presented is applicable to the specific plant involved. Our acceptance applies only to the matters described in the report.

In accordance with procedures established in NUREG-0390, it is requested that FCF publish accepted versions of this report, proprietary and non-proprietary, within 3 months of receipt of this letter. The accepted version shall incorporate this letter and the enclosed evaluation between the title page and the abstract. The accepted versions shall include an "A" (designating accepted) following the report identification symbol.

If our criteria or regulations change so that our conclusions about the acceptability of the report are invalidated, FCF and the licensees referencing the topical report will be expected to revise and resubmit their respective documentation or to submit justification for the continued effective applicability of the topical report without revision of the respective documentation.

Mr. T. A. Coleman

- 2 -

October 26, 1999

This concludes NRC review activity for this report (TAC MA4599). If you have any questions regarding this matter please contact me at (301) 415-1321, or by email at [snb@nrc.gov](mailto:snb@nrc.gov).

Sincerely,



Stewart N. Bailey, Project Manager, Section 2  
Project Directorate III  
Division of Licensing and Project Management  
Office of Nuclear Reactor Regulation

Project No. 693

Enclosure: Safety Evaluation

cc w/encl:

Mr. J. J. Kelly, Manager  
B&W Owners Group Services  
Framatome Technologies, Inc.  
P.O. Box 10935  
Lynchburg, VA 24506-0935

Mr. F. McPhatter, Manager  
Framatome Cogema Fuels  
3315 Old Forest Road  
P.O. Box 10935  
Lynchburg, VA 24506-0935



UNITED STATES  
NUCLEAR REGULATORY COMMISSION  
WASHINGTON, D.C. 20555-0001

SAFETY EVALUATION BY THE OFFICE OF NUCLEAR REACTOR REGULATION

TOPICAL REPORT BAW-10228P, "SCIENCE"

FRAMATOME COGEMA FUELS, INC.

1.0 BACKGROUND

BAW-10228P describes the SCIENCE code package submitted for review by Framatome Cogema Fuels, Inc., (FCF) for use in nuclear analysis of pressurized-water reactor (PWR) cores (Reference 1). SCIENCE is an integrated system of codes specifically designed for performing nuclear analysis of PWRs. The SCIENCE code package consists of core physics tools that are two-dimensional (2D) lattice calculations and three-dimensional (3D) core calculations and data manipulation codes. The SCIENCE code package consists of the codes APOLLO2-F, SMART, and COPILOTE.

The APOLLO2-F and SMART codes contain the physical description (models) of the SCIENCE code package, while COPILOTE serves as the interface between the user and the two physics codes, permitting sequencing and submittal of the calculations through interactive graphical interface.

2.0 TECHNICAL EVALUATION

2.1 Model Description

The underlying function of the SCIENCE code package is the linking of the major core physics codes, APOLLO2-F and SMART. APOLLO2-F calculates the parameters that are required by the SMART code. These parameters are the cross sections and the discontinuity factors, as well as the pin-to-pin reconstruction parameters (Reference 2).

For each type of composition, the parameters generated by the APOLLO2-F code are placed in data files referred to as "data libraries." The data libraries contain information regarding the dependence of these parameters on feedback system variables, such as burnup, xenon, soluble boron, moderator density, fuel temperature, and spectral effects (Reference 3). These libraries are generated in three steps:

- First, APOLLO2-F performs fuel depletion calculations and stores the data as depletion files. The stored data from the fuel depletion calculations account for the heterogeneity of the assembly under normal (reference) conditions and perturbed conditions. The perturbed condition is signified in this case by a change in the water density, thus indicating the spectral differences between actual conditions in the core and the normal reference core depletion.

- Second, APOLLO2-F takes the results of the depletion calculations and uses them to initialize the isotopic concentrations for new calculations in which one or more physical state variables of the assembly are modified with respect to their initial value(s). These calculations are typically referred to as restart calculations. Some of the variables are xenon level, moderator density, fuel temperature, and a variable that is representative of the control rod presence. All this generated data, representing numerous conditions that the assembly may encounter during the cycle depletion in the core, are placed in "restart" files for use by the SMART code.
- Third, APOLLO2-F creates two data files for each type of fuel. One file contains cross sections and discontinuity factors and the other file contains reconstruction data (pin-by-pin power distribution and burnup). These files form the libraries that contain parameters that are a function of the state variables, such as boron and xenon concentrations, burnup, moderator density, spectral history, fuel temperature profile, and control rod locations.

The fuel assembly is numerically fitted and geometrically represented by dividing the fuel assembly into cubic regions to account for all the possible variations that go into making up the assembly. These variations are represented by polynomial expansions, utilizing determined polynomial coefficients to reproduce the assembly parameters calculated by the APOLLO2-F restart calculations at the fitting point.

## 2.2 Description of Codes

APOLLO2-F is an assembly lattice code developed by the Commissariat a l'Energie Atomique and modified by FCF for its design needs. It solves the 99-group transport equation for an assembly geometry and furnishes the homogenized two-group cross sections for the SMART code. The transport equation is solved using the integral-differential equation form that is discretized based on the collision probability method. FCF pointed out that a coupling of the regrouped multicell calculation and the six-group homogeneous calculation permits a good compromise between accuracy and calculation cost.

This coupling is provided by heterogeneous/homogeneous equivalence functions contained in the code. The assembly calculations can be carried out on various geometries (one-eighth of an assembly, one-fourth of an assembly) with different boundary conditions and symmetry. A sophisticated self-shielding model is applied to the cross sections in order to correctly take resonances into account. The flux calculations can be performed with a search for critical buckling to obtain proper spectral weighting. APOLLO2-F contains a fuel depletion module. The reflector constants (radial or axial) are generated from one-dimensional (1D) APOLLO2-F calculations using the code's  $S_N$  option.

The SMART code solves the two-energy group diffusion equation for the core geometry under static or kinetic conditions. It solves a neutron balance equation using the average flux and provides the core power distributions for assemblies and also for each pin (on a pin-by-pin basis) in every assembly. The nodal expansion method is used to solve the neutron balance equation. It is based on a coupling between a coarse mesh finite difference calculation and a calculation of the neutron current at each interface.

The calculation of the nodal currents is performed by solving a 1D diffusion equation at each calculation node interface. The solution for the adjustment of the nodal currents is obtained by making assumptions of the fast and thermal neutron flux shapes on both sides of the interface and building a system of equations that can be solved directly. This solution is referred to as the "two-node" problem. The accuracy of the process is improved by using discontinuity factors, quadratic transverse leakage, and burnup gradients within the node. The burnup and spectral effects are modeled using a microscopic fuel depletion model.

The main depletion chains for the heavy nuclei and the main fission products are explicitly treated by SMART. The two energy group microscopic cross sections required to calculate isotopic depletion are obtained from data generated by the APOLLO2-F code. The microscopic cross sections and the isotopic densities resulting from the depletion calculations provide the macroscopic cross sections for the flux solution. The microscopic cross sections are stored in "multi-parameterized" data libraries from which the core calculation interpolates, depending on the local node conditions. A set of seven parameters is selected for cross section dependency: burnup, boron concentration, xenon, moderator density, fuel temperature, a spectral history parameter, and a control rod presence parameter. The SMART code calculates fuel pin information for power and burnup and reaction rates in the instrument tube by means of a pin reconstruction algorithm. The SMART code also solves the time-dependent two-energy group diffusion equation for 3D core geometry.

COPILOTE is an operating environment rather than a conventional calculational computer code. It is the graphical user interface by which the user processes input and output, controls the flow of data from one code to another, and displays the status of the calculations.

### 2.3 Measurement Comparisons

In Section 4 of the submittal, FCF provided numerous examples comparing the results of APOLLO2-F and the SMART code with measurement data. The data were collected from six reactors (Three Mile Island Unit 1, Oconee Units 1 and 2, McGuire Unit 1, Gravelines Unit 5, and Sequoyah Unit 1). These cores were selected on the basis of obtaining a wide variety of conditions, such as the type of burnable poison, fuel enrichment, loading patterns, and control rod patterns. Reactivity predictions versus core burnup, control rod worth, reactivity coefficients, and power distributions were provided (on a local and global basis) and compared to measured data from operating PWRs.

The agreement between measured data and SCIENCE prediction is generally very good. The SCIENCE results were just as good or better than prior FCF licensed codes predictions. The uncertainties for single bank worths and total bank worths that are supported by the data presented are 15 percent and 10 percent, respectively. Previous FCF methodology (Reference 1) contained a bias difference between the 15x15 and the 17x17 bank worth results. This bias difference was again observed in the SCIENCE methodology. The cause of the bias is due to the different sources of the measured results. The 15x15 data were obtained exclusively from B&W plants. Nearly all of the 17x17 data were obtained from other vendors using various measurement techniques (Reference 4).

Good agreement was achieved for ejected rod worths, critical boron concentrations, temperature coefficients, and power Doppler coefficients. In addition, review of the data shows that SCIENCE accurately predicts the core total peak and radial power peak. The nuclear reliability factors (NRFs) that SCIENCE uses to adjust the predicted local and global power distribution, were found to be less than those previously established NRFs provided in Reference 1. The staff agrees with the presented results.

#### 2.4 Qualification Methods for Future Modifications to the Science Code Package

FCF intends to periodically update the SCIENCE code package to incorporate the latest analytics and computation techniques. Consequently, any code development or improvement of the SCIENCE code package would necessitate benchmarking and validating the SCIENCE code package to ensure that any new feature(s) implemented will produce results in keeping with a standard set of qualification criteria as stated in the submitted Topical Report BAW-10228P.

The method to be used to qualify SCIENCE for future changes is similar to the method presented in this submittal and previous topical report submittals. This method will require that neutron code qualification be based on the ability of the modified SCIENCE code package to predict several key neutronic parameters. Some of these parameters are critical boron or k-effective at hot zero power, critical boron or critical k-effective at hot full power, individual bank rod worths, total rod worths, ejected rod worths, isothermal temperature coefficients, power Doppler coefficients, hot pin power, and hot pellet power (see Table 5.1 of References 1 and 3). These parameters will be recalculated with the modified SCIENCE code package and compared to measured results and new statistics generated along with their associated uncertainties. Subjecting the modified code package to the listed criteria will emphasize the contributions of the implemented features to the code package rather than highlight the differences between the two code packages. Consequently, any modifications to the SCIENCE code package that meet the listed criteria in Tables 5-1 and 5-2 of this submittal will validate the modifications made to the SCIENCE code package. If the changes to the SCIENCE code package meet the criteria, FCF will internally document the changes to the code package and the associated results without notifying the NRC since there were no changes to the uncertainties or their application. However, if changes to the uncertainties occur, FCF will submit supporting documentation to the NRC whenever the method changes affect the uncertainties to be applied in licensing applications.

The methodology and the data provided in this submittal, Topical Report BAW-10228P, form the basis for the current SCIENCE code package. Future application of the current SCIENCE code package to data not provided in this topical report (such as new fuel designs) will require revalidation of the SCIENCE code package.

#### 2.5 Range of Applicability of Benchmarking

The chosen benchmarks in this topical report include the types of fuel and poison that are typically licensed. The data presented in this topical report are sufficient to qualify the SCIENCE code package for the typical fuel types listed in this submittal. If a new fuel design is used that contains materials (poison, mixed oxide fuel and/or hafnium control rods, etc.) outside this collection of benchmarks, additional benchmarks will have to be established. In

accordance with its agreement, (Reference 4), FCF will submit to the NRC staff a description of the new design feature, the new benchmarks, and any impact on the current uncertainty factors.

### 3.0 CONCLUSION

The staff has reviewed the analyses in Topical Report BAW-10228P, "SCIENCE," and finds it acceptable for licensing applications, subject to the following conditions in accordance with FCF's agreement (Reference 4) :

1. The SCIENCE code package shall be applied in such a manner that predicted results are within the ranges of the validation criteria presented in Table 5-1 and the measurement uncertainties presented in Table 5-2.
2. Fuel designs to which the SCIENCE code package will be applied shall be within the validation bases of BAW-10228P. The bases of BAW-10228P are considered valid for the following conditions:
  - 15x15 or 17x17 UO<sub>2</sub> fuel designs.
  - U235 enrichments less than or equal to a maximum of 5.0 w/o.
  - Gadolinia loadings less than or equal to 8.3 w/o (nominal 8.0 w/o).
3. The following uncertainties shall be applied to the SCIENCE code package results:
  - Maximum pin peaking uncertainty of 3.8 percent.
  - Maximum pellet peaking uncertainty of 4.8 percent.
  - Total rod worth uncertainty of 100 percent.
  - Bank rod worth uncertainty of 15 percent.
4. The SCIENCE code package shall only be used for PWR licensing analyses by FCF unless approved by the NRC for use by other organization.

### 4.0 REFERENCES

1. Letter from T. A. Coleman, Vice President of Government Relations, Framatome Cogema Fuels, Inc., to the NRC, regarding the submittal of the SCIENCE code package, dated October 12, 1998.
2. R. Sanchez, J. Mondot, Z. Stankowski, A. Cossic, and I. Zmijarevic, "APOLLO2-F: A User-oriented, Portable Modular Code for Multi-group Transport Assembly Calculations." International Topical Meeting on Advances in Reactor Physics, Mathematics and Computation, Paris, France, April 27-30, 1987.
3. R. Sanchez and M. Vergain, "An Acceleration Procedure for the Iterative Solution of the Flux Current Equations in the APOLLO2-F Code." International Topical Meeting on the Physics of Reactors: Operation and Design Computation, Marseilles, France, PHYSOR 90, April 23-27, 1990.

4. Letter from T. A. Coleman, Vice President of Government Relations, Framatome Cogema Fuels, Inc., to the NRC, regarding the submittal of Topical Report BAW-10228P, "SCIENCE", dated September 23, 1999.

Principle Contributor: T. Attard

Date: October 26, 1999

FRAMATOME COGEMA FUELS

Lynchburg, Virginia

Topical Report BAW-10228-A

December 2000

SCIENCE

Key Words: SCIENCE, APOLLO2-F, SMART, Collision Probability, SN, Nodal Expansion, Kinetics, Core Neutronic Predictions, Benchmarks

ABSTRACT

The SCIENCE nuclear code package is an integrated system of codes to perform the nuclear analysis of PWR cores. It consists of a set of core physics tools based on 2D lattice calculations and 3D core calculations and data manipulation codes. The neutronic models in SCIENCE are APOLLO2-F and SMART. APOLLO2-F performs the 2D lattice calculations and SMART performs the 3D core calculations. SMART is capable of performing both static and kinetic calculations in two or three dimensions.

SCIENCE calculations are compared with measured data from several operating PWR cores and critical experiments. The results from these analyses demonstrate the capability of SCIENCE to accurately model PWR cores.

# Table of Contents

<u>Section</u>	<u>Page</u>
1. INTRODUCTION .....	1-1
2. SUMMARY OF RESULTS AND CONCLUSIONS .....	2-1
3. MODEL DESCRIPTION .....	3-1
3.1 Architecture of the SCIENCE Nuclear Code Package .....	3-1
3.1.1 APOLLO2-F Fuel Depletion Calculations .....	3-1
3.1.2 APOLLO2-F Restart Calculations .....	3-1
3.1.3 Creation of Data Libraries .....	3-1
3.2 THE APOLLO2-F LATTICE CODE .....	3-2
3.2.1 The CEA 93 Cross Section Library .....	3-2
3.2.2 Assembly Calculations .....	3-3
3.2.2.1 Self-Shielding .....	3-5
3.2.2.2 Collision Probabilities .....	3-6
3.2.2.3 Heterogeneous / Homogeneous Equivalence .....	3-11
3.2.2.4 The $S_N$ calculation .....	3-12
3.2.2.5 Fuel Depletion .....	3-15
3.2.3 Reflector Calculation .....	3-16
3.3 THE SMART CORE CODE .....	3-17
3.3.1 Neutron Diffusion Model .....	3-17
3.3.1.1 Nodal Equivalence .....	3-17
3.3.1.2 Nodal Expansion Method (NEM) .....	3-17
3.3.1.2.1 Nodal Flux Calculation .....	3-18
3.3.1.2.2 Reevaluation of the Currents: Nodal Iteration .....	3-20
3.3.1.3 Cross Section Model .....	3-23
3.3.1.3.1 Interpolation in the APOLLO2-F Data Libraries .....	3-23
3.3.1.3.2 Intra-nodal Cross Sections .....	3-24
3.3.1.3.3 Re-Homogenization .....	3-24
3.3.1.4 Convergence Algorithm and Model Coupling .....	3-25
3.3.1.4.1 Inner Iteration .....	3-25
3.3.1.4.2 Outer Iteration .....	3-26
3.3.1.4.3 Nodal Iteration .....	3-26
3.3.1.4.4 TH Feedback Iteration .....	3-26
3.3.2 Kinetics Calculations .....	3-26
3.3.3 Pin Reconstruction .....	3-30
3.3.3.1 Pin Power Reconstruction .....	3-30
3.3.3.1.1 Determination of the Homogeneous Fluxes .....	3-30
3.3.3.1.2 Determination of the Homogeneous Cross Sections .....	3-32
3.3.3.1.3 Determination of the Homogeneous Pin Power .....	3-32
3.3.3.1.4 Determination of the Heterogeneous Pin-by-Pin Power .....	3-32
3.3.3.2 Pin Burnup Reconstruction .....	3-33
3.3.3.3 Detector Response Reconstruction .....	3-33
3.3.4 Depletion Model .....	3-34
3.3.4.1 Depletion Chains .....	3-34
3.3.4.2 Processing the Depletion Equations .....	3-34
3.3.5 Thermal-Hydraulic Model .....	3-36
3.3.5.1 Calculation of Enthalpy and Heat Flux .....	3-37
3.3.5.2 Transition between the Various Flow Regimes .....	3-38
3.3.5.2.1 Wall Temperature Model .....	3-38
3.3.5.2.2 Bubble Detachment Model .....	3-39
3.3.5.3 Void Fraction Calculation .....	3-40

## Table of Contents (cont'd)

<u>Section</u>	<u>Page</u>
3.3.6 Rod Thermal Model .....	3-40
3.3.6.1 Kinetic Thermal Modeling of the Fuel Rod .....	3-41
4. MEASUREMENT COMPARISONS .....	4-1
4.1 Reactivity Analyses .....	4-1
4.1.1 Reactivity Versus Burnup .....	4-2
4.1.2 Hot Zero Power All-Rods-Out Reactivity .....	4-2
4.1.3 Control Rod Worths .....	4-2
4.1.4 Ejected Rod Worths .....	4-3
4.1.5 Isothermal Temperature Coefficients at Zero Power .....	4-4
4.1.6 Power Doppler Coefficients .....	4-4
4.1.7 Reactivity Calculation Statistical Results .....	4-4
4.2 Power Distribution Analyses .....	4-5
4.2.1 Global Power Distributions .....	4-5
4.2.1.1 TMI-1 Cycles 5, 6, 7, 9, and 10 .....	4-6
4.2.1.2 Sequoyah-1 Cycles 1-5 .....	4-7
4.2.1.3 Gravelines-5 Cycle 1 .....	4-8
4.2.1.4 Oconee 1 Cycle 1 Power Transient .....	4-8
4.2.2 Local Pin Power Distributions .....	4-8
4.2.2.1 Critical Experiments .....	4-9
4.2.2.2 APOLLO2-F versus SMART Multi-Assembly .....	4-10
4.3 SMART Kinetics .....	4-11
4.4 Nuclear Reliability Factors .....	4-12
4.4.1 Statistical Results .....	4-12
4.4.2 NRF Determination .....	4-14
5. QUALIFICATION METHOD .....	5-1
5.1 Methods Qualification Criteria .....	5-1
5.2 Range of Applicability of Benchmarks .....	5-3
6. REFERENCES .....	6-1
APPENDIX A - Documented Response to Informal NRC Request for Additional Information .....	A-1

## List of Tables

<u>Table</u>	<u>Page</u>
Table 4-1. Core Characteristics .....	4-16
Table 4-2. HZP Critical K-effective .....	4-17
Table 4-3. Individual Bank Worths .....	4-18
Table 4-4. Total Bank Worths .....	4-20
Table 4-5. Ejected Rod Worths .....	4-21
Table 4-6. HZP Isothermal Temperature Coefficients .....	4-22
Table 4-7. Power Doppler Coefficient.....	4-23
Table 4-8. Reactivity Statistical Results .....	4-23
Table 4-9. Total Rod Worth Statistical Results .....	4-23
Table 4-10. Critical Core Configuration Description .....	4-24
Table 4-11. Summary of Critical Experiments.....	4-25
Table 4-12. Critical Benchmark Statistical Results .....	4-25
Table 4-13. Assembly Loading for Multi-Assembly Problems.....	4-26
Table 4-14. Pin Power Peaking Results for Multi-Assembly Problems .....	4-27
Table 4-15. Conditions for the Rod Drop Test .....	4-28
Table 4-16. Radial Power Statistics.....	4-29
Table 4-17. Peak Power Statistics .....	4-29
Table 4-18. Summary of Local Pin Power Statistics .....	4-30
Table 4-19. NRF Values for SCIENCE.....	4-30
Table 5-1. Methods Qualification Criteria.....	5-4
Table 5-2. SCIENCE Compared to Statistical Criteria.....	5-5

## List of Figures

<u>Figure</u>	<u>Page</u>
Figure 3-1. Architecture of the SCIENCE Code Package .....	3-43
Figure 3-2. APOLLO2-F Assembly Calculation Scheme: Basic Principles.....	3-44
Figure 3-3. APOLLO2-F Assembly Calculation Scheme: Depletions .....	3-45
Figure 3-4. APOLLO2-F Assembly Calculation Scheme: Restart Cases.....	3-45
Figure 3-5. Flux Expansion for Interface Currents.....	3-46
Figure 3-6. Physical Representation for Interface Probabilities .....	3-47
Figure 3-7. Reduction of Cells to Nodes Due to Homogenization .....	3-48
Figure 3-8. Rehomogenization of the Node .....	3-49
Figure 3-9. Overall Diagram of the Iterative Process.....	3-50
Figure 3-10. Coupling of the Models in the Kinetic Calculation .....	3-51
Figure 3-11. Heavy Isotope Depletion Chain in SMART .....	3-52
Figure 3-12. Iodine and Xenon Depletion Chain in SMART.....	3-53
Figure 3-13. Samarium Depletion Chain in SMART .....	3-53
Figure 3-14. Thermal-Hydraulic Boiling Models.....	3-54
Figure 4-1. HFP K-effective Versus Core Burnup .....	4-31
Figure 4-2. TMI 1 Cycle 5 58 EFPD .....	4-32
Figure 4-3. TMI 1 Cycle 5 140 EFPD .....	4-33
Figure 4-4. TMI 1 Cycle 5 206 EFPD .....	4-34
Figure 4-5. TMI 1 Cycle 5 279 EFPD .....	4-35
Figure 4-6. TMI 1 Cycle 6 17 EFPD .....	4-36
Figure 4-7. TMI 1 Cycle 6 79 EFPD .....	4-37
Figure 4-8. TMI 1 Cycle 6 176 EFPD .....	4-38
Figure 4-9. TMI 1 Cycle 6 288 EFPD .....	4-39
Figure 4-10. TMI 1 Cycle 6 403 EFPD .....	4-40
Figure 4-11. TMI 1 Cycle 7 3 EFPD .....	4-41
Figure 4-12. TMI 1 Cycle 7 101 EFPD .....	4-42
Figure 4-13. TMI 1 Cycle 7 241 EFPD .....	4-43
Figure 4-14. TMI 1 Cycle 7 346 EFPD .....	4-44
Figure 4-15. TMI 1 Cycle 9 39 EFPD .....	4-45
Figure 4-16. TMI 1 Cycle 9 549 EFPD .....	4-46
Figure 4-17. TMI 1 Cycle 10 7 EFPD.....	4-47
Figure 4-18. TMI 1 Cycle 10 652 EFPD .....	4-48
Figure 4-19. Sequoyah 1 Cycle 1 133 EFPD.....	4-49
Figure 4-20. Sequoyah 1 Cycle 1 378 EFPD.....	4-50
Figure 4-21. Sequoyah 1 Cycle 2 50 EFPD.....	4-51
Figure 4-22. Sequoyah 1 Cycle 2 301 EFPD.....	4-52
Figure 4-23. Sequoyah 1 Cycle 3 31 EFPD.....	4-53
Figure 4-24. Sequoyah 1 Cycle 3 305 EFPD.....	4-54
Figure 4-25. Sequoyah 1 Cycle 4 17 EFPD.....	4-55
Figure 4-26. Sequoyah 1 Cycle 4 407 EFPD.....	4-56
Figure 4-27. Sequoyah 1 Cycle 5 10 EFPD.....	4-57
Figure 4-28. Sequoyah 1 Cycle 5 394 EFPD.....	4-58
Figure 4-29. Gravelines-5 Cycle 1 Loading Map .....	4-59
Figure 4-30. Gravelines-5 Cycle 1 Poison Loadings.....	4-60
Figure 4-31. Gravelines 5 Cycle 1 25 EFPD .....	4-61
Figure 4-32. Gravelines 5 Cycle 1 90 EFPD .....	4-62
Figure 4-33. Gravelines 5 Cycle 1 153 EFPD .....	4-63
Figure 4-34. Gravelines 5 Cycle 1 183 EFPD .....	4-64
Figure 4-35. Gravelines 5 Cycle 1 207 EFPD .....	4-65

## List of Figures (cont'd)

<u>Figure</u>	<u>Page</u>
Figure 4-36. Gravelines 5 Cycle 1 240 EFPD .....	4-66
Figure 4-37. Gravelines 5 Cycle 1 315 EFPD .....	4-67
Figure 4-38. OCONEE-1 Cycle 1 Power Transient .....	4-68
Figure 4-39. SCIENCE Geometric Modeling of the Critical Experiments .....	4-69
Figure 4-40. Pin Power Distribution Comparison For Core XI Loading 2 .....	4-70
Figure 4-41. Pin Power Distribution Comparison For Core XI Loading 4 .....	4-70
Figure 4-42. Pin Power Distribution Comparison For Core XI Loading 5 .....	4-71
Figure 4-43. Pin Power Distribution Comparison For Core XI Loading 6 .....	4-71
Figure 4-44. Pin Power Distribution Comparison For Core XI Loading 7 .....	4-72
Figure 4-45. Pin Power Distribution Comparison For Core XI Loading 8 .....	4-72
Figure 4-46. Pin Power Distribution Comparison For Core XI Loading 11 .....	4-73
Figure 4-47. Pin Power Distribution Comparison For Core 1 .....	4-74
Figure 4-48. Pin Power Distribution Comparison For Core 5 .....	4-74
Figure 4-49. Pin Power Distribution Comparison For Core 12 .....	4-75
Figure 4-50. Pin Power Distribution Comparison For Core 14 .....	4-75
Figure 4-51. Pin Power Distribution Comparison For Core 18 .....	4-76
Figure 4-52. Pin Power Distribution Comparison For Core 20 .....	4-76
Figure 4-53. Set 6 - Relative % Differences for Multi-Assembly at 0 GWD/MtU .....	4-77
Figure 4-54. Set 6 - Relative % Differences for Multi-Assembly at 24 GWD/MtU .....	4-77
Figure 4-55. Set 12 - Relative % Differences for Multi-Assembly at 0 GWD/MtU .....	4-78
Figure 4-56. Set 12 - Relative % Differences for Multi-Assembly at 8 GWD/MtU .....	4-78
Figure 4-57. Set 12 - Relative % Differences for Multi-Assembly at 34 GWD/MtU .....	4-79
Figure 4-58. 193 Core Layout for Dropped Rod Test .....	4-80
Figure 4-59. 157 Core Layout for Dropped Rod Test .....	4-81
Figure 4-60. Case 1 Rod Drop Simulation .....	4-82
Figure 4-61. Case 2 Rod Drop Simulation .....	4-83
Figure 4-62. Case 3 Rod Drop Simulation .....	4-84
Figure 4-63. Case 4 Rod Drop Simulation .....	4-85
Figure 4-64. Case 5 Rod Drop Simulation .....	4-86
Figure 4-65. Case 6 Rod Drop Simulation .....	4-87
Figure 4-66. Frequency Distribution for Radial Pin Power Data .....	4-88
Figure 4-67. Frequency Distribution for Peak Pellet Power Data .....	4-88
Figure 4-68. Frequency Distribution for Critical Experiments.....	4-89
Figure 4-69. Frequency Distribution for Multi-Assembly Problems.....	4-89

## 1. INTRODUCTION

The SCIENCE nuclear code package is an integrated system of codes to perform the nuclear analysis of PWR cores. It consists of a set of core physics tools based on two dimensional (2D) lattice calculations, three dimensional (3D) core calculations and data manipulation codes. SCIENCE comprises the following major codes:

- APOLLO2-F
- SMART
- COPILOTE

APOLLO2-F and SMART are the codes containing the physical models of the SCIENCE code package.

COPILOTE is the interface with the user; it permits sequencing and submitting the calculations via an interactive graphical interface.

APOLLO2-F is an assembly lattice code developed by the Commissariat à l'Energie Atomique (CEA) and modified by Framatome for its design needs. It solves the 99-group transport equation for an assembly geometry and furnishes the homogenized two-group cross sections for the SMART code. The transport equation is solved using the integral-differential form discretized based on the collision probability method. A coupling of the regrouped multicell calculation and the six-group homogeneous calculation permits a good compromise between accuracy and calculation cost. This coupling is provided by heterogeneous/homogeneous equivalence functions contained in the code. The assembly calculations can be carried out on various geometries (1/8 of an assembly, 1/4 of an assembly), with different boundary conditions and symmetry. A sophisticated self-shielding model is applied to the cross sections in order to correctly take into account resonances. The flux calculations can be performed with a search for critical buckling to obtain proper spectral weighting. APOLLO2-F contains a fuel depletion module. The reflector constants (radial or axial) are generated from one-dimensional (1D) APOLLO2-F calculations using the code's  $S_N$  option.

The SMART code solves the two-energy group diffusion equation for the core geometry under static or kinetic conditions. It solves a neutron balance using the average flux and provides the core power distributions for assemblies and also for each pin in every assembly. The nodal expansion method (NEM) is used to solve the problem. It is based on a coupling between a coarse mesh finite difference calculation and a calculation of the neutron currents at each interface. The evaluation of the currents is used to correct those calculated by finite difference methodology. The calculation of the nodal currents is performed by solving a 1D diffusion equation at each calculation node interface. The solution for the adjustment of the nodal currents is obtained by making assumptions of the fast and thermal neutron flux shapes on both sides of the interface and building a system of equations that can be solved directly. This solution is referred to as the "two-node" problem. The accuracy of the process is improved by using discontinuity factors, quadratic transverse leakage, and burnup gradients within the node.

The burnup and spectral effects are modeled using a microscopic fuel depletion model. The main depletion chains for the heavy nuclei and the main fission products are explicitly treated by SMART. The two energy group microscopic cross sections, required to calculate isotopic depletion, are obtained from data generated by the APOLLO2-F code. The microscopic cross sections and the isotopic densities, resulting from the depletion calculations, provide the macroscopic cross sections for the flux solution. The microscopic cross sections are stored in "multi-parameterized" data libraries from which the core calculation interpolates depending on the local node conditions. A set of seven parameters is selected for cross section dependency: burnup, boron concentration, xenon, moderator density, fuel temperature, a spectral history parameter, and a control rod presence parameter. The SMART code calculates fuel pin information for power and burnup and reaction rates in the instrument tube by means of a pin reconstruction algorithm. The SMART code also solves the time dependent two-energy group diffusion equation for 3D core geometry.

COPILOTE is an operating environment rather than a conventional calculational computer code. It is the graphical user interface by which the user processes input and output, controls the flow of data from one code to another, and displays the status of the calculations.

This topical report comprises six sections: Introduction, Summary of Results and Conclusions, Model Description, Measurement Comparisons, Qualification Method, and References. The capability of SCIENCE to accurately model PWR cores is demonstrated in this report by comparison of calculated and measured data. A summary of the results of these comparisons is given in section 2.

The methodology used by SCIENCE is described in section 3. This includes the theory, assumptions, and equations for the neutronic and isotopic depletion models, kinetic models, and thermal hydraulic models. An overview of the cross section fitting methodology is also provided.

SCIENCE calculations are compared with operating data from TMI-1 (cycles 1-10), Oconee-1 (cycle 1 - including a power transient), Oconee-2 (cycle 1), McGuire-1 (cycle 1), Gravelines-5 (cycle 1) and Sequoyah-1 (cycles 1-5). In addition, comparisons of calculations with critical experiment data are performed. Comparisons between APOLLO2-F and SMART are provided to demonstrate the depletion capabilities of the pin power reconstruction method. Comparisons of the kinetics option of SMART to data from several dropped rod transients are also shown. Section 4 gives a detailed account of these analyses.

Section 5 provides the method employed by FCF to qualify SCIENCE and any future modifications. The calculational scheme in SCIENCE is very flexible and modular. Because of this modularity and the need to permit continuous improvement of methods, FCF will be updating methods in the future. The presentation of this topical provides the qualification of the current SCIENCE code package, and the method that FCF will use to qualify any future SCIENCE model improvements. Section 6 lists the references.

## 2. SUMMARY OF RESULTS AND CONCLUSIONS

The comparisons of predicted and measured core physics parameters, presented in Section 4, demonstrate that the SCIENCE calculational model is an accurate tool for predicting both local and global core behavior. Very good agreement was obtained between measured and calculated control rod bank and total rod worths and the statistics are very similar to those in reference 1. The current SCIENCE results support a 10% total rod worth uncertainty. Additional data points will be obtained and a future submittal made to support the reduced total rod worth uncertainties in references 13 and 14, as summarized in Section 5. In addition, measured and calculated ejected rod worths agree within 12%. Measured critical boron concentrations at zero power and full power generally lie within  $\pm 50$  ppm B of those predicted. Measured and calculated temperature coefficients agree within 1.4 pcm/ $^{\circ}$ F. The calculated Power Doppler coefficients agreed within 1.4 pcm/% FP (full power) of measured results. These comparisons demonstrate SCIENCE's accuracy in predicting core physics parameters. These prediction capabilities are similar to or better than those previously established in reference 1.

The measured and calculated power distribution comparisons show that SCIENCE accurately predicts the core total peak and radial peak. The NRFs (Nuclear Reliability Factors) for SCIENCE are found to be less than the previously established NRFs of 1.048 for the hot pellet power and 1.038 for the hot pin power in reference 1.

SCIENCE can be used to perform physics calculations for the reload designs of pressurized water reactors, to analyze reactivity and power distributions, and to make startup predictions. In addition, a qualification method is provided that defines the method that FCF will use to qualify future method changes to SCIENCE.

### 3. MODEL DESCRIPTION

This section describes the overall architecture of the SCIENCE nuclear code package, the APOLLO2-F Lattice Code, and the SMART Core Code.

#### 3.1 Architecture of the SCIENCE Nuclear Code Package

Core modeling in the SCIENCE nuclear code package is based on the linking of two major core physics codes, APOLLO2-F and SMART. APOLLO2-F (Reference 2) calculates the parameters required for the SMART core calculation. Generally, two types of parameters are provided by the APOLLO2-F code:

- the cross sections (and the discontinuity factors), and
- the pin reconstruction parameters.

For each type of composition, these parameters are arranged in data files, referred to as data libraries. They contain the dependencies of these parameters as a function of the feedback system variables such as burnup, xenon, soluble boron, moderator density, fuel temperature, and spectral effects. The general flow of the SCIENCE nuclear code package is represented schematically in Figure 3-1. The data libraries for SMART calculations are created in three major steps, APOLLO2-F fuel depletion calculations, APOLLO2-F restart calculations, and data library creation.

##### 3.1.1 APOLLO2-F Fuel Depletion Calculations

Fuel depletion is obtained with APOLLO2-F on a heterogeneous representation of the assembly under nominal core conditions. These conditions are referred to as the reference conditions. Another depletion, referred to as "perturbed" depletion is generated. This depletion is characterized by a change in the water density and represents the effect of spectral differences between actual conditions in the core and the reference APOLLO2-F depletion.

##### 3.1.2 APOLLO2-F Restart Calculations

The results from the depletion calculations are used to initialize the isotopic concentrations for the new calculations in which one or more physical state variables of the assembly are modified with respect to their initial values. These calculations are referred as the restart calculations. The restart variables are: boron concentration, xenon level, moderator density, fuel temperature, and a variable for control rod presence. The results of these calculations are collected in restart files representing the states that the assembly can encounter in the core.

##### 3.1.3 Creation of Data Libraries

Two data libraries are created for each type of fuel, one containing cross sections and discontinuity factors and the other local reconstruction data (particularly, pin by pin power distribution and burnup). These data

libraries tabulate the changes in the parameters they contain as a function of the state variables accessible in the core calculation. These variables constitute the SMART core code feedback system. The feedback variables are:

- for the cross-section type data: burnup, boron, xenon, moderator density, fuel temperature, spectral history, and a variable for control rod presence;
- for the reconstruction type data: burnup, boron, xenon, moderator density, spectral history, and a variable for control rod presence.

The assembly fitting space is divided into cubic regions over which the variations in state are assumed to be represented by a polynomial. Polynomial coefficients are determined to reproduce the assembly parameters calculated by the APOLLO-2-F restart calculations at the fit points.

### **3.2 THE APOLLO2-F LATTICE CODE**

This section describes the CEA 93 cross section library used by APOLLO2-F, the assembly calculations performed by APOLLO2-F, and the reflector calculations performed by APOLLO2-F.

#### **3.2.1 The CEA 93 Cross Section Library**

The APOLLO2-F basic neutron data comes from the CEA 93 library provided by the CEA. This library results from recent JEF2.2 evaluations (Reference 3). The CEA 93 library is a 99 energy group library containing, as appropriate for each isotope, the following data:

- Mass, potential cross section,
- Multigroup diffusion cross sections P0 and P1 (0 and 1<sup>st</sup> order in Legendre polynomials),
- Multigroup absorption cross sections,
- Multigroup fission cross sections,
- Multigroup production cross sections,
- Multigroup spectrum for fission neutrons,
- P0 and P1 slowing down matrices,
- Diffusion rates,
- Absorption rates,
- Production rates,
- Fission yields,
- Decay constant,
- Energy released by capturing a neutron,
- Fission energy available, and
- Data necessary for quadrature formulas.

In addition to the isotopic data, the library provides general data such as the values of the 99 group energy mesh.

### 3.2.2 Assembly Calculations

The calculation scheme used by the APOLLO2-F code to generate the parameters required by the SMART calculation is based on treating the spatial and energy effects with four different calculations.

- A flux (or spectrum) calculation with 99 groups for a detailed pin model containing an array of cells (MULTICELL geometry model see Figure 3-2). Typically, this is a 3 by 3 array of cells.
- A heterogeneous transport/homogeneous transport equivalence calculation that performs the homogenization and energy group collapsing.
- A six-group calculation for homogenized cells in a discretized lattice assembly (2D XY geometry).
- A depletion calculation for changing isotopes in the MULTICELL regions.

The basic calculation scheme is presented in Figure 3-2, Figure 3-3, and Figure 3-4. The flux calculation is divided into three main phases: the generation of self-shielded cross sections, the determination of the 99-group flux, and the depletion of the fuel in the MULTICELL model.

Resonance self-shielding is treated independently for each cell in the MULTICELL geometry. The fuel pellet is divided into several concentric rings to take into account the spatial variation of the uranium 238 and plutonium 240 cross sections. The other isotopes (U235, Pu239, Pu241, Pu242, Zr91, etc.) are given an average self-shielding for the pellet.

The 99 group flux is obtained by solving the discretized collision probability integral transport equation. The collision probabilities  $P_{ij}$  that link region  $i$  to region  $j$  are calculated between each of the MULTICELL cells. The various MULTICELL cells are linked to each other using the interface current method. This method permits evaluating inter-cell exchanges by developing flux and current interface functions. The MULTICELL calculations are brought to criticality by finding the critical buckling.

The depletion of the isotopic compositions is performed with the MULTICELL geometry. The fuel depletion chain contains 16 heavy nuclei and 83 fission products for uranium and plutonium. The boron-10 neutron capture depletion chain and the gadolinium isotopic chains are also provided.

The heterogeneous to homogeneous transport equivalence calculation permits spatial homogenization and a six-group energy collapse of the cross sections from the 99-group spectrum calculation. The homogenized cross sections preserve the same reaction rates as the reaction rates in the heterogeneous MULTICELL model. The homogeneous six-group cross-sections are used in the 2D XY lattice calculation.

The 2D XY lattice calculation is performed with a homogenized representation of each of the fuel assembly cells and the outer water gap. The collision probability method or the  $S_N$  method is used to solve the six-group transport equation for the 2D XY geometry model. As in the case of the spectrum calculation, the calculation is brought to criticality by finding the critical buckling.

The assembly parameters required by the nodal code which are contained in the data libraries are taken from the results of this last calculation. These parameters are as follows:

### Macroscopic cross sections

- Absorption cross sections  $\Sigma_{a1}$  and  $\Sigma_{a2}$ ,
- Removal cross section  $\Sigma_r$ ,
- Production cross sections  $\nu\Sigma_{f1}$  and  $\nu\Sigma_{f2}$ ,
- Energy cross sections  $\kappa\Sigma_{f1}$  and  $\kappa\Sigma_{f2}$ ,
- Diffusion coefficients  $D_1$  and  $D_2$  obtained from the leakage coefficient calculation,
- Discontinuity factors (dimensionless): these parameters, specific to the nodal method, are defined as average flux ratios:

$$ADF1 = \frac{\Phi_{g=1}^{surface}}{\Phi_{g=1}^{ave}}, \text{ and}$$

$$ADF2 = \frac{\Phi_{g=2}^{surface}}{\Phi_{g=2}^{ave}}$$

where  $\Phi_g^{surface}$  is the average surface flux associated with group g and  $\Phi_g^{ave}$  the average flux for the calculation node for SMART.

### Microscopic cross sections

for each isotope:

- $\sigma_{a1}, \sigma_{a2}$ : absorption cross sections

for fissile isotopes:

- $\sigma_{f1}, \sigma_{f2}$ : fission cross sections
- $\nu_1, \nu_2$ : number of fission neutrons
- $\kappa_1, \kappa_2$ : fission energy

for certain isotopes:

- $\sigma_{n \rightarrow 2n}$ : cross sections of the type (n, 2n)

### Reconstruction data

- The pin-by-pin power distribution
- The pin-by-pin burnup distribution
- The assembly corner flux ratios for each corner m in the calculation node:

$$CPDF_1^i = \frac{\Phi_1^m}{\Phi_1^{ave}}, \quad CPDF_2^i = \frac{\Phi_2^m}{\Phi_2^{ave}}$$

- The cross sections associated with the detected reaction rates:  $\Sigma_1^{det}, \Sigma_2^{det}$

- The flux shape factors in the instrument tube:

$$Det1 = \frac{\overline{\Phi}_1^{det}}{\Phi_1^{ave}}, \quad Det2 = \frac{\overline{\Phi}_2^{det}}{\Phi_2^{ave}}$$

### 3.2.2.1 Self-Shielding

The 99-group flux calculation determines the multigroup cross section to be used based on both the non-resonant and resonant cross sections. Non-resonant isotopes have cross sections that vary slowly and uniformly with the neutron lethargy. Their multigroup cross sections depend very little on the flux weighting of the energy spectrum. The cross sections to be used for the flux calculations are independent of the geometry and have been tabulated in the CEA 93 library for a representative flux. These multigroup cross sections are referred to as "not self-shielded". For the resonant isotopes, several energy ranges are considered. In the high energy range, the continuum, and where the cross sections vary slowly with the lethargy, the preceding approximation "for not self-shielded" cross sections is valid. In the intermediate range (referred to as the resonance range) and for certain isotopes in the thermal region, the cross sections may change several times within a single energy mesh. For this situation, the effect of self-shielding of the resonant isotopes present for a given geometry is calculated to obtain the multigroup cross section. These cross sections are referred to as "self-shielded".

#### **APOLLO2-F Resonant Treatment**

The heavy isotope resonance range is governed by the slowing down phenomenon. Therefore, the self-shielding data are established for infinite homogeneous geometries assuming that the flux is the solution of a slowing down equation. Thus, the CEA 93 library contains, for each resonant isotope and each group in the resonance range, the reaction rate as a function of the temperature and the dilution (ratio of moderator total cross section and the resonant concentration), as well as the quadrature parameters required to calculate the resonance integrals. APOLLO2-F calculates the self-shielding in the actual geometry of the problem, using the homogeneous medium data outlined above. To solve the slowing down equation, the collision probability equations are employed. It is assumed that the flux can be split into a slow macroscopic structure ( $\Psi$ ) that varies with lethargy and a fine structure ( $\phi$ ) that takes into account the irregularities due to the resonances:

$$\Phi = \Psi\phi$$

The following energy and spatial models are used to solve the slowing down equation:

- energy coupling uses a statistical treatment above 50 eV and a wide resonance treatment below 50 eV,
- spatial interactions use a matrix dilution method, which assumes that all the resonant mixtures are identical.

The self-shielding calculation is carried out on cell geometries consisting of:

- 6 regions in the fuel pellet,
- 1 region in the cladding,

- 1 region in the moderator.

Several annular regions are needed to model the localized formation of plutonium on the pellet periphery during fuel depletion. Each isotope is processed successively such that the isotopes not processed during a calculation stage are considered as not shielded isotopes. The order in which the isotopes are processed depends on the relative importance of the resonance integral. In the case of UO<sub>2</sub>, this order is U238, Pu239, Pu240, Pu241, Pu242, U235, and Zr91.

### 3.2.2.2 Collision Probabilities

Collision probability solutions are available for both the fine group energy mesh, MULTICELL solution and the coarse group energy mesh, 2-D XY lattice solution. The MULTICELL spectrum calculation makes use of the collision probability method to solve the neutron transport integral equation in two dimensions. The cell of interest is assumed to be surrounded by its eight nearest neighbors. The number of cells of interest depends on how many regions ("cells") with different physical characteristics are in the assembly. Each component, dimension, and material for each of the unique cells are modeled explicitly so that no approximations are needed. For example, the unique cells in a PWR assembly would be a fuel pin, a guide tube, an instrument tube, and the water gap between assemblies. The 2-D XY lattice solution is modeled with homogenized cells in assembly geometry. The solution method as presented below applies to either solution.

For reasons of simplicity, the collision probability equations are written assuming isotropic collisions, which permits using first-order Legendre polynomials to develop the transfer cross sections. In APOLLO2-F, a transport correction formula permits taking into account, with an isotropic collision equation, the first order collision anisotropic effect. The following assumptions are used:

- Sources and medium are independent of time (static solution of Boltzmann equation),
- Isotropic medium (no preferential direction for neutron interaction),
- Isotropic sources and collisions in the "laboratory" reference system.

The Boltzmann equation can be written in the following integral form:

$$\Phi(\bar{r}, E) = \iiint_V \frac{e^{-\alpha(\bar{r}', \bar{r})}}{4\pi|\bar{r}' - \bar{r}|^2} q(\bar{r}', E) d^3\bar{r}'$$

with

$$\alpha(\bar{r}', \bar{r}) = \int_0^{|\bar{r}' - \bar{r}|} \Sigma_t \left( \bar{r} - v \frac{\bar{r}' - \bar{r}}{|\bar{r}' - \bar{r}|}, E \right) dv$$

$$q(\bar{r}', E) = \left[ S(\bar{r}', E) + \int_0^\infty dE' \Sigma_s(\bar{r}', E', E) \Phi(\bar{r}', E') \right]$$

The implementation of the collision probability theory implies making a certain number of assumptions; the most important are that:

- using multigroup discretization the energy-dependent problem can be represented by a system of coupled equations, each having the form of a single energy group equation,
- the neutron mean free path  $\alpha$  remains constant for the group  $g$ , which implies that the intra-energy group dependence is ignored, and
- $\Phi$ ,  $\Sigma_s$ ,  $\Sigma_t$ , and  $S$  remain constant over the calculation mesh cells.

It is thus possible to solve the integral form of the Boltzmann equation using the following system of equations:

$$\left\{ \begin{array}{l} \Sigma_{g,t,i} \bar{\Phi}_{g,i} V_i = \sum_j P_{g,i,j} \bar{\Phi}_{g,j} V_j \\ P_{g,i,j} = \frac{1}{V_j} \Sigma_{g,t,i} \iiint_{V_i} d^3\bar{r} \iiint_{V_j} d^3\bar{r}' \frac{e^{-\alpha_g(\bar{r}',\bar{r})}}{4\pi|\bar{r}'-\bar{r}|^2} \end{array} \right.$$

These two equations are the basis for the collision probability method solution, i.e.:

- using the second equation, the  $P_{ij}$  probabilities are calculated for a neutron originating uniformly in the volume  $V_i$  having its first collision in volume  $V_j$  for energy group  $g$
- using the first equation, the average fluxes in each of the volumes are calculated by solving a linear system of equations.

The collision probabilities are obtained by a digital calculation of the integrals. The number of equations can be reduced by considering the following relationships:

#### Conservation relations

All emitted neutrons will inevitably collide somewhere, which implies that summation over all  $j$  locations equals 1.0 ( $\sum P_{ij} = 1$ ), in the absence of leakage.

#### Reciprocity relations

The function  $\frac{e^{-\alpha_g(\bar{r}',\bar{r})}}{4\pi|\bar{r}'-\bar{r}|^2}$  to be integrated is relatively symmetric with respect to  $r$  and  $r'$  and a reciprocity

relation of the form  $V_i \Sigma_{tj} P_{ij} = V_j \Sigma_{ti} P_{ji}$  is obeyed. For example, if the volume and cross section for two cells are identical, then the collision probability of a neutron created in  $i$  interacting in  $j$  equals the collision probability of a neutron created in  $j$  interacting in  $i$ . For a neutron originating in volume  $V_i$ , the probability that it escapes without colliding with surface  $S$  enclosing  $V_i$  is written:  $P_{iS} = 1 - \sum_j P_{ij}$ ,

where the sum is over all the volumes bounded by  $S$ . The application of the reciprocity theorem shows that, in problems where the medium studied is limited in space, this probability is related to the probability  $P_{Si}$  that a neutron entering by a surface  $S$  collides for the first time in volume  $V$ , contained in  $S$ , by the relationship:

$$P_{Si} = \frac{4V_i}{S} \sum_{j \neq i} P_{iS}$$

Based on all these considerations, the collision, leakage, and transmission matrices can be calculated. The collision probability matrix  $P_{ij}$  links any region  $i$  of the calculation pattern to any other region  $j$ . When  $i$  and  $j$  represent all the regions in the assembly lattice, the calculation is referred to as 2D XY lattice calculation. This is the type of calculation performed in the last stage of the APOLLO2-F assembly calculation scheme.

It is possible to reduce the size of the collision probability matrix by using the MULTICELL method. This consists of:

- Reducing the number of regions by grouping together those that have equivalent surrounding cells. The average region thus defined is referred to as a "generator cell".
- Calculating the collision probabilities in an exact manner inside each of the "generator cells".
- Processing the neutronic coupling of the "physical cells" by calculating the collision matrices using the interface current method (Reference 3) with a cylindrical approximation for the cells, i.e. replacing the cell by a cylinder having a radius  $r_c^2 = \text{cell volume}/\pi$ , which therefore has the same volume and a surface  $S_c = 2\pi r_c$  which is smaller than the real surface of the cell.

The obtained matrix  $P_{ij}$  only has zero terms for coupling between the regions belonging to the same domain. The angular fluxes leaving and reentering by the surfaces of the domains are taken to be spatially uniform and either angularly isotropic (UPO option) or anisotropic (UP1 option). The cylindrical cell model does not permit distinguishing the sides of the cell; it is therefore necessary to add an additional model to determine the leakage and transmission probabilities for each side of the cell. This model permits calculating the transmission probabilities between the various sides of a cylindrical cell. The leakage probabilities are obtained more easily using the reciprocity formulas.

The multigroup flux is obtained by a series of iterations coupling the sources and the fluxes that are structured similar to other neutronic solutions. The sources are calculated from the fluxes and the cross sections (outer iterations) and the fluxes are calculated from the imposed sources with the collision probabilities (inner iterations).

### **The Interface current method**

Another important aspect of collision probability (CP) techniques is the *interface current* (IC) method. In this case, a unit PWR assembly is sub-divided into cells and CP matrices are computed for each uncoupled cell. An exact relationship is established between the outgoing angular flux, the internal cell sources and the incoming angular flux. Each flux is represented by a flux expansion by using the Galerkin method<sup>4</sup> and a system is defined whose solutions are the components of the angular flux at the surface of a cell. The detailed flux can then be

reconstructed from the knowledge of interface currents surrounding each cell. In this section, the group  $g$  dependence of the various physical quantities is not shown to reduce the mathematical notation.

At each point  $\vec{r}_s$  of the surface  $\partial V$  surrounding a cell, the outgoing angular flux can be expressed as a double  $P_n$  expansion:

$$\phi^+(\vec{r}_s, \vec{\Omega}) = \sum_{\rho} \varphi_{\rho}^+(\vec{r}_s) \psi_{\rho}(\vec{\Omega}, \vec{N}^+) \quad \text{where } \vec{\Omega} \cdot \vec{N}^+ > 0$$

where  $\vec{N}^+$  is a unit outgoing vector, normal to  $\partial V$ , and located at point  $\vec{r}_s$  and  $\rho = 0$  to 2. The base functions are chosen to be orthogonal and satisfy the following condition:

$$\int_{\vec{\Omega} \cdot \vec{N} > 0} d\Omega (\vec{\Omega} \cdot \vec{N}) \psi_{\nu}(\vec{\Omega}, \vec{N}) \psi_{\rho}(\vec{\Omega}, \vec{N}) = \pi \delta_{\nu\rho}$$

where  $\delta_{\nu\rho}$  is the Kronecker delta function (when  $\nu=\rho$ ,  $\delta=1$ ; otherwise  $\delta=0$ ).

In 2D cases, the base functions ( $\psi_{\rho}$ ) corresponding to a double  $P_1$  expansion illustrated in Figure 3-5 and that satisfy the orthogonal conditions are:

$$\begin{aligned} \psi_0(\vec{\Omega}, \vec{N}) &= 1 \quad (\text{DP}_0 \text{ component}) \\ \psi_1(\vec{\Omega}, \vec{N}) &= 3\sqrt{2} (\vec{\Omega} \cdot \vec{N}) - 2\sqrt{2} \quad (\text{first DP}_1 \text{ component}) \\ \psi_2(\vec{\Omega}, \vec{N}) &= 2(\vec{\Omega} \cdot \vec{N}_{\perp}) \quad (\text{second DP}_1 \text{ component}) \end{aligned}$$

where  $\vec{N}_{\perp}$  is a unit vector perpendicular to  $\vec{N}$  and located in the 2D plane. The neutron balance equation is maintained by using the same expansion for the same outgoing angular flux in a cell as the incoming angular flux in the neighboring cell. Using  $\vec{N}^-$  as the incoming unit normal vector in the neighboring cell, we write

$$\phi^-(\vec{r}_s, \vec{\Omega}) = \sum_{\rho} \varphi_{\rho}^-(\vec{r}_s) \psi_{\rho}(\vec{\Omega}, \vec{N}^-) \quad \text{where } \vec{\Omega} \cdot \vec{N}^- > 0.$$

The expansion coefficients  $\varphi_{\rho}^+(\vec{r}_s)$  and  $\varphi_{\rho}^-(\vec{r}_s)$  are assumed to be uniform along each side of the cell.

They are taken equal to  $\varphi_{\rho,\alpha}^+$  and  $\varphi_{\rho,\alpha}^-$  on surface  $S_{\alpha}$ . In the APOLLO-F lattice code, the two available interface current approximations are the Uniform- $DP_0$  and the Uniform- $DP_1$  approximations identified as UP0 and UP1, respectively.

A cell may contain one or several regions defining the fuel rings, clad, and coolant. A CP method is used to compute the response matrices for each cell. The following matrices are computed:

$P_{ij}$  = CP for a neutron born uniformly in region  $i$  and isotropic in direction to have its first collision in region  $j$  without leaving the cell.

$P_{S_\alpha j}^{(\rho)}$  = CP for a neutron entering from surface  $S_\alpha$  and with an angular distribution  $\psi_\rho(\bar{\Omega}, \bar{N}^-)$  to have its first collision in region  $j$  without leaving the cell.

$P_{iS_\beta}^{(\nu)}$  = CP for a neutron born uniformly in region  $i$  and isotropic in direction to leave the cell by surface  $S_\beta$  with an angular distribution  $\psi_\nu(\bar{\Omega}, \bar{N}^+)$ .

$P_{S_\alpha S_\beta}^{(\rho\nu)}$  = CP for a neutron entering from surface  $S_\alpha$  and with an angular distribution  $\psi_\rho(\bar{\Omega}, \bar{N}^-)$  to leave the cell by surface  $S_\beta$  with an angular distribution  $\psi_\nu(\bar{\Omega}, \bar{N}^+)$ .

The physical representation of these probabilities and surfaces is shown in Figure 3-6. The flux equation for neutrons in each group can be cast into a response-matrix form where the unknowns are the averaged scalar flux  $\phi_j$  that has an interaction in region  $j$  and the components of the angular fluxes along surface  $S_\alpha$  (related to the *interface currents*).

We obtain

$$\begin{aligned}\phi_j &= \sum_{\alpha} \sum_{\rho} 4\pi \phi_{\rho,\alpha}^- P_{S_\alpha j}^{(\rho)} + \sum_i Q_i P_{ij} \\ 4\pi \phi_{\nu,\beta}^+ &= \sum_{\alpha} \sum_{\rho} 4\pi \phi_{\rho,\alpha}^- P_{S_\alpha S_\beta}^{(\rho\nu)} + \sum_i Q_i P_{iS_\beta}^{(\nu)}\end{aligned}$$

where  $Q_j$  are the scattering and fission sources in region  $j$ .

Finally, a pure geometric equation is required to connect the incoming and outgoing angular fluxes from cell to cell for all surfaces. For example, the following equation shows the relationship between the incoming angular fluxes,  $\phi_{\rho,\alpha}^-$  for node  $n$  and the outgoing angular fluxes  $\phi_{\rho,\beta}^+$  for node  $n-1$  of neighboring

cells that share the same surface.  $\phi_{p,\alpha}^- = A_{\alpha,\beta}^{(\rho)} \phi_{p,\alpha}^+$ , where surface  $\alpha$  of node  $n$  is the same surface as  $\beta$  for node  $n-1$  for neighboring square cells. The last three equations form a closed system that can be solved iteratively.

### 3.2.2.3 Heterogeneous / Homogeneous Equivalence

An equivalence process is needed to provide homogenized, few group cross sections for the 2-D XY calculations that will recreate accurate local reaction rates. [

b,c,d,e

]

[

b,c,d,e

] This technique allows a transformation of the homogenized fluxes back to the regions within the cell for future depletion calculations. Additionally, a set of macroscopic cross sections is obtained for the six energy groups associated with each macro-region ("generator cell"). The macro-regions correspond to the different types of unique cells (generator cells) defined during the 99-group calculation.

#### 3.2.2.4 The $S_N$ calculation

The APOLLO2-F code optionally permits calculating the 2D XY lattice flux using the discrete ordinate method by solving the integral-differential equation using the  $S_N$  approximation. It takes into account the anisotropic scattering using the spherical harmonic expansion of the scattering source term of arbitrarily high order. Spatial and angular discretization of the equation leads to a linear system, which is solved by an iterative process. This process comprises three levels: outer iterations, inner iterations, and thermal iterations. Acceleration methods are applied for each level. Collision anisotropy is dealt with explicitly by a cross section development using Legendre polynomials. This solution can be used for either the one dimensional reflector solution or the 2-D XY lattice solution.

The method is implemented for a regular rectangular spatial mesh, so the step prior to the flux calculation of a PWR assembly is a computation of equivalent cross sections using appropriate reaction rates that preserve heterogeneous properties.

In the method of discrete ordinates, a set of discrete directions and associated weights  $\{\hat{\Omega}_d, w_d, d=1, 2, \dots, N_d\}$  is chosen, and the transport equation is evaluated for these directions. This transforms the within-group transport equation into a system of  $N_d$  equations

$$(\hat{\Omega}_d \cdot \bar{\nabla} + \sigma(\bar{r}))\psi^{i+1}(\bar{r}, \hat{\Omega}_d) = \sum_{\ell \geq 0} \sigma_{s\ell}(\bar{r}) \sum_{m=-\ell}^{\ell} Y_{\ell m}(\hat{\Omega}_d) \phi_{\ell m}^i(\bar{r}) + Q(\bar{r}, \hat{\Omega}_d)$$

where  $Y_{\ell m}(\hat{\Omega}_d)$  are the spherical harmonic coefficients, and the angular flux moments  $\phi_{\ell m}(\bar{r})$  are computed by a Gauss-type quadrature formula:

$$\phi_{\ell m}^{i+1}(\bar{r}) = \sum_{d=1}^{N_d} w_d Y_{\ell m}(\hat{\Omega}_d) \psi^{i+1}(\bar{r}, \hat{\Omega}_d).$$

After the discretization in space, this system is solved by iterating on the self-scattering source ( $i$  is the iteration index in the above equations). In each iteration a source problem is solved for the angular flux in each discrete angular direction

$$\hat{\Omega}_d \cdot \bar{\nabla} + \sigma(\bar{r})\psi^{i+1}(\bar{r}, \hat{\Omega}_d) = Q^i(\bar{r}, \hat{\Omega}_d)$$

This is done using the standard  $S_N$  sweep in which the angular flux in the mesh cell interior,  $\psi$ , and on the exiting boundaries,  $\psi^+$ , is computed in terms of incoming angular flux,  $\psi^-$  and volumetric sources,  $Q$ . This computational algorithm can be presented symbolically (with direction and iteration index omitted) by:

$$\psi = CQ + I\psi^-$$

$$\psi^+ = EQ + T\psi^-$$

The vectors  $\psi, \psi^\pm$  and  $Q$  contain spatial moments of the flux and source, and the elements of matrices  $C, I, E$  and  $T$  are collision, surface-to-volume, leakage and transmission coefficients, respectively. The number and the form of these elements, as well as the final algebraic form of the above algorithm, depend on the type of spatial differencing scheme. The code uses two types of methods: classical finite differences, such as linear diamond, and transverse nodal methods. Both are based on the use of a balance equation for each mesh cell.

In the linear nodal method the angular flux for each discrete direction in mesh cell interior and on cell interfaces is represented by a linear function of  $x$  and  $y$  coordinates:

$$\psi(x, y) = \psi_{00} + \psi_{10} P_1(x) + \psi_{01} P_1(y),$$

$$\psi^{x^\pm}(y) = \psi_0^{x^\pm} + \psi_1^{x^\pm} P_1(y) \quad \text{and} \quad \psi^{y^\pm}(x) = \psi_0^{y^\pm} + \psi_1^{y^\pm} P_1(x)$$

where  $\psi^{x^\pm}$  and  $\psi^{y^\pm}$  are surface fluxes on the corresponding faces of a two-dimensional mesh cell. This representation is an approximation of a general Legendre polynomial expansion. The base of  $P_n$  polynomials is used to construct the balance equations for the flux moments.

$$L_{mn}^x + L_{mn}^y + \sigma \psi_{mn} = Q_{mn}$$

$Q_{mn}$  are the source moments of an analogous polynomial representation and the transverse leakage components,  $L_{mn}$ , are of the form

$$L_{0n}^x = \frac{\mu}{\Delta x} (\psi_n^{x+} - \psi_n^{x-}), \quad L_{1n}^x = \frac{\mu}{\Delta x} (\psi_n^{x+} + \psi_n^{x-} - 2\psi_{0n})$$

where  $\mu$  and  $\Delta x$  are the direction cosine and cell thickness in the  $x$  direction, respectively. Analogous expressions hold for  $L_{mn}^y$  terms. These balance equations are used together with additional nodal equations obtained by transverse integration of the integral-differential transport equation within a mesh cell. This gives a set of coupled quasi one-dimensional equations which relate the outgoing flux with the flux in the cell interior and at the incoming surfaces:

$$\psi_n^{x+} = \psi_n^{x-} e^{-\sigma \Delta x / \mu} + \sum_m E_m^x (Q_{mn} - L_{mn}^y)$$

with an analogous expression for  $\psi_m^{y+}$ . The last four equations are solved analytically. The schemes of different degrees of accuracy are obtained by retaining the moments of a specific order for  $\psi$ ,  $\psi^\pm$  and  $L$  terms. The schemes used in the code are identified as follows:

- The **CC** scheme uses only zero-order moments.
- The **CL** scheme retains zero-order moments for surface flux and transverse leakage terms, and  $mn = 00, 10, 01$  for cell interior flux.
- The simplified linear scheme **LL-APPR** uses linear representation both for surface and volumetric flux but with the term  $L_{11}$  neglected in the last equation.
- The term  $L_{11}$  is taken into account in the full linear scheme **LL**.

The iterative solution can be accelerated using either diffusion or transport synthetic acceleration.

### 3.2.2.5 Fuel Depletion

The depletion calculation permits obtaining the characteristics of the fuel as it is irradiated and to create the isotopic concentration tables required for the restart calculations. The isotopic depletion is calculated for the heterogeneous MULTICELL geometry using an effective one-group collapsed flux and cross sections. A predictor/corrector method with parabolic dependence of the fluxes and the reaction rates as a function of local fluence is used to model the time dependence.

The change in isotopic concentration with time is given by the isotopic depletion equations:

$$\frac{\partial N}{\partial t} = AN$$

where matrix  $A$  depends implicitly on time via the flux solution and  $N$  is a vector of all the isotopes treated. The  $A$  matrix is formulated from the following equation for all depletable isotopes ( $i$ ) for each region in the MULTICELL geometry:

$$\frac{\partial N_i(t)}{\partial t} = N_i(t) \left[ -\lambda_{ij} - \phi(t)\sigma_a(t) \right] + N_j(t)\lambda_{ji} + N_k(t)\phi(t)\sigma_{ki}(t)$$

where:

$N$  is the concentration of isotope  $i$ ,  $j$ , or  $k$

$\lambda_{ij}$  is the decay constant from isotope  $i$  to isotope  $j$

$\sigma_a$  is the absorption cross section for isotope  $i$ , and

$\sigma_{ki}$  is the microscopic capture cross section of the reaction  $n + N_k = N_i$  or  $n + N_k = 2n + N_i$ .

The non-diagonal elements of  $A$  correspond to the formation of the isotope and are therefore positive, whereas the diagonal elements represent the destruction of the isotope and are negative.

Starting at time  $t_{i-1}$  for which the concentrations, the microscopic cross sections, and the flux are known for all the materials and regions, the assembly depletion step in terms of a burnup increment, permits determining

the fluence increment to reach time  $t_i$ . The flux and the reaction rates for each region and each depletable isotope are expressed as parabolic functions of the fluence of the region:

$$F(t) = \int_{t_{i-1}}^t \phi(z) dz$$

$$\phi(t) = a_0 + a_1 F + a_2 F^2$$

$$\tau(t) = b_0 + b_1 F + b_2 F^2$$

where the coefficients  $a_0$ ,  $a_1$ ,  $a_2$ ,  $b_0$ ,  $b_1$ , and  $b_2$  are obtained from the values at times  $t_{i-3}$ ,  $t_{i-2}$ , and  $t_{i-1}$ .

The elements of the depletion matrix  $A$  can be transformed from units of time to fluence ( $F$ ). The isotopic depletion equation then becomes:

$$\frac{\partial N}{\partial F} = AN$$

The integration of the depletion equation in this latter form, between times  $t_{i-1}$  and  $t_i$ , permits obtaining the isotopic concentrations at time  $t_i$ . This integration is performed using a 4<sup>th</sup> order Runge-Kutta method. A neutronic solution is performed at  $t_i$  with the predicted isotopes that yields reaction rates and fluxes. The polynomial coefficients ( $a_0$ ,  $a_1$ ,  $a_2$ ,  $b_0$ ,  $b_1$ , and  $b_2$ ) are obtained from the values at times  $t_{i-2}$ ,  $t_{i-1}$ , and  $t_i$  and the depletion equation is integrated again to provide the corrected isotopes at time  $t_i$ .

### 3.2.3 Reflector Calculation

In SMART, the reflector is treated as an explicit node with cross sections. The two-group cross sections are obtained for these regions, from 1D calculations using the  $S_N$  method. Each type of reflector (radial or axial) is characterized by a 1D geometry representing the average material balances encountered by a neutron passing through the region. A 99-group  $S_N$  calculation in the finite difference option is performed for each of the defined 1D geometries. A fourth-order  $S_N$  method is used, which corresponds to an angular flux split in six directions because of the 1D symmetry.

The anisotropy of the collisions is treated by representing the transfer cross sections using first-order Legendre polynomials. The usual two-group cross sections (absorption, removal) are obtained by flux/volume and energy weighting. The discontinuity factors to be applied at the core/reflector interface are determined using a nodal equivalence method. This process is designed so that a SMART calculation using the cross sections and discontinuity factors reproduces the two-energy-group  $S_N$  calculation of reaction rates and currents.

### 3.3 THE SMART CORE CODE

This section provides a description of the methods and equations used in the SMART code.

#### 3.3.1 Neutron Diffusion Model

The SMART code solves the two-energy-group diffusion equation for 3D core geometries. The principal characteristics of the nodal method used are:

- The use of discontinuity factors from the APOLLO2-F lattice calculations to take into account the spatial homogenization.
- The integration of the coupling equations by the nodal expansion method.
- The spatial variation of the cross sections within the node is modeled.
- A convergence process based on four iteration levels, one of which is dedicated to the nodal method referred to as the nodal iteration.

##### 3.3.1.1 Nodal Equivalence

The neutron diffusion model used in the SCIENCE nuclear code package is an advanced two-energy-group nodal model. It uses a diffusion operator for a large mesh calculation. To ensure the coherence between the APOLLO2-F transport calculations and the SMART calculation, the diffusion operator is modified in order to satisfy the following conservation laws:

- The average fluxes in the homogenized node.
- Two-group reaction rates.
- Two-group currents for the homogenized node.
- Two-group surface fluxes.

This modification of the operator is obtained by adding discontinuity factors (Reference 6) to the usual weighted flux/volume cross sections. These factors take into account the numerical approximations of the coupling equations (particularly the leakage model) and the homogenization effects. The equivalence process is completed by a nodal expansion that ensures spatial convergence equivalent to a much finer mesh calculation. Homogenization, when it is associated with an equivalence process, permits reducing the number of nodes (see Figure 3-7), while retaining the accuracy.

##### 3.3.1.2 Nodal Expansion Method (NEM)

The nodal expansion method (Reference 6) is used to integrate the coupling equations between the homogeneous nodes of the centered node finite difference diffusion operator used in the flux

calculation. During the convergence calculation process, the currents at each of the core node interfaces are recalculated to update the finite difference diffusion operator.

### 3.3.1.2.1 Nodal Flux Calculation

The homogeneous diffusion equation is written for each homogeneous node with 3D coordinates (i,j,k):

$$\begin{cases} -\vec{\nabla} \cdot (D_1^{ijk} \vec{\nabla} \Phi_1^{ijk}(\vec{r})) + (\Sigma_{a1}^{ijk} + \Sigma_r^{ijk}) \Phi_1^{ijk}(\vec{r}) = \frac{1}{\lambda} (v \Sigma_{f1}^{ijk} \Phi_1^{ijk}(\vec{r}) + v \Sigma_{f2}^{ijk} \Phi_2^{ijk}(\vec{r})) \\ -\vec{\nabla} \cdot (D_2^{ijk} \vec{\nabla} \Phi_2^{ijk}(\vec{r})) + \Sigma_{a2}^{ijk} \Phi_2^{ijk}(\vec{r}) = \Sigma_r^{ijk} \Phi_1^{ijk}(\vec{r}) \end{cases}$$

where  $\vec{r} = (x, y, z)$ ,  $J_g^{ijk}(\vec{r})$ ,  $\Phi_g^{ijk}(\vec{r})$ ,  $\Sigma_{bg}^{ijk}(\vec{r})$  and  $\lambda$  are respectively:

- The current position within the node (i,j,k) for which the equation applies,
- The neutron current at point (x,y,z) of the node (i,j,k) in group g,
- The flux at point (x,y,z) of the node (i,j,k) in group g,
- The macroscopic cross section for the type b reaction in the group g within the node (i,j,k),
- The effective multiplication factor.

The integration of this equation over each of the nodes (i,j,k) leads to a system of linear equations containing twice as many equations as nodes (two per energy group). These equations represent the neutron balances in each of the energy groups:

$$\begin{cases} \frac{(J_1^{i+} - J_1^{i-})}{h_x^{ijk}} + \frac{(J_1^{j+} - J_1^{j-})}{h_y^{ijk}} + \frac{(J_1^{k+} - J_1^{k-})}{h_z^{ijk}} + (\Sigma_{a1}^{ijk} + \Sigma_r^{i,j,k}) \Phi_1^{ijk} = S_1^{ijk} \\ \frac{(J_2^{i+} - J_2^{i-})}{h_x^{ijk}} + \frac{(J_2^{j+} - J_2^{j-})}{h_y^{ijk}} + \frac{(J_2^{k+} - J_2^{k-})}{h_z^{ijk}} + \Sigma_{a2}^{ijk} \Phi_2^{ijk} = \Sigma_r^{ijk} \Phi_1^{ijk} \end{cases}$$

(in addition to the corresponding equations for the other directions)

$$S_1^{ijk} = \frac{[v \Sigma_{f,1}^{ijk} \Phi_1^{ijk} + v \Sigma_{f,2}^{ijk} \Phi_2^{ijk}]}{\lambda}$$

and where  $J_g^{i+}$ ,  $\Phi_g^{ijk}$ ,  $\Sigma_{tg}^{ijk}$ ,  $D_g^{ijk}$ ,  $h_u^{ijk}$  and  $\lambda$  are, respectively :

- The current in group g between the nodes (i,j,k) and (i+1, j,k),
- The volume average flux for node (i,j,k) in group g,
- The macroscopic cross section for the type t reaction in the group g within the node (i,j,k),
- The diffusion coefficient in group g for node (i,j,k),

- The size of the node (i,j,k) in the u direction,
- The effective multiplication factor of the pattern.

The neutron currents can be broken down into two parts showing the usual finite difference component:

$$J_g^{i+} = -D_g^{(ijk)(i+1,jk)} \left( \frac{\Phi_g^{i+1,jk} - \Phi_g^{ijk}}{(h_x^{i+1,jk} + h_x^{ijk})/2} \right) + \Delta J_g^{i+}$$

where

$$D_g^{(ijk)(i+1,jk)} = \frac{D_g^{i+1,jk} h_x^{i+1,jk} + D_g^{ijk} h_x^{ijk}}{h_x^{i+1,jk} + h_x^{ijk}}$$

and  $\Delta J_g^{i+}$  is, by definition, the difference between the NEM current and its approximation in finite difference. By defining a pseudo-coefficient of diffusion by the formula:

$$\Delta J_g^{i+} = -\tilde{D}_g^{(ijk)(i+1,jk)} \left( \frac{\Phi_g^{i+1,jk} + \Phi_g^{ijk}}{(h_x^{i+1,jk} + h_x^{ijk})/2} \right)$$

the neutron equation can be rewritten in the following form:

For group 1 :

$$\left[ \left( \Sigma_{a1}^{ijk} + \Sigma_r^{i,j,k} \right) + \frac{1}{h_x^{ijk}} \left( \frac{D_1^{(ijk)(i+1,jk)} - \tilde{D}_1^{(ijk)(i+1,jk)}}{(h_x^{ijk} + h_x^{i+1,jk})/2} + \frac{D_1^{(i-1,jk)(ijk)} + \tilde{D}_1^{(i-1,jk)(ijk)}}{(h_x^{i-1,jk} + h_x^{ijk})/2} \right) \right. \\ + \frac{1}{h_y^{ijk}} \left( \frac{D_1^{(ijk)(ij+1,k)} - \tilde{D}_1^{(ijk)(ij+1,k)}}{(h_y^{ijk} + h_y^{ij+1,k})/2} + \frac{D_1^{(ij-1,k)(ijk)} + \tilde{D}_1^{(ij-1,k)(ijk)}}{(h_y^{ij-1,k} + h_y^{ijk})/2} \right) \\ + \left. \frac{1}{h_z^{ijk}} \left( \frac{D_1^{(ijk)(ijk+1)} - \tilde{D}_1^{(ijk)(ijk+1)}}{(h_z^{ijk} + h_z^{ijk+1})/2} + \frac{D_1^{(ijk-1)(ijk)} + \tilde{D}_1^{(ijk-1)(ijk)}}{(h_z^{ijk-1} + h_z^{ijk})/2} \right) \right] \Phi_1^{ijk} \\ - \left[ \frac{1}{h_x^{ijk}} \frac{D_1^{(ijk)(i+1,jk)} + \tilde{D}_1^{(ijk)(i+1,jk)}}{(h_x^{ijk} + h_x^{i+1,jk})/2} \Phi_1^{i+1,jk} + \frac{1}{h_x^{ijk}} \frac{D_1^{(i-1,jk)(ijk)} - \tilde{D}_1^{(i-1,jk)(ijk)}}{(h_x^{i-1,jk} + h_x^{ijk})/2} \Phi_1^{i-1,jk} \right. \\ + \frac{1}{h_y^{ijk}} \frac{D_1^{(ijk)(ij+1,k)} + \tilde{D}_1^{(ijk)(ij+1,k)}}{(h_y^{ijk} + h_y^{ij+1,k})/2} \Phi_1^{ij+1,k} + \frac{1}{h_y^{ijk}} \frac{D_1^{(ij-1,k)(ijk)} - \tilde{D}_1^{(ij-1,k)(ijk)}}{(h_y^{ij-1,k} + h_y^{ijk})/2} \Phi_1^{ij-1,k} \\ + \left. \frac{1}{h_z^{ijk}} \frac{D_1^{(ijk)(ijk+1)} + \tilde{D}_1^{(ijk)(ijk+1)}}{(h_z^{ijk} + h_z^{ijk+1})/2} \Phi_1^{ijk+1} + \frac{1}{h_z^{ijk}} \frac{D_1^{(ijk-1)(ijk)} - \tilde{D}_1^{(ijk-1)(ijk)}}{(h_z^{ijk-1} + h_z^{ijk})/2} \Phi_1^{ijk-1} \right] = S_1^{ijk}$$

For group 2 :

$$\begin{aligned}
& \left[ \sum_{a2}^{ijk} + \frac{1}{h_x^{ijk}} \left( \frac{D_2^{(ijk)(i+1,jk)} - \tilde{D}_2^{(ijk)(i+1,jk)}}{(h_x^{ijk} + h_x^{i+1,jk})/2} + \frac{D_2^{(i-1,jk)(ijk)} + \tilde{D}_2^{(i-1,jk)(ijk)}}{(h_x^{i-1,jk} + h_x^{ijk})/2} \right) \right. \\
& + \frac{1}{h_y^{ijk}} \left( \frac{D_2^{(ijk)(ij+1,k)} - \tilde{D}_2^{(ijk)(ij+1,k)}}{(h_y^{ijk} + h_y^{ij+1,k})/2} + \frac{D_2^{(ij-1,k)(ijk)} + \tilde{D}_2^{(ij-1,k)(ijk)}}{(h_y^{ij-1,k} + h_y^{ijk})/2} \right) \\
& \left. + \frac{1}{h_z^{ijk}} \left( \frac{D_2^{(ijk)(ijk+1)} - \tilde{D}_2^{(ijk)(ijk+1)}}{(h_z^{ijk} + h_z^{ijk+1})/2} + \frac{D_2^{(ijk-1)(ijk)} + \tilde{D}_2^{(ijk-1)(ijk)}}{(h_z^{ijk-1} + h_z^{ijk})/2} \right) \right] \Phi_2^{ijk} \\
& - \left[ \frac{1}{h_x^{ijk}} \frac{D_2^{(ijk)(i+1,jk)} + \tilde{D}_2^{(ijk)(i+1,jk)}}{(h_x^{ijk} + h_x^{i+1,jk})/2} \Phi_2^{i+1,jk} + \frac{1}{h_x^{ijk}} \frac{D_1^{(i-1,jk)(ijk)} - \tilde{D}_1^{(i-1,jk)(ijk)}}{(h_x^{i-1,jk} + h_x^{ijk})/2} \Phi_2^{i-1,jk} \right. \\
& + \frac{1}{h_y^{ijk}} \frac{D_2^{(ijk)(ij+1,k)} + \tilde{D}_2^{(ijk)(ij+1,k)}}{(h_y^{ijk} + h_y^{ij+1,k})/2} \Phi_2^{ij+1,k} + \frac{1}{h_y^{ijk}} \frac{D_2^{(ij-1,k)(ijk)} - \tilde{D}_2^{(ij-1,k)(ijk)}}{(h_y^{ij-1,k} + h_y^{ijk})/2} \Phi_2^{ij-1,k} \\
& \left. + \frac{1}{h_z^{ijk}} \frac{D_2^{(ijk)(ijk+1)} + \tilde{D}_2^{(ijk)(ijk+1)}}{(h_z^{ijk} + h_z^{ijk+1})/2} \Phi_2^{ijk+1} + \frac{1}{h_z^{ijk}} \frac{D_2^{(ijk-1)(ijk)} - \tilde{D}_2^{(ijk-1)(ijk)}}{(h_z^{ijk-1} + h_z^{ijk})/2} \Phi_2^{ijk-1} \right] = \sum_r^{ijk} \Phi_1^{ijk}
\end{aligned}$$

The system of equations thus obtained now only depends on the flux. It can be solved by the two iteration levels traditionally used in the finite difference computer codes: inner and outer iterations. The inner iteration calculates the fluxes in equilibrium with a given source, while the outer iteration determines the source created by the fluxes.

### 3.3.1.2.2 Reevaluation of the Currents: Nodal Iteration

The reevaluation of the neutron currents is made by solving a one-dimensional diffusion equation for each interface separating two adjacent nodes. This equation is obtained by integrating the diffusion equation for the transverse directions assuming that the currents obey Fick's law. For example, for the case of an interface in the  $i$  direction that separates node( $i,j,k$ ) from node( $i+1,j,k$ ), the equations for each of the two nodes are:

#### Equations in group 1

For node ( $i,j,k$ ) =  $l_s$  for left side

$$\begin{aligned}
& -D_1^{l_s} \frac{\partial^2 \Phi_1^{l_s}(x)}{\partial x^2} + \frac{1}{h_y^{l_s}} [J_1^{l_s}(x, y +) - J_1^{l_s}(x, y -)] + \frac{1}{h_z^{l_s}} [J_1^{l_s}(x, z +) - J_1^{l_s}(x, z -)] \\
& + (\sum_{a1}^{l_s} + \sum_r^{l_s}) \Phi_1^{l_s}(x) = \frac{1}{\lambda} (\nu \sum_{f1}^{l_s} \Phi_1^{l_s}(x) + \nu \sum_{f2}^{l_s} \Phi_2^{l_s}(x))
\end{aligned}$$

For node (i+1, j, k) = rs for right side

$$-D_1^{rs} \frac{\partial^2 \Phi_1^{rs}(x)}{\partial x^2} + \frac{1}{h_y^{rs}} [J_1^{rs}(x, y+) - J_1^{rs}(x, y-)] + \frac{1}{h_z^{rs}} [J_1^{rs}(x, z+) - J_1^{rs}(x, z-)] \\ + (\Sigma_{a1}^{rs} + \Sigma_r^{rs}) \Phi_1^{rs}(x) = \frac{1}{\lambda} (\nu \Sigma_{f1}^{rs} \Phi_1^{rs}(x) + \nu \Sigma_{f2}^{rs} \Phi_2^{rs}(x))$$

### Equations in group 2

For node (i, j, k) = ls for left side

$$-D_2^{ls} \frac{\partial^2 \Phi_2^{ls}(x)}{\partial x^2} + \frac{1}{h_y^{ls}} [J_2^{ls}(x, y+) - J_2^{ls}(x, y-)] + \frac{1}{h_z^{ls}} [J_2^{ls}(x, z+) - J_2^{ls}(x, z-)] + \Sigma_{a2}^{ls} \Phi_1^{ls}(x) = \Sigma_r^{ls} \Phi_1^{ls}(x)$$

For node (i+1, j, k) = rs for right side

$$-D_2^{rs} \frac{\partial^2 \Phi_2^{rs}(x)}{\partial x^2} + \frac{1}{h_y^{rs}} [J_2^{rs}(x, y+) - J_2^{rs}(x, y-)] + \frac{1}{h_z^{rs}} [J_2^{rs}(x, z+) - J_2^{rs}(x, z-)] + \Sigma_{a2}^{rs} \Phi_1^{rs}(x) = \Sigma_r^{rs} \Phi_1^{rs}(x)$$

with:

$$J_g^{ijk}(x, y+) = -\frac{D_g^{ijk}}{h_z^{ijk}} \int_z \frac{\partial \Phi_g^{ijk}(x, y+, z)}{\partial y} dz$$

(and symmetrically for the other directions {y-, z+, and z-})

$$\Phi_g^{ijk}(x) = \frac{\iint \Phi_g^{ijk}(x, y, z) dy dz}{\iint_{y,z} dy dz}$$

If we define the transverse leakage for node n by:

$$L_{ts}^n(x) = \frac{1}{h_y^n} [J_g^n(x, y+) - J_g^n(x, y-)] + \frac{1}{h_z^n} [J_g^n(x, z+) - J_g^n(x, z-)]$$

The four equations are written:

$$-D_1^{ls} \frac{\partial^2 \Phi_1^{ls}(x)}{\partial x^2} + (\Sigma_{a1}^{ls} + \Sigma_r^{ls}) \Phi_1^{ls}(x) - \frac{1}{\lambda} (\nu \Sigma_{f1}^{ls} \Phi_1^{ls}(x) + \nu \Sigma_{f2}^{ls} \Phi_2^{ls}(x)) = -L_1^{ls}(x)$$

$$\begin{aligned}
-D_1^{rs} \frac{\partial^2 \Phi_1^{rs}(x)}{\partial x^2} + (\Sigma_{a1}^{rs} + \Sigma_r^{rs}) \Phi_1^{rs}(x) - \frac{1}{\lambda} (\nu \Sigma_{f1}^{rs} \Phi_1^{rs}(x) + \nu \Sigma_{f2}^{rs} \Phi_2^{rs}(x)) &= -L_1^{rs}(x) \\
-D_2^{ls} \frac{\partial^2 \Phi_2^{ls}(x)}{\partial x^2} + \Sigma_{a2}^{ls} \Phi_1^{ls}(x) - \Sigma_r^{ls} \Phi_1^{ls}(x) &= -L_2^{ls}(x) \\
-D_2^{rs} \frac{\partial^2 \Phi_2^{rs}(x)}{\partial x^2} + \Sigma_{a2}^{rs} \Phi_1^{rs}(x) - \Sigma_r^{rs} \Phi_1^{rs}(x) &= -L_2^{rs}(x)
\end{aligned}$$

The current continuity relationships complete the system of equations.

Solving this system of equations leads to a reevaluation of the currents. These currents differ from the finite difference currents by the following quantity :

$$\Delta J_g = J_g^{\text{nodal}} - J_g^{\text{finite differences}}$$

This quantity then permits calculating for each interface the pseudo diffusion coefficients to be used in the finite difference operator by means of the following relationships:

$$\bar{D}_g^{(ijk)(i+1,jk)} = - \frac{\Delta J_g^{i+}}{\left( \frac{\Phi_g^{i+1,jk} + \Phi_g^{ijk}}{(h_x^{i+1,jk} + h_x^{ijk})/2} \right)}$$

The SMART code solves this system by approximating the fast and thermal fluxes with specific functions. The fast flux is assumed to be a fourth order polynomial, whereas the thermal flux is either a fourth order polynomial or a polynomial combined with hyperbolic terms. The choice of the expansion of the thermal flux is based on the variation of the spectrum between the two node cells sharing the interface being analyzed. To reevaluate the currents, it is therefore necessary to build a system constrained by the fluxes and currents of the previous iteration permitting the determination of 10 coefficients per node.

The "two-node problem" stated in this manner makes use of 20 coefficients. These coefficients are calculated as the solution to a system of 20 equations: 4 average flux preservation equations, 4 continuity equations for heterogeneous fluxes and currents, and 12 additional equations obtained by the weighted residual method described below.

Since the function expansion of the flux is an approximation of the real solution, the integration of the transverse-integrated one dimensional diffusion equation with weighting functions is used to define the expansion coefficients for the flux and is called the residual method. The desired equations are obtained by the following relations for each energy group and each direction:

$$\int w_l \left[ -D_g \frac{\partial^2 \phi_g(u)}{h_x^2 \partial u^2} + \Sigma_{fg}(u) \phi_g(u) - S_g(u) + L_g(u) \right] du = 0$$

where  $l = 0, 1,$  or  $2$  and  $w_l$  is an  $l$ th order polynomial and  $S_g(u)$  is the fission source.

The weighting polynomials, expressed in reduced coordinates, are as follows :

$$\begin{aligned} w_0 &= 1 \\ w_1 &= u \\ w_2 &= u^2 - \frac{1}{12} \\ u &= \frac{x}{2h_x} \end{aligned}$$

The transverse leakage, which is one of the nodal iteration constraints coming from previous iterations, is approximated for each of the nodes by a second degree polynomial. The coefficients of these polynomials are fitted to the average values of the nodal leakage and of the leakage of its immediate neighbors.

### 3.3.1.3 Cross Section Model

The cross sections used in the SMART calculation are the result of three separate operations:

- Interpolation in the data libraries obtained from APOLLO2-F results,
- Determination of the intra-nodal cross sections, and
- Re-homogenization of the cross sections.

The determination of the local cross sections is obtained by interpolation in the data libraries containing the APOLLO2-F results representing the possible states that a node can encounter. The variations of the local depletion effects within a node (intra-nodal) can affect the flux solution in a coarse mesh solution. The homogeneous cross section thus has a spatial dependence. The "effective" cross section to be used in the flux calculation is calculated by a flux/volume weighting of the intra-nodal homogeneous cross sections. This procedure is referred to as re-homogenization. The effective cross sections are reevaluated during the feedback iteration process. The above approach is illustrated in Figure 3-8 with a one dimensional example.

#### 3.3.1.3.1 Interpolation in the APOLLO2-F Data Libraries

As mentioned earlier, the data libraries generated by APOLLO2-F depend on seven variables:

- burnup BU
- boron concentration CB
- xenon level XE

- moderator density VS
- effective fuel temperature TC
- spectral parameter PU
- control rod presence parameter IGR

SMART interpolates the needed values from the data libraries as a function of the local conditions of the node. It thus obtains the microscopic cross sections of the various isotopes present in the node. The macroscopic cross sections are obtained by combining the micros with the isotopic densities and/or directly interpolated from the data libraries. For each node, the average and surface cross sections are calculated. These seven values are used to determine the intra-nodal cross sections.

### 3.3.1.3.2 Intra-nodal Cross Sections

The intra-nodal cross sections are determined directly from the surface and average values using the following formulas:

$$\begin{aligned} \Sigma_{rg}^{\text{hom}}(u, v, w) = & \Sigma_{rg} \\ & + (\Sigma_{rg}^{u+} - \Sigma_{rg}^{u-})u + 3(\Sigma_{rg}^{u+} + \Sigma_{rg}^{u-} - 2\Sigma_{rg})(u^2 - \frac{1}{12}) \\ & + (\Sigma_{rg}^{v+} - \Sigma_{rg}^{v-})v + 3(\Sigma_{rg}^{v+} + \Sigma_{rg}^{v-} - 2\Sigma_{rg})(v^2 - \frac{1}{12}) \\ & + (\Sigma_{rg}^{w+} - \Sigma_{rg}^{w-})w + 3(\Sigma_{rg}^{w+} + \Sigma_{rg}^{w-} - 2\Sigma_{rg})(w^2 - \frac{1}{12}) \end{aligned}$$

where  $u$ ,  $v$  and  $w$  are the reduced coordinates inside the node (between  $-1/2$  and  $1/2$ ) for the  $x$ ,  $y$ , and  $z$  coordinates, respectively.  $\Sigma_{rg}$  and  $\Sigma_{rg}^{ds}$  are the average macroscopic cross section in group  $g$  for reaction  $r$  and the macroscopic surface cross section on face  $s$  in direction  $d$  (see 1D representation in Figure 3-8), respectively. These cross sections are obtained by interpolating the data libraries at the average and surface conditions of the node. The above polynomial intra-nodal sections are fitted in this manner to preserve the average value and the six surface values of the node.

### 3.3.1.3.3 Re-Homogenization

Re-homogenization of the cross sections is performed using the following intra-nodal flux form:

$$\begin{aligned} \Phi_g^{\text{hom}}(u, v, w) = & \Phi_g \\ & + (\Phi_g^{u+} - \Phi_g^{u-})u + 3(\Phi_g^{u+} + \Phi_g^{u-} - 2\Phi_g)(u^2 - \frac{1}{12}) \\ & + (\Phi_g^{v+} - \Phi_g^{v-})v + 3(\Phi_g^{v+} + \Phi_g^{v-} - 2\Phi_g)(v^2 - \frac{1}{12}) \\ & + (\Phi_g^{w+} - \Phi_g^{w-})w + 3(\Phi_g^{w+} + \Phi_g^{w-} - 2\Phi_g)(w^2 - \frac{1}{12}) \end{aligned}$$

The integration of the flux and cross section distributions permits obtaining the average effective cross sections to be used in the flux calculation. These cross sections will be reevaluated during the iterative process so that the flux used to weight the cross sections is within the convergence criterion of the final flux solution. The cross sections from the re-homogenization are used in the nodal flux calculation (inner and outer iterations) and in reevaluating the interface neutron currents (nodal iteration).

#### 3.3.1.4 Convergence Algorithm and Model Coupling

The convergence of the calculations is based on four iteration levels:

- Inner iteration
- Outer iteration
- Nodal iteration
- Feedback iteration

The general algorithm implementing these various iteration levels is represented in Figure 3-9. The most internal convergence level, consisting of inner and outer iterations, furnishes a converged flux on the present cross sections. Since this is a static calculation, a K-effective multiplication factor is used. The converged flux is then transmitted to the nodal iteration which determines the currents at the interfaces of the nodes. The pseudo diffusion coefficients determined from the nodal iteration are then used for subsequent iterations.

When convergence is obtained for these three levels, the converged fluxes are transmitted to the thermal-hydraulic and rod thermal models to determine the water and fuel temperatures in each node. These latter values are then used to calculate new cross sections to be used for subsequent iterations. For numerical efficiency reasons, the convergence of the various iteration levels is ensured in a coherent manner by criteria which become tighter as the iterations proceed.

##### 3.3.1.4.1 Inner Iteration

The inner iteration calculates the flux using a finite difference operator with a fixed source. The solving of the linear system is obtained by an iterative process that sweeps the core according to a red and black checkerboard pattern. During the first pass, all the "reds" are calculated with the "black" conditions constant. The second pass calculates the "black" conditions with the new "red" conditions. This process

has the advantage of not favoring any one direction thus maintaining symmetry. The "red" and "black" pass constitutes an inner iteration. To minimize the number of inner iterations to be performed, the process is accelerated by using the Chebytshev semi-cyclic method.

#### 3.3.1.4.2 Outer Iteration

The outer iteration calculates the new neutron source and the new effective multiplication factor (k-effective) for the system using the fluxes calculated by the inner iteration. The k-effective is determined using the Wielandt accelerated power method (method of shifting the eigenvalue).

#### 3.3.1.4.3 Nodal Iteration

The nodal iteration permits reevaluating the node coupling coefficients. It solves the two-node problem for all the interfaces present in the core and determines the finite difference operator changes to be applied to the inner iteration.

#### 3.3.1.4.4 TH Feedback Iteration

This fourth and last iteration level calculates the effect of the power level on the thermal-hydraulic parameters of the core. Since the cross sections of each node depend on the fuel and moderator conditions, which depend on the power level, it is necessary to perform an iteration to ensure coherence between the power, the flux, and the cross sections.

### 3.3.2 Kinetics Calculations

Reactor core kinetics calculations require the explicit coupling of three models (see Figure 3-10) :

- the neutronic model
- the thermal-hydraulic model
- the fuel rod thermal model.

The neutron kinetic equations are classically given by the following formulas :

$$\left\{ \begin{array}{l} \frac{1}{v_1} \frac{\partial \Phi_1^{ijk}(\vec{r}, t)}{\partial t} = -\vec{\nabla} \cdot J_1^{ijk}(\vec{r}, t) - (\Sigma_{a1}^{ijk}(\vec{r}) + \Sigma_r^{ijk}(\vec{r})) \Phi_1^{ijk}(\vec{r}, t) \\ + (1 - \beta^{ijk}(\vec{r})) (v \Sigma_{f1}^{ijk}(\vec{r}) \Phi_1^{ijk}(\vec{r}, t) + v \Sigma_{f2}^{ijk}(\vec{r}) \Phi_2^{ijk}(\vec{r}, t)) + \sum_{i=1}^6 \lambda_i^{ijk}(\vec{r}) C_i^{ijk}(\vec{r}, t) + q_1^{ijk}(\vec{r}, t) \\ \frac{1}{v_2} \frac{\partial \Phi_2^{ijk}(\vec{r}, t)}{\partial t} = -\vec{\nabla} \cdot J_2^{ijk}(\vec{r}, t) - \Sigma_{a2}^{ijk}(\vec{r}) \Phi_2^{ijk}(\vec{r}, t) + \Sigma_r^{ijk}(\vec{r}) \Phi_1^{ijk}(\vec{r}, t) + q_2^{ijk}(\vec{r}, t) \end{array} \right.$$

$$\frac{\partial C_i^{ijk}(\vec{r}, t)}{\partial t} = \beta_i^{ijk}(\vec{r}) \sum_{g=1}^2 v \Sigma_{fg}^{ijk}(\vec{r}, t) \Phi_g^{ijk}(\vec{r}, t) - \lambda_i^{ijk}(\vec{r}) C_i^{ijk}(\vec{r}, t) \text{ for } i=1 \text{ to } 6$$

where :

- $\Phi_g^{ijk}(\vec{r}, t)$  is the flux in energy group g for node (i,j,k)
- $J_g^{ijk}(\vec{r}, t)$  is the current in energy group g for node (i,j,k)
- $\Sigma_{rg}^{ijk}(\vec{r}, t)$  is the type r cross section in group g for node (i,j,k)
- $C_i^{ijk}(\vec{r}, t)$  is the group i precursor concentration for node (i,j,k)
- $\lambda_i^{ijk}(\vec{r}, t)$  is the decay constant for the group i precursors for node (i,j,k)
- $\beta_i^{ijk}(\vec{r}, t)$  is the fraction of neutrons produced in the group i precursors for node (i,j,k)
- $q_g^{ijk}(\vec{r}, t)$  is the external source in group g for node (i,j,k)

The integration of this set of equations for homogeneous node (i,j,k) gives, as in the static case, the following system :

$$\left\{ \begin{array}{l} \frac{1}{v_1} \frac{\partial \Phi_1^{ijk}(t)}{\partial t} = - \frac{J_1^{i+}(t) - J_1^{i-}(t)}{h_x^{ijk}} - \frac{J_1^{j+}(t) - J_1^{j-}(t)}{h_y^{ijk}} - \frac{J_1^{k+}(t) - J_1^{k-}(t)}{h_z^{ijk}} - (\Sigma_{a1}^{ijk} + \Sigma_r^{ijk}) \Phi_1^{ijk}(t) \\ \quad + (1 - \beta^{ijk}) (v \Sigma_{f1}^{ijk} \Phi_1^{ijk}(t) + v \Sigma_{f2}^{ijk} \Phi_2^{ijk}(t)) + \sum_{i=1}^6 \lambda_i^{ijk} C_i^{ijk}(t) + q_1^{ijk}(t) \\ \frac{1}{v_2} \frac{\partial \Phi_2^{ijk}(t)}{\partial t} = - \frac{J_2^{i+}(t) - J_2^{i-}(t)}{h_x^{ijk}} - \frac{J_2^{j+}(t) - J_2^{j-}(t)}{h_y^{ijk}} - \frac{J_2^{k+}(t) - J_2^{k-}(t)}{h_z^{ijk}} - \Sigma_{a2}^{ijk} \Phi_2^{ijk}(t) + \Sigma_r^{ijk} \Phi_1^{ijk}(t) + q_2^{ijk}(t) \end{array} \right.$$

By integrating the preceding system over the time step  $[t_n, t_{n+1}]$  and by applying the  $\theta$ -method, one

obtains :

$$\left\{ \begin{array}{l} \frac{1}{v_1} \frac{(\Phi_1^{ijk}(t_{n+1}) - \Phi_1^{ijk}(t_n))}{\Delta t_n} = \theta \left[ - \frac{J_1^{i+}(t_{n+1}) - J_1^{i-}(t_{n+1})}{h_x^{ijk}} - \frac{J_1^{j+}(t_{n+1}) - J_1^{j-}(t_{n+1})}{h_y^{ijk}} - \frac{J_1^{k+}(t_{n+1}) - J_1^{k-}(t_{n+1})}{h_z^{ijk}} \right. \\ \quad \left. - (\Sigma_{a1}^{ijk} + \Sigma_r^{ijk}) \Phi_1^{ijk}(t_{n+1}) + (1 - \beta^{ijk}) (v \Sigma_{f1}^{ijk} \Phi_1^{ijk}(t_{n+1}) + v \Sigma_{f2}^{ijk} \Phi_2^{ijk}(t_{n+1})) \right. \\ \quad \left. + \sum_{i=1}^6 \lambda_i^{ijk} C_i^{ijk}(t_{n+1}) + q_1^{ijk}(t_{n+1}) \right] + S_1^{ijk}(t_n) \\ \frac{1}{v_2} \frac{(\Phi_2^{ijk}(t_{n+1}) - \Phi_2^{ijk}(t_n))}{\Delta t_n} = \theta \left[ - \frac{J_2^{i+}(t_{n+1}) - J_2^{i-}(t_{n+1})}{h_x^{ijk}} - \frac{J_2^{j+}(t_{n+1}) - J_2^{j-}(t_{n+1})}{h_y^{ijk}} - \frac{J_2^{k+}(t_{n+1}) - J_2^{k-}(t_{n+1})}{h_z^{ijk}} \right. \\ \quad \left. - \Sigma_{a2}^{ijk} \Phi_2^{ijk}(t_{n+1}) + \Sigma_r^{ijk} \Phi_1^{ijk}(t_{n+1}) + q_2^{ijk}(t_{n+1}) \right] + S_2^{ijk}(t_n) \end{array} \right.$$

with

$$\left\{ \begin{array}{l} S_1^{ijk}(t_n) = (1-\theta) \left[ \frac{J_1^{i+}(t_n) - J_1^{i-}(t_n)}{h_x^{ijk}} - \frac{J_1^{j+}(t_n) - J_1^{j-}(t_n)}{h_y^{ijk}} - \frac{J_1^{k+}(t_n) - J_1^{k-}(t_n)}{h_z^{ijk}} \right. \\ \quad \left. - (\Sigma_{a1}^{ijk} + \Sigma_r^{ijk}) \Phi_1^{ijk}(t_n) + (1-\beta^{ijk}) (\nu \Sigma_{f1}^{ijk} \Phi_1^{ijk}(t_n) + \nu \Sigma_{f2}^{ijk} \Phi_2^{ijk}(t_n)) + \sum_{i=1}^6 \lambda_i^{ijk} C_i^{ijk}(t_n) + q_1^{ijk}(t_n) \right] \\ \\ S_2^{ijk}(t_n) = (1-\theta) \left[ -\frac{J_2^{i+}(t_n) - J_2^{i-}(t_n)}{h_x^{ijk}} - \frac{J_2^{j+}(t_n) - J_2^{j-}(t_n)}{h_y^{ijk}} - \frac{J_2^{k+}(t_n) - J_2^{k-}(t_n)}{h_z^{ijk}} - \Sigma_{a2}^{ijk} \Phi_2^{ijk}(t_n) \right. \\ \quad \left. + \Sigma_r^{ijk} \Phi_1^{ijk}(t_n) + q_2^{ijk}(t_n) \right] \end{array} \right.$$

Again, in the same manner as with the static case, an additional set of equations, relating the currents to the average fluxes, is obtained by partially integrating the initial system with respect to (x,y), (y,z) and (x,z).

In addition, making the assumption that the current obeys Fick's law, three transverse equations are obtained. They are written as follows:

$$\left\{ \begin{array}{l} \frac{1}{v_1} \frac{\partial \Phi_1^{ijk}(u,t)}{\partial t} = -\frac{\partial J_{1u}^{ijk}(u,t)}{\partial u} - (\Sigma_{a1}^{ijk}(u,t) + \Sigma_r^{ijk}(u,t)) \Phi_1^{ijk}(u,t) \\ \quad + (1-\beta^{ijk}) (\nu \Sigma_{f1}^{ijk}(u) \Phi_1^{ijk}(u,t) + \nu \Sigma_{f2}^{ijk}(u) \Phi_2^{ijk}(u,t)) + \sum_{i=1}^6 \lambda_i^{ijk} C_i^{ijk}(u,t) - S_{1u}^{ijk}(u,t) + q_1^{ijk}(u,t) \\ \\ \frac{1}{v_2} \frac{\partial \Phi_2^{ijk}(u,t)}{\partial t} = -\frac{\partial J_{2u}^{ijk}(u,t)}{\partial u} - \Sigma_{a2}^{ijk}(u) \Phi_2^{ijk}(u,t) + \Sigma_r^{ijk}(u) \Phi_1^{ijk}(u,t) - S_{2u}^{ijk}(u,t) + q_2^{ijk}(u,t) \\ \\ \frac{\partial C_i^{ijk}(u,t)}{\partial t} = \beta_i^{ijk} \sum_{g=1}^2 \nu \Sigma_{fg}^{ijk}(u,t) \Phi_g^{ijk}(u,t) - \lambda_i^{ijk} C_i^{ijk}(u,t) \text{ for } i=1 \text{ to } 6 \end{array} \right.$$

where u represents x, y or z and S are the transverse leakages in the u direction.

The introduction into the preceding equations of dynamic frequencies defined by:

$$\omega_{gu}^{ijk}(t) = \frac{1}{\Phi_g^{ijk}(u,t)} \frac{\partial \Phi_g^{ijk}(u,t)}{\partial t}$$

$$\omega_{iu}^{ijk}(t) = \frac{1}{C_i^{ijk}(u,t)} \frac{\partial C_i^{ijk}(u,t)}{\partial t}$$

permits eliminating the precursor from the transverse neutronic equations and obtaining the following 1D system:

$$\left\{ \begin{array}{l} \frac{\partial J_{1u}^{ijk}(u, t)}{\partial u} + \tilde{\Sigma}_{i1}^{ijk}(u, t)\Phi_1^{ijk}(u, t) = \chi_p^{ijk}(t)(\nu\Sigma_{f1}^{ijk}(u)\Phi_1^{ijk}(u, t) + \nu\Sigma_{f2}^{ijk}(u)\Phi_2^{ijk}(u, t)) - S_{1u}^{ijk}(u, t) + q_1^{ijk}(u, t) \\ \frac{\partial J_{2u}^{ijk}(u, t)}{\partial u} + \tilde{\Sigma}_{i2}^{ijk}(u, t)\Phi_2^{ijk}(u, t) = \Sigma_r^{ijk}(u)\Phi_1^{ijk}(u, t) - S_{2u}^{ijk}(u, t) + q_2^{ijk}(u, t) \end{array} \right.$$

with:

$$\left\{ \begin{array}{l} \Sigma_{i1}^{ijk}(u, t) = \left( \Sigma_{a1}^{ijk}(u, t) + \frac{1}{\nu_1}\omega_{1u}^{ijk}(t) + \Sigma_r^{ijk}(u, t) \right) \\ \Sigma_{i2}^{ijk}(u, t) = \left( \Sigma_{a2}^{ijk}(u) + \frac{1}{\nu_2}\omega_{2u}^{ijk}(t) \right) \\ \chi_p^{ijk} = 1 - \beta^{ijk} + \sum_{i=1}^6 \frac{\lambda_i^{ijk} \beta_i^{ijk}}{\lambda_i^{ijk} + \omega_{iu}^{ijk}(t)} \end{array} \right.$$

The above one-dimensional equations have the same form as for the static case, which permits solving them in the same manner. The integration of the equation for the group  $i$  precursors in node  $(i,j,k)$  over the time interval  $(t_n, t_{n+1})$  and set  $\Delta t_n = t_{n+1} - t_n$  leads to:

$$C_i^{ijk}(t_{n+1}) = C_i^{ijk}(t_n)e^{-\lambda_i^{ijk}\Delta t_n} + e^{-\lambda_i^{ijk}\Delta t_n} \int_{t_n}^{t_{n+1}} e^{-\lambda_i^{ijk}(t-t_n)} \beta_i^{ijk} \sum_{g=1}^2 \gamma \Sigma_{fg}^{ijk}(t) \Phi_g^{ijk}(t) dt$$

By making the assumption that the fission term varies linearly, it is possible to obtain an expression for the precursors at time  $t_{n+1}$  as a function of their concentrations at  $t_n$  and their fission rates at times  $t_n$  and  $t_{n+1}$ :

$$C_i^{ijk}(t_{n+1}) = a_{1i} C_i^{ijk}(t_n) + a_{2i} \frac{\beta_i^{ijk}}{\lambda_i^{ijk}} \sum_{g=1}^2 \nu \Sigma_{fg}^{ijk}(t_{n+1}) \Phi_g^{ijk}(t_{n+1}) + (1 - a_{1i} - a_{2i}) \frac{\beta_i^{ijk}}{\lambda_i^{ijk}} \sum_{g=1}^2 \nu \Sigma_{fg}^{ijk}(t_n) \Phi_g^{ijk}(t_n)$$

with :

$$a_{1i} = e^{-\lambda_i^{ijk}\Delta t_n} \text{ and } a_{2i} = 1 - \frac{1 - e^{-\lambda_i^{ijk}\Delta t_n}}{\lambda_i^{ijk} \Delta t_n}$$

By replacing the precursor concentrations determined from the preceding formula in the neutron balance equation and then regrouping the terms in  $t_n$  and  $t_{n+1}$ , a constant source system of equations is obtained. This system permits calculating the flux at times  $t_{n+1}$  as a function of the parameters obtained at time step  $t_n$ . The node cell coupling terms are calculated by nodal iteration just as in the static case.

### 3.3.3 Pin Reconstruction

The pin reconstruction results are obtained by a process of de-homogenizing the homogeneous calculation. The SMART reconstruction method uses the average nodal properties calculated by SMART and the APOLLO-2 assembly calculation results stored in the data libraries. It is possible to reconstruct three types of information during the SMART calculation:

- The pin-by-pin power distribution
- The pin-by-pin burnup distribution
- The detector response in the instrument tube

The pin reconstruction of the power or the burnup is performed for a complete assembly or a quarter assembly (Reference 7). The reconstruction is performed in two-dimensions for each node (average in z direction), which is acceptable as long as the node heights are not too large or that there are no axial heterogeneities in the node.

#### 3.3.3.1 Pin Power Reconstruction

The reconstruction of the power in a node n is carried out in four steps:

- Determination of the homogeneous fluxes

$$\begin{cases} \Phi_1^n(x, y) \\ \Phi_2^n(x, y) \end{cases}$$

- Determination of the homogeneous energy cross sections

$$\begin{cases} \kappa_1^n \Sigma_{f1}^n(x, y) \\ \kappa_2^n \Sigma_{f2}^n(x, y) \end{cases}$$

- Determination of the homogeneous power

$$P^{\text{hom},n}(x, y) = \left( \kappa_1^n \Sigma_{f1}^n(x, y) \Phi_1^n(x, y) + \kappa_2^n \Sigma_{f2}^n(x, y) \Phi_2^n(x, y) \right)$$

- Reconstruction of the heterogeneous power

$$P^{\text{rec},n}(x, y)$$

##### 3.3.3.1.1 Determination of the Homogeneous Fluxes

The intra-nodal flux expansions are performed using the following expansions :

$$\left\{ \begin{array}{l} \Phi_1^n(u, v) = \sum_{\substack{i=0 \\ j=0}}^4 a_{ij}^n P_i(u) P_j(v) \\ \Phi_2^n(u, v) = b_{00}^n \Phi_1^n(u, v) + \sum_{\substack{i=0 \\ j=0 \\ i \text{ and } j \neq 0}}^4 b_{ij}^n F_i(u) F_j(v) \end{array} \right.$$

where:

u, v and w are the usual reduced coordinates of the reconstruction pattern (assembly or quarter assembly),  
n is the number of the reconstructed node,

$$\Phi_g^n(u, v) = \int_{w_{\min}}^{w_{\max}} \Phi_g^n(u, v, w) dw \quad ,$$

(wmin is the lower elevation of node n, wmax is the upper elevation of node n), and:

$$P_i(u) = u^i$$

$$F_0(u) = 1$$

$$F_1(u) = \sinh(\zeta_u u)$$

$$F_2(u) = \cosh(\zeta_u u)$$

$$F_3(u) = \sinh(2\zeta_u u)$$

$$F_4(u) = \cosh(2\zeta_u u)$$

$$\text{with } \zeta_u = h_u \sqrt{\frac{\sum a_2^n}{D_2^n}}$$

Knowledge of the intra-nodal fluxes is based on the determination of 13 coefficients per group. It is therefore necessary to reconstruct 13 constraints per group using the homogeneous nodal calculation to obtain the intra-nodal flux.

The corner homogeneous fluxes are added to the nine node parameters provided by the nodal calculation (average flux, surface fluxes and currents) to complete the system of equations. The calculation of the fluxes in the four corners of the node is based on an estimation of the homogeneous flux corrected by the heterogeneous flux continuity constraints. The homogeneous flux in the corner located at the intersection of faces Si and Sj of node cell n is given by the formula:

$$\Phi_{g,S_i,S_j}^n = \Phi_{g,S_i}^n + \Phi_{g,S_j}^n - \Phi_g^n$$

Since a corner is shared by four nodes, four different evaluations of the homogeneous flux exist at this point. Unlike the homogeneous flux, the heterogeneous flux must be continuous. The four estimations of the homogeneous flux are used to calculate four estimations of the heterogeneous flux.

$$\begin{aligned} \Phi_g^{\text{het},n} &= \text{cpdf}_g^n \Phi_g^n \\ \Phi_g^{\text{het},k} &= \text{cpdf}_g^k \Phi_g^k \\ \Phi_g^{\text{het},l} &= \text{cpdf}_g^l \Phi_g^l \\ \Phi_g^{\text{het},m} &= \text{cpdf}_g^m \Phi_g^m \end{aligned}$$

where: k, l, and m are the node cells having a common corner with n. The cpdf factor, referred to as the corner point discontinuity factor, is obtained from the data libraries generated from the APOLLO2-F results. It is defined for corner c in group g by:

$$\text{cpdf}_{g,c} = \frac{\Phi_{g,c}^{\text{het}}}{\Phi_g} \text{ where } \Phi_g \text{ is the assembly average flux.}$$

The continuity of the heterogeneous flux at the corner is imposed by defining the heterogeneous flux as the average of the four prior estimates. The homogeneous flux corresponding to node n is then obtained by dividing the continuous component by the corresponding cpdf.

#### 3.3.3.1.2 Determination of the Homogeneous Cross Sections

The re-homogenization process requires the reconstruction of intra-nodal homogeneous cross sections. The same technique is applied to the  $\kappa\Sigma_{fg}$  cross sections to represent gradients through the node. However, this technique does not account for the very localized effects of spectral spatial variations and their influence on plutonium formation. This effect is modeled using the following spectral history parameter:

$$\text{SH} = \frac{\int \left[ \frac{\Phi_1 / \Phi_2}{\text{surface}} \right]_{\text{surface}} d\text{BU}}{\int \left[ \frac{\Phi_1 / \Phi_2}{\text{average}} \right]_{\text{average}} d\text{BU}}$$

The  $\kappa\Sigma_{fg}$  variations due to spectral interactions are tabulated in the fine reconstruction data file generated with APOLLO2-F results. This dependency is obtained by comparing two APOLLO2-F assembly depletions carried out under different spectral conditions by modifying the water temperature.

#### 3.3.3.1.3 Determination of the Homogeneous Pin Power

The homogeneous power distributions and cross sections are obtained directly from the homogeneous power inside node n from the formula:

$$P^{\text{hom},n}(x, y) = \left( \kappa_1^n \Sigma_{f1}^n(x, y) \Phi_1^n(x, y) + \kappa_2^n \Sigma_{f2}^n(x, y) \Phi_2^n(x, y) \right)$$

#### 3.3.3.1.4 Determination of the Heterogeneous Pin-by-Pin Power

The last reconstruction step is the multiplicative superposing of the normalized heterogeneous power shape function from the APOLLO2-F assembly calculation to the homogeneous power shape. The heterogeneous power shape is interpolated as a function of the nodal local conditions from the

APOLLO2-F data library. The result is then normalized to ensure the equality between the homogeneous assembly power and the summation of the pin-by-pin power:

$$P^{rec,n}(x, y) = \zeta P^{hom,n}(x, y) P^{het,n}(x, y)$$

where:  $\zeta$  is the renormalization constant

$P^{rec,n}(x,y)$  is the reconstructed pin power for pin x,y in node n

$P^{hom,n}(x,y)$  is the homogeneous power for pin x,y in node n

$P^{het,n}(x,y)$  is the APOLLO2-F heterogeneous power distribution corresponding to the node n conditions for pin x,y

### 3.3.3.2 Pin Burnup Reconstruction

In a manner analogous to the power reconstruction, SMART calculates the pin-by-pin burnup distribution. Two steps are necessary.

- determination of the homogeneous burnup distribution for node n:

As with the cross sections, the homogeneous burnup distribution  $BU^{hom,n}(x,y)$  is broken down in terms of a second order polynomial. The five expansion coefficients are obtained by imposing compliance with the nodal surface and average burnups.

- Determination of the heterogeneous burnup distribution:

Similarly, the rod-by-rod burnup distribution is obtained by a multiplicative superposition of an assembly burnup  $BU^{het,n}(x,y)$  taken from the APOLLO2-F calculation on the homogenized burnup distribution. The function obtained is renormalized by  $\xi$  to preserve the average value of the nodal burnup :

$$BU^{rec,n}(x, y) = \xi BU^{hom,n}(x, y) BU^{het,n}(x, y)$$

### 3.3.3.3 Detector Response Reconstruction

In SMART, the reconstruction of the detector response in the instrument tube is carried out in two stages:

- Determination of the homogeneous flux in the instrument tube:

The flux expansions determined for the power reconstruction are used to evaluate the homogeneous flux seen by the instrument tube.

- Reconstruction of the detector response:

The detector response (reaction rate)  $A$  of a group is calculated by superposing a heterogeneity factor for the instrument tube (referred to as the instrumentation discontinuity factor) on the local homogeneous flux values, i.e.:

$$A^{rec,n}(x_i, y_i) = \sum_{det,l}'' \Phi_1^{hom,n}(x_i, y_i) F_1^{det,n} + \sum_{det,l}'' \Phi_2^{hom,n}(x_i, y_i) F_2^{det,n}$$

where:

$F_g^{det,n} = \left[ \frac{\Phi_g^{det,n}}{\Phi_g} \right]$  is the instrument discontinuity factor for node n obtained from the data library from the APOLLO2-F results at the local conditions seen by the assembly instrument tube cell, and  $\sum_{det,g}''$  is the detector cross section of assembly n determined under the same conditions.

### 3.3.4 Depletion Model

SMART performs the microscopic depletion of the primary heavy isotopes and fission products. To accomplish this, the depletion model uses the local microscopic cross sections (average values per node), the nuclei decay constants and the isotopic densities present in the node.

The following reactions are treated:

- **Neutronic reactions (under irradiation)**
  - ⇒ Radiative capture
  - ⇒ Induced fission
  - ⇒ n → 2n reaction
- **Radioactive disintegration**
  - ⇒ α decay
  - ⇒ β decay

#### 3.3.4.1 Depletion Chains

The depletion chains can be configured through the input. The current standard depletion chains contain two large groups of isotopes:

- Heavy isotopes (see Figure 3-11):  
**U234, U235, U236, U238, NP237, PU238, PU239, PU240, PU241, PU242, AM241, AM242M, AM242, CM242, CM243 and CM244**
- Fission products (see Figure 3-12 and Figure 3-13)  
**I135, XE135, PM147, PM148, PM148M, PM149, SM149**

#### 3.3.4.2 Processing the Depletion Equations

Let k be a nucleus participating in the microscopic depletion. The isotope k production and depletion paths are indicated in the following table.

Isotope k production paths	Isotope disappearance paths
Decay of another isotope	Decay to another isotope
Capture of another isotope	Absorption (capture or fission)
Fission	Reaction $n \rightarrow 2n$
Reaction $n \rightarrow 2n$	

The average density  $N_k$  of isotope k in a depletion node, is represented by the depletion equation:

$$\frac{dN_k}{dt} = \sum_{ic} \Gamma_{ic,k} N_{ic} (\sigma_{ic,1} \Phi_1 + \sigma_{ic,2} \Phi_2) + \sum_{if} Y_{if,k} N_{if} (\sigma_{if,1} \Phi_1 + \sigma_{if,2} \Phi_2) + \sum_{in2n} N_{in2n} \sigma_{kn2n,1} \Phi_1 + \sum_{il} \lambda_{il,k} N_{il} - N_k \left[ \lambda_k + (\sigma_{ka,1} \Phi_1 + \sigma_{ka,2} \Phi_2) + (\sigma_{kf,1} \Phi_1 + \sigma_{kf,2} \Phi_2) + \Phi (\sigma_{kn2n,1} \Phi_1 + \sigma_{kn2n,2} \Phi_2) \right]$$

with:

ic: Isotopes leading to k by radiative capture reaction

if: Isotopes leading to k by fission

in2n: Isotopes leading to k by  $n \rightarrow 2n$  reaction

il: Isotopes leading to k by radioactive decay

$\Gamma_{ic,k}$ : Fraction of captures leading to k

$Y_{if,k}$ : Fission yield from isotope if to k

$\lambda_{il,k}$ : Decay constant of isotope il to k

$\lambda_k$ : Decay constant of isotope k

where:

$N_{ic}$ ,  $N_{if}$ ,  $N_{in2n}$ , and  $N_{il}$  are the average densities of the isotopes involved by capture reactions, fission reactions,  $n \rightarrow 2n$  reactions, and decay to isotope k, respectively,

$\sigma_{ir,g}$ : microscopic cross section for reaction r of isotope i in group g, and

$\Phi_g$ : Average nodal flux in group g.

Note:

- $n \rightarrow 2n$  type reactions exist only for fast neutrons.
- the isotopic densities are obtained by solving a system of first order equations whose coefficients depend on the fluxes and cross sections.

This system can be written:

$$\frac{dN_k}{dt} = G_k - L_k N_k$$

with:

$$G_k = \sum_{ic} \Gamma_{ic,k} N_{ic} (\sigma_{ic,1} \Phi_1 + \sigma_{ic,2} \Phi_2) + \sum_{if} Y_{if,k} N_{if} (\sigma_{if,1} \Phi_1 + \sigma_{if,2} \Phi_2) + \sum_{in2n} N_{in2n} \sigma_{kn2n,1} \Phi_1 + \sum_{il} \lambda_{il,k} N_{il}$$

$$L_k = \left[ \lambda_k + (\sigma_{ka,1} \Phi_1 + \sigma_{ka,2} \Phi_2) + (\sigma_{kf,1} \Phi_1 + \sigma_{kf,2} \Phi_2) + (\sigma_{kn2n,1} \Phi_1 + \sigma_{kn2n,2} \Phi_2) \right]$$

The time step  $[t_{n-1}, t_n]$  was chosen sufficiently small so that the isotopic densities used in  $G_k$  remain constant and the densities at time  $t_n$  are determined from those at  $t_{n-1}$  by the relationship:

$$N_k(t_n) = \frac{G_k}{L_k} + \left[ N_k(t_{n-1}) - \frac{G_k}{L_k} \right] e^{-L_k(t_n - t_{n-1})}$$

A third order approximation of the exponential function permits writing :

$$N_k(t_n) \cong \frac{G_k(t_n - t_{n-1}) + N_k(t_{n-1})(1 - L_k(t_n - t_{n-1})/2)}{1 + L_k(t_n - t_{n-1})/2}$$

In practice, the order of processing the isotopes is set and the most recent determinations of the isotopic densities are used to correct the  $G_k$ , using the formula :

$$\bar{N}_j = \frac{N_j(t_n) + N_j(t_{n-1})}{2}$$

This method permits an update of the depletion effects on the coefficients of the differential system within the time step.

### 3.3.5 Thermal-Hydraulic Model

The SMART code has a closed-channel thermal-hydraulic model. A channel is a vertical column of nodes. The SMART thermal-hydraulic model calculates the outlet and average values of the enthalpy, the density and the fluid void fraction for each node. It also calculates the outside contact temperature of the cladding of the fuel rods present in the node. The average moderator and clad surface temperatures are used as boundary conditions, respectively, for the static and kinetic fuel rod thermal models. Water density or specific volume is used by the feedback system to functionalize the cross sections used in the neutronic model.

This model deals with four flow regimes that the reactor coolant can encounter when it rises in a heated channel, from the single phase liquid state to bulk boiling:

- Single phase flow with no boiling.

- Highly subcooled boiling flow with bubble formation on the walls, but no bubble detachment.
- Slightly subcooled boiling flow with bubble detachment.
- Bulk boiling flow.

### 3.3.5.1 Calculation of Enthalpy and Heat Flux

The SMART thermal-hydraulic model is based on the following assumptions :

- constant pressure over the entire core volume
- mass velocity constant along each thermal-hydraulic channel
- no transfer between channels (closed channel model)
- enthalpy or temperature at inlet to channel is known

Given these assumptions, the enthalpy is defined by the following differential equation :

$$\rho \frac{\partial H}{\partial t} + \rho u \frac{\partial H}{\partial z} = s + \frac{\partial P}{\partial t}$$

where  $\rho$ ,  $u$ ,  $P$  and  $s$  are, respectively, the fluid density, its velocity, the pressure and the power density.

The enthalpy at the top outlet from the node is obtained by integrating the differential equation over the volume of the node and over the time step  $(t_n, t_{n+1})$ , the inlet enthalpy being equal to the outlet enthalpy of the lower node. The integration with respect to time is performed using the  $\theta$ -method.

This permits calculating the enthalpy at the outlet of node  $ijk$  for time step  $(t_n, t_{n+1})$  :

$$H_{ijk+1/2}^{n+1} = \frac{E_{ijk} \Delta z_k + \theta G_{ij}^n H_{ijk-1/2}^{n+1} - (1-\theta) G_{ij}^n (H_{ijk+1/2}^n - H_{ijk-1/2}^n) - \frac{1}{2} \frac{\Delta z_k}{\Delta t_n} \rho_{ijk}^n (H_{ijk-1/2}^{n+1} - H_{ijk+1/2}^n - H_{ijk-1/2}^n)}{\theta G_{ij}^n + \frac{1}{2} \frac{\Delta z_k}{\Delta t_n} \rho_{ijk}^n}$$

- $ijk - 1/2$  represents the lower boundary of node  $ijk$
- $ijk + 1/2$  represents the upper boundary of node  $ijk$
- $z_k$  represents the height of  $ijk$
- $G_{ij}$  is the mass flow rate in thermal-hydraulic channel  $ij$
- $t_n$  is the length of the time step  $t_{n+1} - t_n$
- $E_{ijk} \Delta z_k$  represents the fluid heating power over node  $ijk$  for time step  $t_{n+1} - t_n$ . It is the sum of the radiated power density ( $s_r$ ) from the fuel to the fluid from energy deposition of neutrons and gammas, the power density transmitted ( $s_T$ ) to the fluid through the fuel cladding, and the energy from the pressure forces expressed by the following equation :

$$E_{ijk} = \left[ s_{Rijk} + s_{Tijk} + \frac{(P^{n+1} - P^n)}{\Delta t_n} \right] / \Omega$$

with  $\Omega$  being the relative flow area of the fuel assembly. The average enthalpy of the node is the average of the node inlet and outlet enthalpies. The heat flux transmitted to the fluid by the fuel cladding is calculated as follows :

$$\Phi_{ijk} = \frac{s_{Tijk}}{HP \times \Omega}$$

where HP is the heated perimeter per area of flow in the fuel assembly.

### 3.3.5.2 Transition between the Various Flow Regimes

The transition between the four flow regions of the thermal-hydraulic model is illustrated by the scheme in Figure 3-14. Three criteria enter in the calculation. The first criterion concerns the thermodynamic quality of the node defined as follows:

$$\chi_{ijk} = \frac{H_{ijk} - H_{sat}}{H_{fg}}$$

where :

- $H_{ijk}$  is the enthalpy of node  $ijk$
- $H_{sat}$  is the enthalpy of the saturated liquid
- $H_{fg}$  is the heat of vaporization

The bulk boiling regime is reached when the thermal-hydraulic quality is positive. The second and third criteria concern the heated wall temperature and the subcooled state of the node cell.

Three conditions can exist when the quality is zero. If the wall temperature is less than the boiling temperature, the fluid is in a single phase liquid condition. When the wall temperature exceeds the local boiling temperature, the fluid is in one of the two subcooled boiling regimes. The passage from a highly subcooled regime to a slightly subcooled regime occurs when the subcooled temperature is such that bubble detachment (nucleate boiling) begins to occur.

#### 3.3.5.2.1 Wall Temperature Model

The wall temperature is given by the following formula:

$$T_{paroi}^{ijk} = T_{ijk} + \frac{\Phi_{ijk}}{u_{ijk}}$$

where:

- $T_{ijk}$  is the average temperature of node  $ijk$
- $\Phi_{ijk}$  is the heat flux crossing the hot wall of node  $ijk$
- $u_{ijk}$  is the single phase heat transfer coefficient of the Colburn model (Reference 8)

The Colburn model coefficient is determined by the following formula:

$$u_{ijk} = 0.03 \frac{K_{ijk}}{D_{h,ij}} Pr^{1/3} Re_{ijk}^{0.8}$$

where  $Re$  is the Reynolds number,  $Pr$  the Prandtl number and  $D_{h,ij}$  the hydraulic diameter.

The temperature at which boiling appears on the hot wall is determined using the following Jens and Lottes correlation:

$$T_{lim} = T_{sat} + 1.9 \Phi^{\frac{1}{4}} e^{\frac{P}{900}}$$

### 3.3.5.2.2 Bubble Detachment Model

The subcooled state is defined by:

$$\theta_{ijk} = T_{sat} - T_{ijk}$$

It is compared with a limit value  $\theta_{lim}$  determined using the Bowring model for high pressures (Reference 9) and Levy model for low pressures (Reference 10). The high pressure model is given by the correlation :

$$\theta_{lim} = 1.8631 \cdot 10^{-5} [14.0 + 0.0068P] \frac{3600.0 \Phi_{ijk} \rho_{f,ijk}}{G \alpha_{ij}}$$

The low pressure model is given by the correlation :

$$\theta_{lim} = \frac{\Phi_{ijk}}{u'_{ijk}} - Q_{ijk} F(\Pr, Y_{BL,ijk})$$

where :

- $u'_{ijk}$  is the single phase transfer coefficient in the Dittus-Boelter model (Reference 8).
- $Q_{ijk}$ ,  $F$  and  $Y_{BL}$  are defined :

$$Q_{ijk} = \frac{\Phi_{ijk}}{c_{pf,ijk} G} \sqrt{\frac{8}{f}}$$

( $f$  and  $c_{pf,ijk}$  are, respectively, the single phase friction and the heat capacity).

$$Y_{BL,ijk} = \frac{0.015}{\mu_{ijk}} \sqrt{g\sigma D_h \rho_{f,ijk}}$$

( $\sigma$  and  $g$  are, respectively, the surface tension and the acceleration of gravity).

$$\text{If } 0 \leq Y_{BL} \leq 5 \quad F(\text{Pr}, Y_{BL}) = \text{Pr} \cdot Y_{BL}$$

$$\text{If } 5 \leq Y_{BL} \leq 30 \quad F(\text{Pr}, Y_{BL}) = 5 \left\{ \text{Pr} + \ln \left[ 1 + \text{Pr} \left( \frac{Y_{BL}}{5} - 1 \right) \right] \right\}$$

$$\text{If } Y_{BL} \geq 30$$

$$F(\text{Pr}, Y_{BL}) = 5 \left\{ \text{Pr} + \ln(1 + 5 \text{Pr}) + 0.5 \ln \left( \frac{Y_{BL}}{30} \right) \right\}$$

### 3.3.5.3 Void Fraction Calculation

The void fraction is calculated using the Griffith et al. correlation (Reference 11) for both the high pressure and low pressure models in the case of the highly subcooled boiling regime and with the two-phase flow model of Zuber et al. (Reference 12) for slightly subcooled boiling.

### 3.3.6 Rod Thermal Model

The calculation of thermal feedback requires knowing the properties of the moderator (boron concentration, density and temperature of the water) and the fuel temperature in each node as a function of time. The rod thermal model provides the temperature of the fuel rods given the deposited power in the pellet and the outer surface temperature of the cladding. A flow chart of this process is shown in Figure 3-10.

When SMART is used for the static calculation, the fuel temperature rise (FTR) above the moderator temperature can be used to determine the fuel temperature. The FTR is tabulated as a function of the power level and the burnup for each type of assembly. The table can be constructed from results with a licensed fuel rod thermomechanical code.

When SMART is used for the kinetic calculation, the relationship between fuel temperature, coolant temperature, burnup and power is not constant. The calculation requires the complete modeling of

the heat transfer between the fuel rod and the primary coolant in order to determine the coolant and the fuel temperature.

SMART uses a fuel rod thermal model with the surface temperature of the cladding as a boundary condition that is calculated by the thermal-hydraulic model. The rod thermal conditions are determined as average conditions for each node. The thermal model describing this average uses one dimensional cylindrical geometry. The material properties (cladding and pellet) and the pellet-clad gap come from the fuel rod thermomechanical code. The power distribution inside the pellet required for the calculation is tabulated as a function of burnup and enrichment obtained from APOLLO2-F results. The SMART rod thermal model permits representing a cylindrical or annular pellet type fuel rod.

### 3.3.6.1 Kinetic Thermal Modeling of the Fuel Rod

The fuel rod thermal model solves the following 1D thermal equation :

$$-\vec{\nabla} \cdot \vec{\varphi}(r, t) + \dot{q}'''(r, t) = \rho C_p(T) \frac{\partial T(r, t)}{\partial t}$$

where:

- $r$  is the radial coordinate
- $\vec{\varphi}$  is the heat flux
- $T$  is the temperature
- $\dot{q}'''$  is the power density
- $\rho$  is the density of the medium
- $C_p$  is the heat capacity

#### Initializing the spatial and temporal boundary conditions

The temperature distribution at the start of the transient  $T(r,0)$  is calculated by neglecting the time-derivative terms in the 1D heat equation. The following special boundary conditions are applied:

$$\partial T / \partial r = 0 \text{ with respect to } r = r_i, \text{ where } r_i \text{ is the inner radius of the problem}$$

$$T(r_o, t) = T_s, \text{ where } r_o = \text{outer radius of the problem}$$

The first equality expresses a zero temperature gradient for the pellet internal radius ( $r_i = 0$  if the pellet is without a central hole). The second equality requires that the boundary condition of the thermal fuel rod model is equal to the clad surface temperature ( $T_s$ ) given by the thermal-hydraulic model.

#### **Solution of the system**

The spatial discretization of the 1D heat equation is obtained by integrating it over the calculation mesh with the assumption that all quantities are constant and equal to their centered values. The temporal

discretization is then obtained by integrating the preceding equation over a time step using the  $\theta$ -method. The pellet is represented by cells with a mesh consisting of equal distant concentric rings. The cladding and the pellet-clad gap are represented by a radial mesh. By indexing the cells from 1 to N and by considering that index  $i$ -cell has an inside radius of  $r_i$  and an outside radius of  $r_{i+1}$ , the differential heat equation is written :

$$-2[r_{i+1}\varphi(r_{i+1}) - r_i\varphi(r_i)] + (r_{i+1}^2 - r_i^2) \left[ \dot{q}_i''' - \rho_i C_{pi} \frac{\partial T_i}{\partial t} \right] = 0$$

Applying Fick's law  $\varphi = -K \frac{\partial T}{\partial r}$  (where K is the thermal conductivity) to the cell interfaces permits writing the interface fluxes as a function of the temperatures of the adjacent cells :

$$\varphi(r_i) = -H_{i,i+1} (T_{i+1} - T_i)$$

$$\text{or } H_{i,i+1} = 2 \left[ \frac{r_{i+1} + r_i}{K_{i+1}} + \frac{r_i + r_{i-1}}{K_i} \right]^{-1}$$

By replacing  $\varphi$  by its expression as a function of T, the differential heat equation becomes :

$$-2[r_i H_{i,i+1} (T_{i+1} - T_i) - r_{i-1} H_{i-1,i} (T_i - T_{i-1})] + (r_i^2 - r_{i-1}^2) (\dot{q}_i''' - \rho_i C_{pi} \frac{\partial T_i}{\partial t}) = 0$$

Integration over time step  $\Delta t_n = t_{n+1} - t_n$  and applying the  $\theta$ -method result in a discretization of the equation according to the following expression :

$$-2\theta \Delta t_n \left[ r_i H_{i,i+1}^{n+1} (T_{i+1}^{n+1} - T_i^{n+1}) - r_{i-1} H_{i-1,i}^{n+1} (T_i^{n+1} - T_{i-1}^{n+1}) \right] - \rho_i^{n+1} C_{pi}^{n+1} (r_i^2 - r_{i-1}^2) T_i^{n+1}$$

$$= \dot{q}_i^{n+1} (r_i^2 - r_{i-1}^2) - \rho_i^n C_{pi}^n T_i^n + 2(1-\theta) \Delta t_n \left( r_i H_{i,i+1}^n (T_{i+1}^n - T_i^n) - r_{i-1} H_{i-1,i}^n (T_i^n - T_{i-1}^n) \right)$$

After grouping the known terms resulting from the previous time step in a constant C, the discretized equation is reduced to the following equation :

$$A_i^{n+1} T_{i+1}^{n+1} + \alpha_i^{n+1} T_i^{n+1} + B_i^{n+1} T_{i-1}^{n+1} = C_i$$

This system is solved in a non-iterative manner by using a recursive method.

Figure 3-1. Architecture of the SCIENCE Code Package

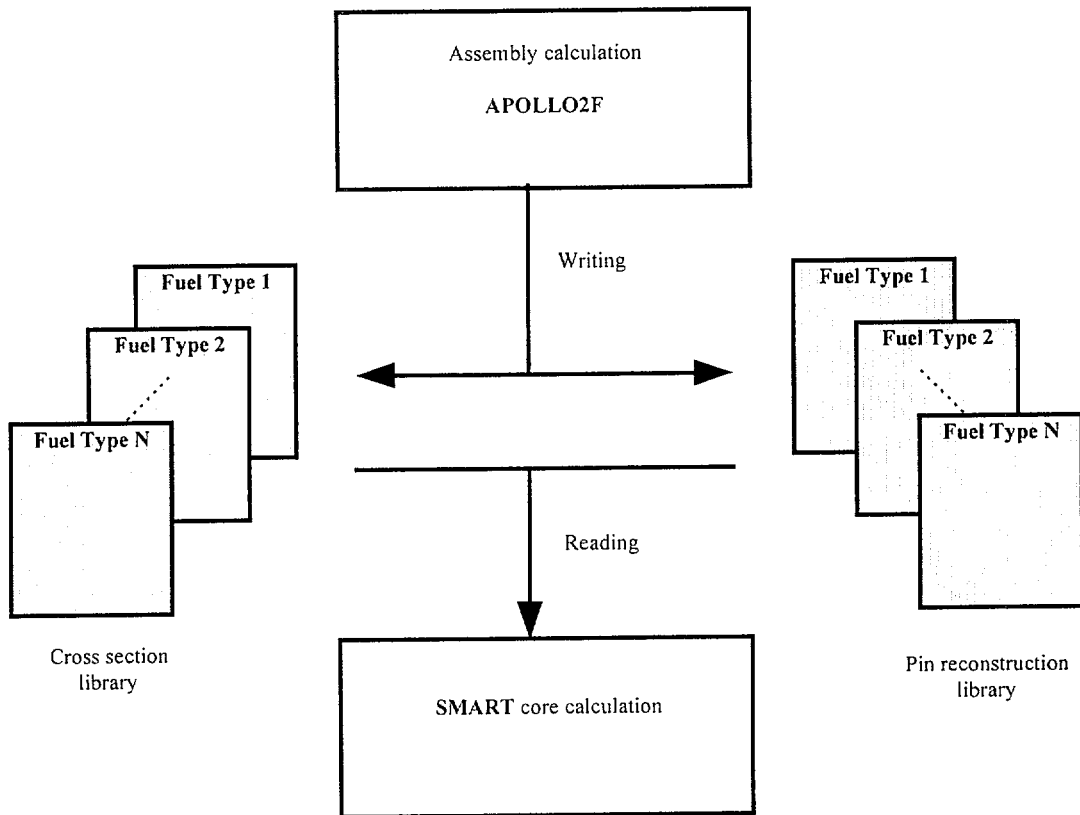
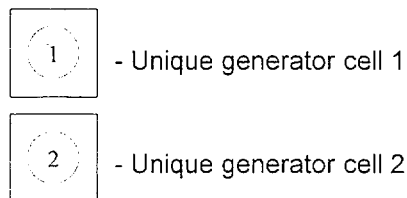
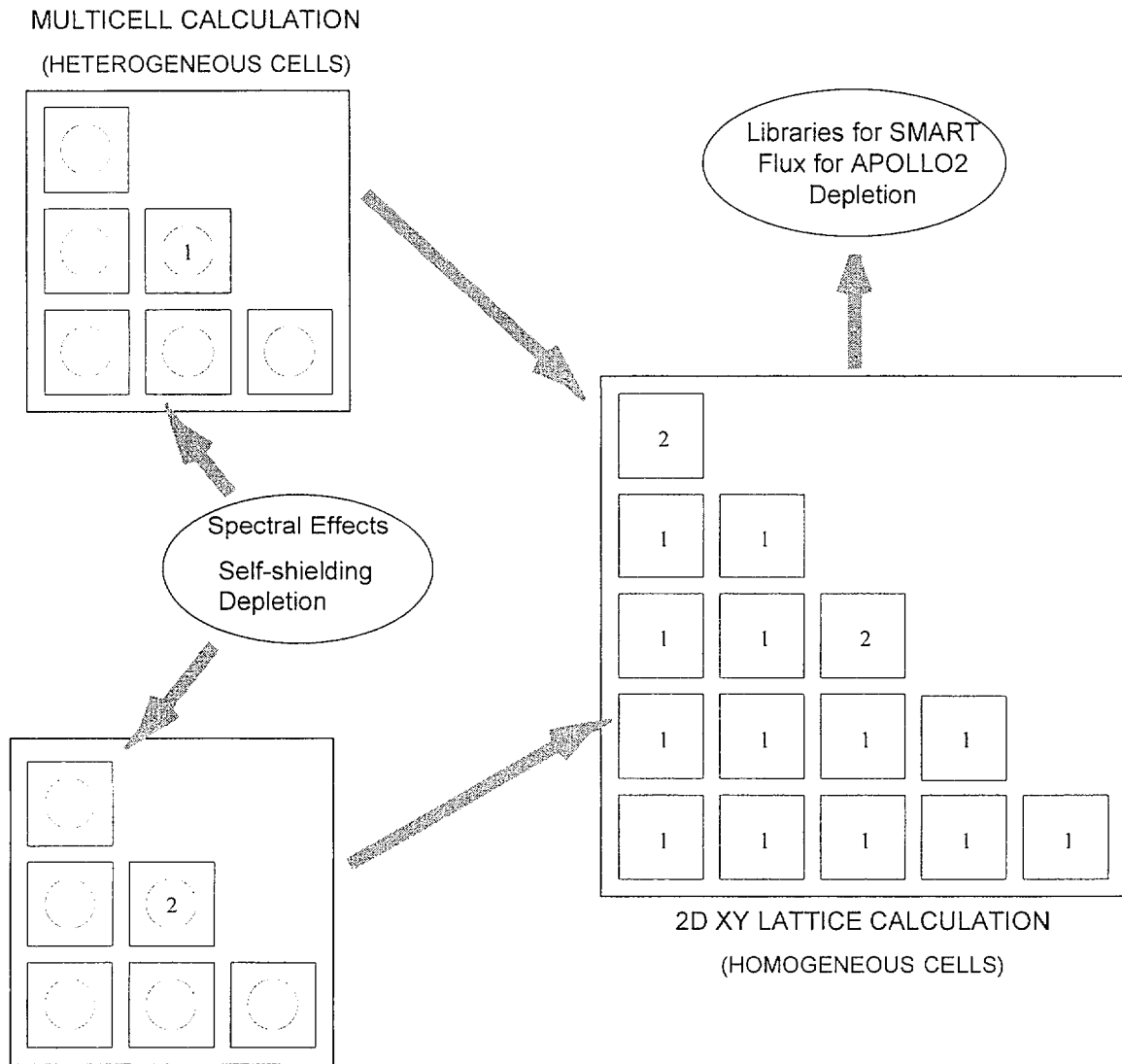
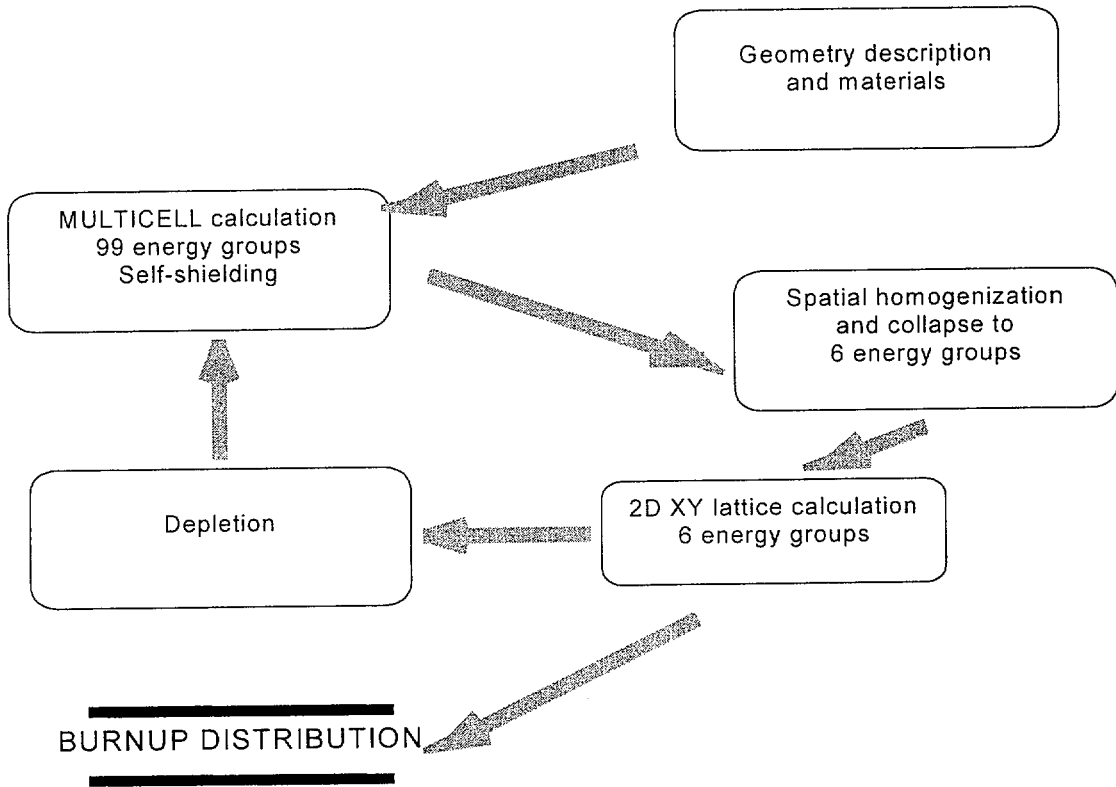


Figure 3-2. APOLLO2-F Assembly Calculation Scheme: Basic Principles



**Figure 3-3. APOLLO2-F Assembly Calculation Scheme: Depletions**



**Figure 3-4. APOLLO2-F Assembly Calculation Scheme: Restart Cases**

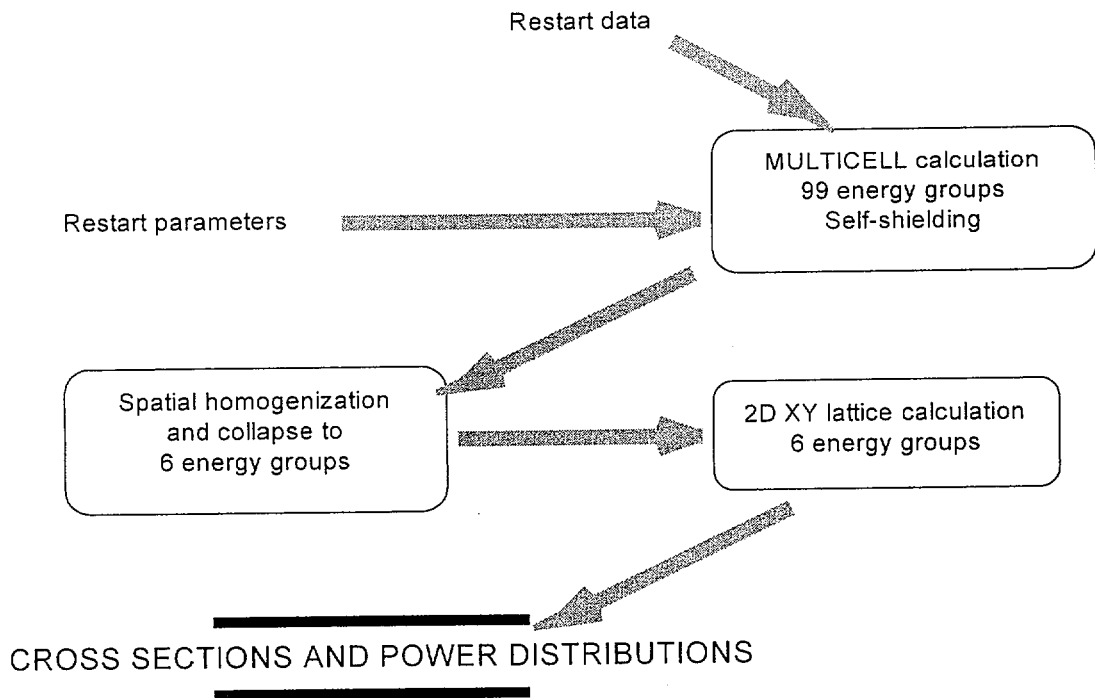


Figure 3-5. Flux Expansion for Interface Currents

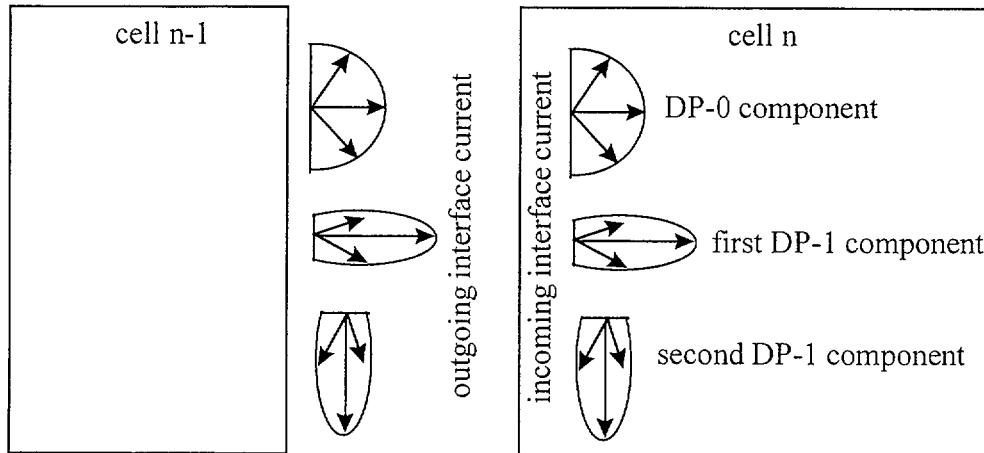
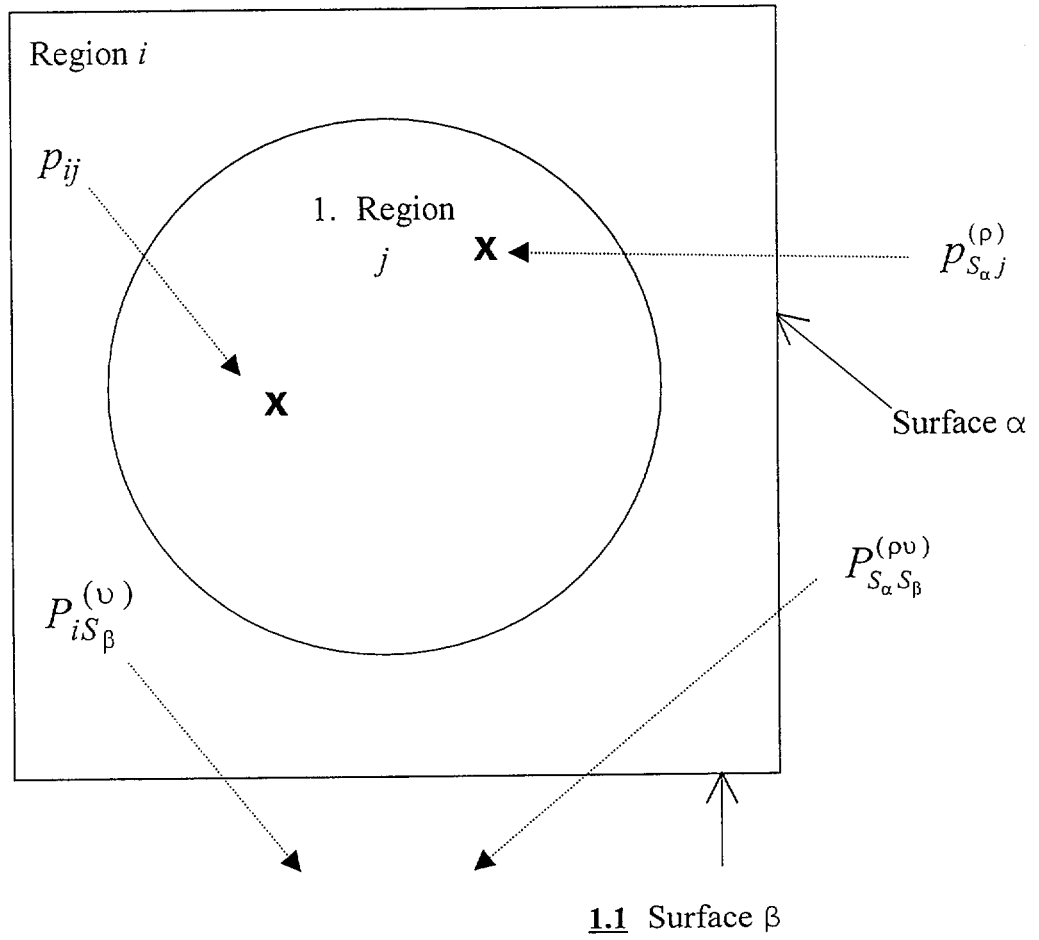


Figure 3-6. Physical Representation for Interface Probabilities

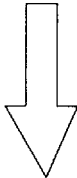
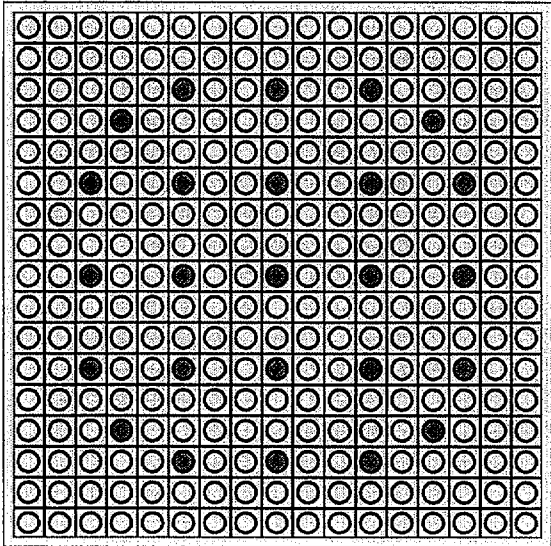


$X$  = neutron interaction

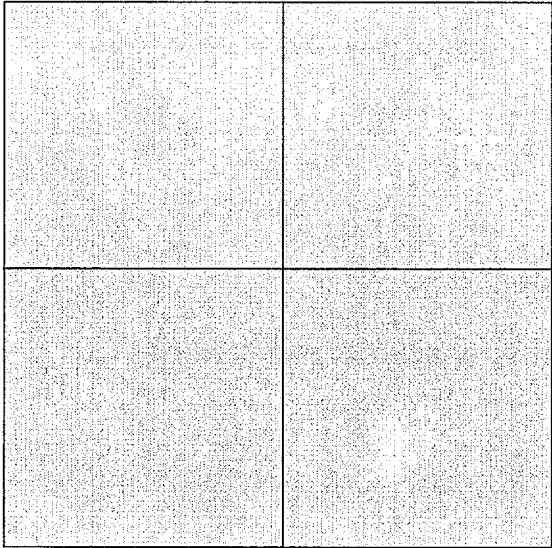
—————▶ Probability of neutron path occurring

Figure 3-7. Reduction of Cells to Nodes Due to Homogenization

Rod -by-rod representation



Homogenization



homogeneous representation  
with four node cells per assembly

Figure 3-8. Rehomogenization of the Node

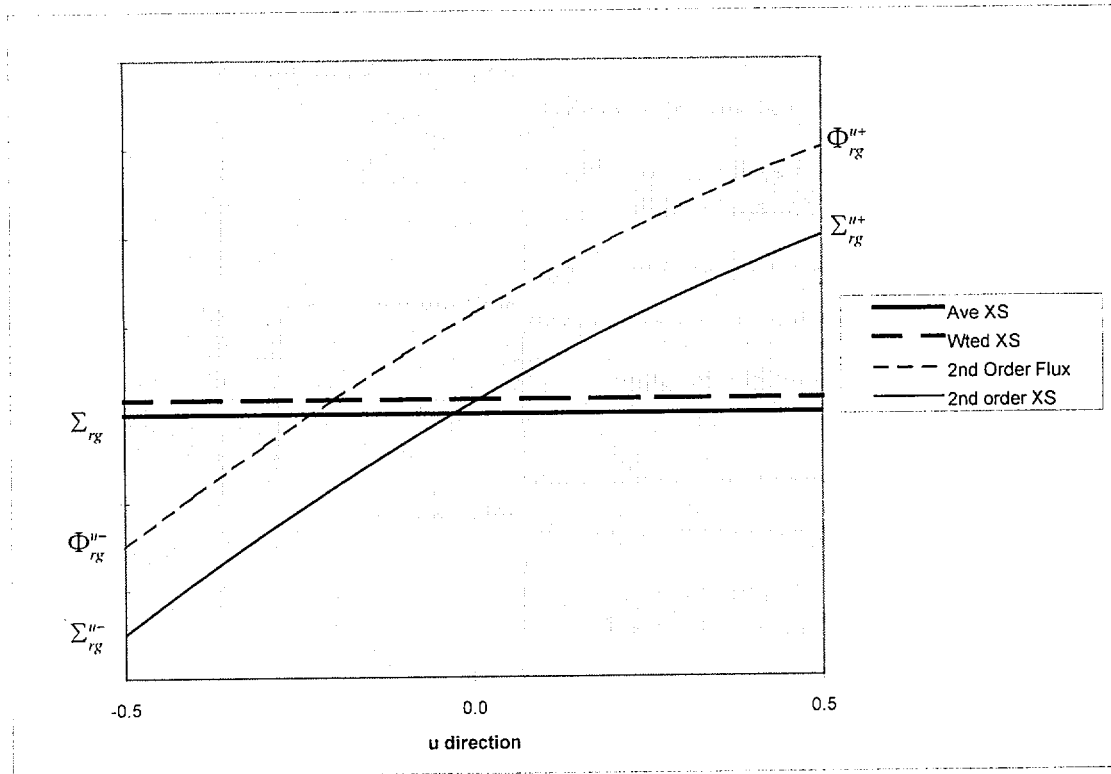


Figure 3-9. Overall Diagram of the Iterative Process

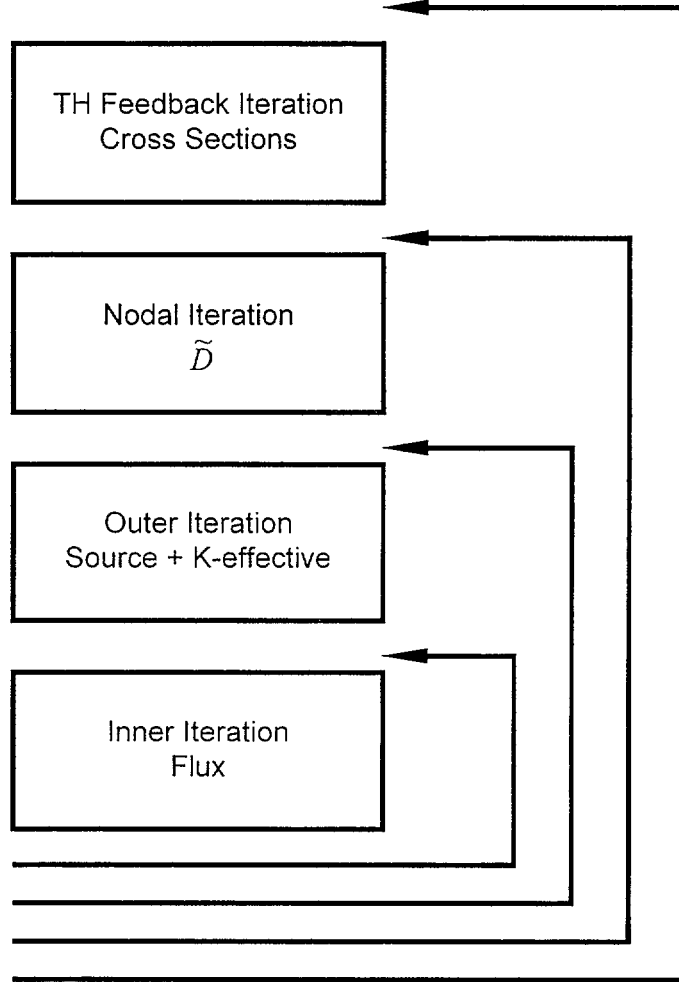


Figure 3-10. Coupling of the Models in the Kinetic Calculation

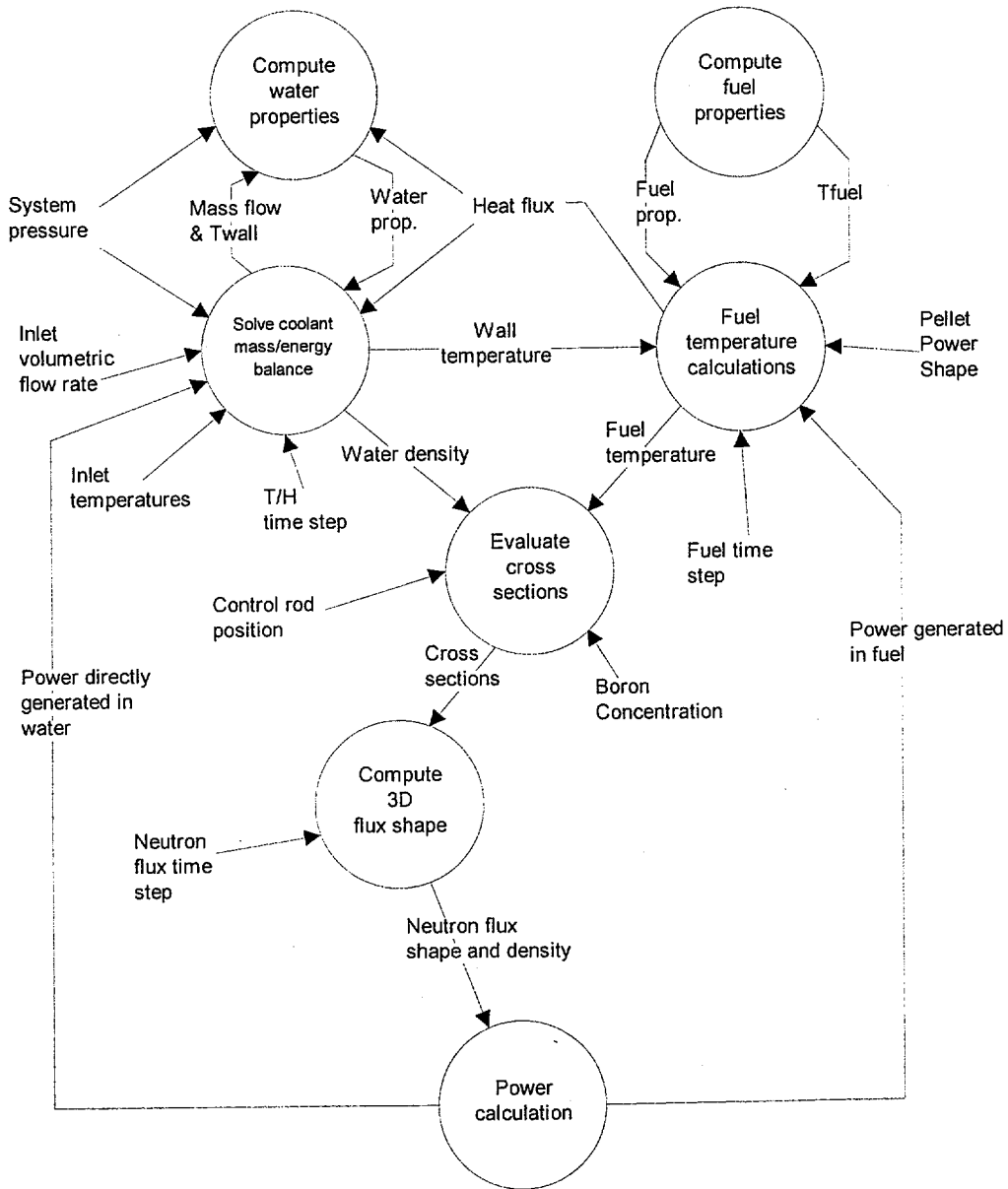


Figure 3-11. Heavy Isotope Depletion Chain in SMART

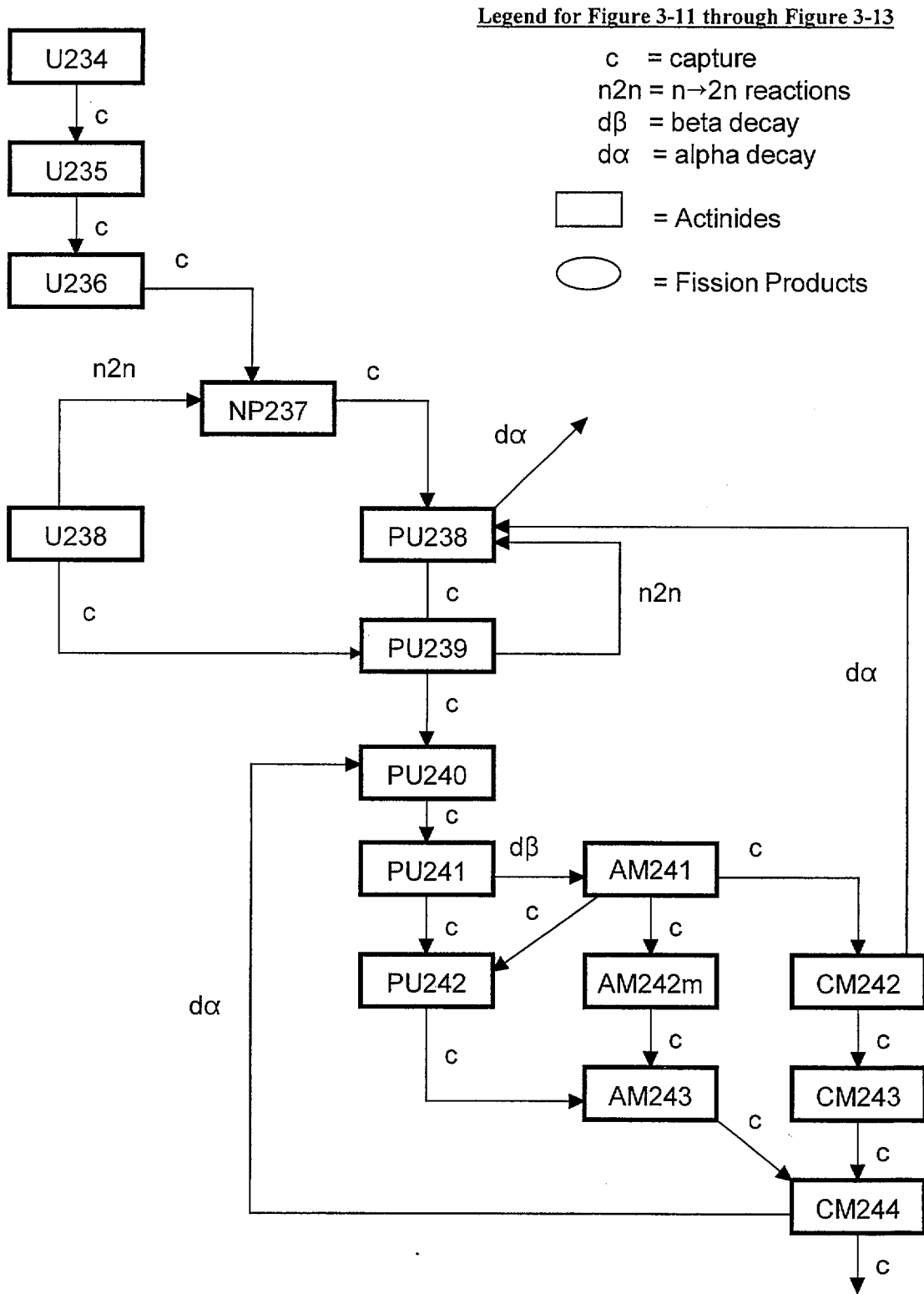


Figure 3-12. Iodine and Xenon Depletion Chain in SMART

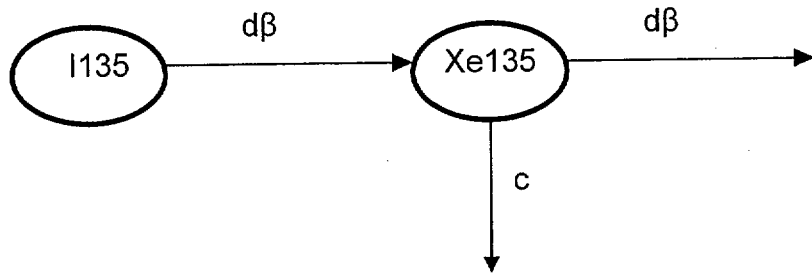


Figure 3-13. Samarium Depletion Chain in SMART

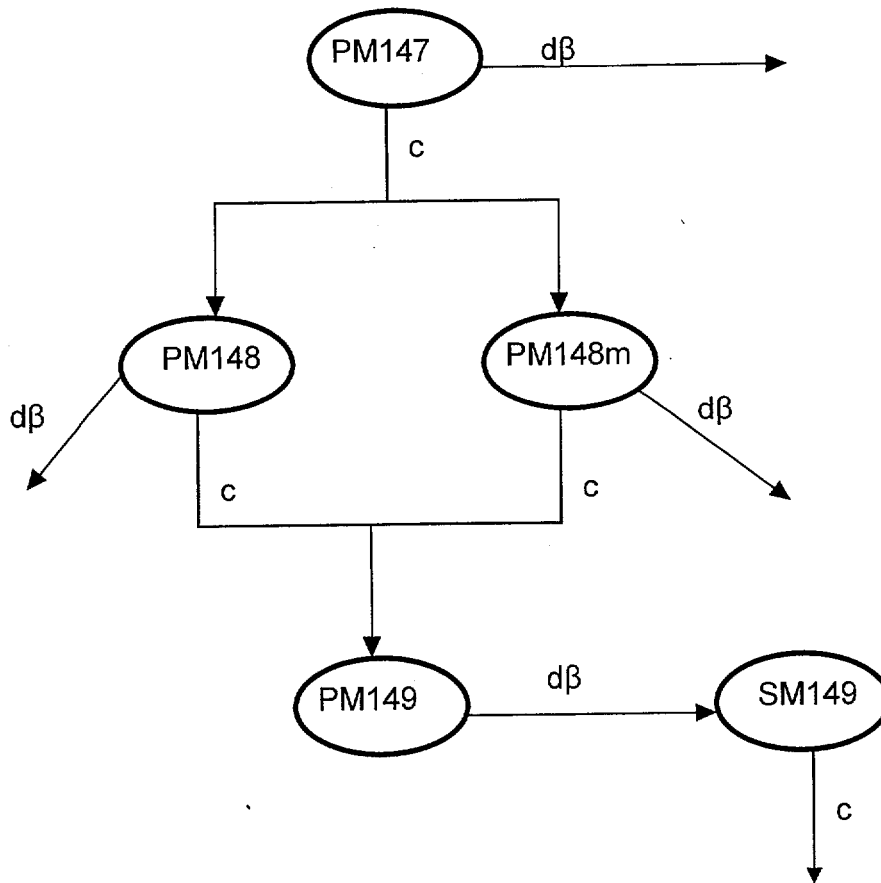
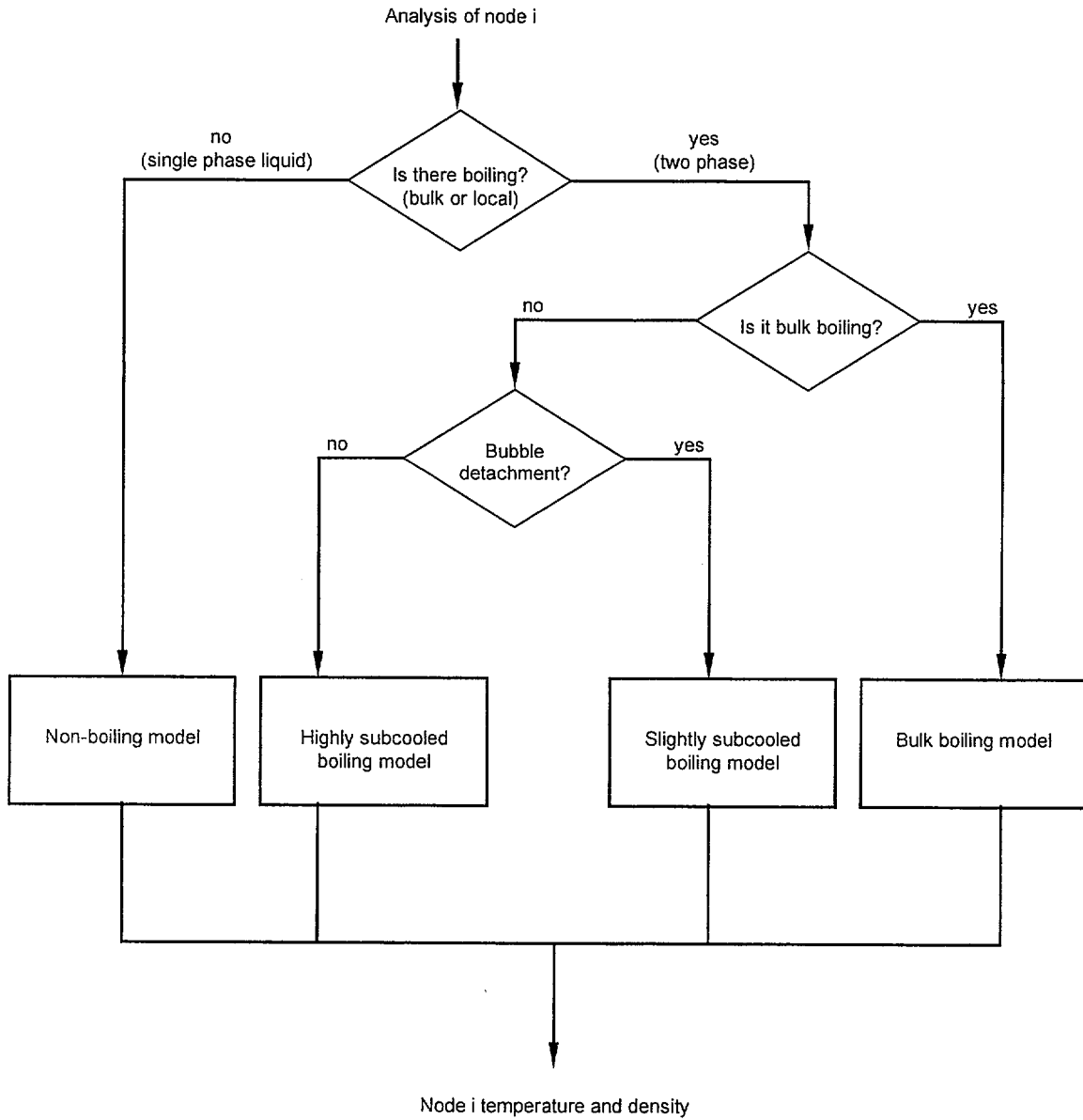


Figure 3-14. Thermal-Hydraulic Boiling Models



## 4. MEASUREMENT COMPARISONS

In this section, SMART predicted values are compared with measurements and APOLLO2-F results. The Reactivity Analyses Section (4.1) provides predictions for reactivity versus core burnup data, control rod worths, and reactivity coefficients. The Power Distribution Analyses Section (4.2) provides global power distribution comparisons to measured data from operating pressurized water reactors, comparisons of predicted pin power distributions to critical experiment measurements, and pin power comparisons of SMART to APOLLO2-F using four quarter assembly calculations (referred to as 4x1/4 problems). Results for the kinetics option in SMART are provided in Section 4.3. The Nuclear Reliability Factors for the hot pin power (2-D) and the hot pellet power (3-D) are determined for the SCIENCE system in section 4.4.

The calculations are performed with SMART, using cross section data from single-assembly APOLLO2-F calculations. All SMART calculations are performed using three-dimensional geometry except as noted. A one-quarter core representation is used for all the cores except as noted. Each fuel assembly is represented with four radial nodes and sixteen to eighteen axial fuel nodes. Both radial and axial reflector nodes are modeled using the APOLLO2-F  $S_N$  method.

Different options in APOLLO2-F are used for the different types of calculations. The primary options were:

- 1) the 2-D XY UP0 option in APOLLO2-F to generate the data libraries for SMART for the PWR core benchmarks,
- 2) the 2-D XY UP1 option in APOLLO2-F for all the calculations in the 4x1/4 benchmarks, and
- 3) the 2-D XY  $S_N$  option in APOLLO2-F to generate the data libraries for SMART for the critical core benchmark results.

The 2-D XY  $S_N$  option is the most accurate method for the critical core benchmarks and ejected rod worths, and FCF plans to use this option for licensing calculations. Discussions are provided in each subsection demonstrating that the results provided herein with options 1 and 2 adequately represent the results that can be expected with the  $S_N$  option. For clarity, the particular code within SCIENCE from which the results are directly obtained will be used in the following discussions even though the results are dependent upon both APOLLO2-F and SMART. SCIENCE will be used in the discussions when referring to the overall capability and/or accuracy of the code system.

### 4.1 Reactivity Analyses

Reactivity calculations from SMART are compared with measured data in this section. The measured data are taken from TMI-1, Oconee-1, Oconee-2, McGuire-1, Gravelines-5, and Sequoyah 1.

The key features of these cores are listed in Table 4-1. The reactivity data is compiled for critical boron versus burnup, HZP critical borons, control rod worths (bank, total, and ejected), Isothermal Temperature Coefficients, and Power Doppler Coefficients. A statistical summary of the results is also included. The calculations are performed with SMART, using cross section data from single-assembly APOLLO2-F calculations using the UP0 algorithm. Assembly calculations are performed with both the UP0 and  $S_N$  methods. Based on a review of the comparison of results of the two methods, no significant impact is estimated for critical K-effective predictions, ITCs, and Doppler Power coefficients. An improvement in the ejected rod worth results is seen with the  $S_N$  model and the bank worths are slightly affected. These impacts are discussed in the respective sections. The comparisons that follow demonstrate that the SCIENCE system accurately predicts core reactivity parameters.

#### 4.1.1 Reactivity Versus Burnup

The SMART core models are depleted at the measured critical conditions defined by burnup, core power, equilibrium xenon, rod position, and boron concentration. The cores analyzed are Sequoyah-1 cycles 1 through 5, TMI-1 cycles 1 through 10, and Gravelines-5 cycle 1. The SMART K-effectives from these depletions are shown versus core burnup in Figure 4-1. The average K-effective and standard deviation are [ b,c,d,e ], respectively. Greater than [b,c,d] of the points are within  $\pm 0.005$ . This correlates approximately to the predicted critical boron concentrations being within  $\pm 50$  ppm.

#### 4.1.2 Hot Zero Power All-Rods-Out Reactivity

The K-effectives for the HZP BOC critical boron concentration are obtained for cycle 1 of McGuire-1, cycle 1 of Oconee-1, cycle 1 of Oconee-2, cycles 1 through 5 of Sequoyah-1, cycles 1 through 10 of TMI-1, and cycle 1 of Gravelines-5 and are shown in Table 4-2. The average K-effective and standard deviation are [ b,c,d,e ], respectively. [ b,c,d,e ] are within  $\pm 0.005$ . This correlates approximately to the predicted critical boron concentrations being within  $\pm 50$  ppm.

#### 4.1.3 Control Rod Worths

Total control rod pattern and individual regulating bank worths are calculated to establish the validity of shutdown capability during normal and accident conditions and to maintain criticality during startup and power maneuvers. To verify the accuracy of SMART's predictions, zero power rod worth measurements using boron dilution and rod swap are compared to the predictions. The individual rod bank worths are calculated for cycle 1 of McGuire-1, cycle 1 of Oconee-1, cycle 1 of Oconee-2, cycles 1 through 5 of Sequoyah-1, cycles 1 through 10 of TMI-1, and cycle 1 of Gravelines-5. The majority of the rod worths presented are measured with boron dilution. The rod worths in Sequoyah 1 cycles 2 through 5 except for the reference bank are measured with the rod swap method.

The results of these calculations are compared to measurements in Table 4-3 in terms of the relative percent difference and the difference in pcm. The mean for the individual banks is [b,c,d] and the standard deviation is [b,c,d].

All the banks passed the measurement acceptance criteria when SMART was used for the predicted data for born diluted measurements of rod worths. Only [b,c,d,e] would not have passed the measurement review criteria of 15% or 100 pcm for a rod swap test bank. Because the rod swap method uses pre-calculated parameters to infer the worth of the test bank and non-FCF methods were used to define this measured bank worth, SMART was used to calculate the rod swap parameters for this bank. The measured worth of control bank B becomes [b,c,d,e] when the SMART rod swap parameters are used. This result is [b,c,d,e] difference that would have satisfied the review criteria. The calculated rod swap parameters were repeated with SMART for the remaining test banks for cycle 2. The resultant mean and the standard deviation for the entire individual banks are reduced from [b,c] to [b,c] and from [b,c] to [b,c], respectively. This example illustrates one of the reasons why the rod swap method is a slightly less accurate measurement technique than boron dilution. Therefore, estimating the calculational accuracy by combining the rod swap data with the boron dilution data yields conservative results.

The sum of the measured worths of all the individual banks is used to estimate the total pattern worth. For B&W plants, Bank 8 is a non-trippable Axial Power Shaping Rod and is not included in the sum. The banks that are summed the results are shown in Table 4-4. The mean is [b,c,d] in magnitude and the standard deviation is [b,c,d]. This standard deviation is smaller than the value reported in Reference 1.

Rod worths are recalculated on two cores with the  $S_N$  method. [

b,c,d,e

], the results reported above support the use of the  $S_N$  option. The agreement between the SMART calculations and measurement is excellent.

#### 4.1.4 Ejected Rod Worths

Ejected rod worths are calculated in licensing analyses to verify that these worths do not exceed the value used in the safety analysis calculations to evaluate the consequences of this accident. The SMART calculated ejected rod worths using the  $S_N$  option are compared to measured results for 2 cores. The ejected rod worths are calculated using 3-D, full-core geometry for TMI-1 cycle 1 and McGuire-1 cycle 1. The results of the relative percent differences between predicted and measured are shown in Table 4-5. The ejected rod worths are consistently predicted [

b,c,d,e

] using the  $S_N$  method.

#### 4.1.5 Isothermal Temperature Coefficients at Zero Power

During zero power physics testing, isothermal temperature coefficients are measured at HZP conditions for several different soluble boron concentrations and control rod configurations. The difference between the predicted and measured temperature coefficients are compared in Table 4-6. The comparison of the measured and predicted values results in a mean of [b,c,d,e] and standard deviation of [b,c,d,e] in units of pcm/°F. These are excellent results.

#### 4.1.6 Power Doppler Coefficients

Power Doppler Coefficients are calculated for TMI-1 cycle 1 and McGuire-1 cycle 1. These values for the differences are shown in Table 4-7. The mean of [b,c,d,e] pcm/%FP and standard deviation of [b,c,d,e] pcm/%FP indicate an excellent prediction of the Power Doppler Coefficients.

#### 4.1.7 Reactivity Calculation Statistical Results

The estimated mean and standard deviation are listed in Table 4-8 for the reactivity parameters calculated. In general, SCIENCE is more accurate than the results with our currently licensed method. The SCIENCE results for individual rod worths, total bank worths, ejected rod worths, ITCs, and Power Doppler Coefficients show improved accuracy through either a reduced bias or standard deviation. The HZP critical K-effective mean and standard deviation is very consistent with the HFP results. A bias has been observed between the 15x15 and 17x17 total bank worths in previous results, and SCIENCE shows a similar bias. The cause of the different observed biases between the fuel or plant types is believed to be a bias between the different sources of the measured results rather than the calculated results. All the 15x15 measured results were obtained from B&W plants. All but one of the measured 17x17 bank worths are from cores that used another vendor's precursor data and measurement techniques. The most recent startup rod worth measurements for the Sequoyah units using FTI's reactivity measurement system and FCF's precursor data show similar results to the 15x15 comparisons. The mean and standard deviation of these recent startup comparisons for cycles 9 and 10 of the Sequoyah 1 and 2 units are [ b,c,d,e ], respectively, with CASMO3/NEMO methodology. The [b,c] bias from these 17x17 results is much closer to the 15x15 results [b,c,d,e] shown in Table 4-9 for the current licensing basis than for the 17x17 results of [b,c,d] also shown in Table 4-9. Therefore, FCF concludes that any analytical models in our current methods or in SCIENCE are not causing the observed bias between fuel or plant types. Since a total rod worth uncertainty of 10% was justified in reference 1 and the SCIENCE results are similar to reference 1, therefore, a 10% total rod worth uncertainty is applicable for SCIENCE predictions.

Since Reference 1 was submitted, additional data was collected over several years that allowed the total rod worth uncertainty to be reduced. These reduced uncertainties were recorded in reference 13 and

14 for B&W designed plants and Westinghouse designed plants, respectively. Since these reduced uncertainties were based on significantly more data points than can be provided at this time for SCIENCE, the reduced rod worth uncertainties can not be justified. However, an estimate can be made of what the rod worth results would be with the  $S_N$  method relative to the reduced uncertainties. In Table 4-9, the average bias between the  $S_N$  and the UP0 method [ b,c,d,e ] for total rod worths. These estimated statistics are compared to the results that determined the total rod worth uncertainties for B&W designed plants and Westinghouse designed plants in reference 13 and 14, respectively. The adjusted SCIENCE mean and standard deviation are less than the values used to generate the reduced uncertainties. [

b,c,d,e

]However, because of the limited number of total rod worth SCIENCE calculations currently available, FCF plans to provide a later submittal to the NRC after more data is compiled with the  $S_N$  method to validate the reduced uncertainties with SCIENCE. As stated above, the 10% total rod worth uncertainty is conservative and applicable for SCIENCE predictions.

## **4.2 Power Distribution Analyses**

Power distribution comparisons are used to define the Nuclear Reliability Factors (NRF) for the hot pin power (2-D) and the hot pellet power (3-D). The ability of SCIENCE to predict pin powers is dependent upon both global and local power predictions. The SMART global power distributions are compared to measured data at commercial power plants to determine the global error term. The SMART code calculates the local pin power from the pin power reconstruction method. These results are compared to suitable reference values to formulate the local error components of the NRF. The global power distribution results (section 4.2.1) and the local power distribution results (section 4.2.2) are later used to derive the NRFs for the SCIENCE system in section 4.4.

### **4.2.1 Global Power Distributions**

Comparisons of SMART power distributions to measured values are provided for several cores. These cores include TMI-1 cycles 5, 6, 7, 9, and 10, Sequoyah-1 cycles 1 through 5, and Gravelines-5 cycle 1. The same SMART models that are described in 4.1 are used for the global power distribution predictions. The calculations are performed with SMART, using cross section data from single-assembly APOLLO2-F calculations using the UP0 algorithm. Assembly and core calculations are performed with both the UP0 and  $S_N$  method. Based on the comparison from the results of the two methods, no significant difference is observed between the two methods for the power distribution predictions. Table 4-1 provides a description of each of the cores modeled. Also, a power transient for Oconee-1 cycle 1 as simulated with SMART to assure that the transient xenon option is performing properly.

#### 4.2.1.1 TMI-1 Cycles 5, 6, 7, 9, and 10

TMI-1 is a B&W designed reactor with 177 fuel assemblies that uses fixed incore detectors. The selection of the cycles is based on establishing the best estimation of the calculational uncertainty. Those cores with the lowest measurement uncertainty provide the best source of information. Cycles 1 through 4 are eliminated because these cores had older magnesium oxide insulated detectors that had large signal leakage errors. The older detectors were replaced with aluminum oxide insulated detectors in cycle 5. Cycle 8 results are not used because most of the detectors were near the end of their expected lifetime that results in a high depletion correction error for the measurement. These detectors were replaced in cycle 9. The power distributions for cycles 5, 6, 7, 9, and 10 are analyzed at several times during each cycle.

Cycle 5 is an out-in-in shuffle scheme where the fresh fuel is placed primarily on the periphery of the core and moved inward for the next two cycles. The measured and predicted power distributions are shown in Figure 4-2 through Figure 4-5 for this cycle. Cycle 5 has a Ag-In-Cd Axial Power Shaping Rod (black APSR) in assembly L12. Each box in these figures represents a graph of the assembly axial power distribution and the boxes are arranged in an eighth core representation. The solid line in the box represents the power from SMART and the "X" represents the power from each of the 7 incore detectors in the assembly. The detectors are located midway between the spacer grids and the measurements are processed assuming that no grid depressions exist. This assumption allows a consistent comparison between measured and predicted results without accounting for the grids. The scale of the y-axis for each graph is 0 to 2. The x-axis for each graph begins with the bottom of the core. Note in Figure 4-5 that the APSR was fully withdrawn.

Cycles 6 and 7 are 18-month cycles with an Inconel (gray) APSR in location L12. The fresh fuel is loaded in the central region of the core in a checkerboard pattern. The fresh fuel in the interior of the core has burnable poison rod assemblies (BPRAs). The power distributions for cycle 6 are shown in Figure 4-6 through Figure 4-10. The power distributions for cycle 7 are shown in Figure 4-11 through Figure 4-14.

Cycles 9 and 10 are 24-month cycles with a Inconel (gray) APSR in location L12. The fresh fuel is loaded in the central region of the core in a checkerboard pattern. The fresh fuel in the interior of the core has burnable poison rod assemblies (BPRAs). The fresh fuel assemblies near the periphery are arranged in a T configuration (three in a row with another assembly next to the middle assembly). Several power maps are analyzed for each cycle. The power distributions for cycle 9 nearest to BOC and EOC are shown in Figure 4-15 and Figure 4-16, respectively. Cycle 10 is very similar to cycle 9 except that several assemblies contained 4 fuel pins with 2.0 wt% Gadolinia. The power distributions for cycle 10 nearest to BOC and EOC are shown in Figure 4-17 and Figure 4-18, respectively. Note in cycle 10 that some of the peak differences are larger than the other cycles. These larger differences represent a skewing of the axial

offset in local areas of the core that were correlated to crud formation. Because crud formation is not a part of the neutronics model, these peak comparisons are not used in the statistics. The radial power comparisons were kept because these results are not significantly impacted.

The overall agreement of the predictions with the measurements for all 5 cycles is exceptional.

#### 4.2.1.2 Sequoyah-1 Cycles 1-5

Sequoyah -1 is a Westinghouse designed reactor containing 193 fuel assemblies that uses moveable incore detectors. The instrument reaction rate comparisons are shown with calculated and measured results and are labeled power distribution comparisons. The reaction rate measurement data from the Sequoyah 1 moveable incore system are available and are used to infer the SMART power distribution capability. Since the reaction rate is actually the measured parameter, the comparison of the measured reaction rates with SMART reaction rates provides the best indication of the accuracy of SMART. Since the conversion of the measured reaction rates to measured power would use calculated parameters from SMART, the comparison of the reaction rates is equivalent to comparing power. Also, the measured flux trace includes the grid depressions. Since the grids are homogenized for the cross sections input to the SMART code, a grid factor for each type of grid is applied to the predicted peak for licensing calculations. This factor accounts for the increased peak between two grid locations due to the local grid flux depressions. However, a grid factor was not applied to the SMART results and the application of grid factors is discussed later in Section 4.4. (Note that grid factors were not needed for comparisons using the fixed incore detector system.) Several power maps are evaluated and the power maps nearest to BOC and EOC are presented. These two maps are representative of the other maps and represent the extremes of the cycle.

Cycle 1 is a typical cycle 1 core with pyrex burnable poison rods. Power distribution maps are shown with calculated and measured results in Figure 4-19 through Figure 4-20 for cycle 1. Each box in these figures represents a graph of the assembly axial power distribution and the boxes are arranged in a quarter core representation. The solid line in the box represents the power from measured flux traces and the "X" represents the SMART power value at the midpoint between the spacer grids. The scale of the y-axis for each graph is 0 to 2. The x-axis for each graph begins with the bottom of the core. Note that the measured results are not presented for some eighth core locations because these locations are not instrumented in Westinghouse designed plants.

Cycle 2 and cycle 3 are a mixture of an out-in-in and an in-out-in shuffle schemes. Cycles 4 and 5 are in-out-in shuffle schemes with burnable poison in the fresh fuel assemblies. The fresh fuel assemblies loaded in the interior of the core contained pyrex burnable poison rods in cycles 2 and 3. Wet Annular Burnable Absorbers (WABA) are introduced in cycle 3 and used exclusively in cycle 4. Integral Fuel

Burnable Absorbers are introduced in cycle 5. Power distribution comparisons are shown in Figure 4-21 through Figure 4-28 for cycles 2 through 5.

The predictions are in excellent agreement with the measurements for all 5 cycles.

#### 4.2.1.3 Gravelines-5 Cycle 1

Gravelines-5 is a typical three loop, 157 fuel assembly, 2775 MWt French power reactor. Cycle 1 contains fuel assemblies of three different enrichments loaded in a checkerboard pattern. Each fuel assembly has a 17x17 pin lattice with 264 fuel pins. The excess reactivity is controlled by soluble boron, borosilicate glass (pyrex burnable absorber pins) in the guide tubes, and fuel pins containing 8.0 wt% gadolinium oxide mixed with UO<sub>2</sub> (0.25 wt% U<sup>235</sup>). Figure 4-29 and Figure 4-30 show the core loading pattern and poison locations for cycle 1, respectively.

The reaction rate measurement data from the Gravelines-5 moveable incore system are used to infer the SMART power distribution capability. The instrument reaction rate comparisons are shown with calculated and measured results in Figure 4-31 through Figure 4-37 for cycle 1 and are labeled power distribution comparisons. Each box in these figures represents a graph of the assembly axial power distribution and the boxes are arranged in an eighth core representation. The solid line in the box represents the power from measured flux traces and the "X" represents the SMART power value at the midpoint between the spacer grids. The scale of the y-axis for each graph is 0 to 2. The x-axis for each graph begins with the bottom of the core. Fuel for Gravelines-5 contained INCONEL grids. Again, a grid factor was not applied to the SMART comparisons to measured results.

The predictions for this core containing Gadolinia are in excellent agreement with the measurements.

#### 4.2.1.4 Oconee 1 Cycle 1 Power Transient

The Oconee-1 cycle 1 power transient discussed in reference 15 is simulated with the SMART code. Figure 4-38 provides a graph of the power level, axial imbalance, and total power peak versus time for the SCIENCE simulation. Measured values of axial imbalance and total peak are represented with a "■" on this graph. These comparisons demonstrate that SCIENCE can model the effects of a xenon transient.

#### 4.2.2 Local Pin Power Distributions

The local pin power distributions predicted by the SMART pin power reconstruction method is tested using two types of analyses. The first analysis compares predicted and measured results from critical

experiments to determine the accuracy of the SCIENCE methodology to calculate the local pin power distribution within a fuel assembly for a small core.

The second analysis compares SMART calculated results to APOLLO2-F calculated results for several 4x1/4 configurations (multi-assembly). The SMART calculations utilize single-assembly APOLLO2-F cross section data. The APOLLO2-F 4x1/4 calculations directly model the spectral interaction between neighboring assemblies and individual pin depletion effects. SMART accounts for the spectral interaction and gradients between assemblies based on the methodology presented in section 3. This analysis tests the SMART methodology for incorporating local effects on the pin power distributions. Several different fuel assembly loadings were depleted and compared in this analysis.

#### 4.2.2.1 Critical Experiments

Thirteen critical experiments were fueled with UO<sub>2</sub> fuel and contained varying numbers of H<sub>2</sub>O cells, pyrex rods, and Gadolinia rods as shown in Table 4-10. The UO<sub>2</sub> experiments were conducted by the B&W Lynchburg Research Center as part of the Physics Verification Program<sup>16</sup> and the DOE Gadolinia project<sup>17</sup>. Cross section data are generated based on single-assembly APOLLO2-F calculations with the S<sub>N</sub> option. A two-dimensional SMART model is used with four nodes per assembly. The outer fuel region geometry is approximated as shown in Figure 4-39. These experiments provide a sufficient data base to determine the accuracy of the SCIENCE pin power reconstruction methodology. These experiments form the basis of the calculational error with uniform material properties within the assembly (i.e. no burnup).

The calculated pin powers for the thirteen critical experiments are compared to the measured fuel pin powers from each critical. These fuel pins represented one-eighth of the fuel assembly that is positioned in the center of the core. The first eleven of the critical experiments represent a 15x15 lattice of fuel pins and resemble the FCF Mark B fuel assembly configuration. The last two experiments represent a CE 16x16 fuel assembly with large water holes.

The overall results are presented in Table 4-11. The K-effective is calculated using a simple geometric buckling correction to the two dimensional calculations. The reactivity predictions are very good having a mean of [b,c,d,e] and a standard deviation of [b,c,d,e] for the thirteen experiments.

Figure 4-40 through Figure 4-52 show pin power distribution comparisons of calculated and measured data for all the criticals analyzed. These power distributions are relative to an average assembly power density of 1.0 for the center assembly. These criticals are representative of typical assemblies that would exist in a power reactor and show the power distribution within an assembly. The results are excellent. No biases are observed around water holes or poisons. An overprediction of the power next to the center water hole in Figure 4-51 and Figure 4-52 appears to be present for the CE fuel lattice. The CE fuel lattice has 4 fuel cell locations for each water hole whereas the other lattices have only one fuel cell.

However, reference 17 indicates that a detector that displaces water is located in one of the 4 center pin locations but does not note which one. The SCIENCE model has no detector modeled and will over predict the power in this location. This conclusion is supported by the accurate prediction of power peaking around the other water holes.

The measurement uncertainty for the local pin power distributions is obtained for the two sets of critical experiments. The measurement error in the early set of critical experiments is obtained from information in reference 16 resulting in a mean of [b,c ] and a standard deviation of [b,c ]. The measurement error in the Gadolinia critical experiments can be estimated directly from results in reference 17. Each pin was measured 3 times resulting in 711 pin measurements with a mean of [b,c ] and a standard deviation of [b,c ]. The second set of experiments was performed nearly 10 years after the first set and the measurement error reflects the improved measurement techniques.

The calculated error is estimated by subtracting the measured variance from the observed variance for each set of experiments. The calculated error for each set is combined to obtain the total estimated calculational error. These results are shown in Table 4-12 and the calculational error is nearly the same as the measurement error for each group of critical experiments.

#### 4.2.2.2 APOLLO2-F versus SMART Multi-Assembly

The multi-assembly depletion problems are analyzed with APOLLO2-F (in multi-assembly format) and SMART. The multi-assembly problems consist of two different fuel assembly types loaded in a checkerboard 4x1/4 fuel assembly pattern. A 14x14 even lattice fuel assembly design without an instrument tube in the center is used because of a code limitation that did not allow half pins on all reflective boundaries. The cross section information for the SMART calculations is obtained from single-assembly APOLLO2-F calculations using the UP1 solution method. A list of the various multi-assembly problems is provided in Table 4-13. The problems listed include a variety of fuel assembly designs. Variations between assemblies include enrichment loadings, burnable poison loadings, removed burnable poison, burnup, and fuel containing Gadolinia. The initial burnup for an assembly is generated in two different manners. The first is a single-assembly depletion (flat), while the second is a depletion in a previous multi-assembly configuration (labeled with "from set x"). Each of the fifteen multi-assembly problems is depleted as indicated and the local pin powers throughout the depletion are compared.

The multi-assembly results are used to define the errors of using single assembly APOLLO2-F cross sections in SMART and pin power reconstruction relative to a fine mesh calculation. The UP1 option is used both in generating the cross sections for SMART and in the APOLLO2-F solution.[

b,c,d,e

]

Therefore, no significant impact on the differences is estimated for running the  $S_N$  method on the multi-assembly calculations and these results are applicable to the  $S_N$  method.

Table 4-14 provides a summary of the results of the local pin powers from each multi-assembly problem. All power producing pins are considered in the statistical results except the pins containing Gadolinia. In the Gadolinia pins, the power is much less than 1.0, is not close to the peak pin, and is therefore not relevant for peak pin statistics. The pin reconstruction methodology provides excellent results. The maximum peak to peak relative difference for all the problems is [b,c]. The standard deviation of the local pin powers is at or below [b,c] for each of these cases. The mean and standard deviation for the entire set of cases is [ b,c,d,e ], respectively with 16801 data points. Pin power relative percent differences are provided for test sets 6 and 12 at BOC and EOC of the depletion in Figure 4-53 through Figure 4-57. These latter results provide examples of the local differences between the two methods for pyrex fuel and Gadolinia fuel. This benchmark demonstrates the ability of SMART to predict pin powers with burnup effects using the coarse mesh solution (4 nodes per assembly) with its pin power reconstruction method.

### **4.3 SMART Kinetics**

This section provides the benchmarking for the SMART kinetics option. This option comprises three distinct time dependent models, neutronics, thermal hydraulic, and fuel temperature models. To test the dependencies of all three models, dropped rod tests at operating power reactors are simulated with the kinetics option in SMART. The core conditions for the drop tests are shown in Table 4-15. These tests include conditions at BOC, MOC, and EOC and a reload core that represent a wide range of variations of cross sections, coefficients, and delayed neutron fractions. The four excore responses were recorded versus time at 0.002 second intervals as well as the dropped rod velocity versus time. The position of the excore detectors relative to the dropped rod locations are shown in Figure 4-58 and Figure 4-59 for 193 plants and 157 plants, respectively. The noise level of the measured signals is removed by using a second order lead lag filter. The measured and predicted excore signals are compared versus time during the event.

The fuel and clad thermal parameters from SMART are utilized. The excore response is simulated in SMART by using a weighted average of the peripheral assembly powers nearest the respective detectors. Six of these SMART simulations are presented in Figure 4-60 through Figure 4-65. The measured excore responses are labeled with a prefixed "M" and the calculated is prefixed by a "C". The measured data can be distinguished from the calculated data by observing that that the measured data is somewhat "noisy" and the calculated data is smooth. The first five simulations are half core symmetric and only the two different calculated excore values (labeled C1 and C3) are shown. As illustrated, the SMART responses are within 1% of the measured results for most of the data presented. Figure 4-64 and Figure 4-65 have power response differences slightly larger than 1% and but still less than 2%. These deviations in

Figure 4-64 could be easily be caused by differences between the measured and predicted dropped rod worth, beta effective, and/or the gap conductance of the fuel temperature model. The regulating bank position was in automatic control during the test taken in Figure 4-65 and is not simulated with SMART. When the core power decreased as the rod was dropped, the automatic control system started withdrawing the regulating rods to maintain average temperature and initial power demand. This explains the step wise increases of power in the measured responses in Figure 4-65 compared to a smooth, lower power response given by SMART. This figure also shows four different responses for each of the four detectors because of the asymmetry of the dropped rods relative to the detectors. All the predicted results agree well with measurements.

In conclusion, the dropped rod transient significantly exercises all three time dependent models of SMART. The local changes in the peripheral powers as well as the overall core power test the global and local response of the neutronic portion of the model. The power change from 50 % power to the reduced power tests both the fuel temperature and the moderator temperature portions of the kinetic models. In conclusion, these results provide a valid test of SMART's kinetic capabilities to perform transient simulations for "best estimate" and/or safety related licensing calculations with appropriate bounding parameters and assumptions.

#### **4.4 Nuclear Reliability Factors**

The Nuclear Reliability Factors (NRF) for SCIENCE are determined for the hot pin power (2D) and the hot pellet power (3D). Each NRF is composed of two error terms, one for the global power prediction (section 4.2.1) and the other for the radial-local prediction (radial local is the ratio of the peak radial pin power to assembly average power). The SCIENCE core global power distributions are compared to measured data to determine the global error term. The SCIENCE code using the pin power reconstruction option (section 4.2.2) is used to predict the radial-locals. These predictions are compared to suitable reference values to formulate the errors for the radial-local component of the NRF. The results of 4.2.1 and 4.2.2 are then used to derive the NRFs for the SCIENCE system.

The previous sections provided SCIENCE predictions for numerous core configurations containing various fuel assembly designs. Some of the fuel designs examined are Mark B (15x15 fuel lattice) with and without BP, Westinghouse STD fuel (17x17 fuel lattice) with and without Pyrex BP, WABA BP and IFBA. The core configurations include out-in-in, in-out-in, and in-in-out shuffle schemes, gray and black APSRs, 177 fuel assembly cores, 157 cores with Gadolinia, and 193 fuel assembly cores. This database is representative of the cores FCF will license and is sufficient to derive NRFs for SCIENCE. In the following sections, the statistical results (section 4.4.1) are presented for the global power distributions and the local pin power distributions and the NRFs (section 4.4.2) are derived.

#### 4.4.1 Statistical Results

The sample mean and standard deviation of the relative difference between predicted and reference can be calculated for each of the comparisons by using the following formulas.

$$a = \frac{p}{m} - 1$$

where  $p$  = the predicted value,  
 $m$  = the reference value, and  
 $a$  = the relative difference of predicted to measured value where the value could be either radial, peak, or local pin power.

Alternatively, the results could also be compiled as an absolute difference as in the following equation.

$$a = p - m$$

where  $a$  in this case is the difference of the predicted to the reference value

In general, statistical information is computed for  $a$ . The frequency plots are viewed to determine whether the data has any strange behavior such as extreme skewing or double peaks that could indicate biases in the calculations rather than random errors. A normality check is also performed to determine whether statistics for a normal distribution can be used. If the test for normality fails, then the 95/95 tolerance/confidence factor for normal distributions may not be valid. The uncertainty factor is calculated with both normal assumptions and with the actual distributions that are not normal. The non-parametric tolerance/confidence limit is applicable for both normal and non-normal distributions. The most conservative of the two will be used as the uncertainty. The uncertainty is defined as a one-sided 95/95 tolerance/confidence limit. When uncertainty factors are composed of different components, the components can be statistically combined. Discussions are given below for the Nuclear Reliability Factors (NRFs) for peak pin and peak pellet.

The NRFs for the peak pin and peak pellet are determined from three components representing the global and local peaking variations. The reference value for the global power distributions is the measured data. The statistical summaries for each of the cycles analyzed for the global power distributions are shown in Table 4-16 and Table 4-17 for the assembly radial powers and peak assembly powers, respectively. The TMI cores utilized 52 detector locations for the radial comparisons. The two detector locations with the highest predicted powers for each of the 52 detector locations are used for the peak statistic resulting in 104 data points for each time in life. The Sequoyah and Gravelines radial and assembly peak data utilized all functional detector locations for the radial. The two highest mid-grid values are used to determine the peak values.

The grids are homogenized in SMART and do not model the grid depressions which will under predict the peak when the measured data includes the grid depressions. [

b,c,d,e

]

The frequency plots are shown in Figure 4-66 and Figure 4-67 for radial and assembly power data, respectively. The ninth bar represents 0.0% and each bar width represents  $0.25 \cdot \sigma$ . No unusual behavior is observed in these figures. [

b,c,d,e

]

The statistical results for the local pin power distribution errors are determined from combining the two analyses that were performed. The comparison to the critical experiments provides the error of SCIENCE when predicting intra-assembly peaking, while the multi-assembly benchmark calculations provide any additional error which occurs due to the severe gradients and depletion effects that occur in a PWR core. The statistical results for the local pin power are shown in Table 4-18. The frequency plots are shown in Figure 4-68 and Figure 4-69 for the critical experiments and the Multi-Assembly results, respectively. No unusual behavior is observed in these figures. [

b,c,d,e

]

#### 4.4.2 NRF Determination

A Monte Carlo method is utilized to combine the uncertainties, and the non-parametric tolerance method from reference 19 is used with the Monte Carlo simulation to obtain the Calculated Nuclear Reliability Factors (CNRFs).

The Monte Carlo simulation randomly samples the data from each of the three components of the error terms for both the predicted value and reference value. These three components are the global assembly values and the two radial local components. The three predicted values are multiplied together to simulate an actual SCIENCE calculation. Similarly, the resultant reference value is obtained and divided by the predicted value. This result is the multiplier to apply to the prediction to obtain the reference value. Satterthwaite's approximation<sup>20</sup> is used to determine the equivalent degrees of freedom for the number of

samples for the Monte Carlo simulation. For this sample size the non-parametric tolerance limit equation is used to determine the point on the simulated distribution that represents the one-sided 95%/95% statistical tolerance/confidence limit for when SCIENCE under predicts the reference value.

The results of the Monte Carlo simulation are shown in Table 4-19. An analytical method assuming normality is also used as a cross-check of the Monte Carlo results, and these results are also listed in Table 4-19. The largest NRFs for either method for the hot pellet power and hot pin power are [b,c,d,e ], respectively. For initial implementation, FCF will continue to use the current 1.048 and 1.038 for hot pellet powers and hot pin powers, respectively, for licensing analyses with SCIENCE.

Table 4-1. Core Characteristics

Core	Cycle	Cycle Length EFPD	Type of Burnable Poison (BP)	Distinguishing Features	Regulating bank position at full power
TMI-1 177 FA Core 15x15 Lattice	1	466	B <sub>4</sub> C in Al <sub>2</sub> O <sub>3</sub> in GT	Interior checkerboard pattern of lowest enriched fuel and higher enriched fuel with BP. Highest enriched fuel is on periphery.	inserted
	2	256	none	Out-In -In	inserted
	3	287	none	Out-In -In	inserted
	4	274	none	Out-In -In	inserted
	5	302	none	Out-In -In	withdrawn
	6	421	B <sub>4</sub> C in Al <sub>2</sub> O <sub>3</sub> in GT	In-Out-In	withdrawn
	7	475	B <sub>4</sub> C in Al <sub>2</sub> O <sub>3</sub> in GT	In-Out-In	withdrawn
	8	509	B <sub>4</sub> C in Al <sub>2</sub> O <sub>3</sub> in GT	In-Out-In	withdrawn
	9	639	B <sub>4</sub> C in Al <sub>2</sub> O <sub>3</sub> in GT	In-In -Out, 4 Fresh fuel assemblies arranged in a T pattern	withdrawn
	10	660	B <sub>4</sub> C in Al <sub>2</sub> O <sub>3</sub> in GT + 2 wt% Gadolinia	In-In -Out, 4 Fresh fuel assemblies arranged in a T pattern	withdrawn
Oconee-1 177 FA Core 15x15 Lattice	1	BOC Only	none		inserted
Oconee-2 177 FA Core 15x15 Lattice	1	BOC Only	B <sub>4</sub> C in Al <sub>2</sub> O <sub>3</sub>	Interior checkerboard pattern of lowest enriched fuel and higher enriched fuel with BP. Highest enriched fuel is on periphery.	inserted
McGuire-1 193 FA Core 17x17 Lattice	1	BOC Only	Pyrex in GT	Interior checkerboard pattern of lowest enriched fuel and higher enriched fuel with BP. Highest enriched fuel is on periphery.	withdrawn
Gravelines-5 157 FA Core 17x17 Lattice	1	325	Pyrex in GT + 8 wt% Gadolinia	Interior checkerboard pattern of lowest enriched fuel and higher enriched fuel with BP or Gadolinia. Highest enriched fuel is on periphery.	withdrawn gray rods inserted
Sequoyah 1 193 FA Core 17x17 Lattice	1	390	Pyrex in GT	Interior checkerboard pattern of lowest enriched fuel and higher enriched fuel with BP. Highest enriched fuel is on periphery.	withdrawn
	2	305	Pyrex in GT	Mixture of Out-In -In and In-Out-In	withdrawn
	3	343	Pyrex or WABA in GT	Mixture of Out-In -In and In-Out-In	withdrawn
	4	426	WABA in GT	In-Out-In	withdrawn
	5	446	WABA in GT + IFBA	In-Out-In	withdrawn

GT - Guide Tubes

WABA - Wet Annular Burnable Absorber - B<sub>4</sub>C in Al<sub>2</sub>O<sub>3</sub> with annular region of water

IFBA - Integral Fuel Burnable Absorber - ZrB<sub>2</sub> coating on fuel pellets

x-x-x Represents the general location of fuel batch for each burn with the first denoting fresh fuel

Table 4-2. HZP Critical K-effective

Plant	Cycle	K-eff	notes
McGuire 1	1		ARO
	1		CD in
	1		CC-CD in
	1		CB-CD in
	1		CA-CD in
	1		SE-CD in
	1		SD-CD in
	1		SC-CD in
Oconee 1	1		ARO
Oconee 2	1		ARO
Sequoyah 1	1		ARO
	2	[b,c,d,e]	ARO
	3		ARO
	4		ARO
	5		ARO
TMI 1	1		ARO
	2		ARO
	3		ARO
	4		ARO
	5		ARO
	6		ARO
	7		ARO
	8		ARO
	9		ARO
	10		ARO
Gravelines	1		ARO

**Table 4-3. Individual Bank Worths**

Plant	Cycle	Bank	Predicted Worth (pcm)	Measured Worth (pcm)	% difference [P-M]/M*100	difference [P-M]
McGuire 1	1	CD		669		
	1	CC		1250		
	1	CB		996		
	1	CA		695		
	1	SE		840		
	1	SD		755		
	1	SC		1011		
Sequoyah 1	1	CA	[b,c,d,e]	348	[b,c,d,e]	
	1	CB		1331		
	1	CC		997		
	1	CD		1362		
	1	SC		1190		
	1	SD		812		
	2	CA*		257		
	2	CB*		725		
	2	CC*		722		
	2	CD		871		
	2	SA*		511		
	2	SB*		741		
	2	SC*		393		
	2	SD*		396		
	3	CA*		221		
	3	CB*		628		
	3	CC*		532		
	3	CD		871		
	3	SA*		611		
	3	SB*		516		
	3	SC*		480		
	3	SD*		497		
	4	CA*		320		
	4	CB*		589		
	4	CC*		758		
4	CD	963				
4	SA*	337				
4	SB*	687				
4	SC*	396				
4	SD*	388				
5	CA*	238				
5	CB*	777				
5	CC*	823				
5	CD*	886				
5	SB	968				
5	SC*	423				
5	SD*	426				
* Used Rod Swap						
Gravelines	1	R	b,c,d,e	1443	b,c,d,e	
	1	G1		504		
	1	SB		1187		
	1	N1		973		
	1	G2		910		
	1	N2		602		
	1	SC		692		
1	SA	486				

**Table 4-3. Individual Bank Worths (Cont'd)**

Plant	Cycle	Bank	Predicted Worth (pcm)	Measured Worth (pcm)	% difference [P-M]/M*100	difference [P-M]
TMI 1	1	5	[b,c,d,e]	1100	[b,c,d,e]	
	1	6		1230		
	1	7		1210		
	2	5		690		
	2	6		1020		
	2	7		810		
	3	5		1131		
	3	6		1013		
	3	7		799		
	4	5		1453		
	4	6		1072		
	4	7		1477		
	5	5		954		
	5	6		863		
	5	7		1400		
	6	5		1531		
	6	6		759		
	6	7		964		
	7	5		1220		
	7	6		934		
	7	7		926		
	8	5		1214		
	8	6		927		
	8	7		974		
	9	5		1134		
	9	6		817		
	9	7		889		
	10	5		1400		
	10	6		713		
	10	7		956		
Oconee 1	1	8	520			
	1	7	1090			
	1	6	1100			
	1	5	680			
	1	4	590			
	1	3	2810			
	1	2	2020			
	1	1	2920			
Oconee 2	1	8	370			
	1	7	1150			
	1	6	1210			
	1	5	1140			

Table 4-4. Total Bank Worths

Plant	Cycle	Banks	Predicted Worth (pcm)	Measured Worth (pcm)	% difference [P-M]/M*100
McGuire 1	1	all	[b,c,d,e]	6216	[b,c,d,e]
Oconee 1	1	1-7		11210	
Oconee 2	1	5-7		3500	
Sequoyah 1	1	all		6040	
	2	all		4445	
	3	all		4357	
	4	all		4438	
	5	all except SA		4542	
TMI 1	1	5-7		3540	
	2	5-7		2520	
	3	5-7		2943	
	4	5-7		4002	
	5	5-7		3217	
	6	5-7		3254	
	7	5-7		3080	
	8	5-7		3115	
	9	5-7		2840	
	10	5-7		3069	
Gravelines	1	all		6797	

**Table 4-5. Ejected Rod Worths**

Core	Ejected Location	Worth (pcm)		% Difference
		Predicted	Measured	
TMI-1 Cycle 1	F2	[b,c,d,e]	690	[b,c,d,e]
McGuire-1 Cycle 1	D12		432	

**Table 4-6. HZP Isothermal Temperature Coefficients**

Plant	Cycle	Predicted ITC (pcm/F)	Measured ITC (pcm/F)	Difference (P-M)
McGuire 1	1		-0.60	
	1		-0.53	
	1		-1.83	
	1		-2.20	
	1		-5.86	
	1		-7.00	
	1		-6.75	
	1		-8.90	
	1		-10.53	
Oconee 1	1		8.10	
	1		5.10	
	1		11.30	
Oconee 2	1		4.10	
	1		2.90	
	1		-0.60	
Sequoyah 1	1		-1.01	
	1		-4.80	
	1		-8.00	
	1		-9.70	
	1		-12.65	
	2		-2.54	
	2		-5.05	
	3		-2.37	
	3	[b,c,d,e]	-4.47	[b,c,d,e]
	4		-2.15	
	4		-1.56	
	5		-3.35	
	5		-2.83	
TMI 1	1		4.49	
	1		-6.04	
	2		0.94	
	2		-5.30	
	3		-0.33	
	3		-6.47	
	4		0.28	
	4		-10.80	
	5		-2.25	
	5		-12.96	
	6		0.57	
	7		2.41	
	8		1.50	
	9		3.13	
	10		2.13	
Gravelines	1		-0.13	
	1		-3.48	
	1		-1.28	
	1		-5.07	
	1		-3.47	
	1		-8.67	
	1		-8.16	

**Table 4-7. Power Doppler Coefficient**

Core	Power Level, %	Power Doppler Coefficient (pcm/%FP)		Difference, P-M
		Predicted	Measured	
TMI-1 Cycle 1	96	[b,c,d,e]	-11.4	[b,c,d,e]
McGuire 1 Cycle 1	30		-13.6	
	50		-12.7	
	75		-11.6	

**Table 4-8. Reactivity Statistical Results**

[b,c,d,e]

**Table 4-9. Total Rod Worth Statistical Results**

[b,c,d,e]

**Table 4-10. Critical Core Configuration Description**

Critical Core ID	Reference Core	Description
CXIL2	CXIL2	15x15, UO <sub>2</sub> pin configuration, 17 water filled locations/assembly, 2.46 wt % <sup>235</sup> U
CXIL4	CXIL2	15x15, UO <sub>2</sub> pin configuration, 13 water filled and 4 Pyrex filled locations/assembly, 2.46 wt % <sup>235</sup> U, 12.6 wt % B <sub>2</sub> O <sub>3</sub> in Pyrex
CXIL5	CXIL2	15x15, UO <sub>2</sub> pin configuration, 13 water filled and 4 Pyrex filled locations/assembly, 2.46 wt % <sup>235</sup> U, 12.6 wt % B <sub>2</sub> O <sub>3</sub> in Pyrex
CXIL6	CXIL2	15x15, UO <sub>2</sub> pin configuration, 9 water filled and 8 Pyrex filled locations/assembly, 2.46 wt % <sup>235</sup> U, 12.6 wt % B <sub>2</sub> O <sub>3</sub> in Pyrex
CXIL7	CXIL2	15x15, UO <sub>2</sub> pin configuration, 9 water filled and 8 Pyrex filled locations/assembly, 2.46 wt % <sup>235</sup> U, 12.6 wt % B <sub>2</sub> O <sub>3</sub> in Pyrex
CXIL8	CXIL2	15x15, UO <sub>2</sub> pin configuration, 1 water filled and 16 Pyrex filled locations/assembly, 2.46 wt % <sup>235</sup> U, 12.6 wt % B <sub>2</sub> O <sub>3</sub> in Pyrex
CXIL11	CXIL2	15x15, UO <sub>2</sub> pin configuration, 1 water filled and 16 Al <sub>2</sub> O <sub>3</sub> locations/assembly, 2.46 wt % <sup>235</sup> U
C1	C1	15x15, UO <sub>2</sub> pin configuration, 2.46 wt % <sup>235</sup> U
C5	C1	15x15, UO <sub>2</sub> pin configuration with 12 Gd pins, 2.46 wt % <sup>235</sup> U, 4.00 wt % Gd <sub>2</sub> O <sub>3</sub> / 1.94 wt % <sup>235</sup> U
C12	C12	15x15, UO <sub>2</sub> pin configuration, 2.46 wt % <sup>235</sup> U outer zone and 4.02 wt % <sup>235</sup> U inner zone
C14	C12	15x15, UO <sub>2</sub> pin configuration with 12 Gd pins, 4.00 wt % Gd <sub>2</sub> O <sub>3</sub> / 1.94 wt % <sup>235</sup> U, 2.46 wt % <sup>235</sup> U outer zone and 4.02 wt % <sup>235</sup> U inner zone
C18	C18	16x16 CE UO <sub>2</sub> pin configuration, 2.46 wt % <sup>235</sup> U outer zone and 4.02 wt % <sup>235</sup> U inner zone
C20	C18	16x16 CE UO <sub>2</sub> pin configuration with 16 Gd pins, 4.00 wt % Gd <sub>2</sub> O <sub>3</sub> / 1.94 wt % <sup>235</sup> U, 2.46 wt % <sup>235</sup> U outer zone and 4.02 wt % <sup>235</sup> U inner zone

**Table 4-11. Summary of Critical Experiments**

[b,c,d,e]

**Table 4-12. Critical Benchmark Statistical Results**

[b,c,d,e]

Table 4-13. Assembly Loading for Multi-Assembly Problems

Set #	Final Burnup of Problem GWD/MTU	Fuel Assembly 1		Fuel Assembly 2	
		wt% U <sup>235</sup> BP Loading	Initial Burnup GWD/MTU	wt% U <sup>235</sup> BP or Gad Loading	Initial Burnup GWD/MTU
1	30	3.5 none	30 flat	3.5 none	0
2	30	3.5 none	0	3.5 none	30 from set 1
3	30	3.5 none	0	2.5 none	0
4	30	3.5 none	30 from set 3	2.5 none	0
5	30	3.5 none	0	2.5 none	30 from set 4
6	24	2.5 none	0	3.5 12 Pyrex	0
7	30	2.5 none	24 from set 6	3.5 12 Pyrex	0
8	30	2.5 none	0	3.5 12 Pyrex	24 from set 7
9	34	3.5 none	0	4.0 12 Gad 8%	0
10	34	3.5 none	34 from set 9	4.0 12 Gad 8%	0
11	34	3.5 none	0	4.0 12 Gad 8%	34 from set 10
12	34	3.5 none	0	4.0 8 Gad 8% 8 Gad 2%	0
13	34	3.5 none	34 from set 12	4.0 8 Gad 8% 8 Gad 2%	0
14	34	3.5 none	0	4.0 4 Gad 4%	0
15	34	3.5 none	34 from set 14	4.0 4 Gad 4%	0

**Table 4-14. Pin Power Peaking Results for Multi-Assembly Problems**

[b,c,d,e]

**Table 4-15. Conditions for the Rod Drop Test**

Case	Plant	Cycle	Core Burnup MWD/MTU	% Power	Boron ppm	Regulating Bank Position, Steps	Initial Axial Offset	Location of Dropped Rods
1	193	1	700	50.0	802	217	-10.6	F6+K10
2	193	1	4340	50.0	666	185	-6.7	K6+F10
3						187	-4.7	K4+F12
4						223	23.6	E5+L11
5	193	1	11575	50.1	160	231	21	F6+K10
6	157	3	10575	50.0	175	200/211 <sup>a</sup>	15.5	K2+P10

<sup>a</sup> Regulating bank is in automatic control of the temperature. Initial and final state listed.

**Table 4-16. Radial Power Statistics**

[b,c,d,e]

**Table 4-17. Peak Power Statistics**

[b,c,d,e]

**Table 4-18. Summary of Local Pin Power Statistics**

[b,c,d,e]

**Table 4-19. NRF Values for SCIENCE**

[b,c,d,e]

Figure 4-1. HFP K-effective Versus Core Burnup

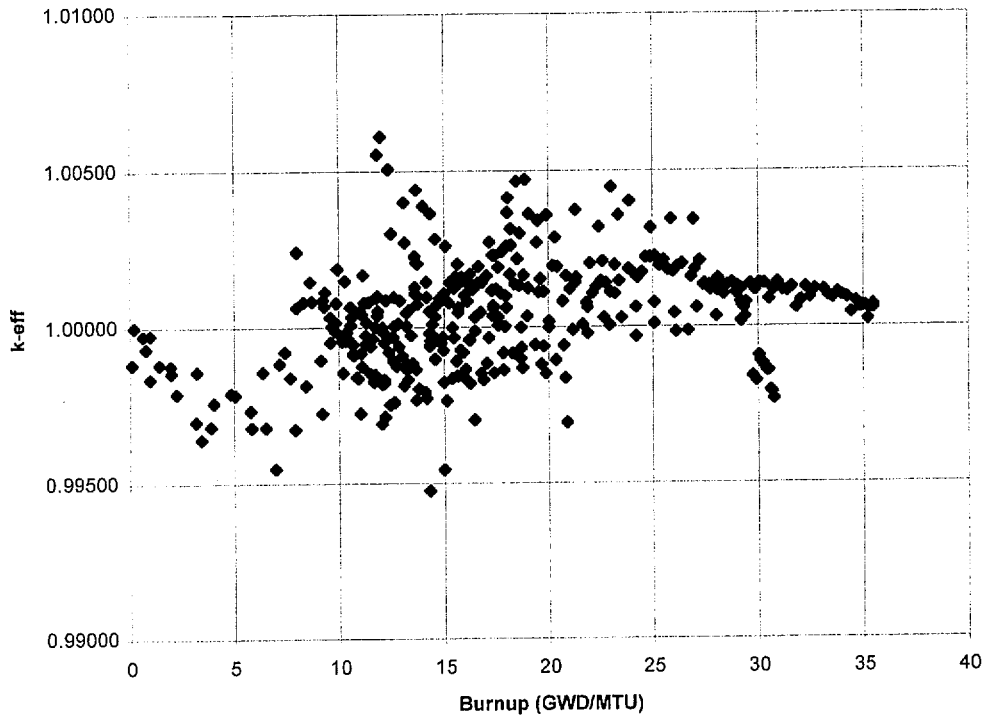


Figure 4-2. TMI 1 Cycle 5 58 EFPD

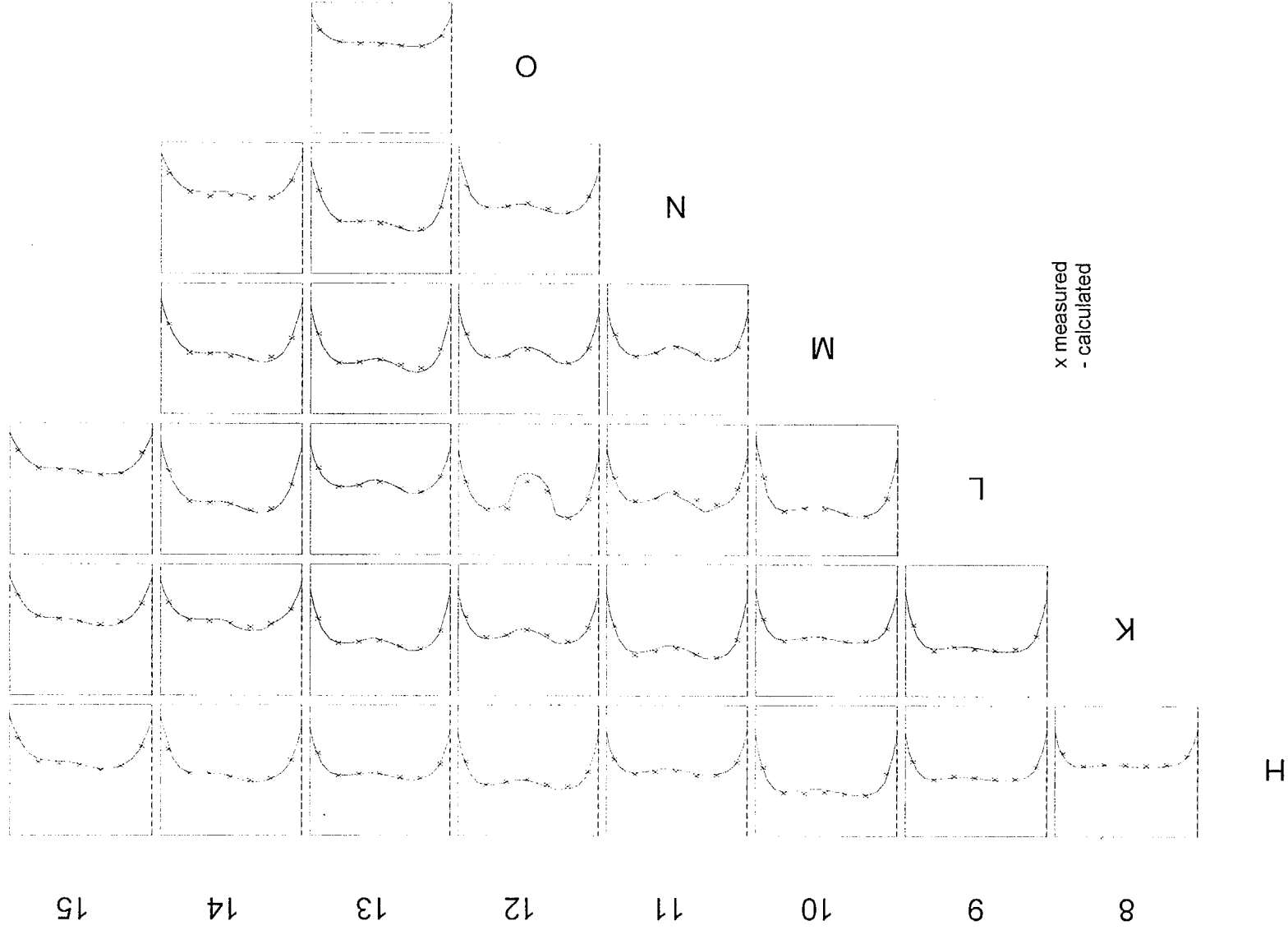


Figure 4-3. TMI 1 Cycle 5 140 EFPD

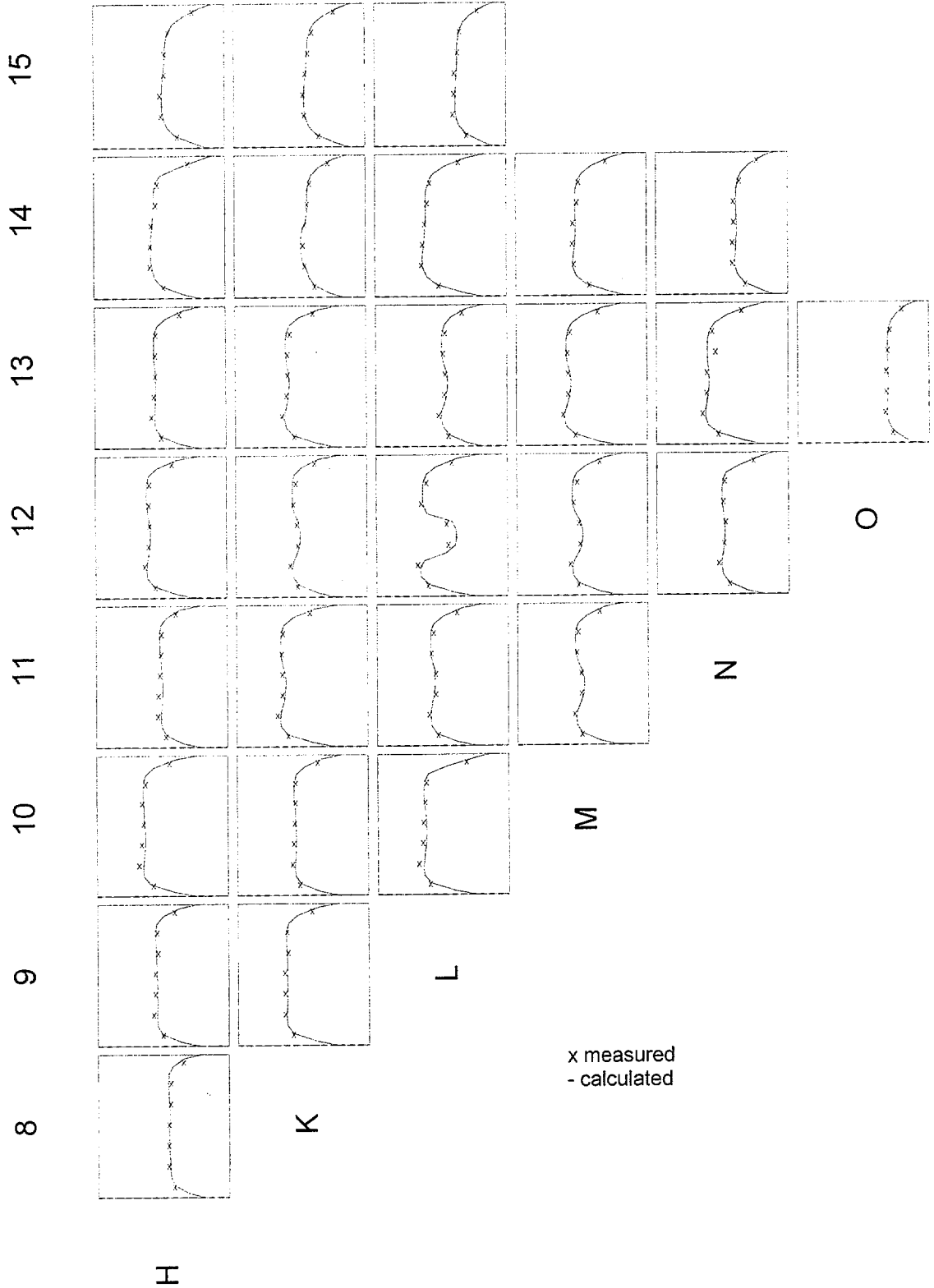


Figure 4-4. TMI 1 Cycle 5 206 EFPD

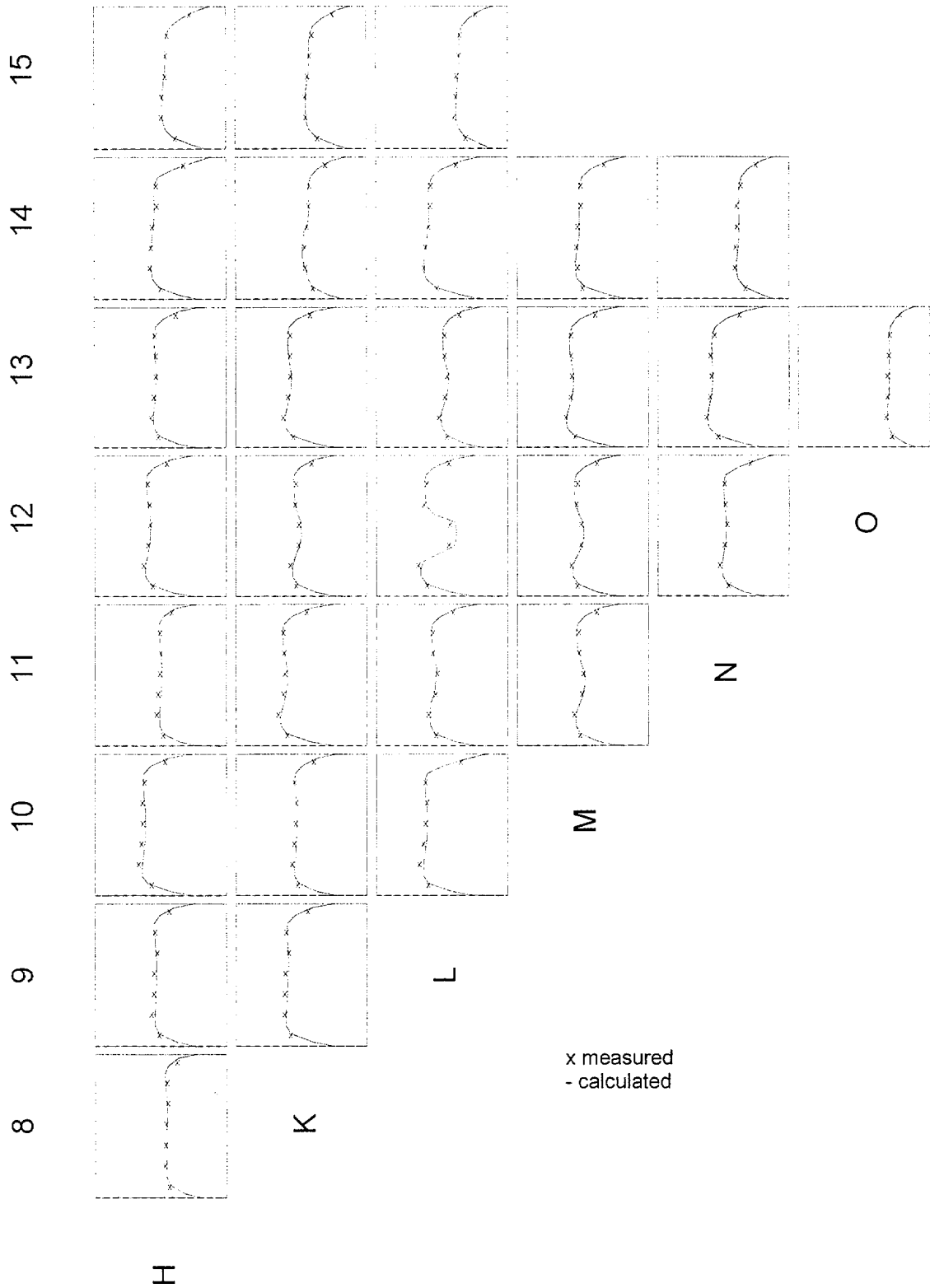


Figure 4-5. TMI 1 Cycle 5 279 EFPD

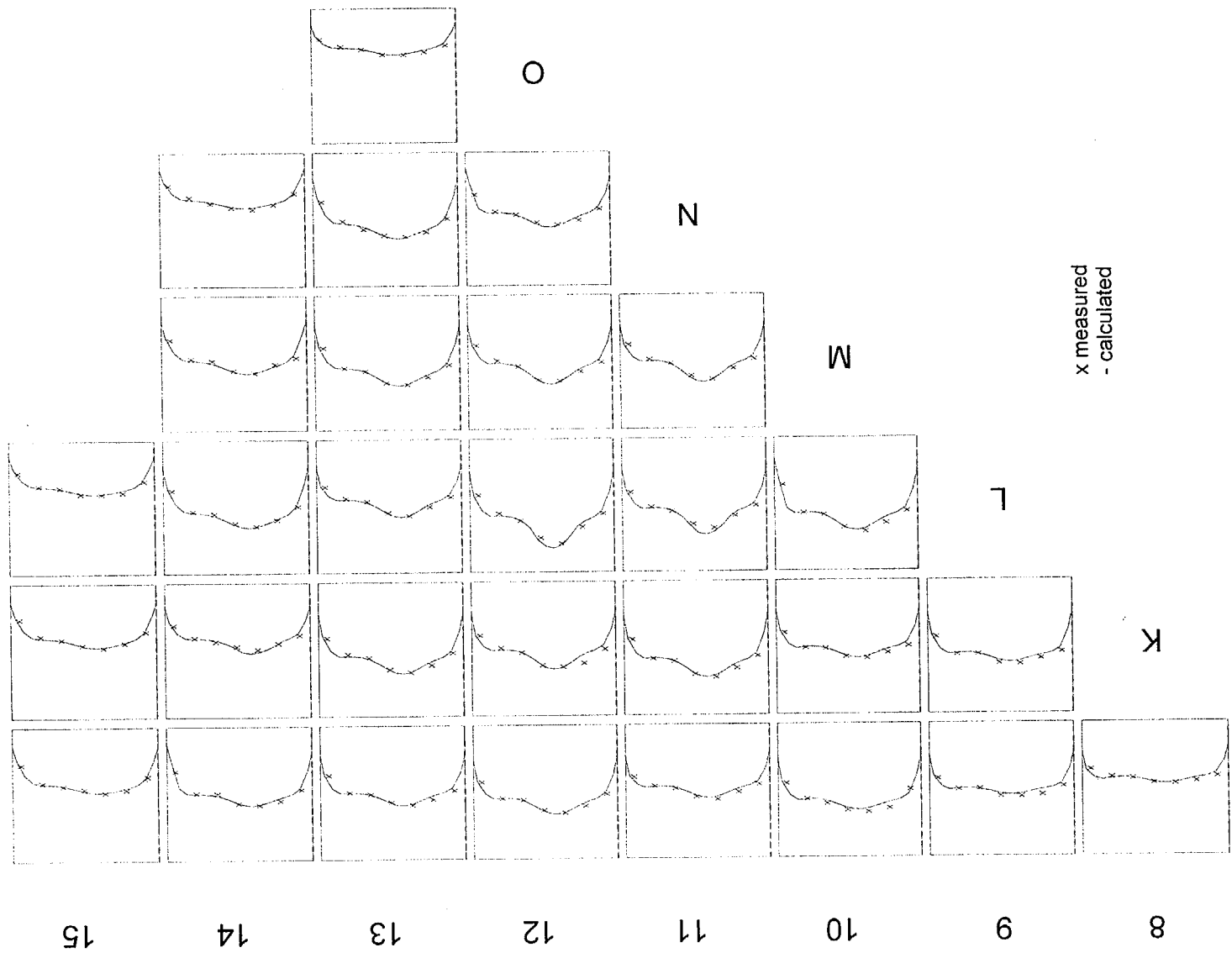


Figure 4-6. TMI 1 Cycle 6 17 EFPD

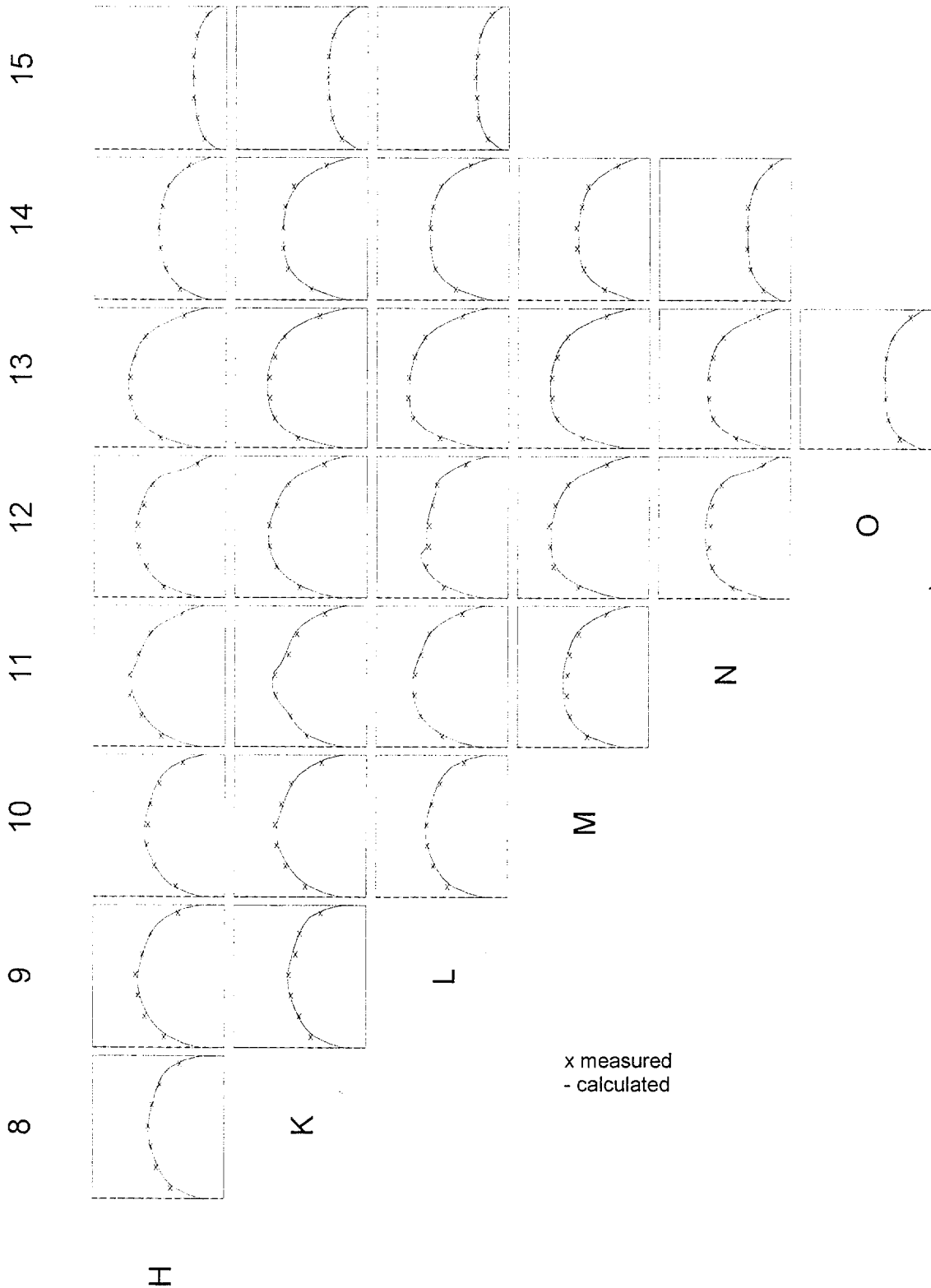


Figure 4-7. TMI 1 Cycle 6 79 EFPD

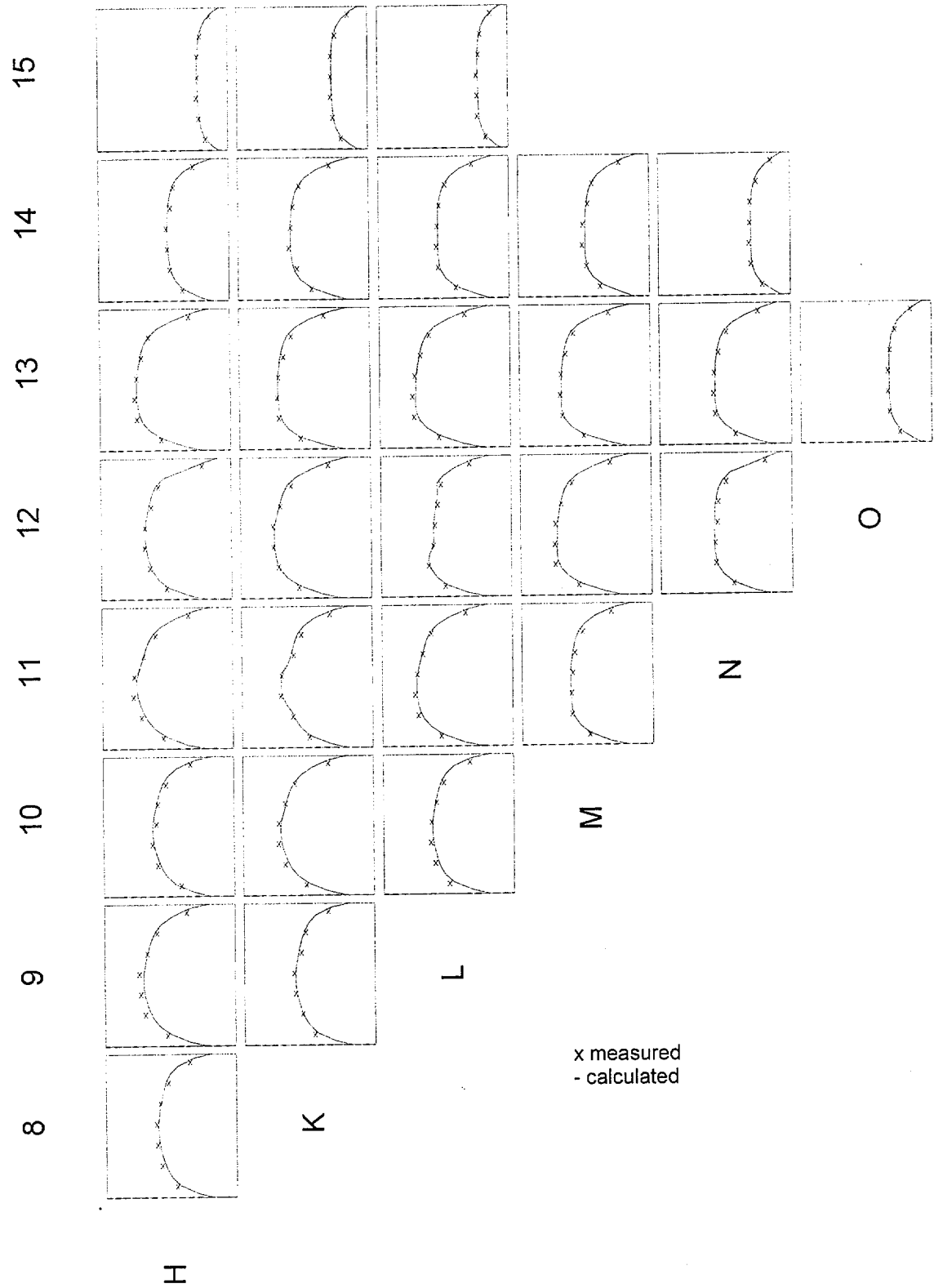


Figure 4-8. TMI 1 Cycle 6 176 EFPD

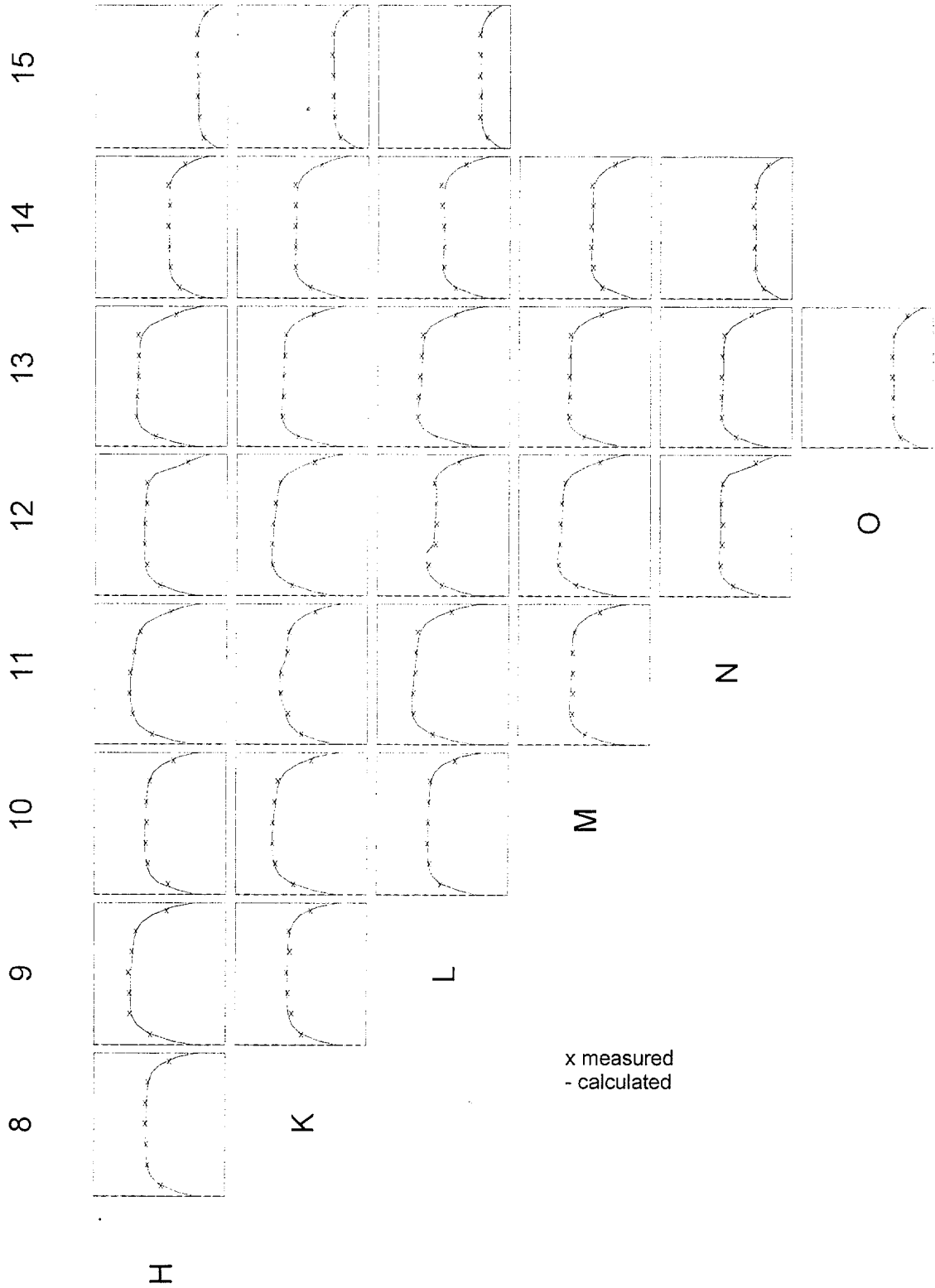


Figure 4-9. TMI 1 Cycle 6 288 EFPD

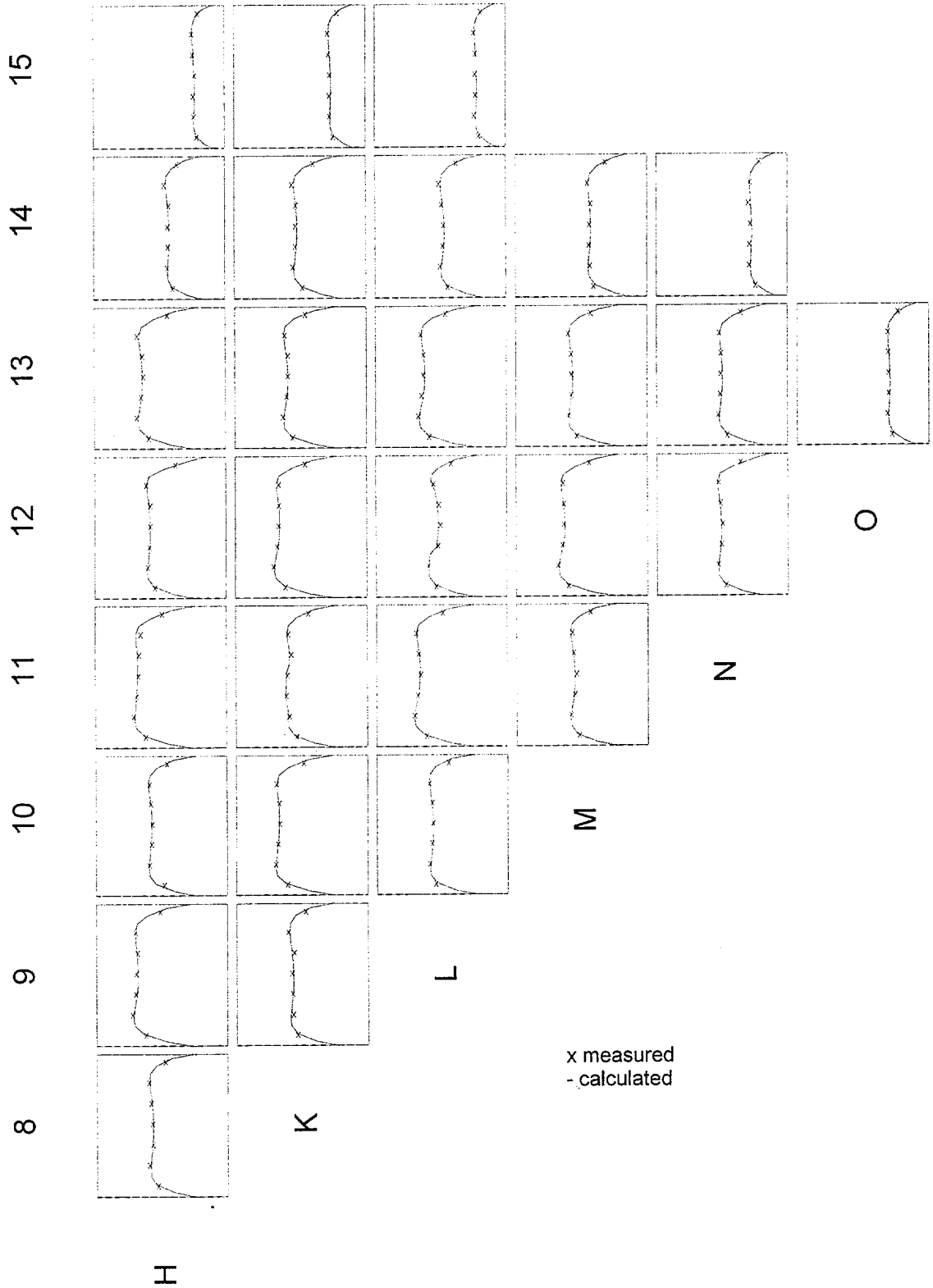


Figure 4-10. TMI 1 Cycle 6 403 EFPD

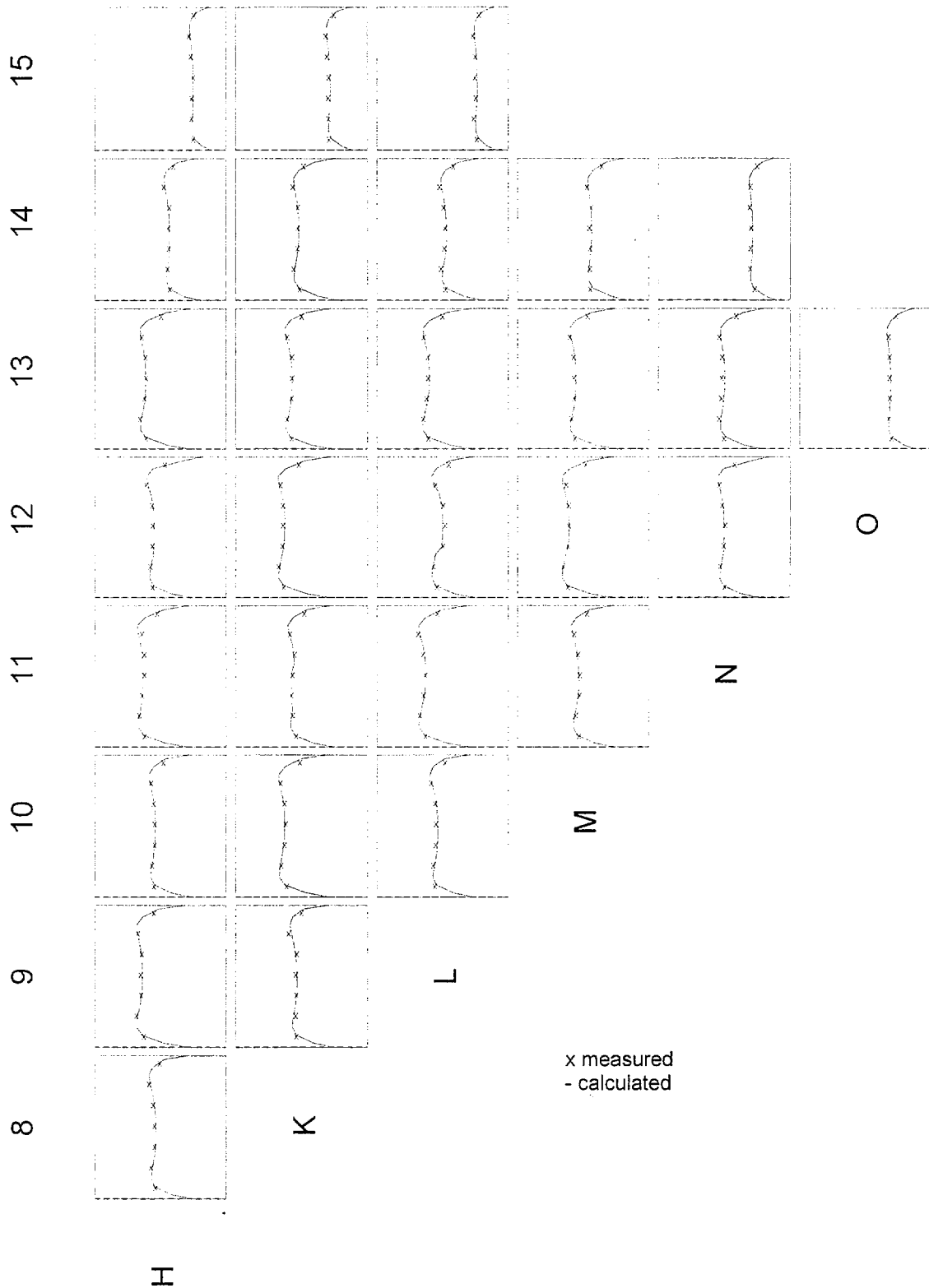
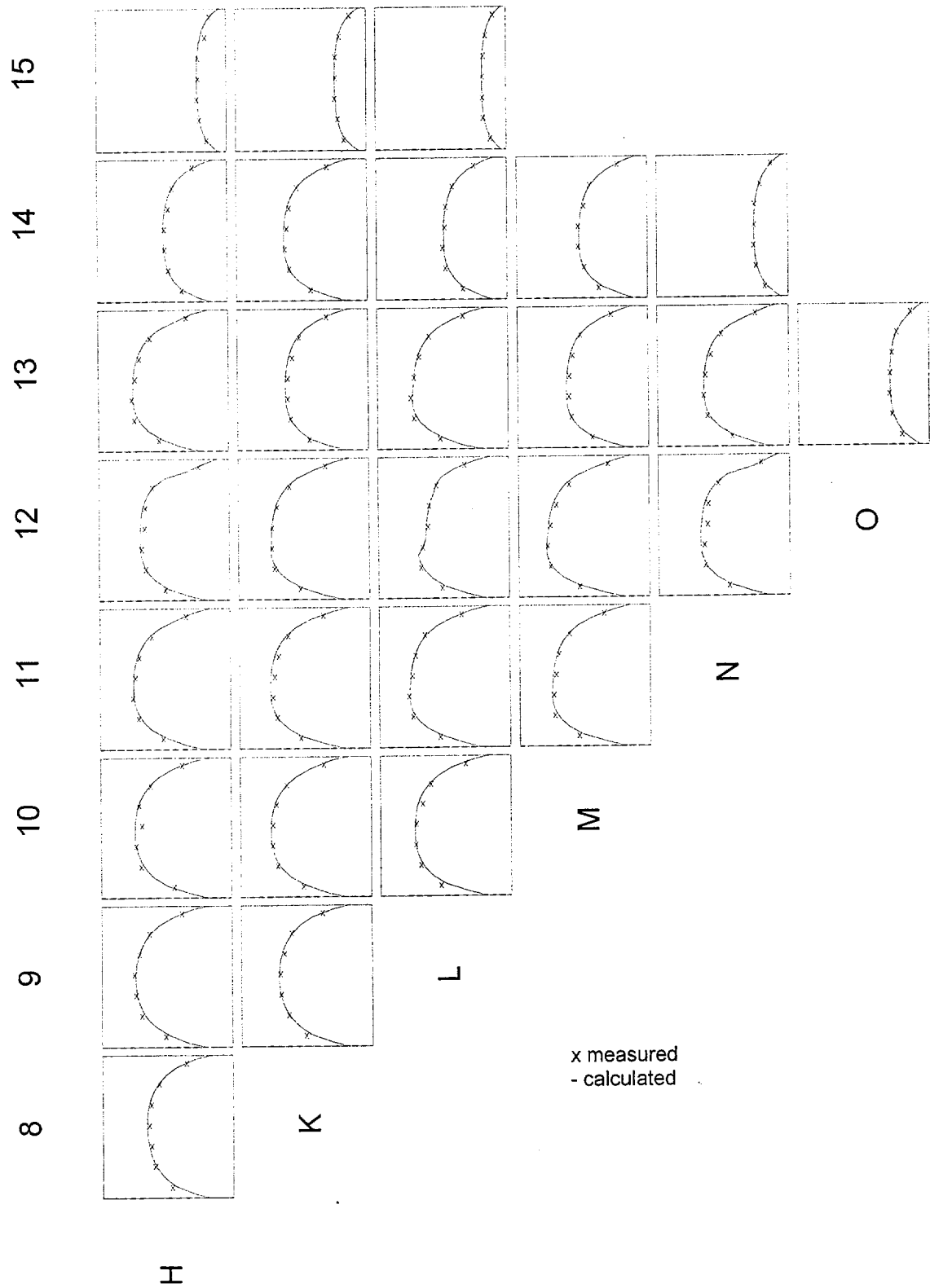


Figure 4-11. TMI 1 Cycle 7 3 EFPD



x measured  
- calculated

Figure 4-12. TMI 1 Cycle 7 101 EFPD

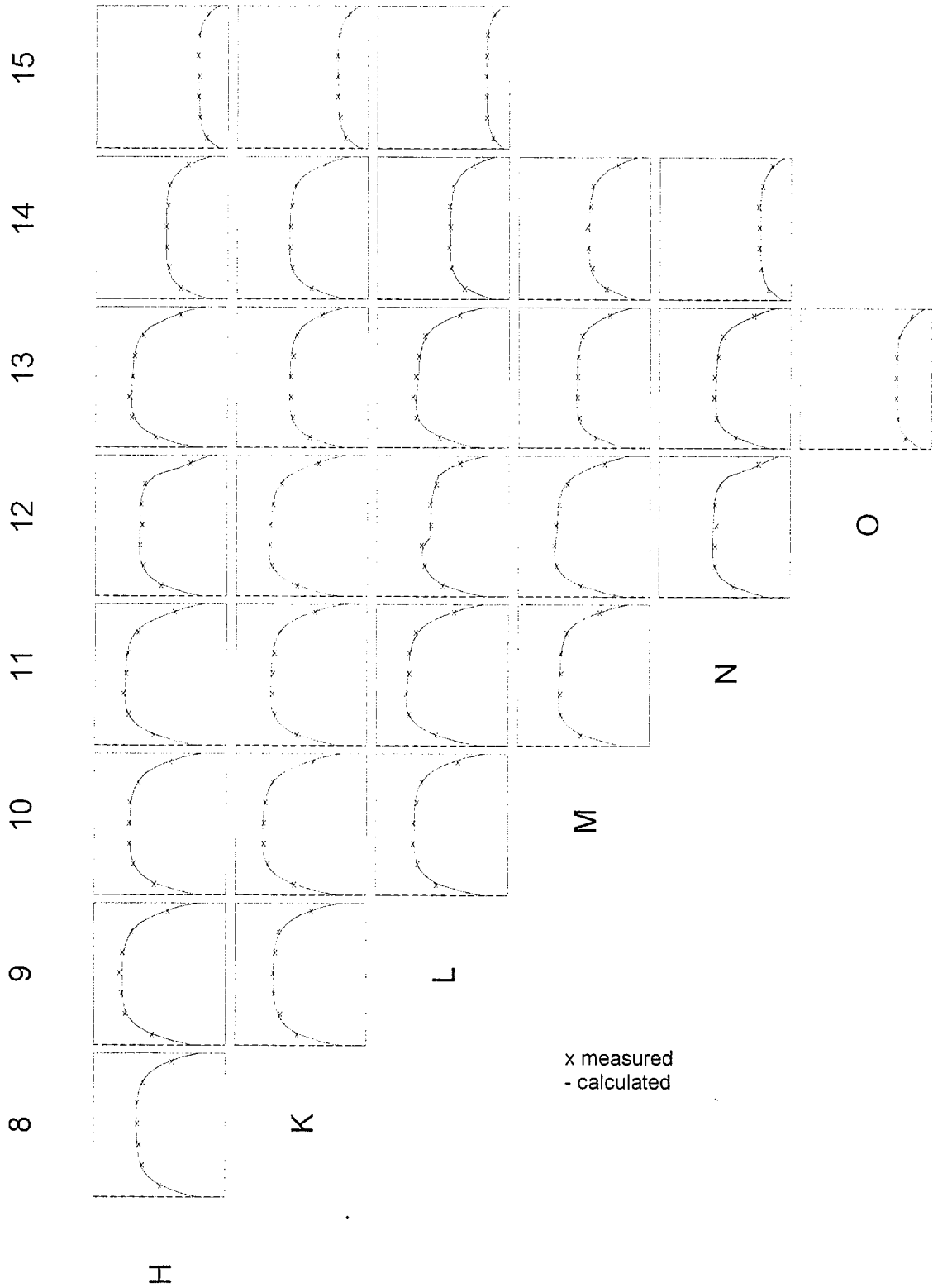


Figure 4-13. TMI 1 Cycle 7 241 EFPD

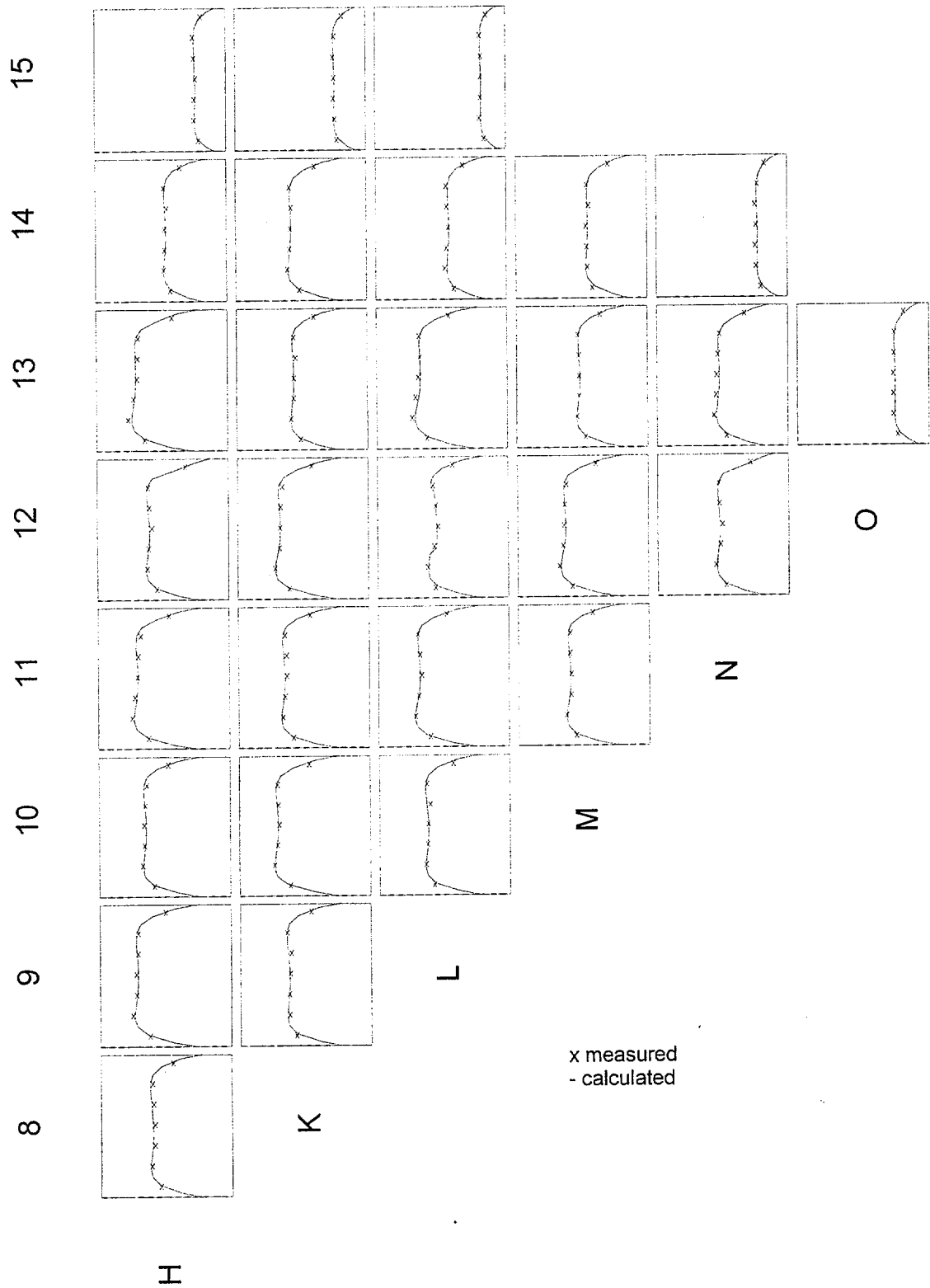


Figure 4-14. TMI 1 Cycle 7 346 EFPD

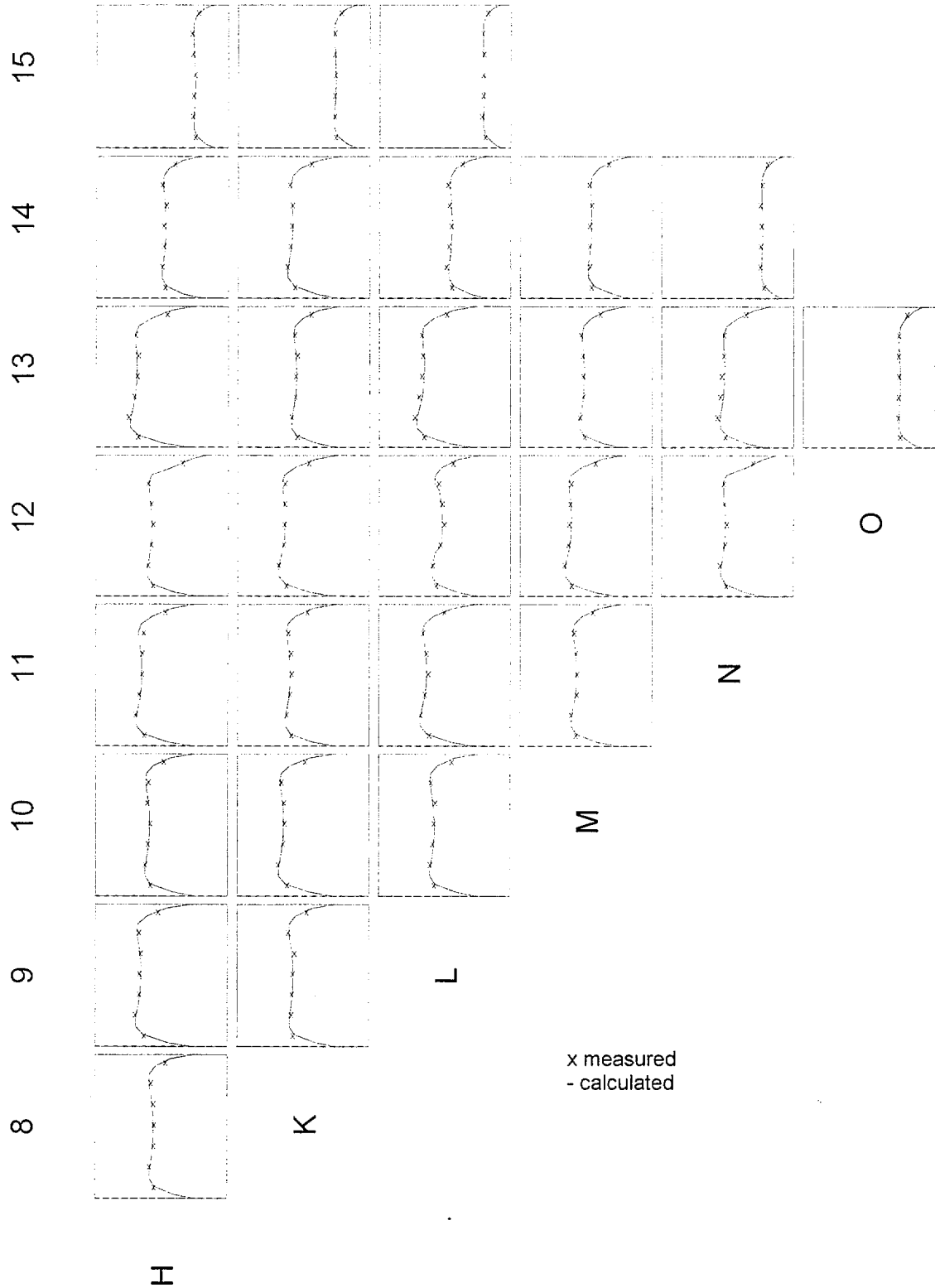
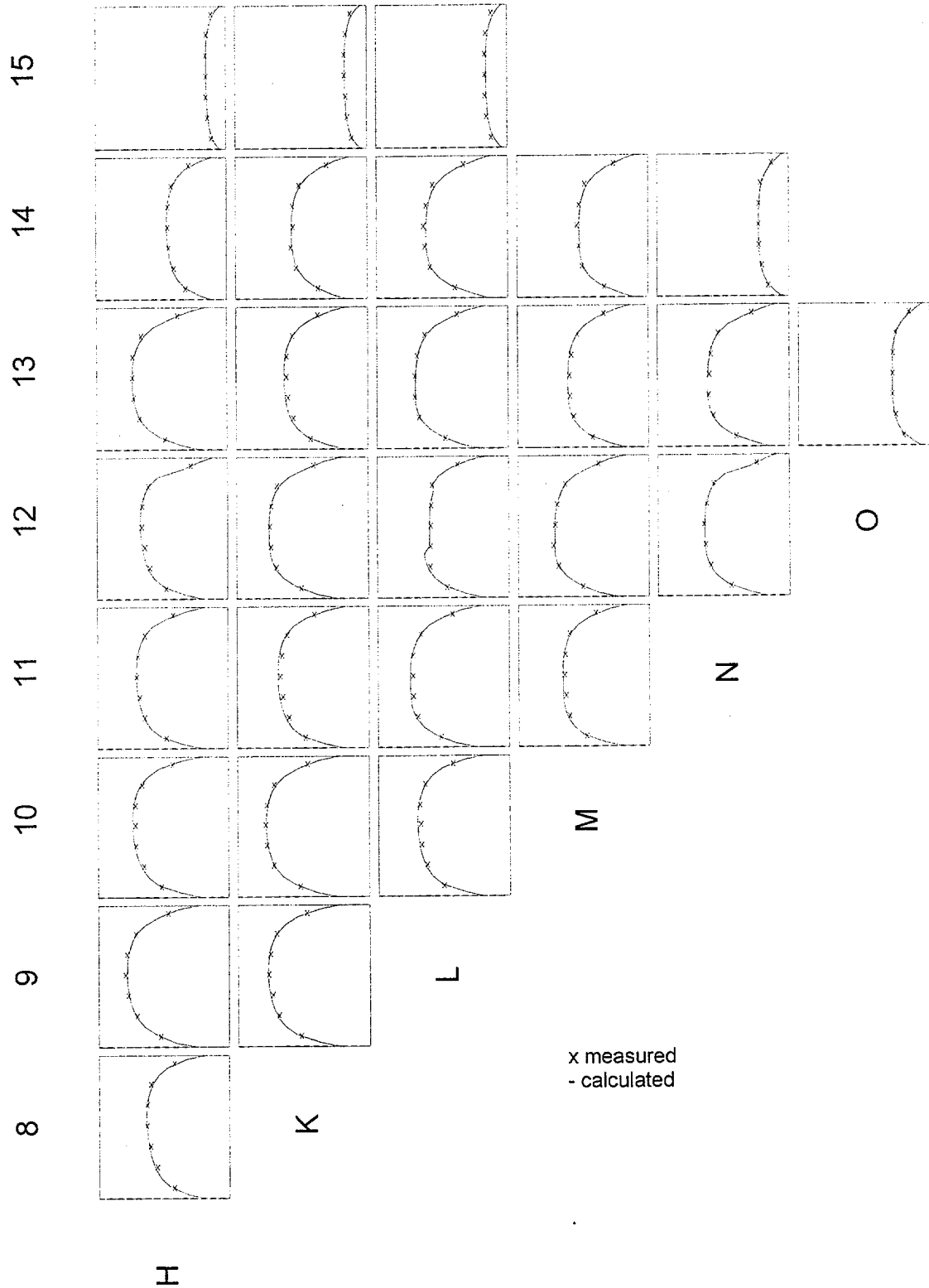


Figure 4-15. TMI 1 Cycle 9 39 EFPD



x measured  
- calculated

Figure 4-16. TMI 1 Cycle 9 549 EFPD

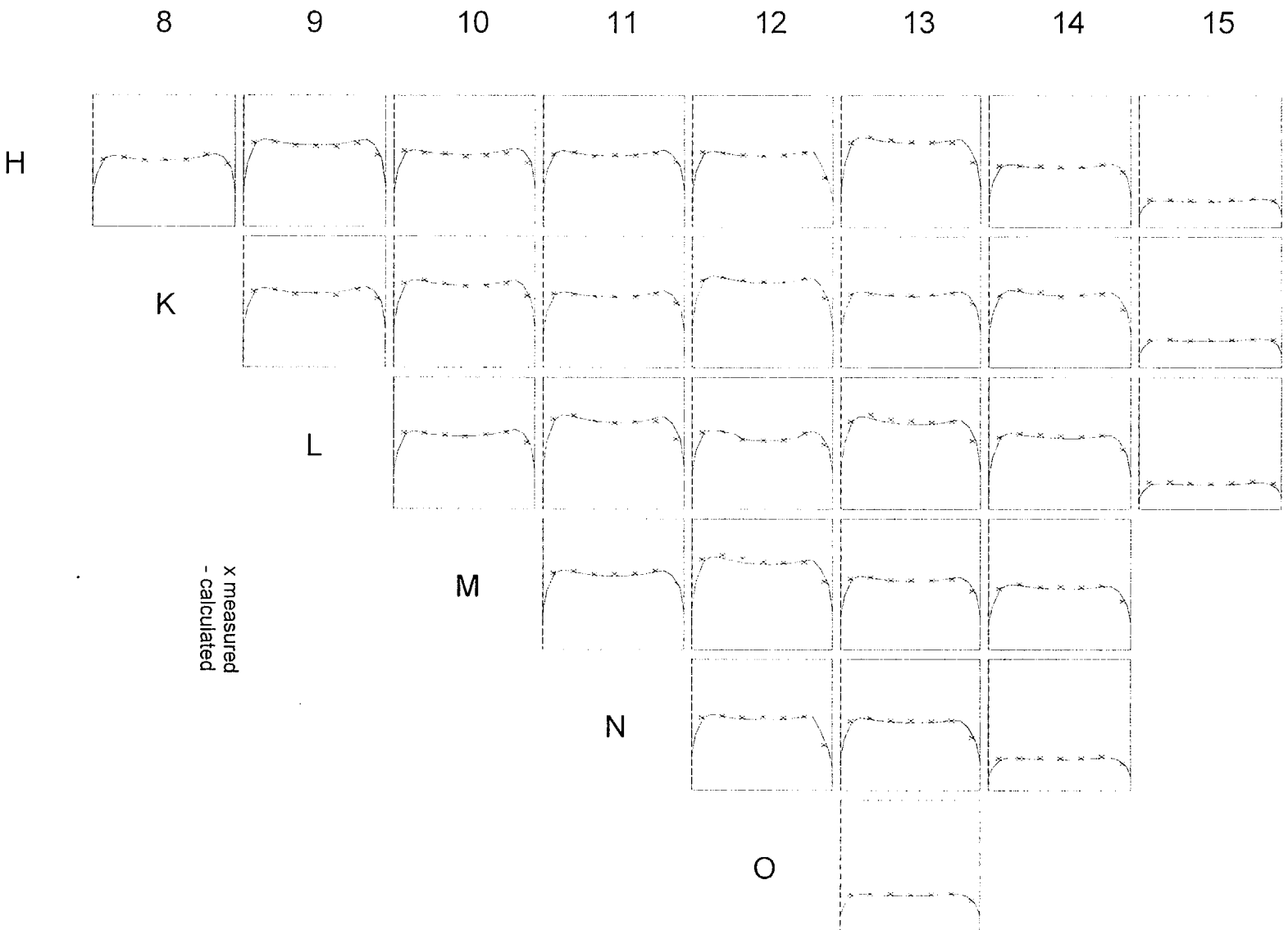


Figure 4-17. TMI 1 Cycle 10 7 EFPD

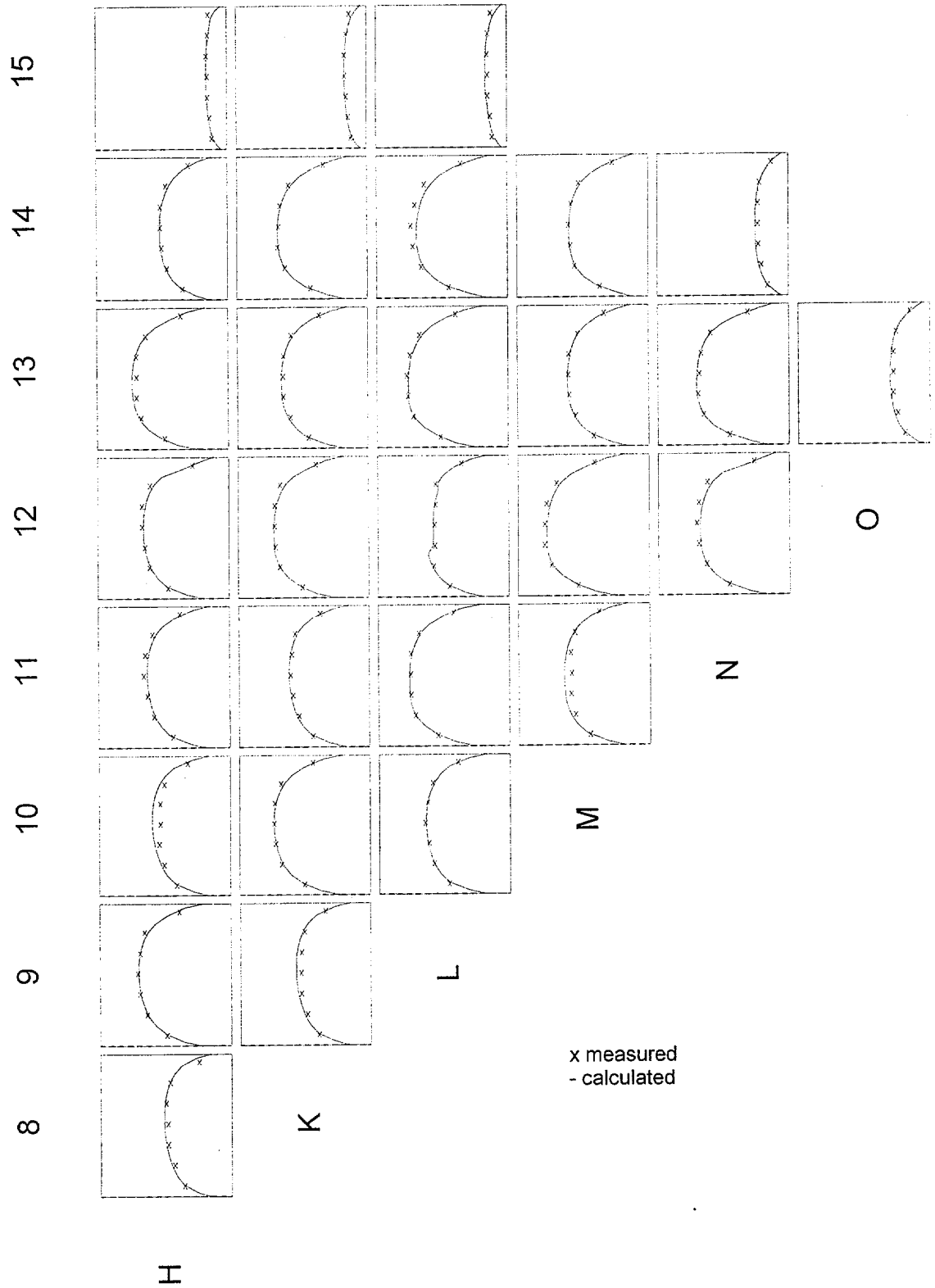


Figure 4-18. TMI 1 Cycle 10 652 EFPD

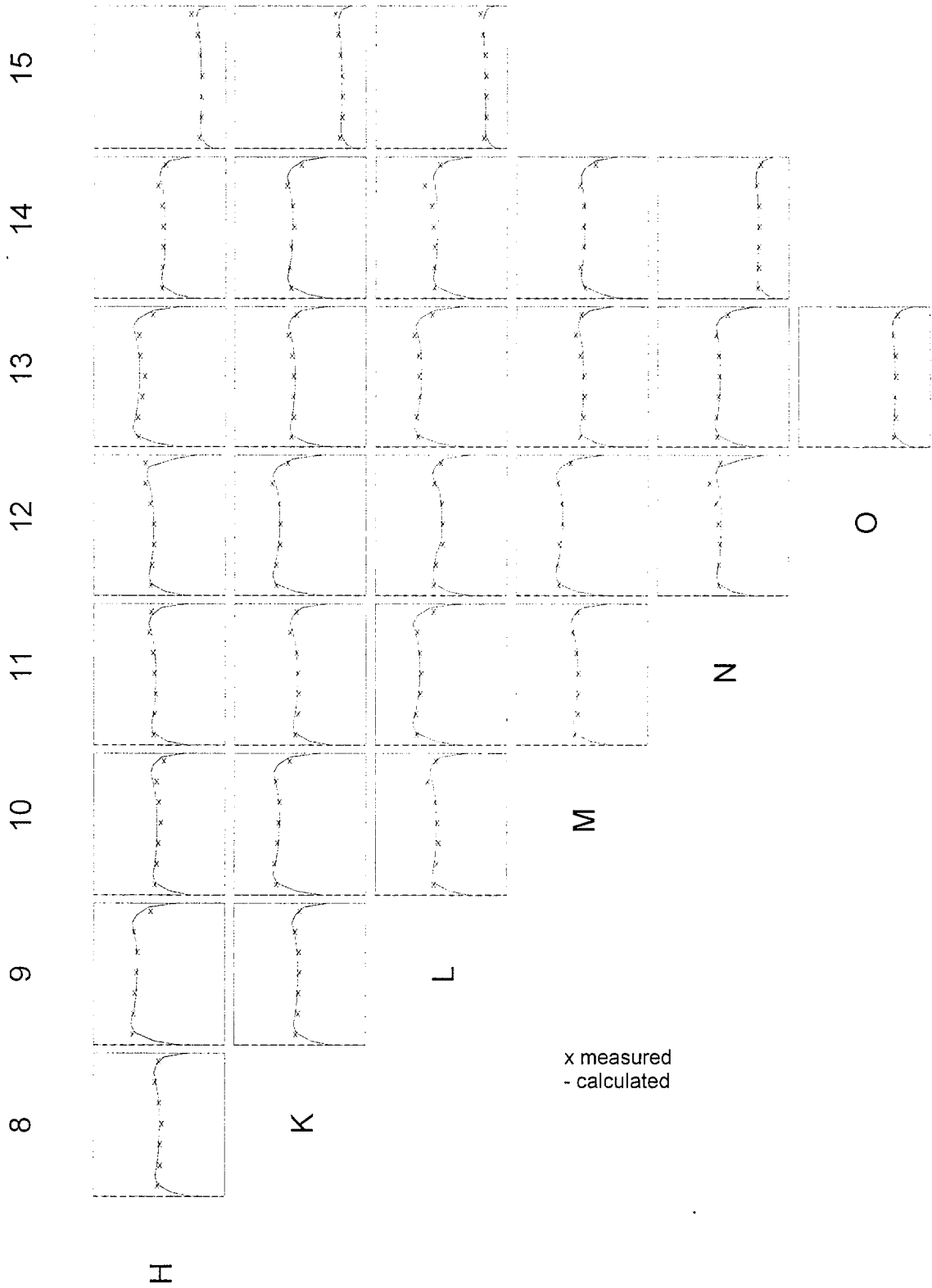


Figure 4-19. Sequoyah 1 Cycle 1 133 EFPD

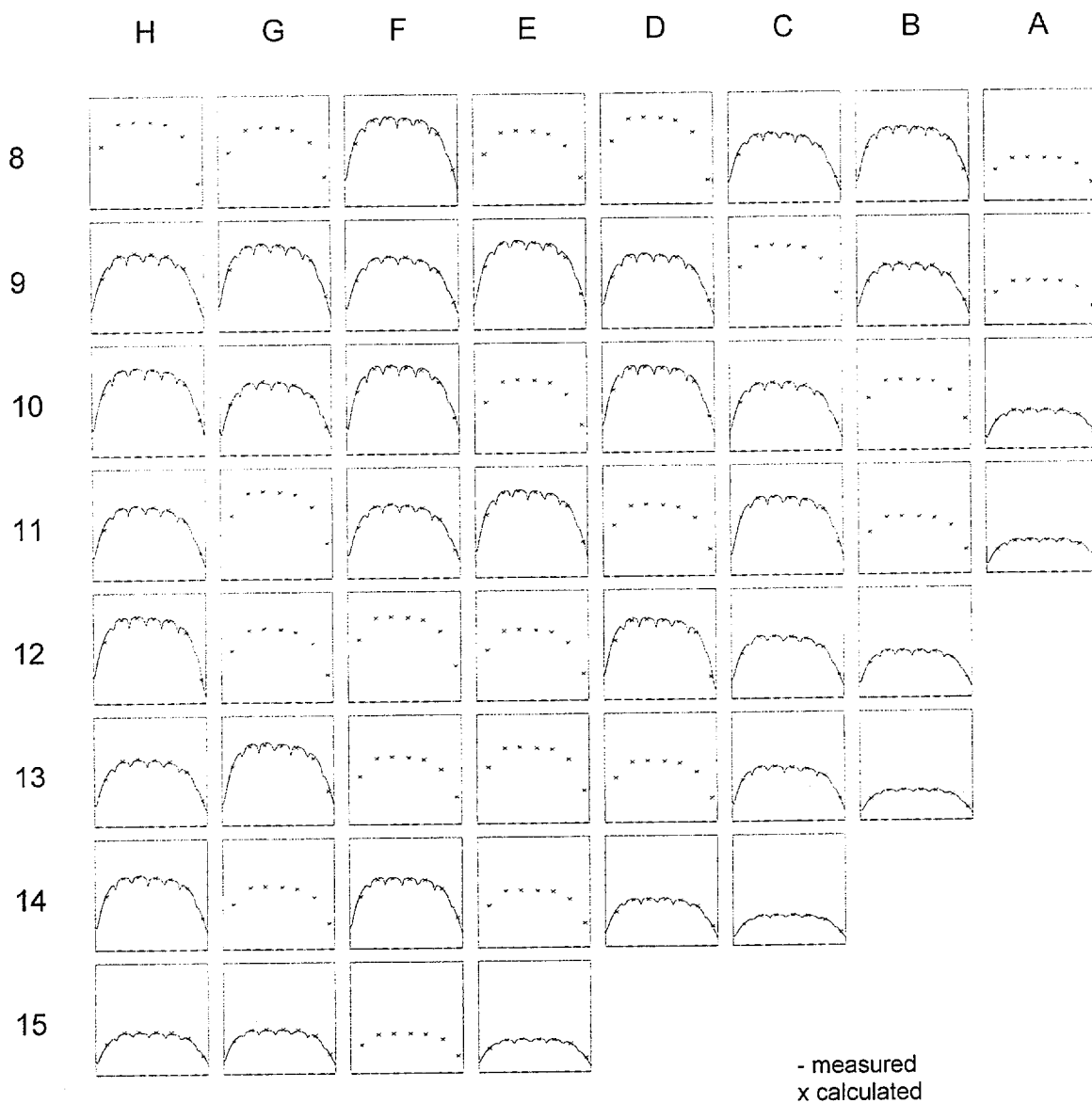
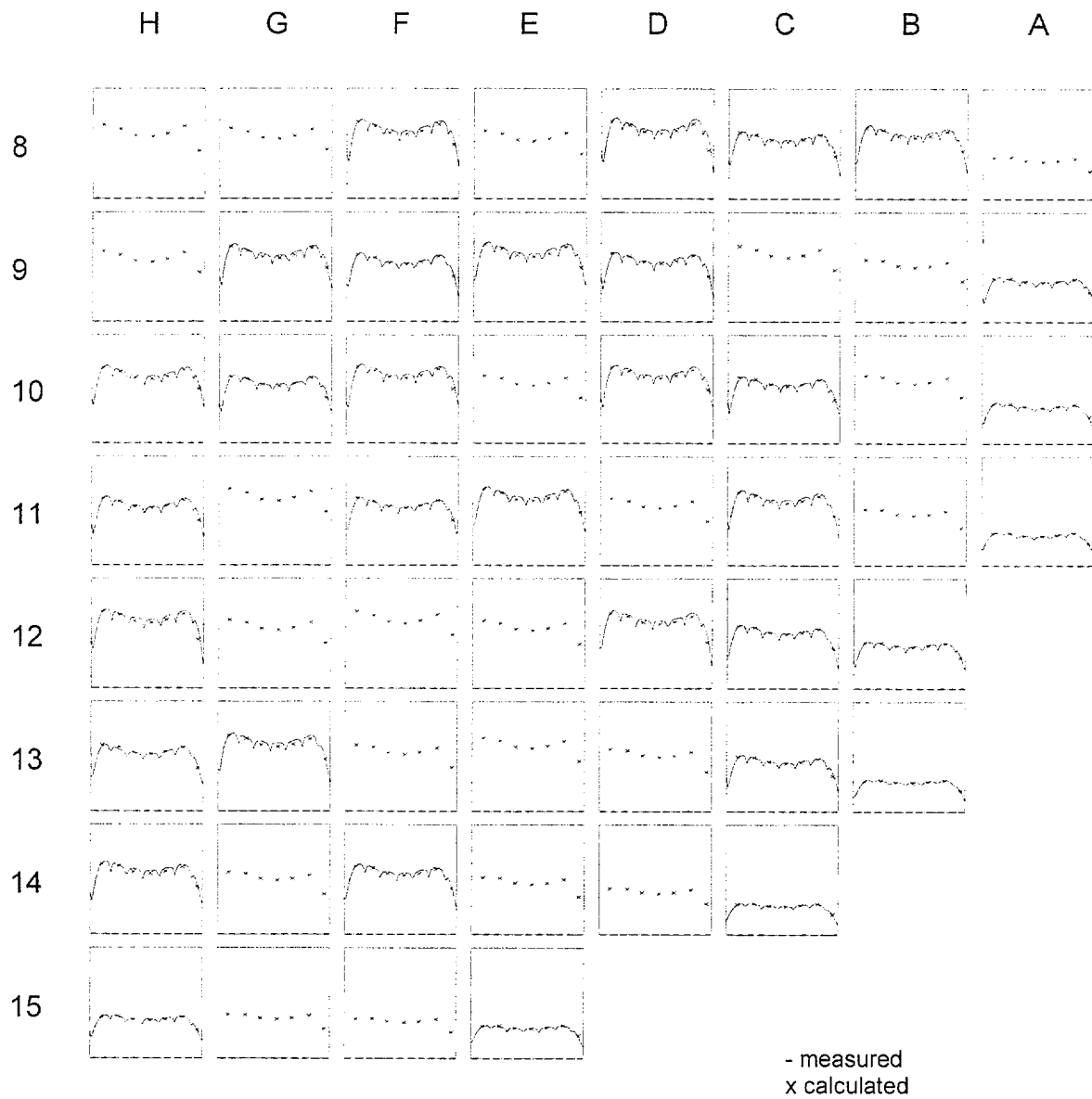


Figure 4-20. Sequoyah 1 Cycle 1 378 EFPD



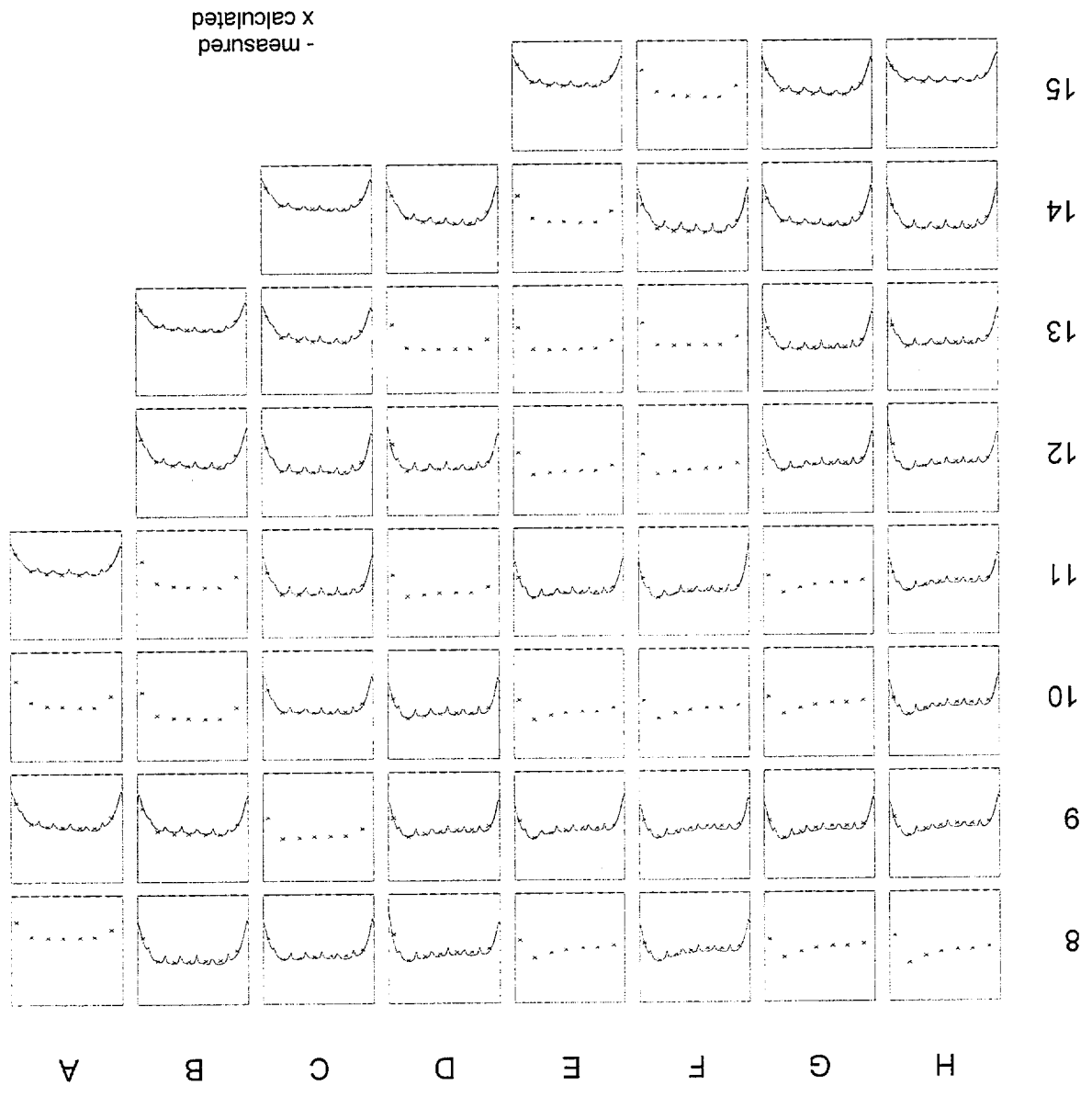


Figure 4-21. Sequoyah 1 Cycle 2 50 EFPD

Figure 4-22. Sequoyah 1 Cycle 2 301 EFPD

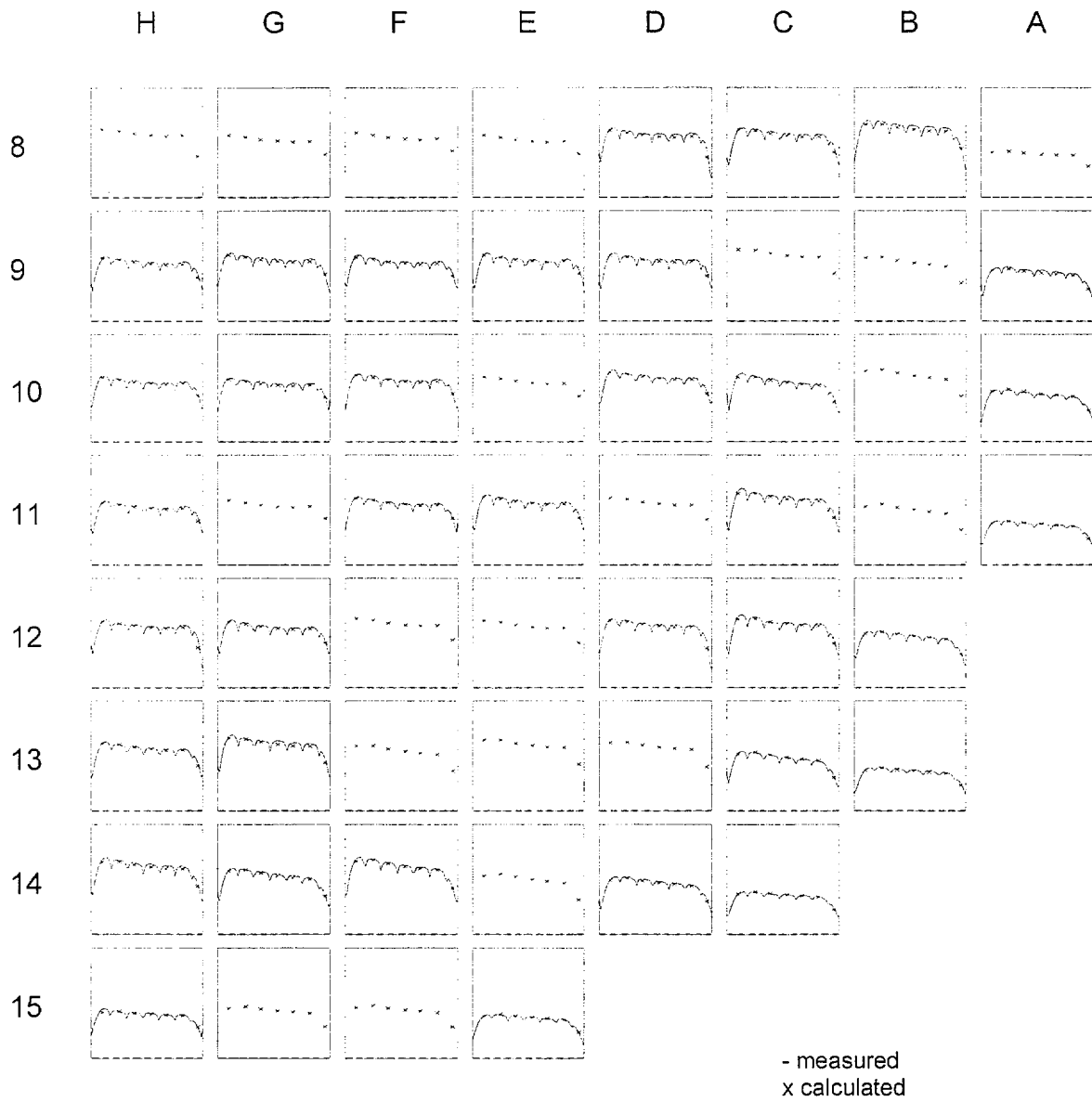
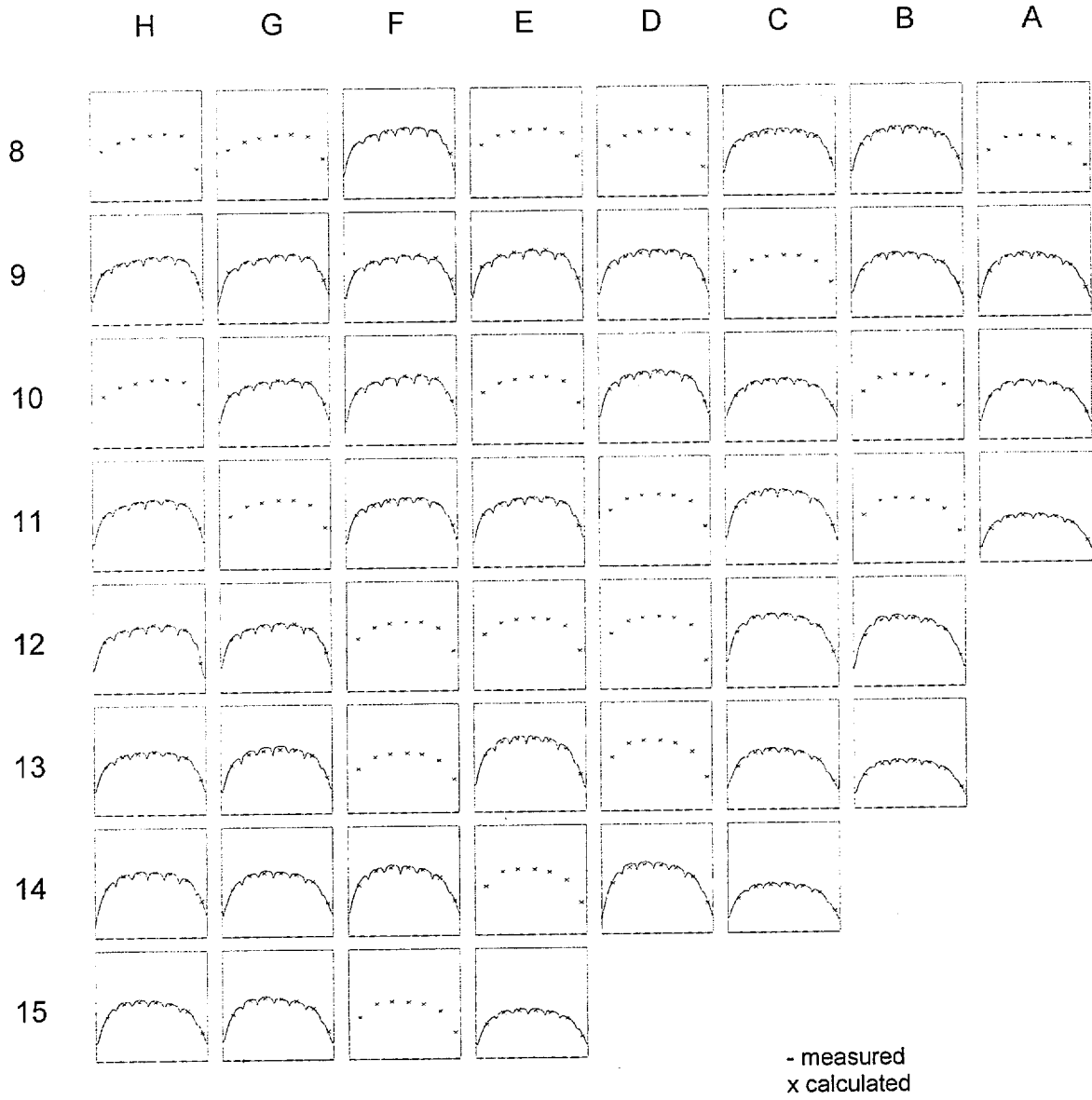


Figure 4-23. Sequoyah 1 Cycle 3 31 EFPD



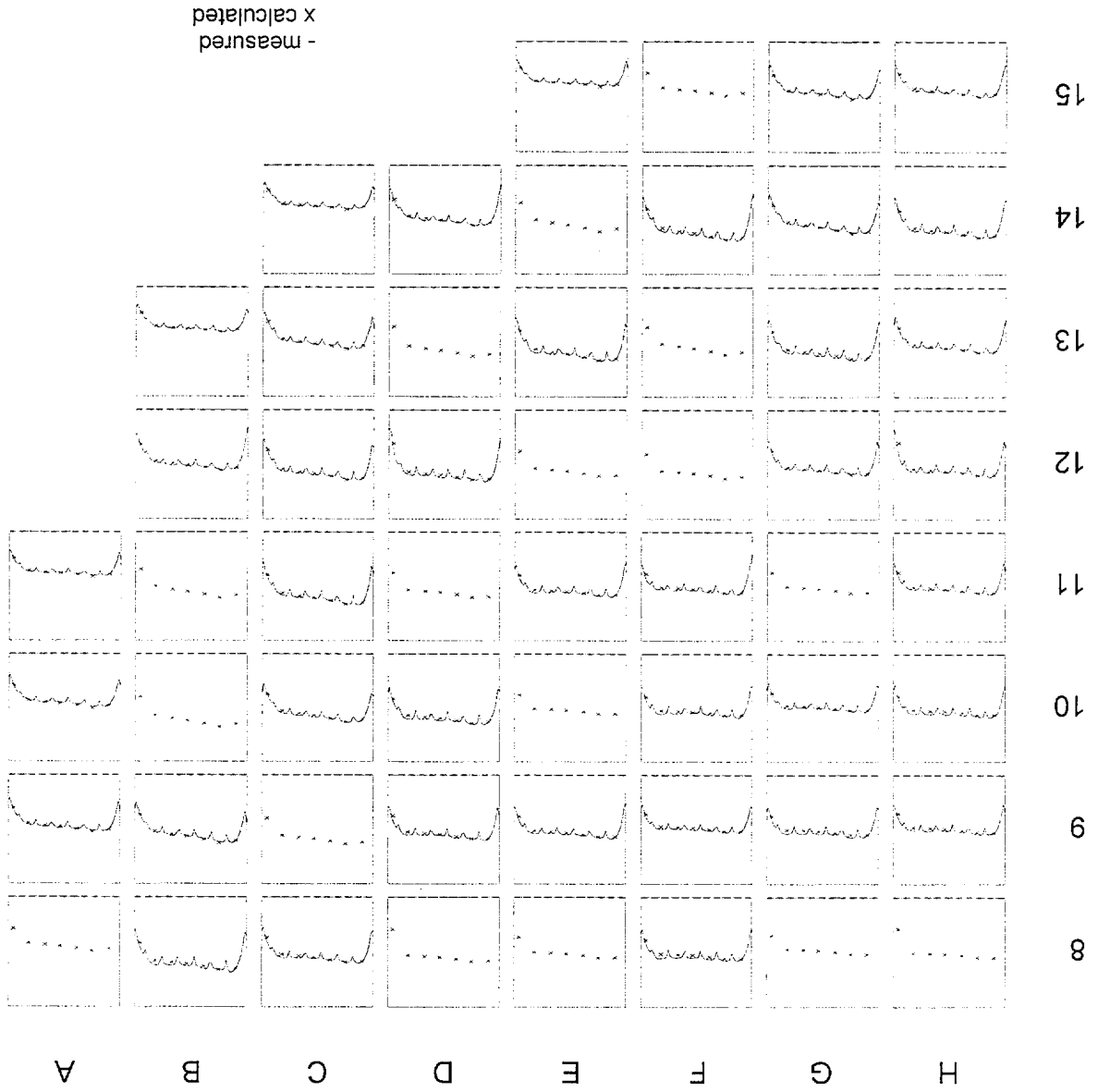


Figure 4-24. Sequoyah 1 Cycle 3 305 EPPD

Figure 4-25. Sequoyah 1 Cycle 4 17 EFPD

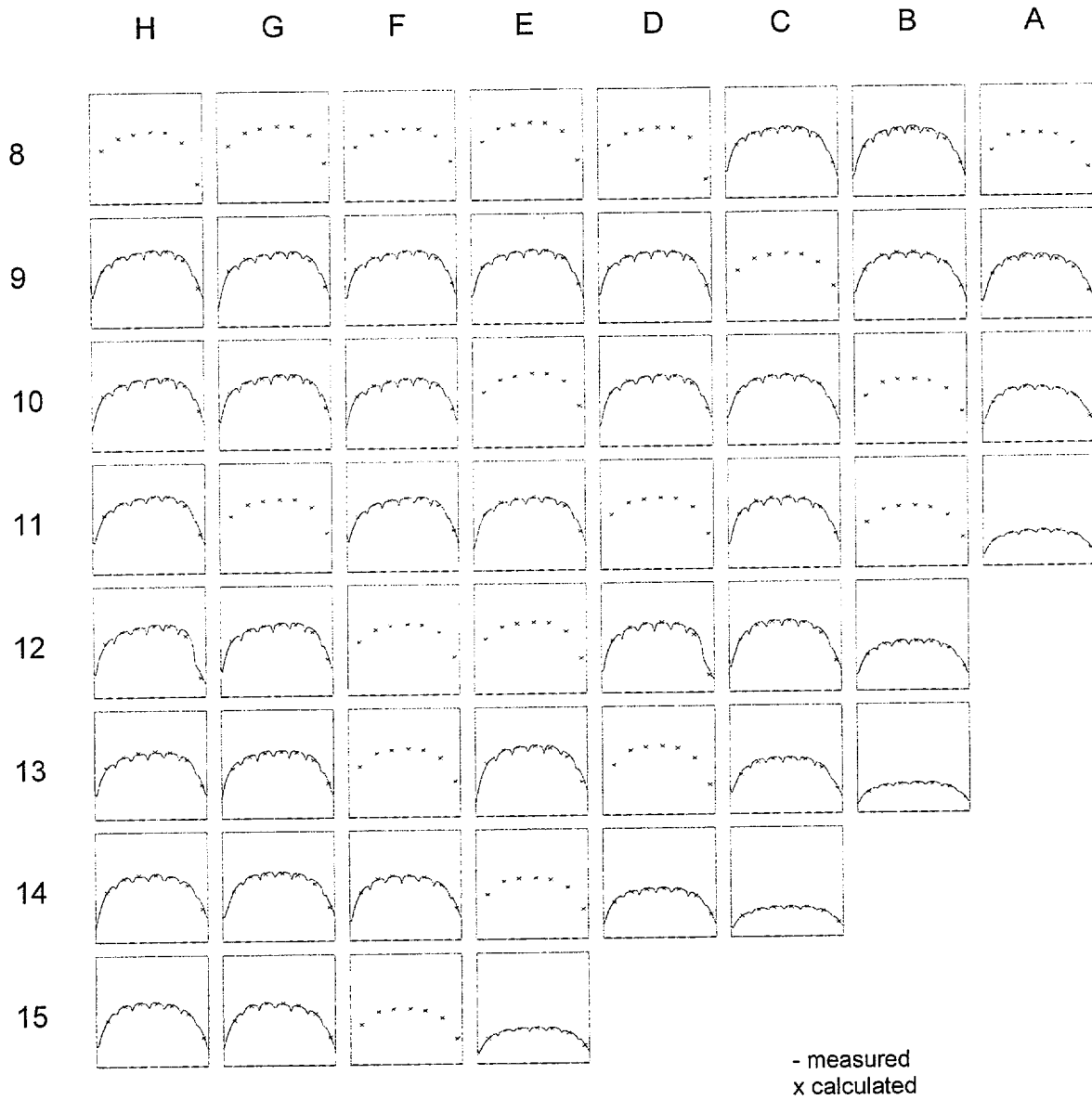


Figure 4-26. Sequoyah 1 Cycle 4 407 EFPD

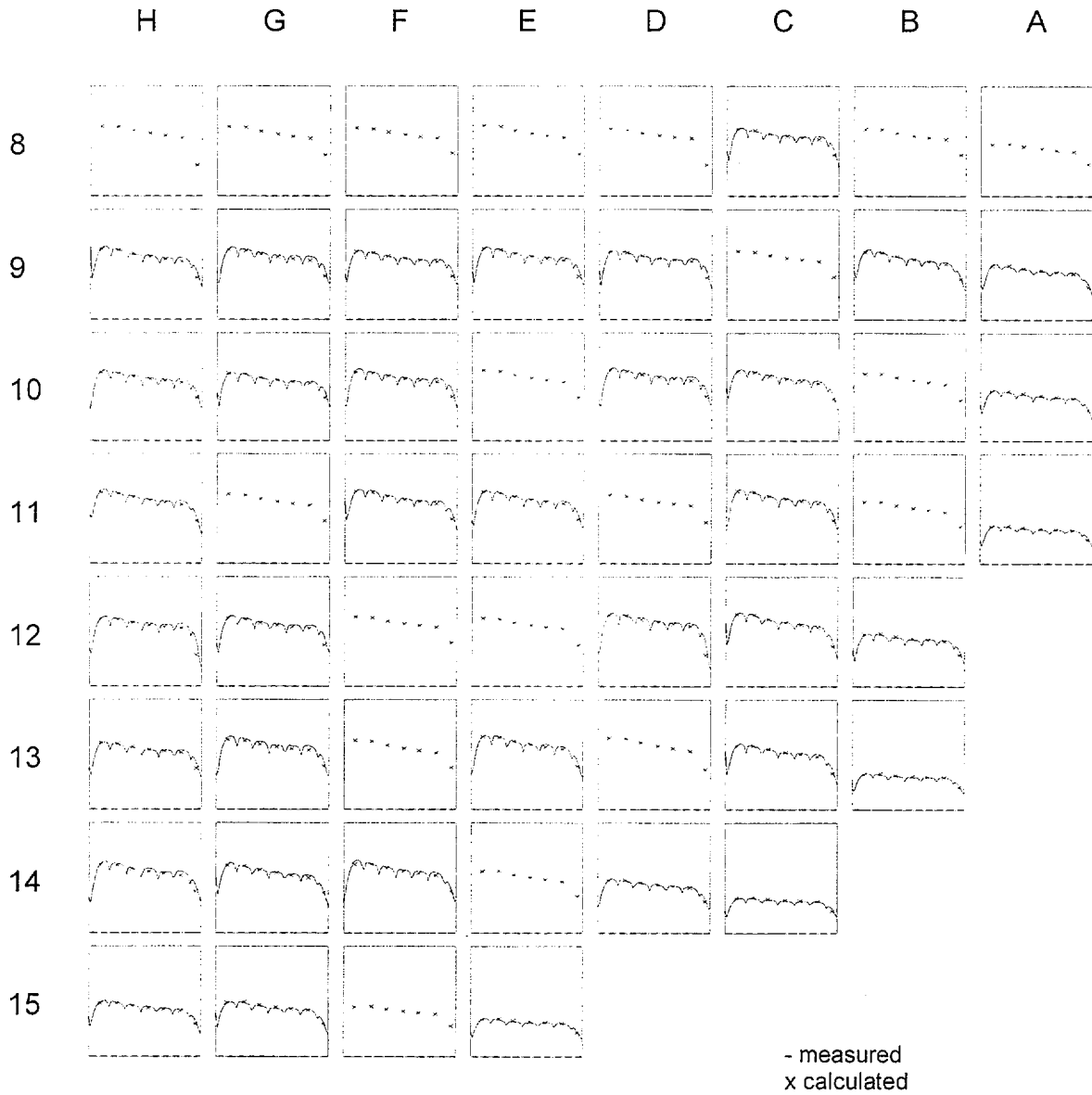


Figure 4-27. Sequoyah 1 Cycle 5 10 EFPD

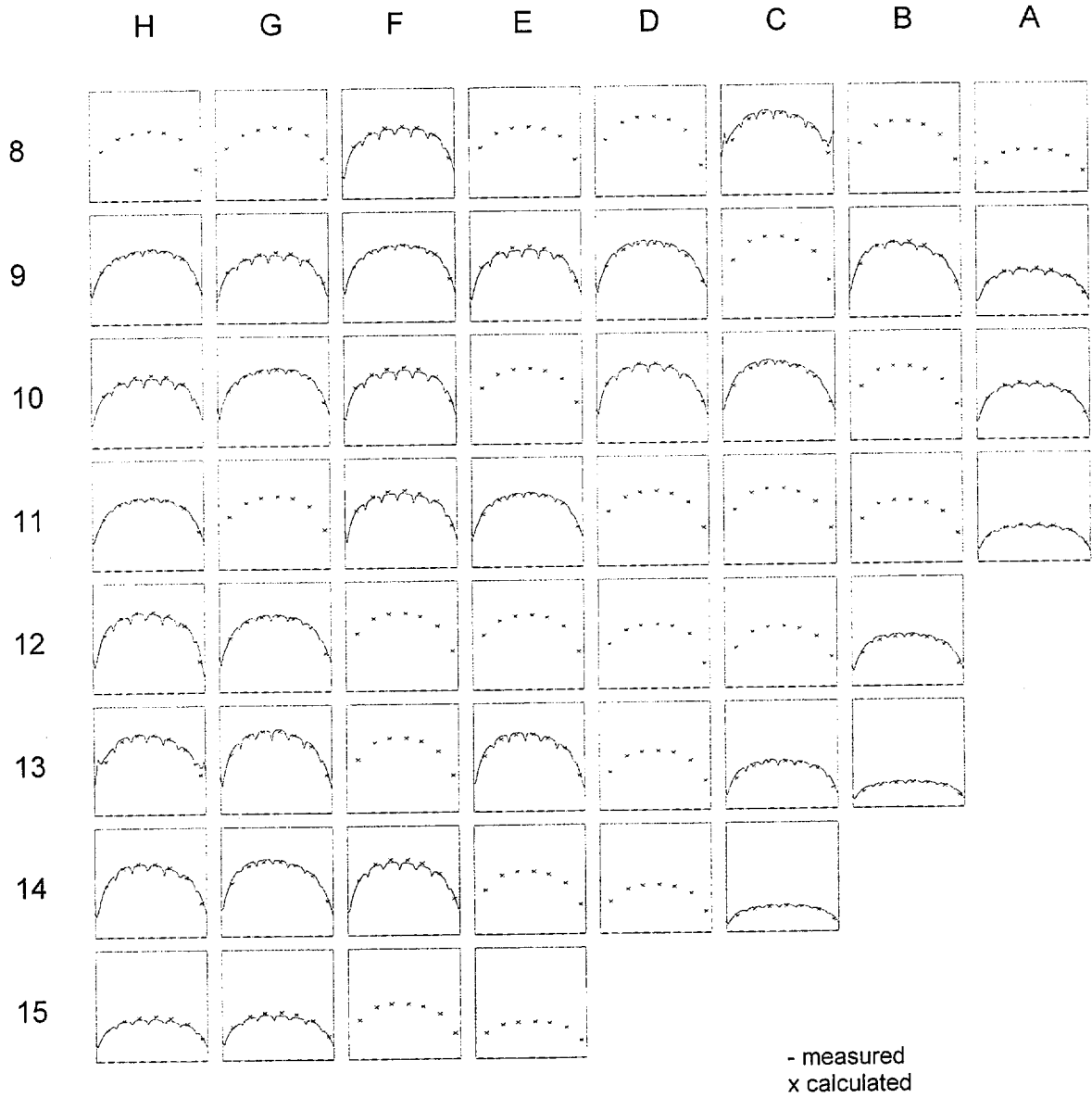


Figure 4-28. Sequoyah 1 Cycle 5 394 EFPD

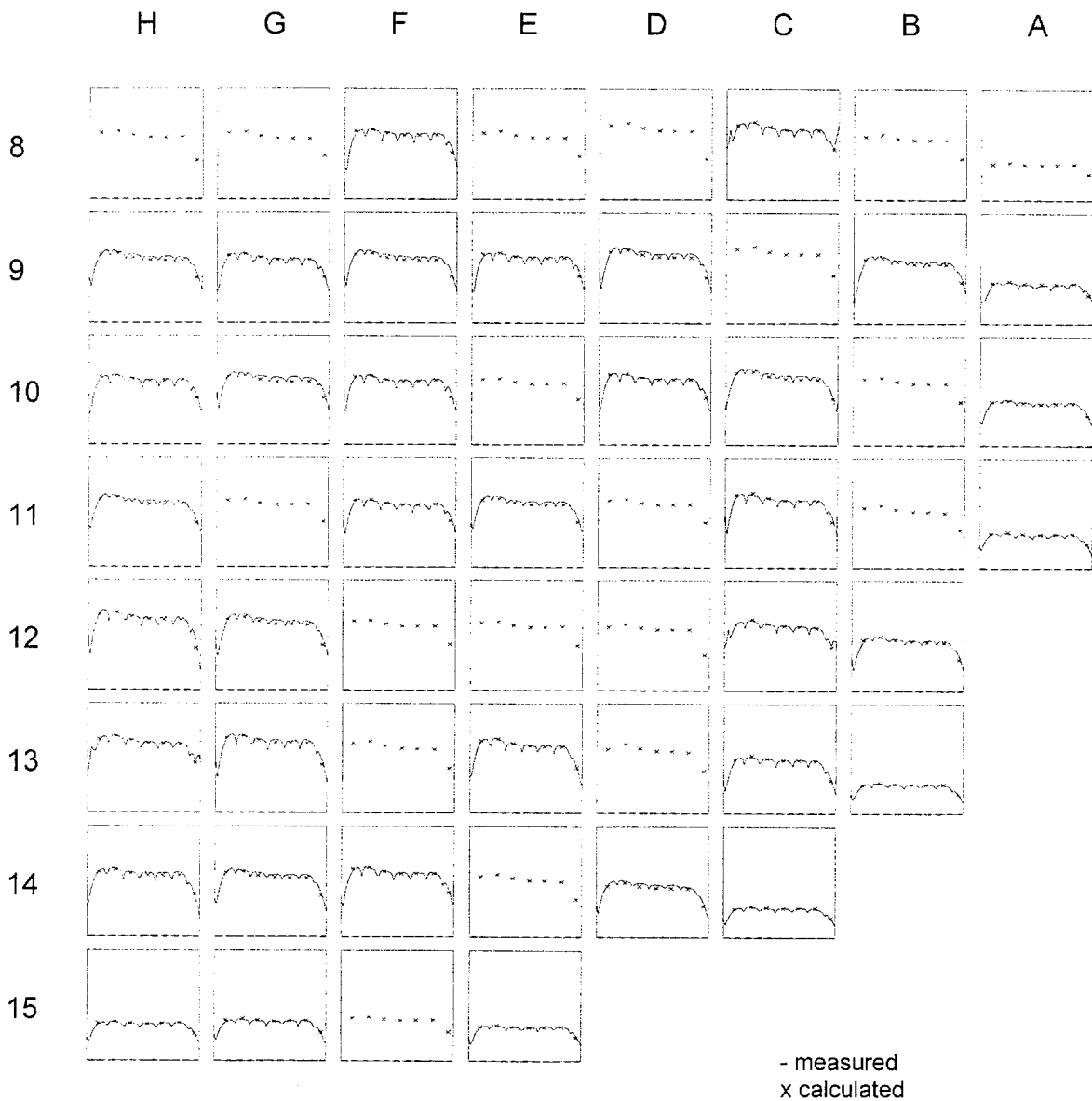
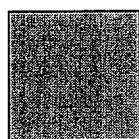
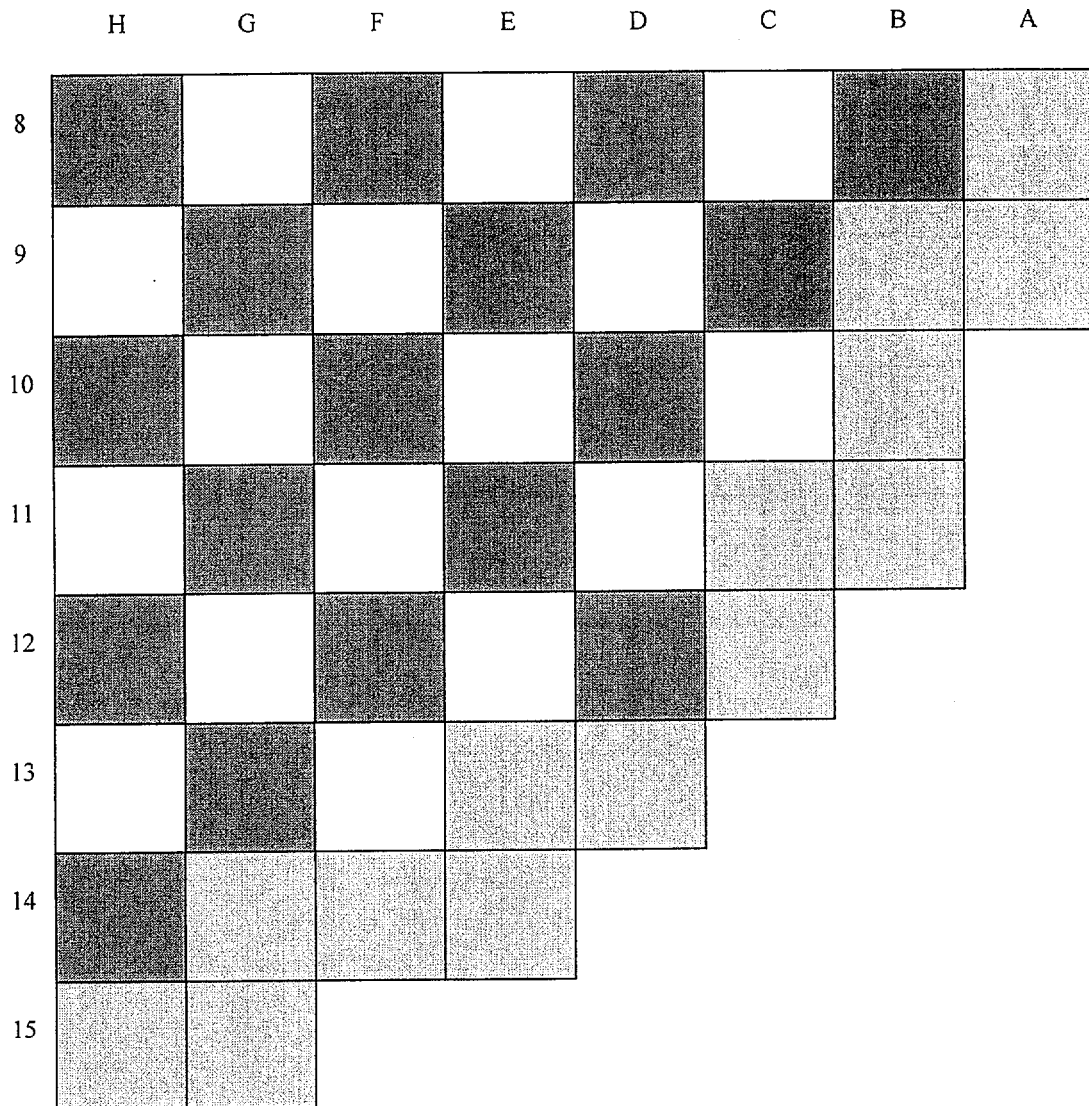
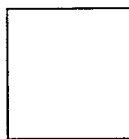


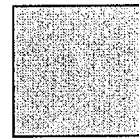
Figure 4-29. Gravelines-5 Cycle 1 Loading Map



Region 1  
1.80 w/o U235



Region 2  
2.40 w/o U235



Region 3  
3.10 w/o U235

Figure 4-30. Gravelines-5 Cycle 1 Poison Loadings

	H	G	F	E	D	C	B	A
8		G 12		G 12		8		
9	G 12		12		8		G 16	
10		12		8		12		
11	G 12		8		12	G 16		
12		8		12				
13	8		12	G 16				
14		G 16						
15								

XX
----

Number of Pyrex Pins

G YY
---------

Number of Gadolinia Rods at 8 w/o GAD

Figure 4-31. Gravelines 5 Cycle 1 25 EFPD

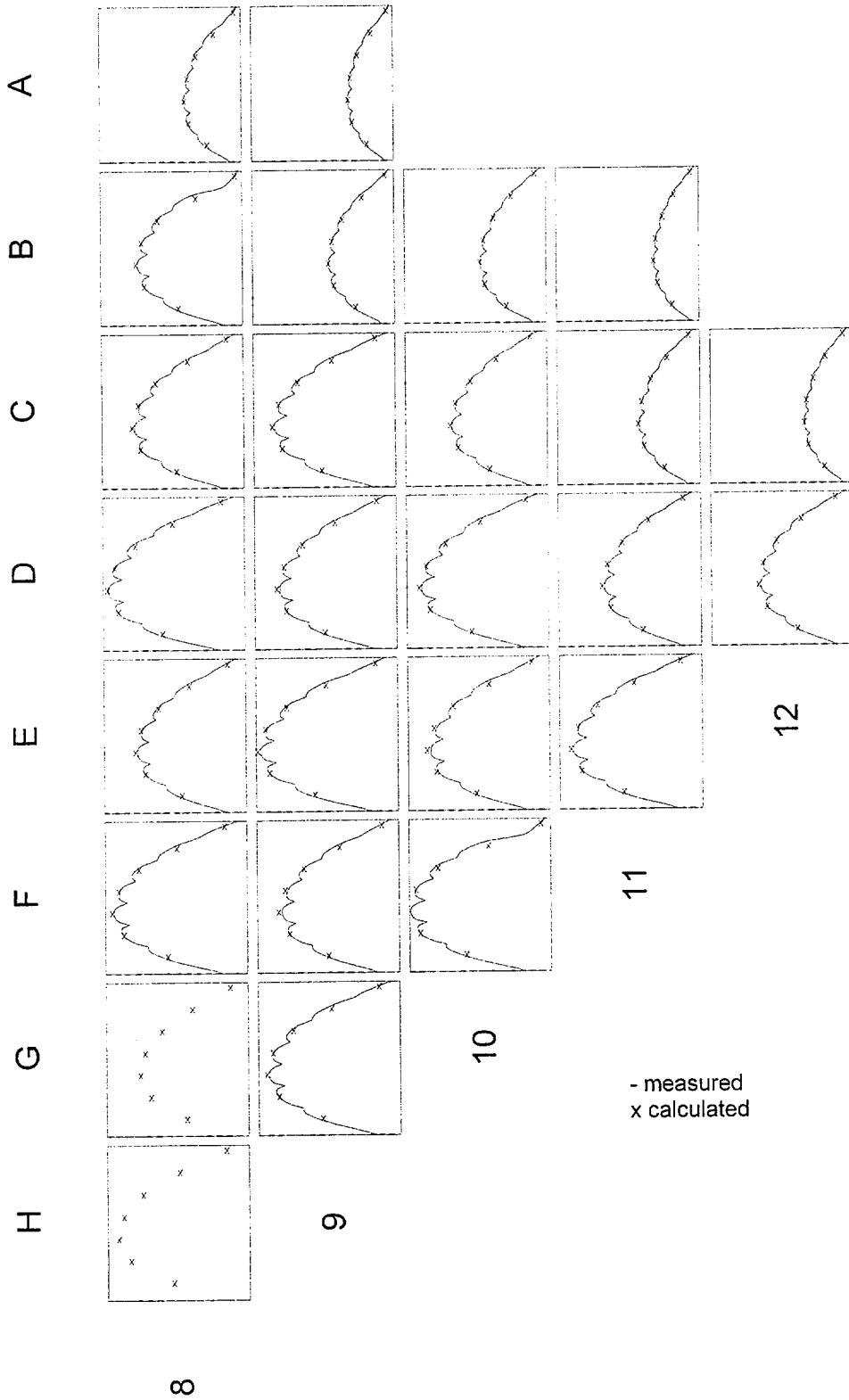


Figure 4-32. Gravelines 5 Cycle 1 90 EFPD

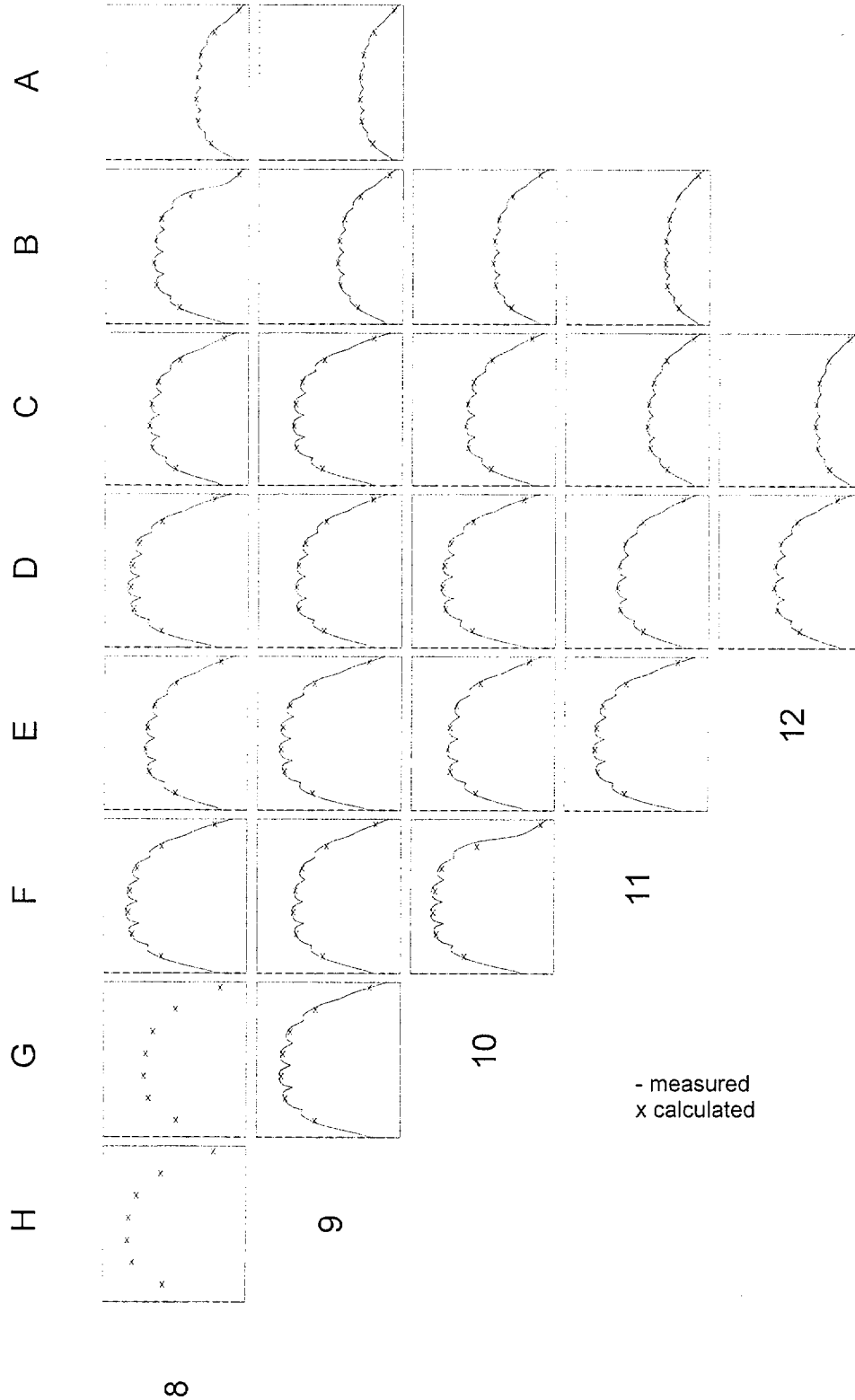


Figure 4-33. Gravelines 5 Cycle 1 153 EFPD

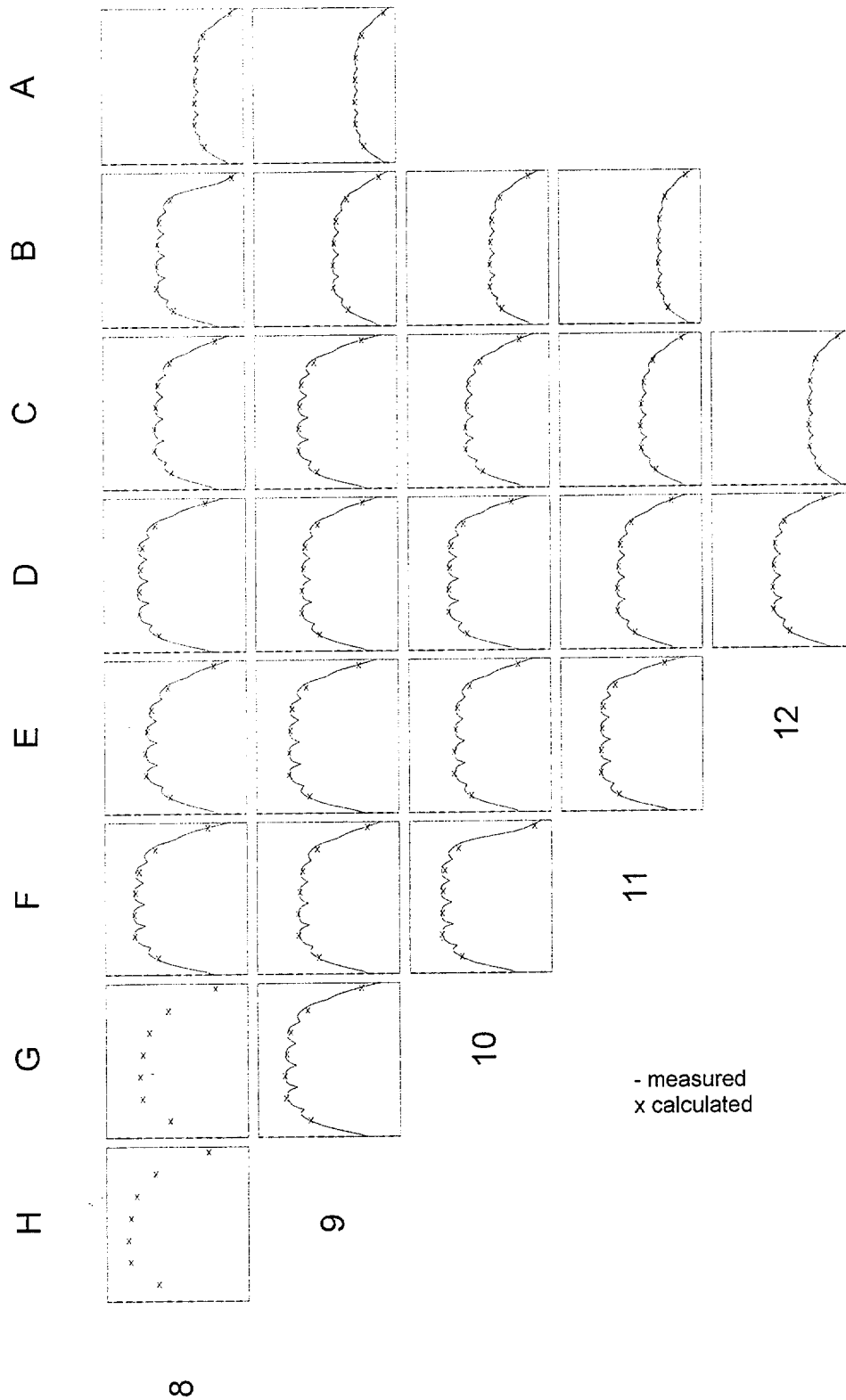


Figure 4-34. Gravelines 5 Cycle 1 183 EFPD

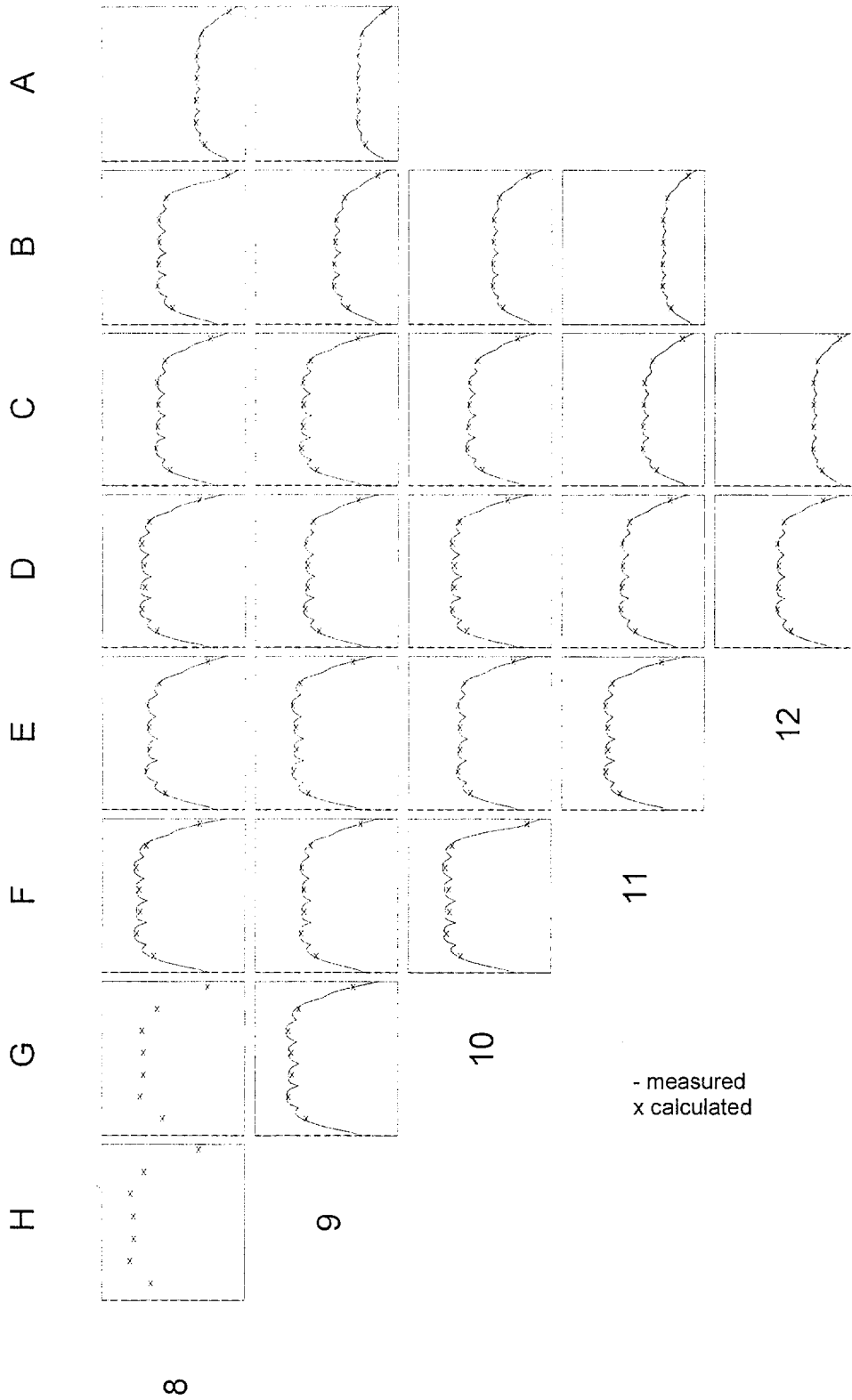


Figure 4-35. Gravelines 5 Cycle 1 207 EFPD

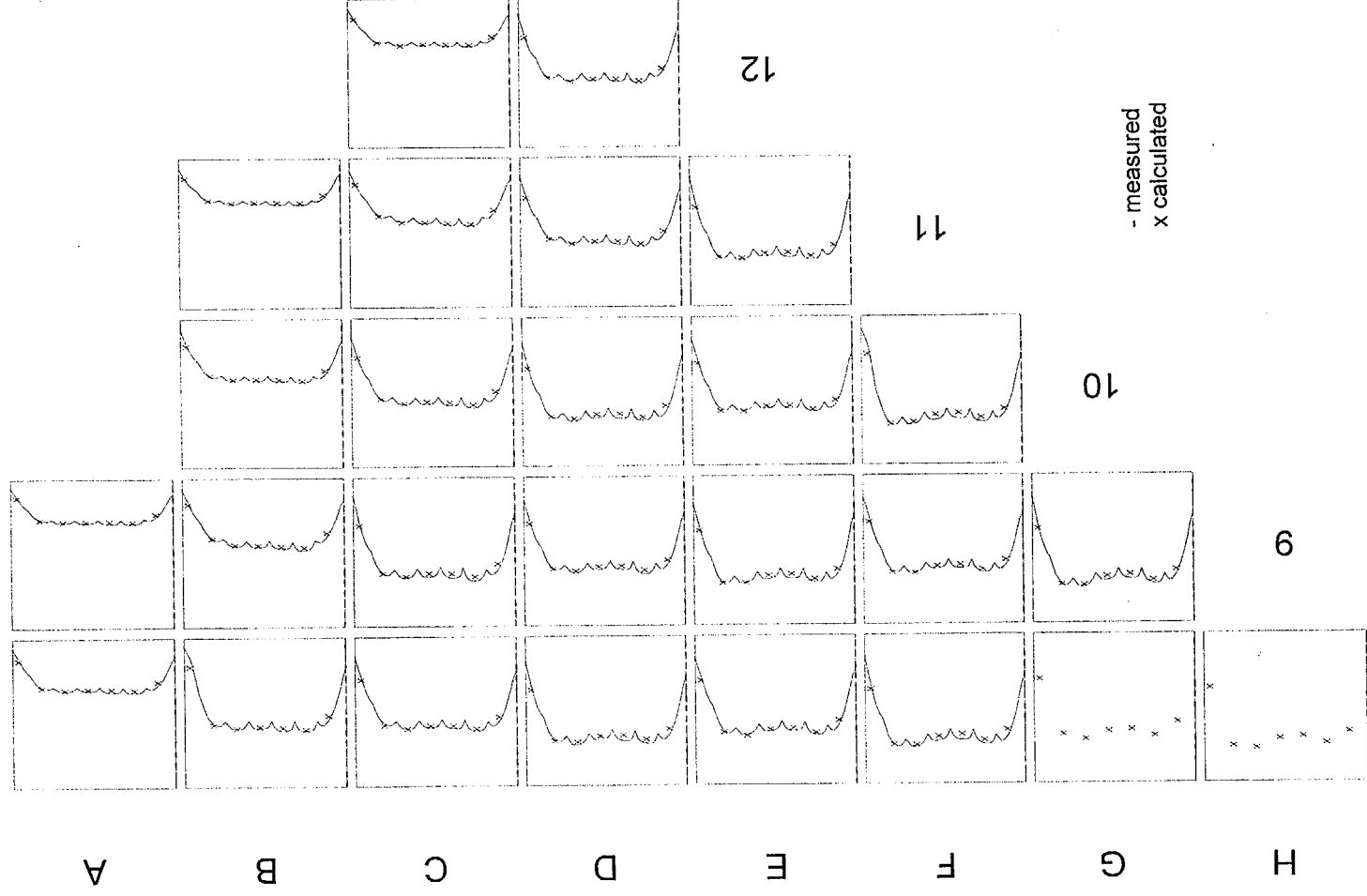


Figure 4-36. Gravelines 5 Cycle 1 240 EFPD

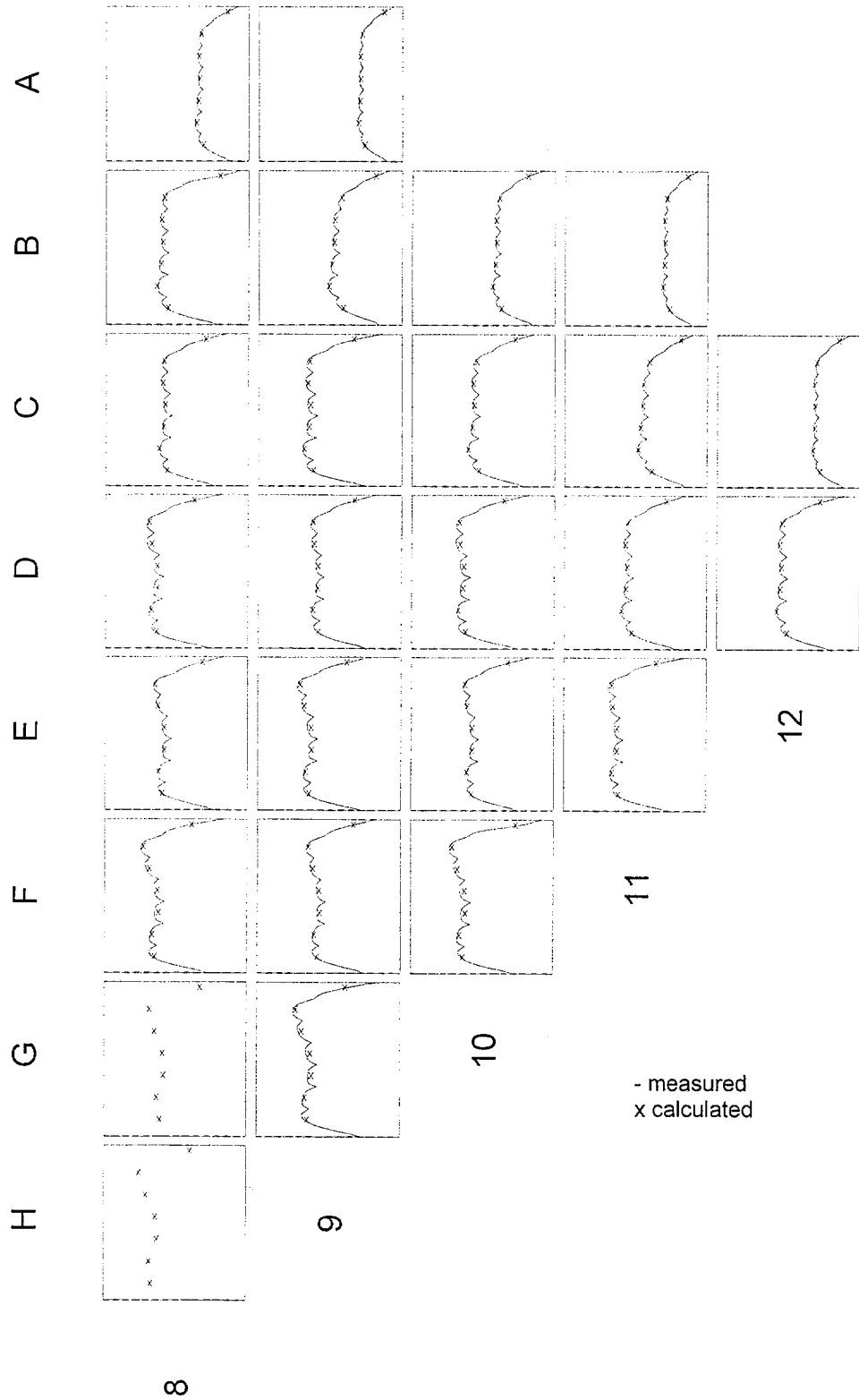


Figure 4-37. Gravelines 5 Cycle 1 315 FRPD

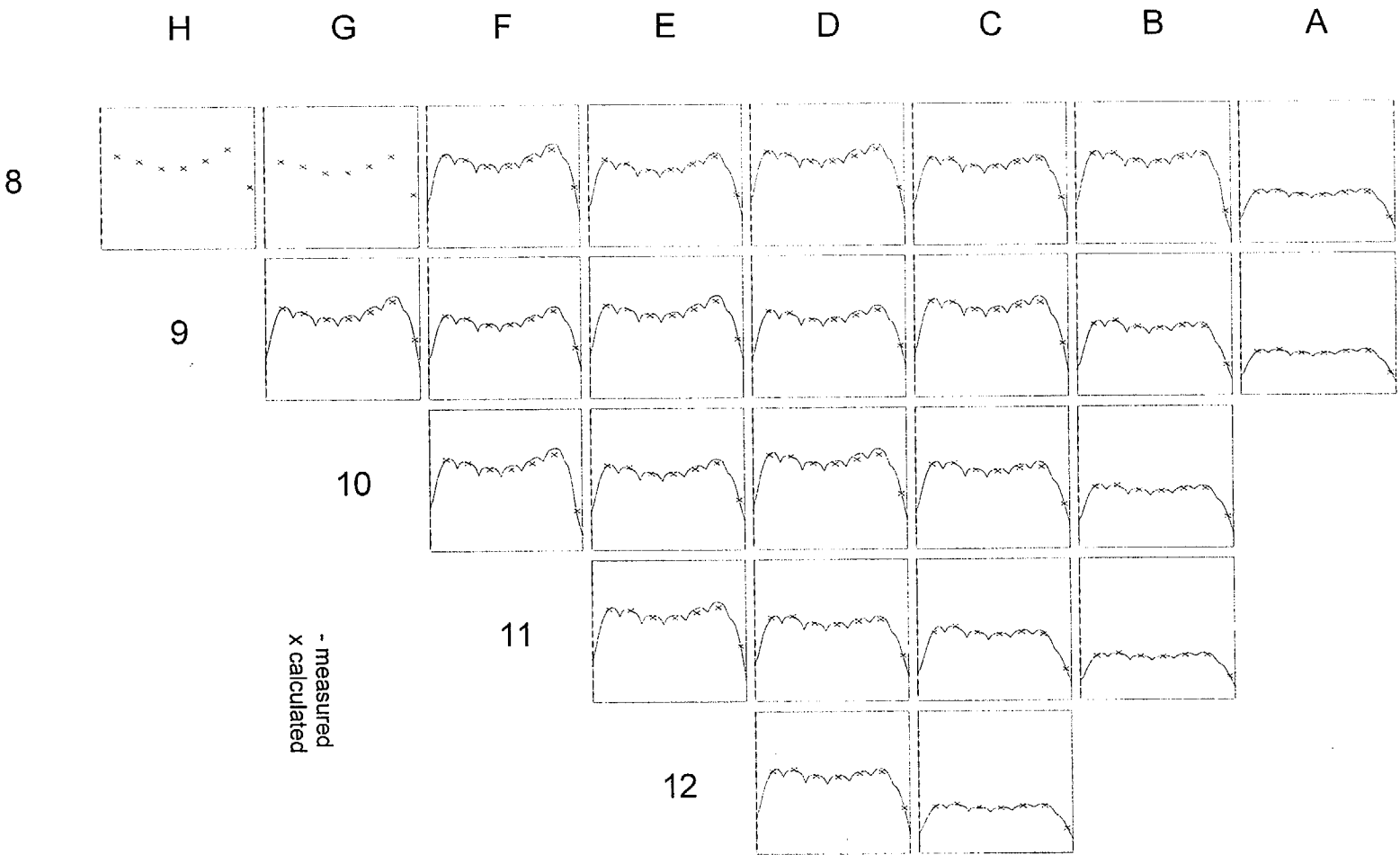


Figure 4-38. OCONEE-1 Cycle 1 Power Transient

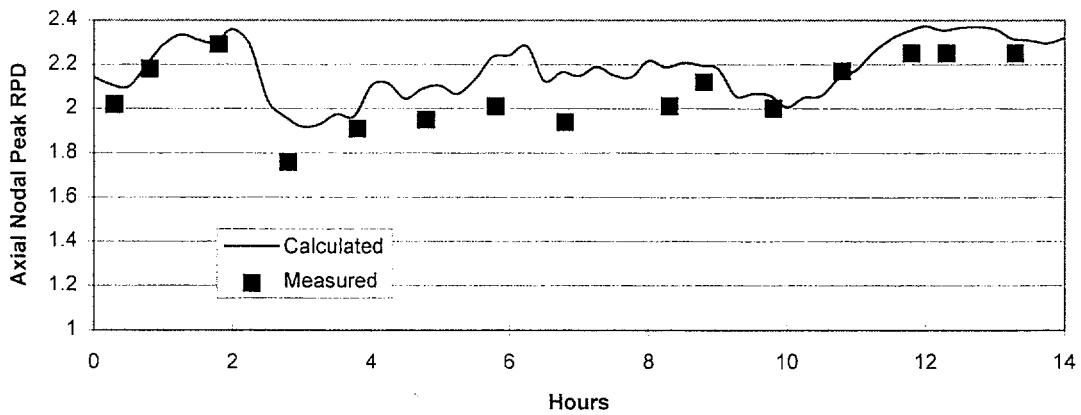
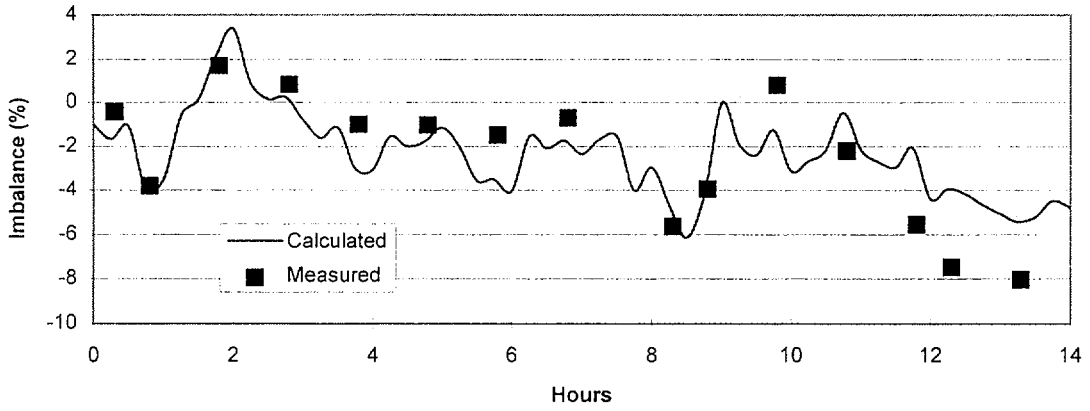
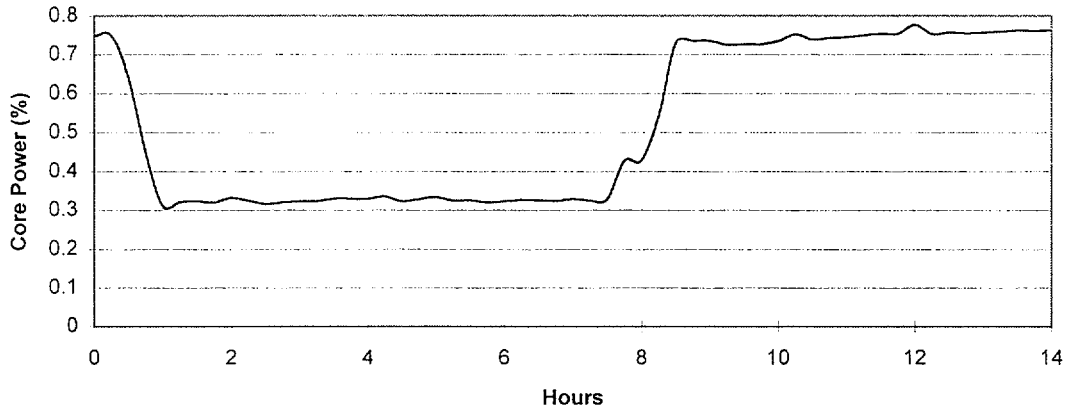
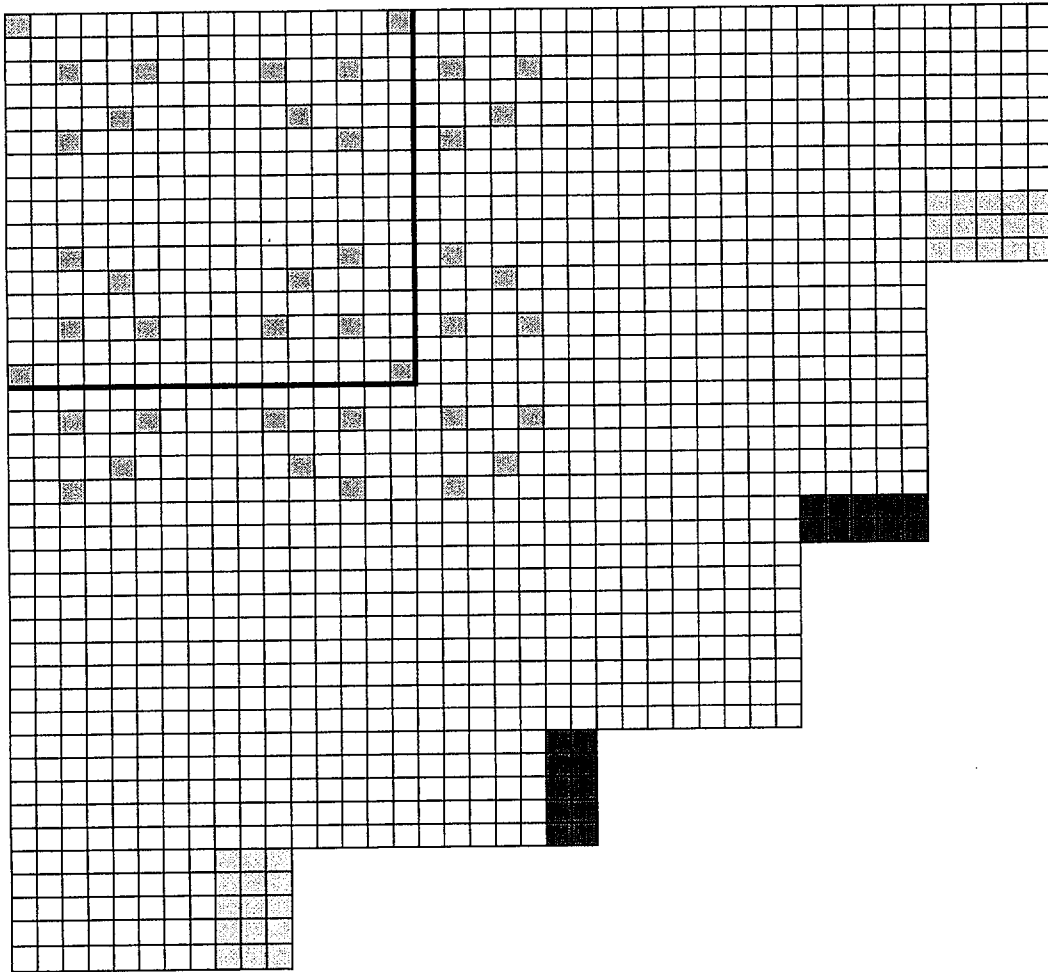


Figure 4-39. SCIENCE Geometric Modeling of the Critical Experiments



- fuel region in experiment, but not in SCIENCE model



- fuel region not in experiment but included in SCIENCE model



- boundary from inner enrichment zone to outer enrichment zone



- position of water holes and/or perturbing pins



- fuel pin

**Figure 4-40. Pin Power Distribution Comparison For Core XI Loading 2**

[b,c,d,e]

**Figure 4-41. Pin Power Distribution Comparison For Core XI Loading 4**

[b,c,d,e]

**Figure 4-42. Pin Power Distribution Comparison For Core XI Loading 5**

[b,c,d,e]

**Figure 4-43. Pin Power Distribution Comparison For Core XI Loading 6**

[b,c,d,e]

**Figure 4-44. Pin Power Distribution Comparison For Core XI Loading 7**

[b,c,d,e]

**Figure 4-45. Pin Power Distribution Comparison For Core XI Loading 8**

[b,c,d,e]

**Figure 4-46. Pin Power Distribution Comparison For Core XI Loading 11**

[b,c,d,e]

**Figure 4-47. Pin Power Distribution Comparison For Core 1**

[b,c,d,e]

**Figure 4-48. Pin Power Distribution Comparison For Core 5**

[b,c,d,e]

**Figure 4-49. Pin Power Distribution Comparison For Core 12**

[b,c,d,e]

**Figure 4-50. Pin Power Distribution Comparison For Core 14**

[b,c,d,e]

**Figure 4-51. Pin Power Distribution Comparison For Core 18**

[b,c,d,e]

**Figure 4-52. Pin Power Distribution Comparison For Core 20**

[b,c,d,e]

**Figure 4-53. Set 6 - Relative % Differences for Multi-Assembly at 0 GWD/MtU**

[b,c,d,e]

**Figure 4-54. Set 6 - Relative % Differences for Multi-Assembly at 24 GWD/MtU**

[b,c,d,e]

**Figure 4-55. Set 12 - Relative % Differences for Multi-Assembly at 0 GWD/MtU**

[b,c,d,e]

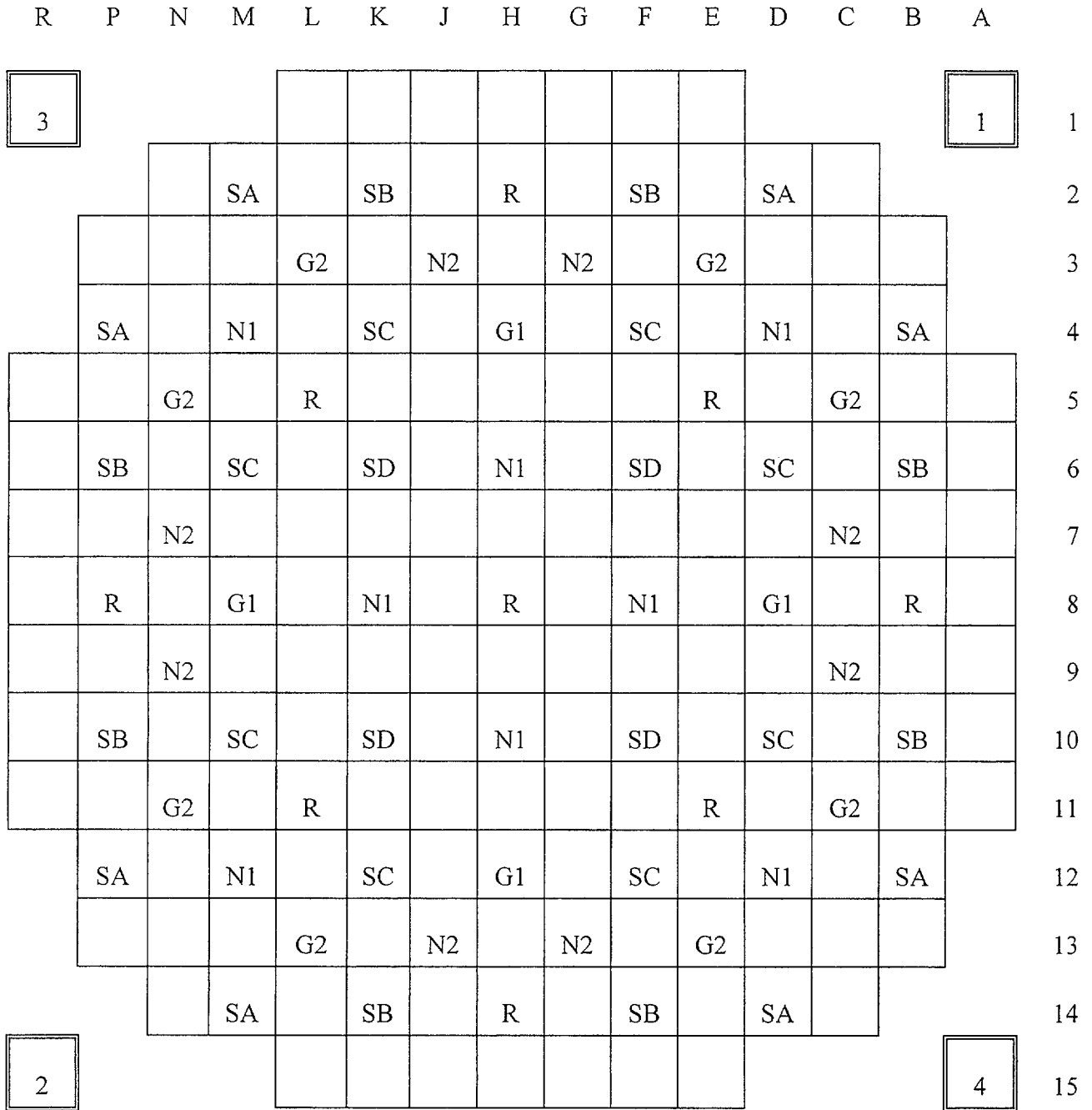
**Figure 4-56. Set 12 - Relative % Differences for Multi-Assembly at 8 GWD/MtU**

[b,c,d,e]

**Figure 4-57. Set 12 - Relative % Differences for Multi-Assembly at 34 GWD/MtU**

[b,c,d,e]

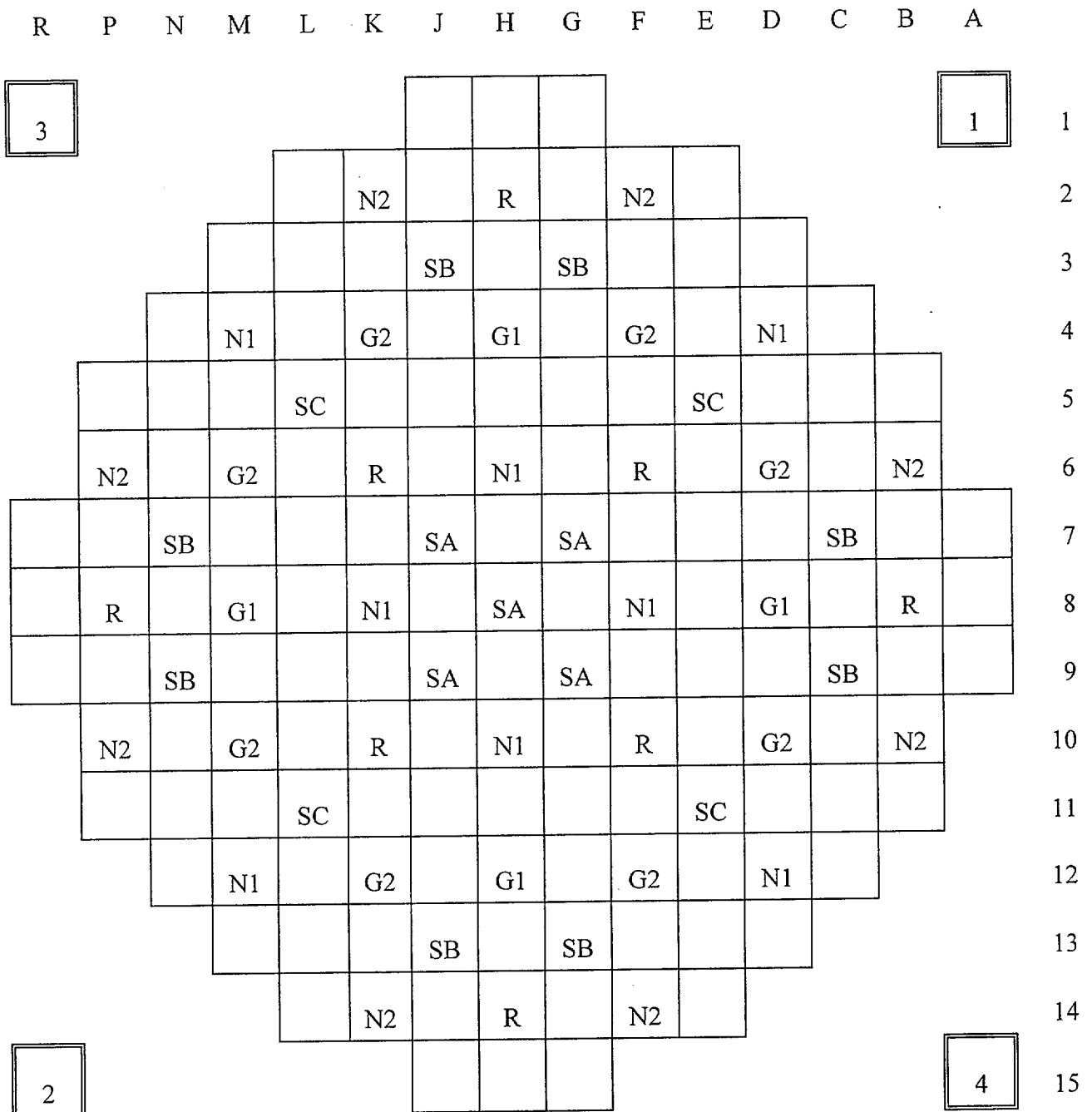
Figure 4-58. 193 Core Layout for Dropped Rod Test



# Excore Detector

ID Rodded Location

Figure 4-59. 157 Core Layout for Dropped Rod Test



#

Excure Detector

ID

Rodded Location

Figure 4-60. Case 1 Rod Drop Simulation

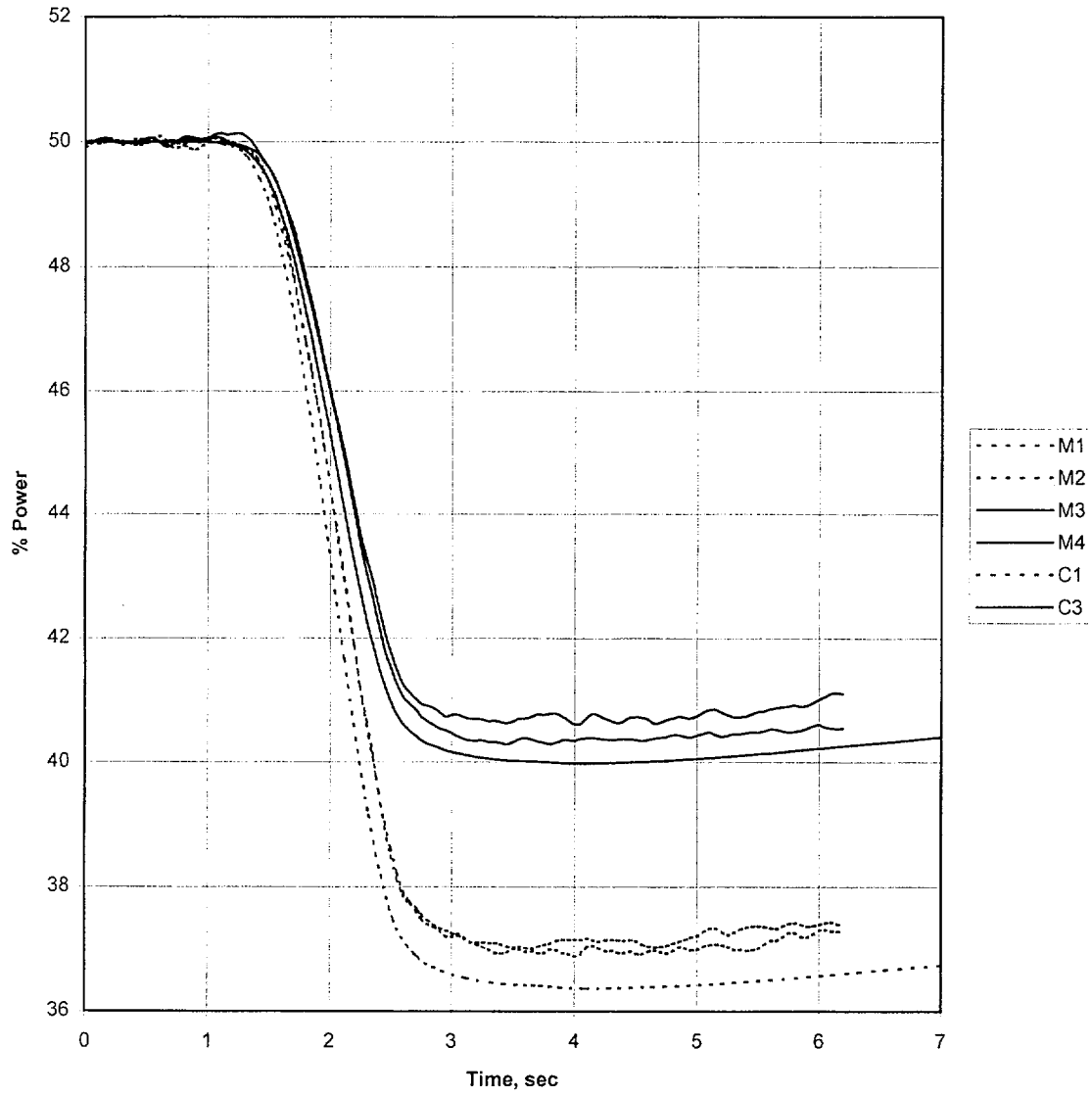


Figure 4-61. Case 2 Rod Drop Simulation

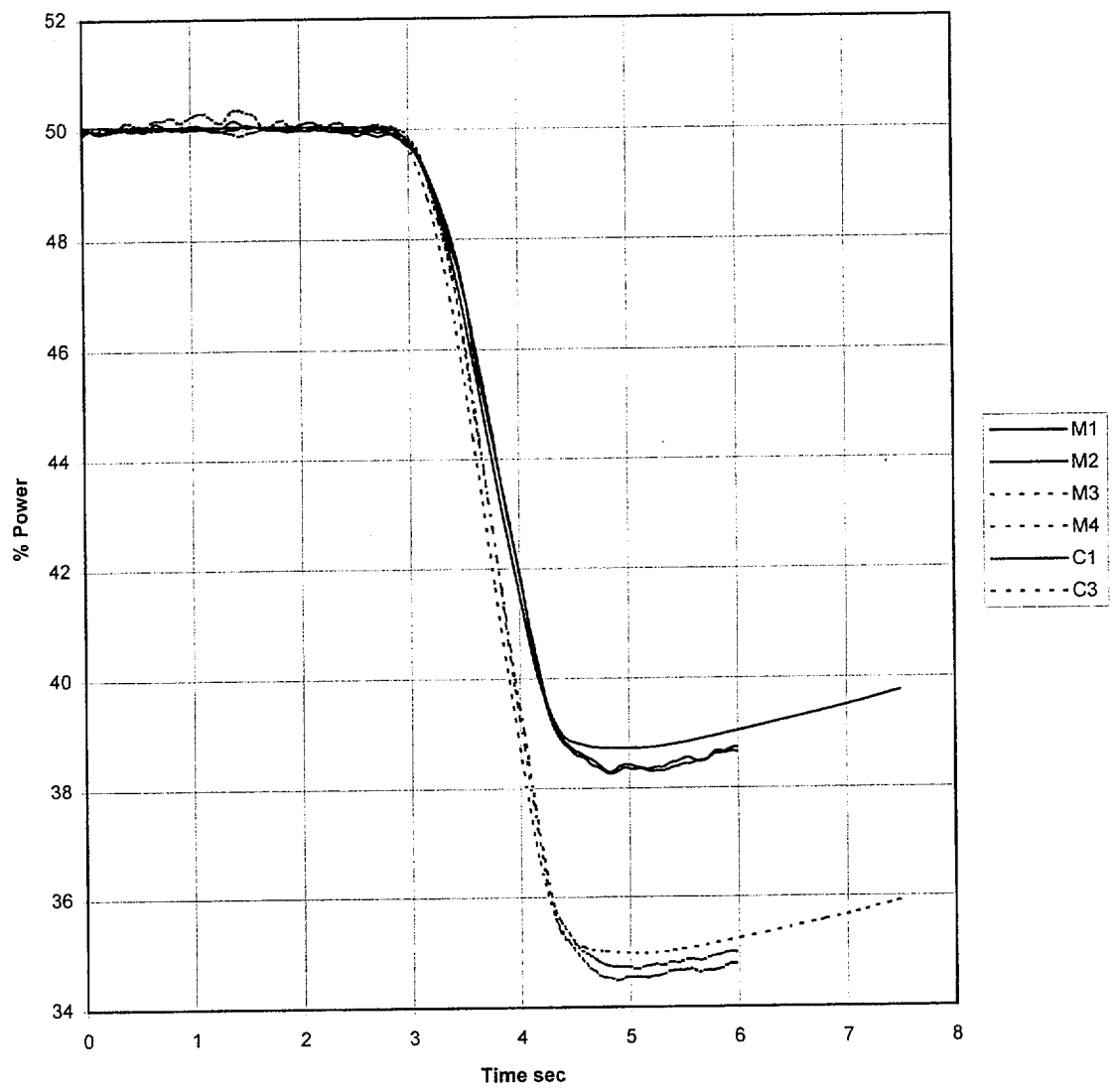


Figure 4-62. Case 3 Rod Drop Simulation

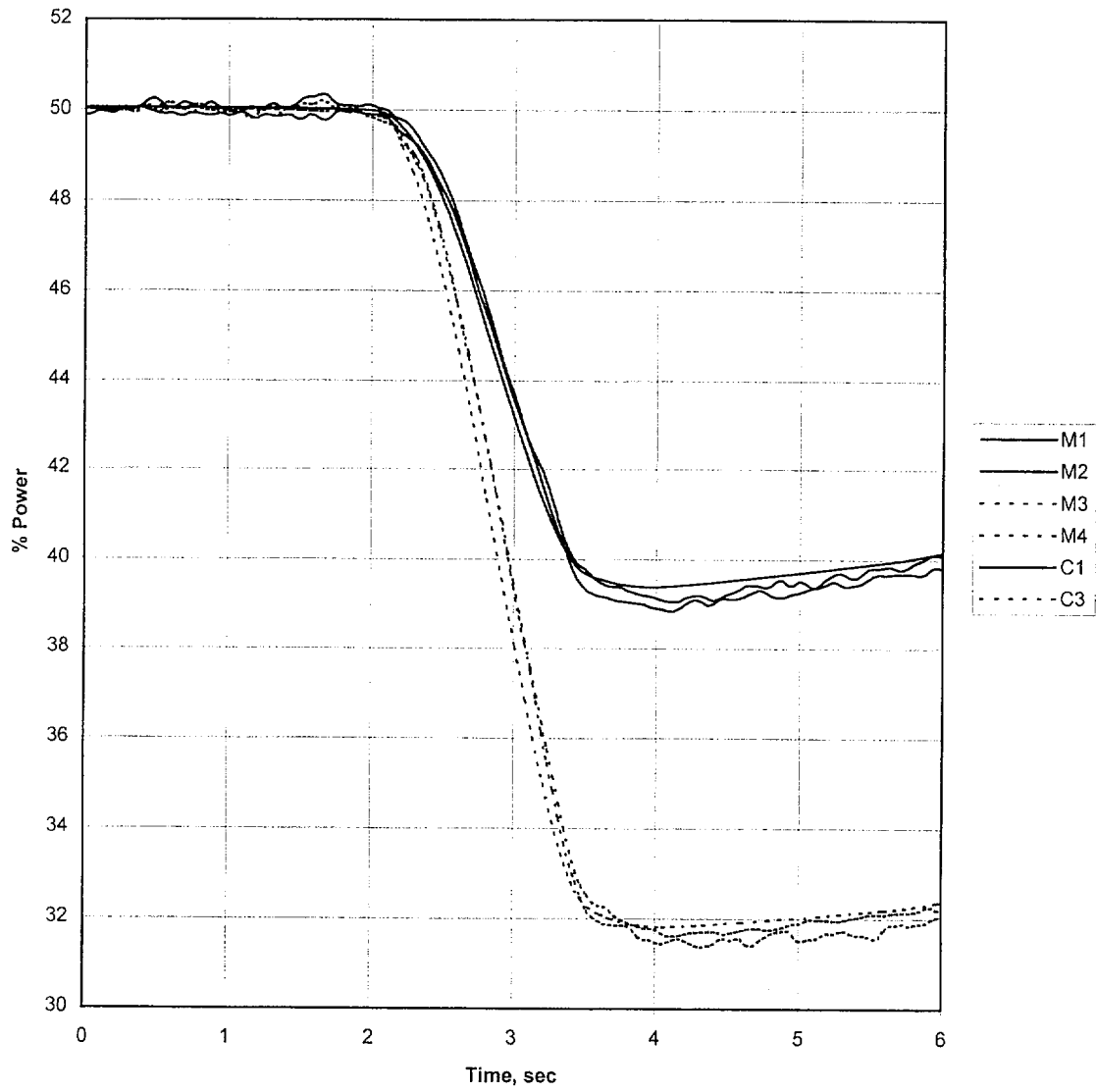


Figure 4-63. Case 4 Rod Drop Simulation

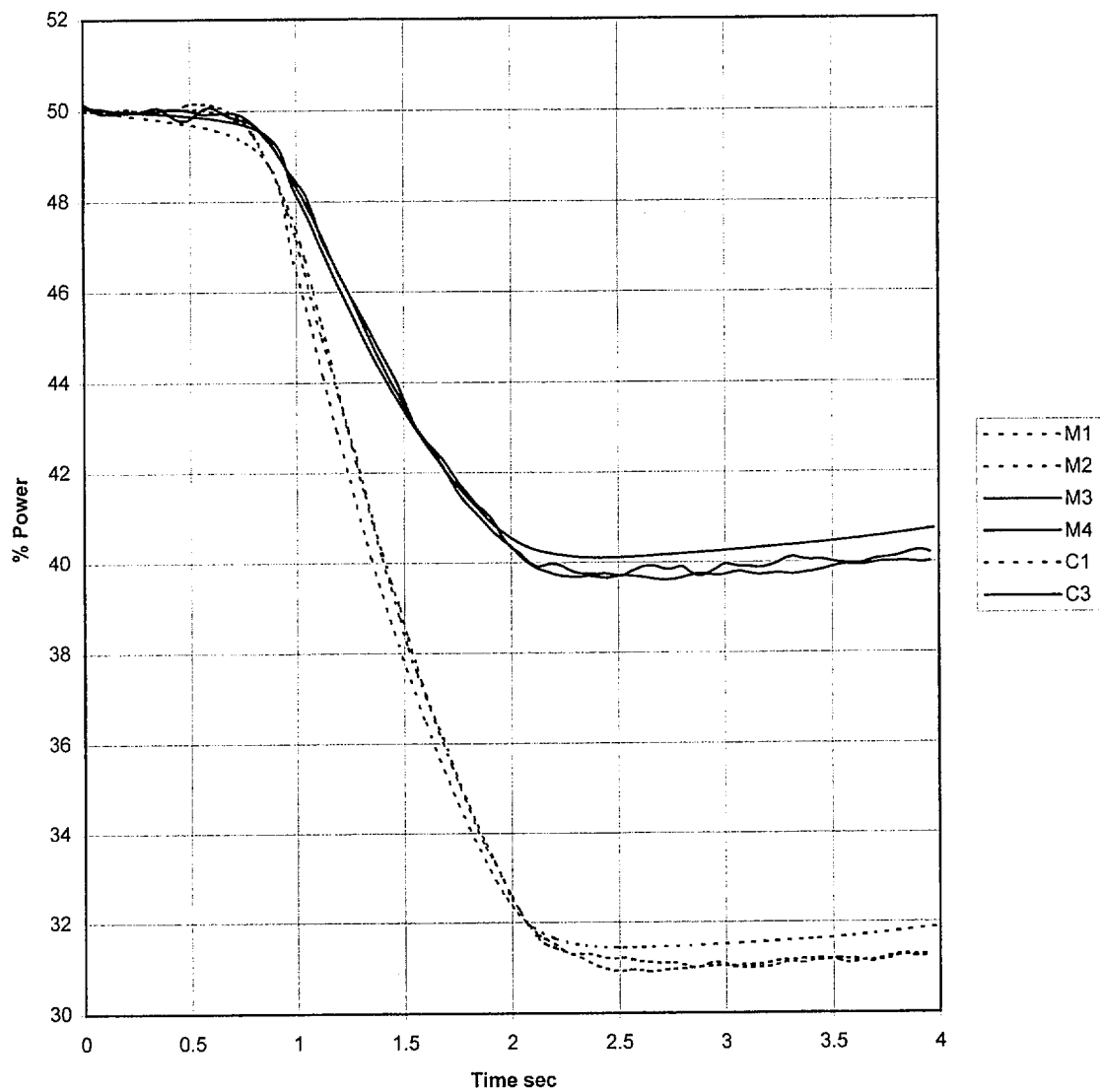


Figure 4-64. Case 5 Rod Drop Simulation

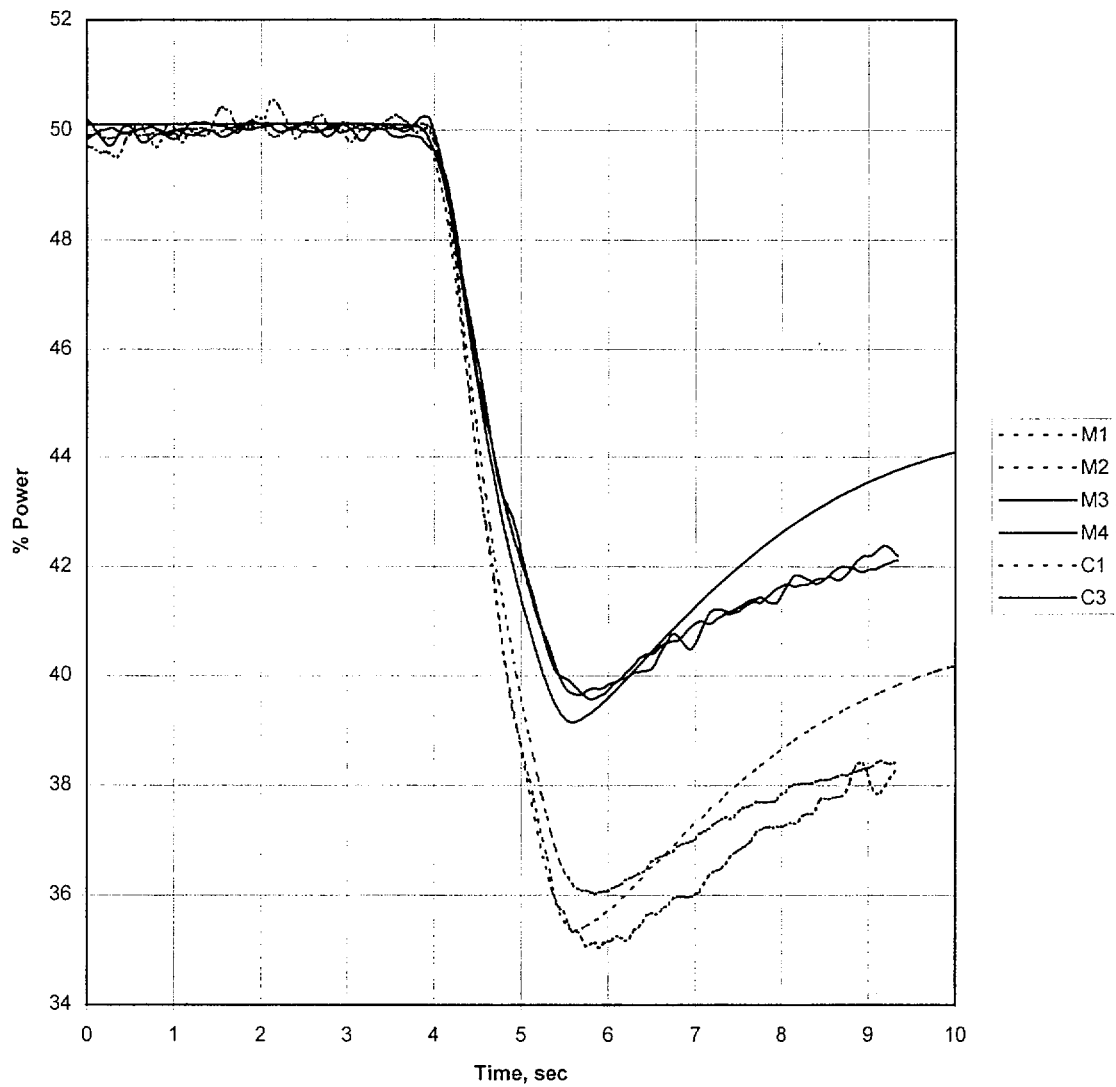


Figure 4-65. Case 6 Rod Drop Simulation

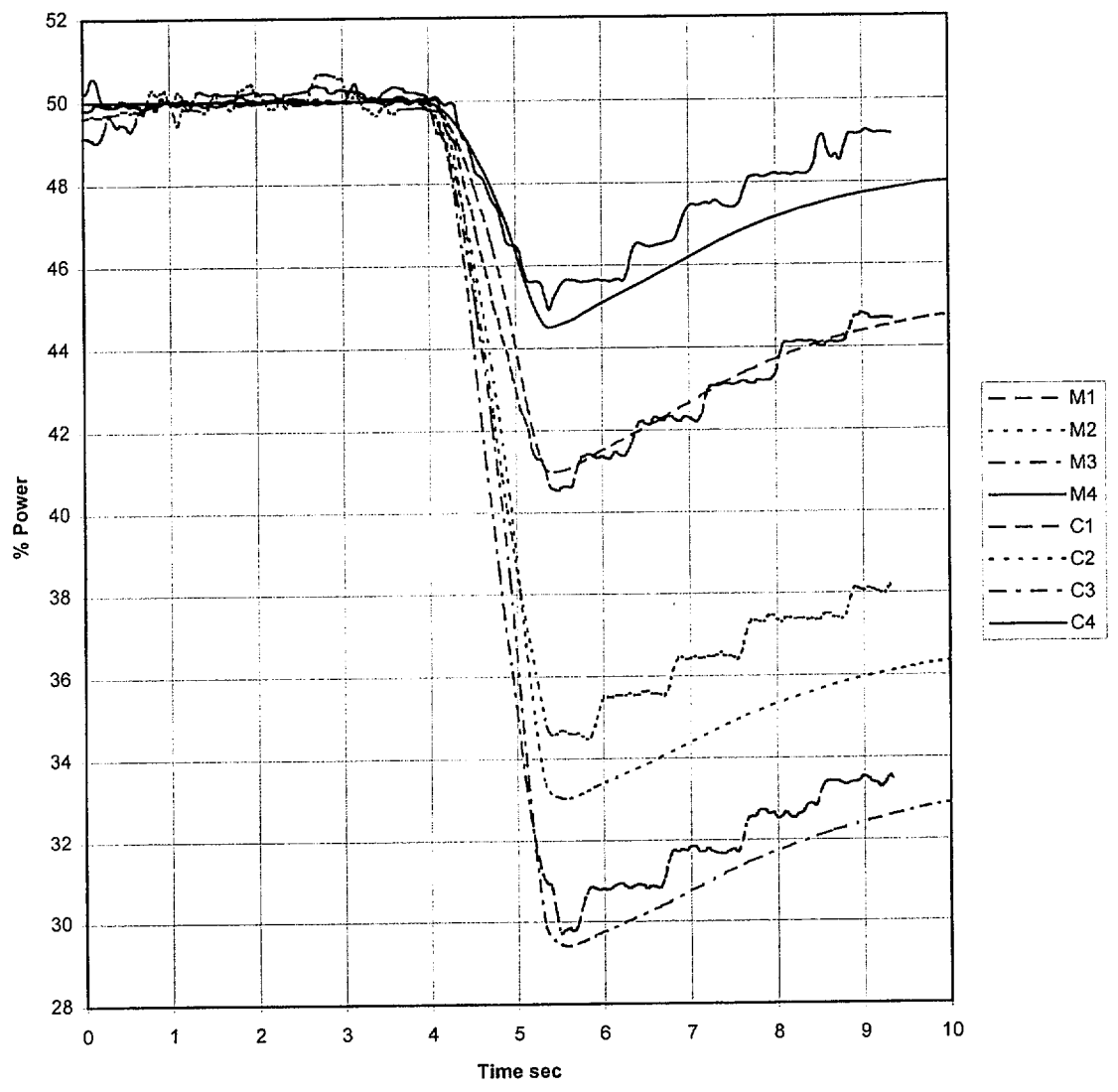


Figure 4-66. Frequency Distribution for Radial Pin Power Data

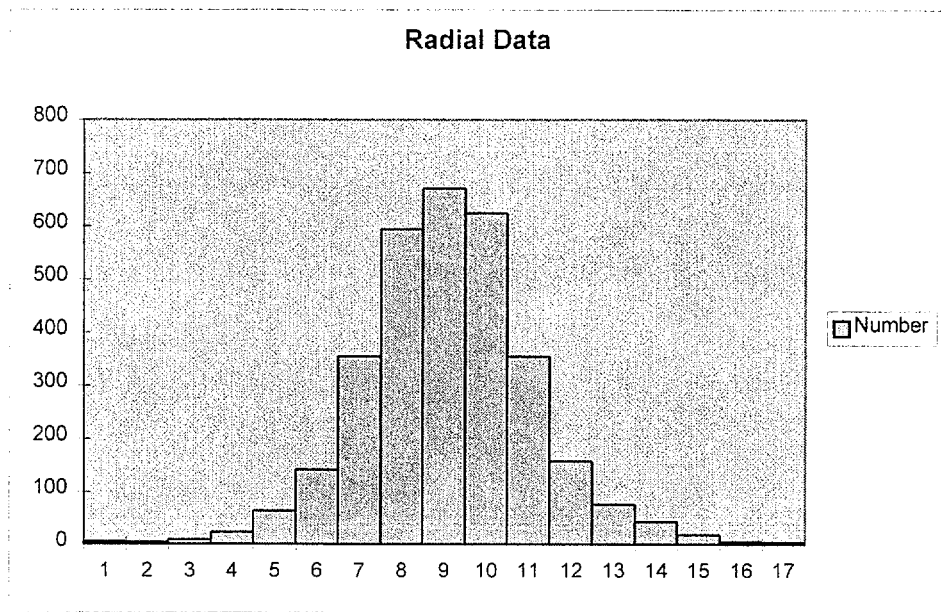


Figure 4-67. Frequency Distribution for Peak Pellet Power Data

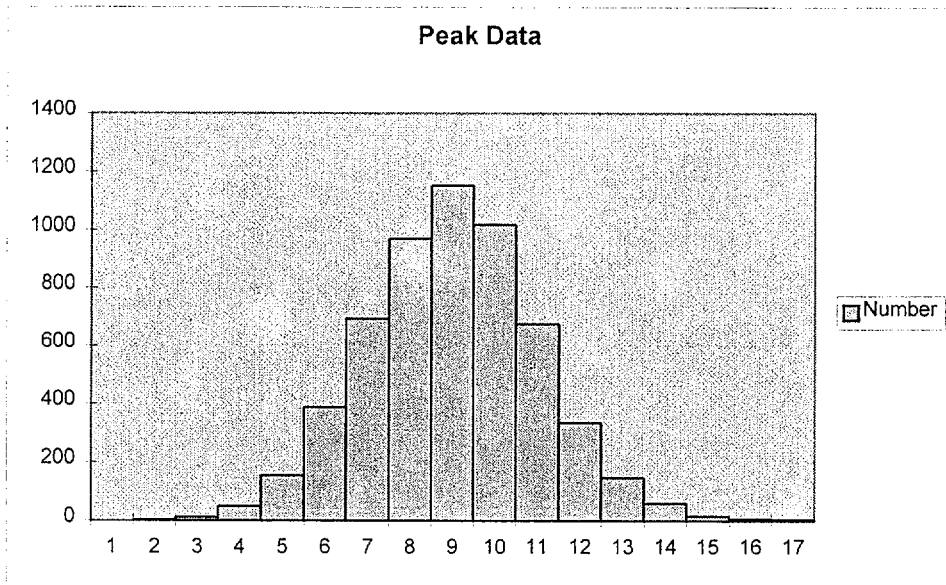


Figure 4-68. Frequency Distribution for Critical Experiments

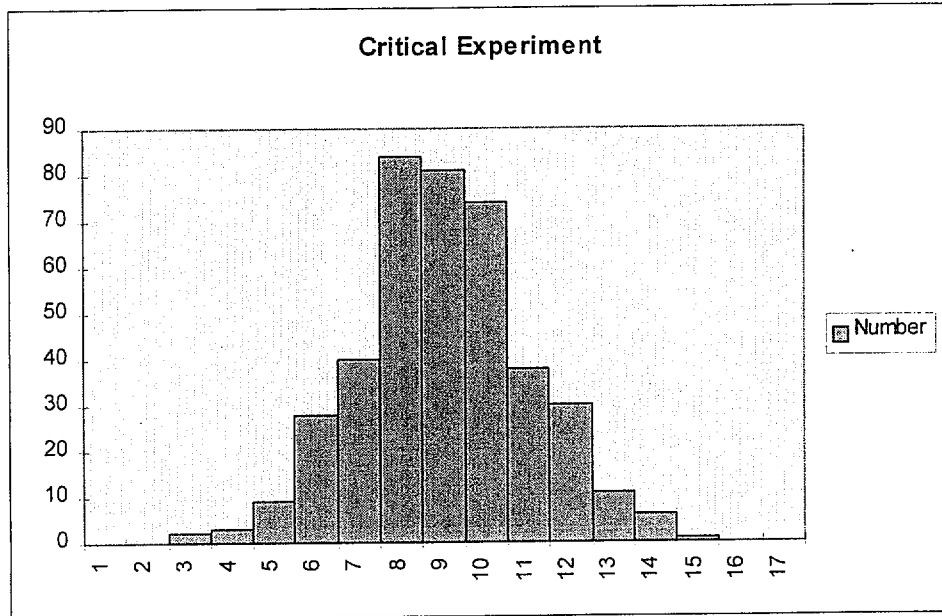
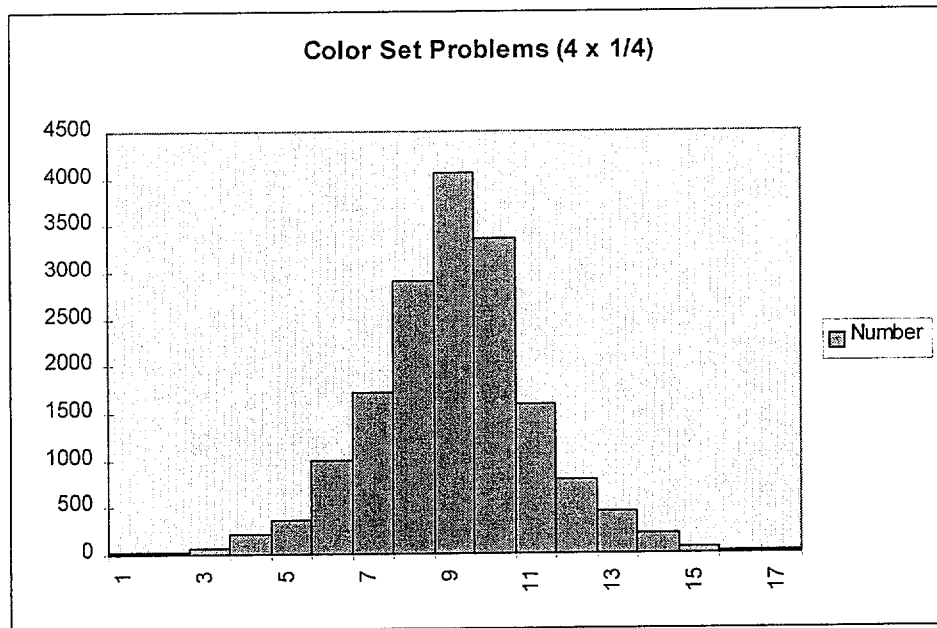


Figure 4-69. Frequency Distribution for Multi-Assembly Problems



## 5. QUALIFICATION METHOD

The purpose of this section is to provide the method that FCF will use to implement future changes to the SCIENCE methodology. The data in the previous section provided a qualification basis for the current SCIENCE code package. Future modifications to the equations, algorithms, and methods in the SCIENCE package can be used in licensing applications as long as certain criteria are met. This section provides the methods qualification criteria and range of applicability of the benchmarks.

### 5.1 Methods Qualification Criteria

In the past, neutronics methods have generally been acceptable if the results from the methodology changes were similar to or better than previous results. This is indeed still our goal in methods development. However, at this time the method accuracy is approaching the measurement accuracy and improvements in the methods will not necessarily guarantee more accurate results for every parameter every time a new feature is implemented. Therefore, a list of methods qualification criteria that must be met by the results of future changes to the methods has been defined and is discussed in this section. Supporting documentation will be submitted to the NRC whenever the method change affects the uncertainties to be applied in licensing applications.

The method to be used to qualify SCIENCE for future changes is similar to the method presented in this and previous topical submittals. The neutronic code qualification is based on the ability of the code to predict several key neutronic parameters. The parameters are critical boron or critical K-effective at HZP, critical boron or critical K-effective at HFP, individual bank rod worths, total rod worths, ejected rod worths, isothermal temperature coefficients, power Doppler coefficients, hot pin power, and hot pellet power. These parameters will be calculated and compared to measured results and the statistics will be generated. If the results meet the criteria, then the methodology changes can be used for licensing applications. The difference between the method presented in this section and the previously submitted methods is that the criteria are based upon the absolute accuracy expected from the codes as opposed to the relative accuracy to the previous code system.

The methods qualification criteria are listed in Table 5-1. The basis for each criterion is discussed. Many of the criteria are the same as the typical test acceptance criteria provided in reference 21, which are applicable to the cores that FCF licenses. A bounding approach rather than a tolerance/confidence limit is used for critical k-effectives for both HFP and HZP. The approach is that  $\leq 5\%$  of the points are above the +500 pcm criteria and  $\leq 5\%$  of the points are below the -500 pcm criteria. The allowed number of points failing the criteria is the same as a one-sided tolerance/confidence limit for an infinite sample that does not require normality. The impact relative to safety analysis is only a one-sided effect so that 5% on either side is acceptable. This approach is justified because the distribution of

the predicted critical k-effective differences from plant to plant is not necessarily normal or random. The critical k-effective criteria presented above for both the HFP and HZP are reasonable screening criteria based on two observations. The critical K-effective criterion of  $\pm 500$  pcm approximately correlates to the  $\pm 50$  ppm test criterion in reference 21. In addition, the startup procedures at the plants use a review criterion of  $\pm 500$  pcm.

A 95/95 tolerance/confidence limit calculated from the data for the single bank worths should be less than 15% which is the test criterion in units of % for the single bank worth measurements. This value is also supported by reference 21. The current criterion for the total control rod worth is defined as the 10% uncertainty for SCIENCE and is also supported by reference 21.

The number of available measured ejected rod worths is limited so that a reasonable statistical uncertainty is not easily obtained. The presented ejected rod worth data is limited to 2 measured data points. The magnitudes of the measured ejected rod worths are similar to single bank worths and will have similar measurement uncertainties. Therefore, the single bank worth test acceptance criteria which is  $\pm 15\%$  or  $\pm 100$  pcm whichever is larger is the methods qualification criterion and each of the predictions of the ejected rod worth must be within this criterion.

A 95/95 tolerance/confidence limit calculated from the data for the isothermal temperature coefficient should be less than 2 pcm/ $^{\circ}$ F which is the test criterion for the isothermal temperature coefficient measurements in reference 21.

Because the number of available Doppler power or fuel temperature coefficients is limited and the measurement uncertainty can be large, two approaches are used. First, a bounding approach is used so that each of the power Doppler coefficient calculations should be within  $\pm 2.0$  pcm/%power of the measurement. To ensure that the overall power defect is adequate, another approach is included. The absolute value of the difference of the means for the HZP and HFP critical K-effectives should be less than 200 pcm. This criterion confirms that the overall average power defect error is less than 200 pcm.

The criteria for maximum pin and pellet power peaking are the current uncertainties, which are 3.8 % and 4.8%, respectively. Where the above criteria are defined as uncertainty factors, a one sided 95/95 tolerance/confidence limit will be calculated with the method already discussed in section 4.4.

Therefore, results from a method change that meet the listed criteria in Table 5-1 validate the method change. In the case of method changes that meet the criteria, FCF will internally document the changes of the methods and the results. In this case, no notification will be sent to the NRC since there is no change to the uncertainties and their application. For example, if FCF changes the SMART calculations [ b,c,d,e ] or the APOLLO2[ b,c,d,e ] is changed, FCF intends to show that these changes meet the acceptance criteria and document internally only. The current SCIENCE

results are presented as an example of a comparison of the qualification method criteria in Table 5-2. In Table 5-2 the SCIENCE results meet all the criteria.

In the case where a lower uncertainty is calculated and FCF intends to use the lower uncertainty, FCF will provide a submittal to the NRC containing the description of the methods responsible for the improved results, the results of the new methods that support the new uncertainty, and how FCF intends to use the uncertainty. The resulting new uncertainty will then become the new criterion. For example, after enough data are accumulated, FCF will submit the results for total rod worth predictions that validate the reduced total rod worth uncertainties in references 13 and 14. Once this submittal is reviewed, these uncertainties become the method qualification criteria for the next method change.

## **5.2 Range of Applicability of Benchmarks**

The chosen benchmarks in this topical include the types of fuel and poison to be licensed. For example, FCF fuel can contain uranium, uranium with other isotopics from burnup, water holes, soluble boron, boron poisons (B4C, WABA, and Pyrex burnable poisons), AgInCd control rods, and/or uranium fuel containing Gadolinia. The benchmarks in this topical are sufficient to qualify the code for types of fuel that contain these materials. It also includes IFBA and structural materials such as SS and INCONEL. If a new fuel design contains poisons or fuel outside this collection of benchmarks, new benchmarks will be added. For example, if a new fuel design is beyond existing bounds of the analysis such as MOX fuel and/or Hafnium control rods, additional benchmarks will be performed. A submittal will be sent to the NRC which includes the new design feature, a description of the new benchmarks, and any impact on the current uncertainty factors.

FCF will continue to monitor its methods with respect to current cycle designs with its core follow studies. Core follow studies will also be performed to confirm applicability of FCF's neutronic methods prior to licensing any new plants that FCF does not currently license. Additionally, newly acquired data from operating plants will be added to this data base as appropriate to ensure that the results of the methods keep pace with the features of the currently designed cores.

Table 5-1. Methods Qualification Criteria

Parameter (% relative difference or difference between predicted and measured values)	Criteria	Criteria Definition
HFP Critical K-Effective	5%	The number of data above +500 pcm should be less than or equal to the criterion. The number of data below -500 pcm should be less than or equal to the criterion.
HZP Critical K-Effective	5%	The number of data above +500 pcm should be less than or equal to the criterion. The number of data below -500 pcm should be less than or equal to the criterion.
Single Bank Worths, %	15%	95/95 tolerance confidence limit should be less than criterion
Total Bank Worths, %	10.0%	95/95 tolerance confidence limit should be less than criterion
Ejected Rod	15% or 100 pcm	The absolute value of each datum should be less than one or the other criterion
HZP Isothermal Temperature Coefficient, pcm/°F	2.0	95/95 tolerance confidence limit should be less than criterion
Power Doppler Coefficient, pcm/%power	2.0	The absolute value of each datum should be less than the criterion.
Average K-effective difference between HZP to HFP	200 pcm	The absolute value of the difference of the means for the HZP and HFP critical K-effectives should be less than the criterion.
Peak pin,	3.8%	95/95 tolerance confidence limit should be less than criterion
Peak Pellet	4.8%	95/95 tolerance confidence limit should be less than criterion

Table 5-2. SCIENCE Compared to Statistical Criteria

Parameter (% relative difference or difference between predicted and measured values)	Criteria	SCIENCE	Acceptable
HFP Critical K-Effective	≤5%	[b,c,d,e]	yes
HFP Critical K-Effective	≤5%		yes
HZP Critical K-Effective	≤5%		yes
Single Bank Worths, %	<15%		yes
Total Bank Worths, %	<10.0%		yes
Ejected Rod	<15% or 100 pcm		yes
HZP Isothermal Temperature Coefficient, pcm/°F	<2.0		yes
Power Doppler Coefficient, pcm/%power	<2.0		yes
Average K-effective difference between HZP to HFP	<200 pcm		yes
Peak pin	<3.8%		yes
Peak Pellet	<4.8%		yes

## 6. REFERENCES

- 1 G. H. Hobson et al, "NEMO—Nodal Expansion Method Optimized," BAW-10180-A, Rev. 1, B&W Fuel company, Lynchburg, Virginia, March 1993.
- 2 R. SANCHEZ, J. MONDOT, Z. STANKOWSKI, A. COSSIC, I. ZMIJAREVIC, "APOLLO2: A User-oriented, Portable Modular Code for Multigroup Transport Assembly calculations," International Topical Meeting on advances in Reactor Physics, Mathematics and Computation, Paris, 27-30 April 1987.
- 3 R. SANCHEZ, M. VERGAIN, "An Acceleration Procedure for the Iterative Solution of the Flux-Current Equations in the APOLLO2 Code," International conference on the physics of reactors: operation and design computation, Marseilles, PHYSOR 90, 23-27 April 1990.
- 4 S. Nakamura, Computational Methods in Engineering and Science, J. Wiley & Sons, 1977.
- 5 D.G. Luenberger, Introduction to Linear and Nonlinear Programming, Addison Wesley, 1973.
- 6 K. KOEBKE, "Advances in homogenization and dehomogenization," Proceedings of ANS/ENS International Topical Meeting, Munich (1981), Volume 2, p. 59.
- 7 K.R. REMPE, K.S. SMITH, A.F. HENRY, "SIMULATE-3 Pin-Power Reconstruction: Methodology and benchmarking," Proc. Intl. Reactor Physics Conference, Volume III, p. 19, Jackson Hole, Wyoming, 1988.
- 8 J.G. COLLIER, "Convective Boiling And Condensation," McGraw-Hill, 1972.
- 9 R.W. BOWRING, "Physical model based on bubble detachment and calculation of steam in the subcooled region of a heated channel," OECD Halden Reactor Project, Report HPR-10, 1962.
- 10 S. LEVY, "Forced convection subcooled boiling - Prediction of vapor volumetric fraction," International Journal of Heat and Mass Transfer, Volume 10, pp. 951-965, 1967.
- 11 P. GRIFFITH, J.A. CLARK & W.M. ROSENOW, "Void volumes in subcooled boiling system," ASME-AIChE Heat Transfer Conference, paper 58-HT-19, Chicago, August 1958.
- 12 N. ZUBER, F.W. STAUB, G. BIJWARD & P.K. KROEGER, "Steady state and transient void fraction in two phase flow systems," EURAE C, GEAP-5417, Joint US-EURATOM Research and Development Program, Volume 1, 1967.
- 13 NRC Letter, Robert Jones to J. H. Taylor, "Acceptance of Revised Measurement Uncertainty for Control Rod Worth Calculations," January 26, 1996.
- 14 NRC Letter, James E. Lyons to J. H. Taylor, "Acceptance of Revised Measurement Uncertainty for Westinghouse 193 Plant Control Rod Worth Calculations," April 14, 1997.
- 15 H. A. Hassan, et al., "Power Peaking Nuclear Reliability Factors," BAW-10119P, Babcock & Wilcox, Lynchburg, Virginia, June 1977.
- 16 M. N. Baldwin and M. E. Stern, "Physics Verification Program -- Part III, Tasks 4, Summary Report", BAW-3647-20, Babcock & Wilcox, Lynchburg, Virginia, March 1971.

- 17 L. W. Newman et al., "Urania Gadolinia: Nuclear Model Development and Critical Experiment Benchmark," DOE/ET/34212-41, BAW-1810, April 1984.
- 18 "Assessment of the Assumption of Normality (Employing Individual Observed Values)," American National Standard N15.15 (1974).
- 19 P. N. Somerville, "Tables for Obtaining Non-Parametric Tolerance Limits," Annals of Mathematical Statistics, Volume 29, No. 2, pp. 599-601 (1958).
- 20 C. A. Bennett and F. L. Franklin, Statistical Analysis in Chemistry and in the Chemical Industry, John Wiley & Sons, New York, New York (1961).
- 21 "Reload Startup Physics Tests for Pressurized Water Reactors," American National Standard ANSI/ANS-19.6.1-1997, August 1997.

Appendix A

Documented Response for Informal  
NRC Request for Additional Information

# FRAMATOME COGEMA FUELS

September 23, 1999  
GR99-193.doc

U. S. Nuclear Regulatory Commission  
ATTN: Document Control Desk  
Washington, DC 20555

Subject: Topical Report BAW-10228P, "SCIENCE."

Gentlemen:

During of the course of the review of the subject topical report, Framatome Cogema Fuels (FCF) has provided additional information to the NRC for the purpose of clarifying certain portions of the document. The purpose of this letter is to provide a formal submittal of that information.

Attachment 1 includes the responses to three questions that were raised by the NRC reviewer. This attachment discusses revisions to portions of BAW-10228P. These revisions will be included in the accepted (A) version of the report after the SER is issued. Attachment 2 is a summary of the applications that the SCIENCE code may be used for as well as certain limitations on the code and its use. FCF will restrict its use of SCIENCE to those items listed in Attachment 2.

FCF is not aware of any additional technical issues related to BAW-10228P. In order to complete the engineering activities, including training, associated with the implementation and procedure documentation, NRC approval of SCIENCE is requested by October 31, 1999.

Very truly yours,



T. A. Coleman, Vice President  
Government Relations



Framatome Cogema Fuels  
3315 Old Forest Road, P.O. Box 10935, Lynchburg, VA 24506-0935  
Telephone: 804-832-3000 Fax: 804-832-3663

Attachment 1

- 1) Please clarify the significance of the negative bias in table 4-9 and the difference in the bias between 15x15 and 17x17 rod worth results.

The negative bias for the "SCIENCE Adjusted for  $S_N$ " rod worths results implies that the rod worths are conservatively underpredicted relative to the measured results for the 15x15 fuel.

Section 4.1 was also modified to more clearly address this issue. The modified section 4.1 will be included in the accepted (A) version of BAW-10228P.

- 2) In table 5-2, please provide a description of each criterion.

Section 5 was modified to more clearly define each criterion. The modified section 5 will be included in the A version of BAW-10228P.

In addition, why is the criterion for critical K-effective not in terms of a tolerance factor?

Plant to plant biases in k-effectives are both observed and accounted for in our application methodology. This approach is consistent with reference A that states "This bias is taken into account when the model is used to make AROCBC predictions." There are plant dependent phenomenon that could cause a bias from plant to plant that are impractical to resolve. The power level, moderator temperature, and  $B^{10}$  depletion from soluble boron biases at the plant are some plant dependent characteristics that could produce critical K-effective biases.

- 3) In section 5, a discussion is provided for the case where a lower uncertainty is calculated with new methodology and FCF intends to use the lower uncertainty. FCF states that they will provide a submittal to the NRC. The NRC requests that the submittal also include a description of the methods responsible for the improved results.

The text in section 5 was updated to include this request. The updated text in section 5 will be included in the A version of BAW-10228P.

References

- A) BAW 10120P-A, "Comparison of Core Physics Calculations with Measurements," J. J. Woods et al, March 1978.

Attachment 2

SCIENCE Applications

1. The SCIENCE code package shall be applied in a manner that predicted results are within the ranges of the validation criteria, presented in section 5 and illustrated in Table 5-2.
  
2. Fuel designs to which the SCIENCE code package will be applied shall be within the validation bases of BAW-10228P. The bases of BAW-10228P are considered valid for the following conditions:
  - 15x15 or 17x17 UO<sub>2</sub> fuel designs
  - U235 enrichments less than or equal to a maximum of 5.0 w/o.
  - Gadolinia loadings less than or equal to 8.3 w/o (nominal 8.0 w/o).
  
3. The following uncertainties shall be applied to the SCIENCE code package results:
  - Maximum pin peaking uncertainty of 3.8%
  - Maximum pellet peaking uncertainty of 4.8%
  - Total rod worth uncertainty of 10%
  - Bank rod worth uncertainty of 15%
  
4. The SCIENCE code package shall only be used for PWR licensing analyses by FCF unless approved by the NRC for use by other organizations